ISBN 978-82-326-4190-1 (printed ver.)
ISBN 978-82-326-4191-8 (electronic ver.)
ISSN 1503-8181

Doctoral theses at NTNU, 2019:297

Marnix van den Berg

Discrete Numerical Modelling of the Interaction Between Broken Ice Fields and Structures

Marnix van den Berg

Doctoral thesis

Doctoral theses at NTNU, 2019:297

NTNU
Norwegian University of Science and Technology
Thesis for the Degree of
Philosophiae Doctor
Faculty of Engineering
Department of Civil and Environmental
Engineering

NTNU
Norwegian University of
Science and Technology

NTNU
Norwegian University of
Science and Technology

NTNU

Marnix van den Berg

Discrete Numerical Modelling of the Interaction Between Broken Ice Fields and Structures

Thesis for the Degree of Philosophiae Doctor

Trondheim, October 2019

Norwegian University of Science and Technology
Faculty of Engineering
Department of Civil and Environmental Engineering

NTNU
Norwegian University of
Science and Technology

NTNU
Norwegian University of Science and Technology

Thesis for the Degree of Philosophiae Doctor

Faculty of Engineering
Department of Civil and Environmental Engineering

ISBN 978-82-326-4190-1 (printed ver.)
ISBN 978-82-326-4191-8 (electronic ver.)
ISSN 1503-8181

Doctoral theses at NTNU, 2019:297

Printed by NTNU Grafisk senter

Abstract

Loads from broken ice may be the design load for structures or operations in ice covered waters. An accurate determination of the broken ice loads is important in the design phases of such structures and operations. A more accurate load assessment will lead to safer and more economical designs. In the past, loads from broken ice have been mainly assessed by full-scale measurements and scale-model tests. However, both methods have several downsides. For instance, full-scale measurements are expensive and can only be performed on existing structures and operations. It is uncertain to what extend the results from scale-model tests can be directly scaled to full-scale equivalent conditions. Numerical modelling can be a valuable additional tool to assess loads from broken ice. Numerical models can help clarify the relevant interaction phenomena. In addition, numerical models can be used to predict ice loads in conditions for which no scale-model tests or full-scale measurements are available.

In this thesis, a novel implicit three dimensional discrete element method is derived. The method can be classified as a non-smooth discrete element method (NDEM). However, the method is able of handling both smooth as well as non-smooth contacts. Ice-ice and ice-structure contact forces are implicitly calculated in each time step by solving a mixed linear complementarity problem. The contact restoring forces are calculated using the exact contact geometry and the material properties of the interacting bodies. The newly derived discrete element method (DEM) and contact models are combined with a hydrodynamic model based on skin friction and form drag coefficients, and an ice failure model based on a semi-analytical solution approach. The combined model is subsequently used to study interaction phenomena in the interaction between structures and a broken ice field.

First, the model is applied to study the effect of floe shape on the load experienced by vertical-sided structures interacting with a broken ice field. A sensitivity study is performed in which the influence of other model parameters on the floe shape effect is assessed. The results show that the floe shape is an important parameter in the assessment of ice loads on vertical-sided structures in broken ice, in ice concentrations ranging from 30% to 70%. Loads from a broken ice field with square floes can be up to 88% higher than loads from an equivalent broken ice field with more natural floe shapes.

Secondly, the variability in ice-tank test results in broken ice tests is assessed. It is found that important ice load properties such as the mean ice load, load standard deviation and the maximum load are strongly influenced by changes in the initial positions of ice floes. It is shown that the variability observed in the numerical simulations can be linked to specific interaction events, such as the formation of a force chain between the structure and the tank wall. The interaction events that occur in the numerical simulations are also observed in the physical ice tank tests, showing that the resulting load variability is not merely a numerical phenomenon. The load variability can be partly accounted for by considering the change in ice concentration during a test run. Based on this, it is recommended that ice tank tests be equipped with a camera system capable of capturing the complete broken ice field during a test, rather than only the ice in the direct vicinity of the structure. Such system would enable the post-processing of the visual data, such that the ice concentration change during the test can be calculated and taken into account.

The investigated phenomena of floe shape effects and test result variability demonstrate that numerical modelling is a valuable tool, in addition to scale-model testing and full-scale measurements, to study the interaction between structures and broken ice.

Preface

This work has been submitted in partial fulfilment of the requirements for the PhD degree at the Faculty of Engineering Science and Technology of the Norwegian University of Science and Technology (NTNU). The candidate was supervised by Professor Sveinung Løset (Department of Civil and Environmental Engineering and co-supervised by Associate Professor Raed Lubbad (Department of Civil and Environmental Engineering).

This thesis was funded by the Research Council of Norway through NTNU's Research Centre for Sustainable Arctic Marine and Coastal Technology (SAMCoT) and by the participating companies.

Declaration of authorship

Publications included in the thesis:

1. van den Berg, M., Lubbad, R. and Løset, S. (2018), 'An Implicit Time-Stepping Scheme and an Improved Contact Model for Ice-Structure Interaction Simulations', *Cold Regions Science and Technology* **155**, 193–213.

   van den Berg developed the described method and wrote the paper. The co-authors helped in the method development and in writing the manuscript.

2. van den Berg, M. (2016), A 3-D Random Lattice Model of Sea Ice, *in* 'Arctic Technology Conference. St. Johns, Newfoundland and Labrador'.

   van den Berg wrote the entire paper and generated all presented results.

3. van den Berg, M., Lubbad, R. and Løset, S. (2017), Accuracy of a Non-Smooth Time Stepping Scheme with Non-Rigid Contacts for Ice-Structure Interaction, *in* 'Proceedings of the 24th International Conference on Port and Ocean Engineering under Arctic Conditions', Busan, Korea.

   van den Berg wrote the paper and generated the presented simulation results. The co-authors helped in writing the paper.

4. van den Berg, M., Lubbad, R. and Løset, S. (2019*a*), The effect of floe shape on the interaction of vertical-sided structures with broken ice, *in* 'Proceedings of the 25th International Conference on Port and Ocean Engineering under Arctic Conditions', Delft, The Netherlands.

   van den Berg wrote the paper and generated the presented simulation results. The co-authors helped in writing the paper.

5. van den Berg, M., Lubbad, R. and Løset, S. (2019*b*), 'The effect of ice floe shape on the load experienced by vertical- sided structures interacting with a broken ice field', *Marine Structures* **65**, 229–248.

   van den Berg performed the described simulations and wrote the paper. The co-authors helped with the determination of parameters to be varied in the sensitivity study and in writing the paper.

6. van den Berg, M., Lubbad, R. and Løset, S. (submitted), 'Variability in the results of ice-tank tests with broken ice', *submitted to Marine Structures*

van den Berg performed the described simulations and wrote the paper. The co-authors helped in finding relevant ice tank test data and in writing the paper.

Other publications to which the author contributed during the course of the PhD study, but which are not included in the thesis:

1. Lubbad, R., Løset, S., Lu, W., Tsarau, A. and van den Berg, M. (2018*a*), 'An overview of the Oden Arctic Technology Research Cruise 2015 (OATRC2015) and numerical simulations performed with SAMS driven by data collected during the cruise', *Cold Regions Science and Technology* **156**, 1–22.

   van den Berg was the main developer of the model used to perform the numerical simulations and generated the demonstrated simulation results. van den Berg partly wrote the section describing the numerical method.

2. Lubbad, R., Løset, S., Lu, W., Tsarau, A. and van den Berg, M. (2018*b*), Simulator for Arctic Marine Structures (SAMS), *in* 'Proceedings of the ASME 2018 37th International Conference on Ocean, Offshore and Arctic Engineering', American Society of Mechanical Engineers.

   van den Berg was the main developer of the model used to perform the numerical simulations.

3. Tsarau, A., van den Berg, M., Lu, W., Lubbad, R. and Løset, S. (2018), Modelling Results With a New Simulator for Arctic Marine Structures-SAMS, *in* 'ASME 2018 37th International Conference on Ocean, Offshore and Arctic Engineering', ASME.

   van den Berg was the main developer of the model used to perform the numerical simulations and wrote part of the case studies section.

4. van den Berg, M. and Løset, S. (2015), A concept design for a meso-scale floater to measure downward bending failure ice loads, *in* 'Proceedings of the 23rd International Conference on Port and Ocean Engineering under Arctic Conditions', Trondheim, Norway.

   van den Berg partly developed the concept design and wrote the paper. The co-author helped in the development of the concept design and in writing the paper.

5. Raza, N., van den Berg, M., Lu, W. and Lubbad, R. (2019), Analysis of Oden Icebreaker Performance in Level Ice using Simulator for Arctic Marine Structures (SAMS), *in* 'Proceedings of the 25th International Conference on Port and Ocean Engineering under Arctic Conditions', Delft, The Netherlands.

   van den Berg is the main developer of the numerical simulator that is used, he performed the numerical simulations and helped in writing the paper.

6. van den Berg, M., Lubbad, R., van den Berg, M. and Lubbad, R. (2015), The application of a non-smooth discrete element method in ice rubble modeling, *in* 'Proceedings of the 23rd International Conference on Port and Ocean Engineering under Arctic Conditions', Trondheim, Norway.

   van den Berg performed the described simulations, analysed the results and wrote the paper. The co-author helped in writing the paper.

Acknowledgements

First of all, I would like to thank my supervisor Professor Sveinung Løset and co-supervisor Associate Professor Raed Lubbad for their guidance, trust and support during this project. In moments of doubt, you reassured me and helped me to stay motivated. The opportunities you offered to gain real-life Arctic experience on Oden and on Svalbard were very valuable.

I greatly appreciate the entertaining lunch discussions and movie night with my friends and colleagues from NTNU, Dr. Wenjun Lu, Dr. Andrei Tsarau, Dr. Torodd S. Nord, Dr. Sergey Kulyakhtin, Dr. Anton Kulyakhtin, Anna Pustogvar, Runa A. Skarbø, Dr. Åse Ervik, Lars Einar Stieng, Martina Salomon, Helene Seyr, Julie Lepage, Dr. Gordon Steward, Dennis Monteban, Hongtao Li, Evgenii Salganik, Ilija Samardzija, Weichi Wang, Dr. Tu Ying, Dr. Arun Kamath and Dr. Wolfgang Kempel. You always made it fun to be in Trondheim again. Wenjun and Andrei, it was a great experience to work with you on the combined model which I used to perform the analyses that make up an important part of the PhD work. Without your contributions on hydrodynamics and ice failure, this would not have been possible.

I would also like to thank Professor Jørgen Amdahl, Associate Professor Ekaterina Kim, Dr. Zhaolong Yu, Professor Roger Skjerne and Dr. Øivind Kåre Kjerstad for the interesting and broadening collaborations we had thought ArcISo. Further, I would like to thank Sigurd Pettersen and Adjunct Professor Stein Inge Dale of Ceetron solutions for their programming suggestions and comments.

It was a privilige to work with my Arctic colleagues from TU Delft, Chris Keijdener, Dr. Hayo Hendrikse, Dr. Renate van Vliet, Professor Andrei Metrikine, Jeroen Hoving and Associate Professor Kay Riska. You always provided a sounding board for my ideas when one was needed. Andrei, thank you for the hospitality provided at TU Delft, and for getting me involved in this project. My room mates Chris, Hayo, Renate, Frank Renting, Yaxi Peng, and Andrei Faragao made it worthwhile to come to office daily and discuss the benefits and downsides of PhD life.

Finally, and most importantly, I want to thank my wife Moniek, my son Jan and my parents Annemarie and Ebart for keeping their trust and their continued support in the last five years. Moniek and Jan, Thank you for putting up with my frequent

trips to Norway and the absent-mindedness that the PhD sometimes caused. I know it was not always easy for you when I was away from home, and you had to take care of Jan by yourself. I am grateful that you gave me the freedom to pursue this goal.

List of abbreviations

NDEM	non-smooth discrete element method
MLCP	mixed linear complementarity problem
CSE	crushing specific energy
AABB	axis-aligned bounding box
GJK	Gilbert-Johnson-Keerthi
DOF	degrees of freedom
COG	centre of gravity
COD	crack opening displacement
LEFM	linear elastic fracture mechanics
HSVA	Hamburg Ship Model Basin
PIC	particle in cell
CEM	cohesive element method
SPH	smooth particle hydrodynamics
CFD	computational fluid dynamics

Contents

Chapter 1

Introduction

Structures that may encounter drifting ice must be designed to withstand ice loads. Under certain conditions, loads from broken ice fields may be the governing design load for a structure. The conditions under which loads from broken ice may be the governing design load include: structures supported by ice management; structures in rivers; and structures capable of evacuating the location when ice conditions become too severe. A proper understanding of the ice loads that may result from sets of field parameters can lead to a more accurate definition of the design requirements and abandonment criteria for such structures. This may contribute to safer structures and operations in ice covered waters.

Model-scale tests and the analysis of full-scale data have historically been the two main methods of assessing the loads from broken ice. Although model-scale testing and full-scale data analysis remain valuable tools in assessing the loads from broken ice, both methods also have various shortcomings:

full-scale measurements:

- What can be measured depends on the conditions that occur; there is no control over the test conditions.
- Only existing full-scale structures in operation can be analysed; no data can be acquired on novel structure geometries.
- Only some parameters that are of influence on the ice load can be measured; there is no full overview of the loading conditions.
- There may be a high uncertainty in the measured loads, depending on the measurement techniques used.
- It is expensive and time consuming to carry out the measurements, given the remote locations of many structures loaded by ice, and the harsh environments at these locations.

model-scale testing:

- It is often unclear if broken ice loads measured in model scale can be scaled to full-scale. The scaling may affect the ice failure mode.
- Model-scale ice is often too strong compared to the full-scale-equivalent conditions the test intends to model.
- The ice floe size in relation to the tank size, the ice floe shape, and floe edge roughness may significantly influence the ice loading in an undesirable manner.
- The interaction length is limited, and the ice conditions are often non-stationary, leading to a questionable statistical significance of the test results.
- The tests have limited repeatability - uncontrollable conditions, such as the initial positions of ice floes, may have a significant influence on the measured ice loads.

Numerical simulations can contribute to a more complete understanding of the loads from broken ice. Once a numerical model has been created, none of the shortcomings of full-scale measurements and model-scale testing apply, and the numerical model can be used to test for a much wider range of environmental parameters than would be possible in model-scale tests or full-scale measurements.

In this thesis, a numerical model is developed for the application case of interaction between structures and broken ice. More specifically, the model's primary area of applicability are interaction scenarios in which:

- The inertia of individual intact ice floes significantly influences the ice loads experienced by the structure.
- The interaction between the floes in the broken ice field influences the loads experienced by the structure.

For such interaction scenarios, discrete models are the most logical model choice. Continuum models, meaning, in this context, models that approximate the whole broken ice field as a continuum, are not capable of capturing both the inertial effects of individual ice floes as well as the influence of floe interactions.

In current engineering practice, a distinction is often made in the assessment of ice loads between different load-limiting mechanisms; limit stress, limit force and limit momentum. The developed model is intended for scenarios in which all three

limiting mechanisms should be considered. As an example, consider a moored structure in a drifting broken ice field where the ice floes are roughly of the same size as the structure. Such conditions often occur when ice is broken by environmental forces such as gravity waves, wind and current stress, or by ice management. When a single ice floe impacts the structure, the load is initially limited by limit stress. Local crushing will occur, and the contact area between the ice floe and the structure increases, as does the ice load. This process will continue until the ice floe is stopped by the structure (limit momentum) or fails in another manner, such as splitting. The ice floe in direct contact with the structure experiences forces from wind and current drag, as well as forces from the interaction with other ice floes (limit force). Since the structure is moored, both the peak ice loads (for local damage) as well as the time-averaged ice loads (for loading on the mooring system) are important. Therefore, all occurring interaction processes must be taken into account in a numerical model for this scenario; the local crushing failure, other failure modes like bending or splitting failure, the dynamics of individual intact ice floes, and the interaction between ice floes in a broken ice field.

Interaction between broken ice and structures is a complicated process. There are many factors that may contribute to the load and resistance experienced by a structure interacting with broken ice, and that pose challenges to the accurate numerical representation of the occurring processes. For example:

- many simultaneously contacting ice bodies,
- complicated, and (seemingly) random body geometries,
- difficult to estimate and highly variable ice material properties,
- complicated hydrodynamic effects,
- complicated and continuous dynamic fractures and failures.

This combination of factors makes ice-structure interaction different from any other engineering problem. A numerical model will need to simplify some or all of the above-mentioned factors. To what extent the parameters can (and need to) be simplified depends on the processes to be investigated and limiting factors such as the available computing power and computation time, as well as the availability and accuracy of input parameters. The broad range of occurring processes and the different requirements that may be put upon numerical models, has led to a broad range of models and modelling types. The different modelling types ap-

plied in ice-structure interaction modelling, as well as state-of-the-art application examples of discrete numerical modelling in studies on ice structure interaction, are discussed in Chapter 2.

The numerical method developed in this thesis can be classified as a non-smooth discrete element method (NDEM). The method is capable of accurately capturing the contact restoring forces in accordance with the contact assumptions that are made. A contact model is defined based on the exact contact geometry and the material properties of the interacting bodies. The combination of NDEM with an accurate contact model that uses both the contact geometry as well as the material properties of the interacting bodies is novel in the field of ice structure interaction. Hydrostatic and hydrodynamic forces are included in the model, as is ice failure. The different components of the model are highlighted in Figure 1.1. The numerical method is derived in Chapter 3.

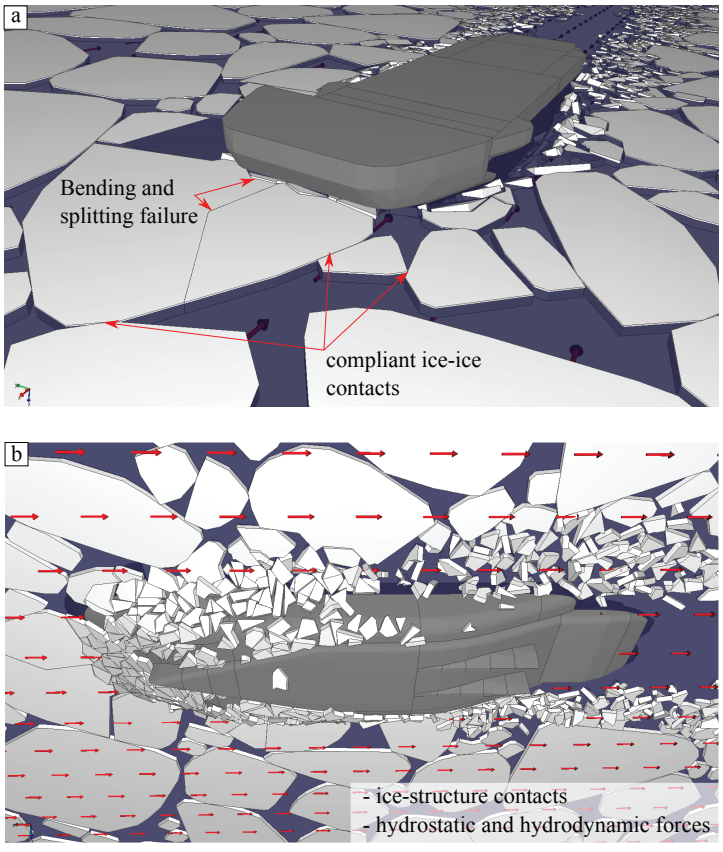

Figure 1.1: Overview sketch highlighting the components of the numerical model. Above-water view (a) and underwater view (b).

The model is applied to study the effect of floe shape in the interaction of vertical-sided structures and broken ice, and to study the variability in ice tank test results to changes in the initial positions of ice floes. Both phenomena are currently poorly understood, and the numerical modelling results show that floe-shape effects and result variability should be taken into account in the design and interpretation of ice tank tests in broken ice. These applications of the numerical model are described in Chapter 4.

Chapter 5 discusses important questions regarding the purpose, the development process, the validation and the application of numerical models of ice-structure interaction.

Finally, Chapter 6 summarizes the main results of the studies performed in this thesis, and gives recommendations that follow from these results.

Chapter 2

State of the art

Discrete numerical modelling has been applied in research on ice-structure interaction for over 30 years. This chapter gives an overview of the most important and most recent contributions in numerical modelling of ice-structure interaction and its applications. First, an overview of possible modelling techniques is given. Then, this chapter presents an overview of studies on ice-structure interaction phenomena in which discrete numerical modelling techniques are applied. Lastly, the important topic of model parameter determination is discussed.

2.1 Numerical modelling approaches

Model: "*A representation of some object, behavior, or system that one wants to understand.*" (Koperski, 2019).

Models are an important scientific tool to understand the world and to extrapolate upon direct observations. Modelling approaches can be subdivided in three categories:

- empirical models,
- phenomenological models,
- physics-based models.

Empirical models are based on measurements and/or observations. A model is constructed or fitted to the measurements, with little or no consideration of the underlying physics. Phenomenological models aim to capture a specific phenomenon by modelling the processes that are important for that specific phenomenon. All other factors are simplified as much as possible. Physics-based models are constructed starting from the fundamental laws of physics. The aim is to better understand an observed phenomenon by accurately capturing the underlying physics in

a model. The distinction between the modelling types is not rigid. Most models are constructed using a combination of empirical, phenomenological and physics-based components.

In the context of ice-structure interaction, the earliest models were of the empirical kind. Early models consisted of formulas that were fitted to measured or observed data. The first numerical models were used in the sixties. An example is Matlock's model (Matlock et al., 1969); a phenomenological model for the prediction of ice-induced vibrations.

Physics-based models of ice-structure interaction often rely on a subdivision of the calculation domain into parts. A distinction can be made between continuum and discrete models, although there are also models that combine continuum and discrete approaches. In addition, there are models that are not easily classified as either continuum or discrete.

Continuum models apply a variant of the finite element method (FEM), whereas discrete models use the discrete element method (DEM). Which modelling technique is most applicable depends on the phenomenon one wants to model. Modelling approaches that are not easily classified as either continuum or discrete include the particle-in-cell (PIC) method, the Peridynamics method, smooth particle hydrodynamics (SPH) and the cohesive element method (CEM). The method developed in this thesis can be classified as a discrete element method.

2.1.1 The discrete element method

Discrete element methods model physical phenomena by considering the motion of many interacting bodies. DEM was introduced by Cundall and Strack (1979). DEM's can be divided in two types: *smooth* discrete element methods (SDEM) and *non-smooth* methods (NDEM). In NDEM, the positions and velocities of bodies are not required to be smooth functions. A major difference between smooth and non-smooth methods is the solution procedures that are applied to find the contact responses. Whereas smooth methods use explicit time integration procedures in combination with penalty functions, non-smooth methods necessitate the use of implicit time integration procedures.

Because of the implicit solution procedure, the stability in NDEM methods is independent from the time step size. This allows for time step sizes that are often several orders of magnitude larger than the time step sizes used in SDEM. However, each time step is more computationally demanding in NDEM. Which method is most efficient (for a comparable level of accuracy) depends on the modelled scenario.

The Non-smooth discrete element method

Two procedures can be used to resolve the contact responses in NDEM; contacts can be resolved sequentially or the contact response can be solved simultaneously (Erleben, 2005).

In sequential methods, the order in which the contact forces or impulses should be applied is determined based on the velocities of the bodies and the contact distances. The contact responses are sequentially applied to the bodies in the order in which the contacts are predicted to occur. In each contact response, the effect on the velocity of the contact forces or impulses occurring earlier is taken into account. The time step in this method is governed by the frequency by which the contacts occur; the solution method makes an estimate of the exact collision time based on an extrapolation of the body positions and velocities. In this method, resting contacts can pose a challenge, although solutions have been conceived to deal with resting contacts as well. This method is described in, among others, Mirtich (1996). In ice-structure interaction, this method is applied by Daley et al. (2012); Alawneh et al. (2015).

The method developed in this thesis considers the contacts simultaneously. Simultaneous contact response methods extrapolate the body positions and velocities to find all potential collisions within a pre-defined time step size. All collisions in this time step are assumed to occur at the beginning of the time step. The impulse response at each contact is calculated while taking into account the impulses that occur at other contacts. A system of equations and inequalities is formulated which takes into account the contact geometries, the inertia and velocity of the bodies, and any external (non-contact) forces working on the system. The resulting system of equations and inequalities can be formulated as a Linear Complementarity Problem (LCP) or a Mixed Linear Complementarity Problem (MLCP). An MLCP contains equations as well as inequalities.

The MLCP can be formulated in different ways. Lötstedt (1982) gave a formulation in which the body accelerations and contact forces are the solution of the formulated system, and showed that a solution always exists for zero-friction contacts. Baraff (1989) also used an accelleration based formulation and included friction. However, a solution cannot always be found using this formulation if friction is included (Baraff, 1993). Anitescu and Potra (1997) showed that a solvable system with contact friction can be formulated if the LCP is formulated such that the body velocity change and contact impulse are the unknowns. Such formulations were constructed by Moreau (1988); Stewart and Trikle (1996). Most early NDEM methods treat contacts as rigid. NDEM methods that deal with com-

pliant as well as rigid contacts were formulated by Jean (1999); Moreau (1999); Lacoursière (2007); Krabbenhoft et al. (2012); Tasora et al. (2013); Servin et al. (2014).

The method derived in this thesis is also capable of handling both rigid (non-smooth) and compliant (smooth) contacts. The difference between previously applied methods and the method described in this thesis is that the current method assures energy conservation for continuous linear contacts. This property follows from the use of the Newmark-Beta method (Newmark, 1959) in the derivation of contact compliance parameters. The other methods are derived from an implicit Euler or similar schemes, and therefore result in numerical damping. Because the implicit time integration scheme is the defining feature of the method derived in this thesis, rather than the smooth or non-smooth nature of the contacts that are resolved, the method is described as an implicit DEM method, rather than as a non-smooth method. This terminology was adapted earlier by Stewart and Trikle (1996). Servin et al. (2014), on the other hand, describe their similar method as semi-smooth DEM.

2.2 The modelling of interaction between structures and broken ice

One of the first applications of DEM to ice-structure interaction processes was described in Hocking et al. (1985). In this study, the application of DEM to ice ridge-cone interaction was described. Other notable early work was performed by Mark Hopkins (Hopkins et al., 1991; Hopkins and Hibler III, 1991*a*,*b*,*c*; Hopkins, 1992) and Sveinung Løset (Løset, 1994*a*,*b*). Although the work by Hopkins does not include a structure, the demonstrated modelling capabilities included all the components needed for the modelling of ice-structure interaction.

Current developments and applications of DEM modelling in research on ice-structure interaction can roughly be divided per country. A single modelling technique is predominantly applied in each country. This likely results from the fact that DEM ice-structure modelling studies often originate from a single institution or a single research group in each country.

In Canada, sequential NDEM is predominantly applied (Daley et al., 2012, 2014; Alawneh et al., 2015). The focus in this method is mainly on computational efficiency. An important feature of the method is that it uses the GPU, and can perform simulations faster than real time. An SDEM model has been developed by C-Core (Morgan, 2016; Yulmetov et al., 2017). The primary aim of this model is to study ice ridge-structure interaction.

The research from Finland applies SDEM (Ranta et al., 2017, 2018*b*,*c*,*a*; Polojärvi and Tuhkuri, 2009; Paavilainen et al., 2009; Polojärvi et al., 2015; Gong et al., 2019). The SDEM model originating from Aalto University has been applied extensively in studying discrete ice-structure interaction phenomena. This is one of the most well established models in the ice-structure interaction modelling community. The model has been applied to study the statistics of ice loads resulting from the ice failure process (Ranta et al., 2017, 2018*b*,*c*,*a*) and to study the resistance and mechanical properties of ice rubble Polojärvi and Tuhkuri (2009); Polojärvi et al. (2015); Gong et al. (2019). Models from China (Liu and Ji, 2018; Ji et al., 2015) and Russia (Karulin and Karulina, 2017) also apply SDEM.

Recent Norwegian studies apply NDEM (Lubbad and Løset, 2011; Metrikin, 2014; Yulmetov et al., 2016; Metrikin et al., 2015; Nicolas et al., 2019; Lubbad et al., 2018*a*; Lu and Amdahl, 2019; Tsarau et al., 2018; Raza et al., 2019; Lubbad et al., 2018*b*; van den Berg et al., 2018, 2019*b*,*a*; van den Berg, 2016; van den Berg et al., 2015, 2017; Su et al., 2019). The method presented in this thesis can be considered as part of this group of studies. The methods from Norway focus on the 3D modelling of ships and structures interacting with a broken ice field. Models from France (Rabatel et al., 2015) and Japan (Konno and Mizuki, 2006; Konno et al., 2011) also apply NDEM. Konno and Mizuki (2006); Konno et al. (2011) study the resistance of a ship in a brash ice channel.

The PIC method is applied to study the interaction between a structure and a broken ice field by Sayed and Kubat (2011); Sayed and Barker (2011); Islam et al. (2019). The use of the peridynamics method is demonstrated by Liu et al. (2018). The CEM method is applied by, among others, Lu, Lubbad and Løset (2014); Zhang et al. (2019). Studies describing the applications of peridynamics and CEM mainly focus on the method and validation of the method applicability. So far, these methods are seldomly used to study the ice-structure interaction process itself.

A promising new numerical model is demonstrated by Janßen et al. (2017). Janßen et al. (2017) combines DEM with Computational Fluid Dynamics (CFD). Existing DEM models applied in ice-structure interaction often consider the fluid dynamics in a greatly simplified manner. This weakness can potentially be resolved by the combination of DEM with CFD.

2.3 Physical parameters in DEM models of ice structure interaction

Discrete numerical models of ice-structure interaction simplify parts of the physical processes because of constraints on calculation time and computer power. What processes are simplified, and how the simplification is achieved, depends

on the model demands. The simplification of physical processes introduces the need for model input parameters. Some of these parameters, such as the gravitational acceleration and the density of water, can be accurately estimated. Other model parameters have a higher degree of uncertainty. In DEM models of broken ice-structure interaction, simplifying representative coefficients are often specified for:

- hydrodynamics,
- contact behaviour,
- ice mechanical properties.

For most coefficients, there is currently no agreement within the ice modelling community on how representative values can be determined and what values should be used. The following sections give an overview of methods and sources that can be/are used to determine model input parameters.

2.3.1 Hydrodynamics

Existing DEM methods applied in ice-structure interaction often use simplifying approximations to estimate the hydrodynamic forces because of the high computational load associated with more advanced hydrodynamics models. The simplified approximation of hydrodynamic forces limits the model applicability to low interaction velocities (reducing the significance of hydrodynamic forces) or necessitates the tuning of the hydrodynamic coefficients to specific interaction scenarios. Some studies that apply DEM modelling in ice-structure interaction do not describe at all how hydrodynamic forces are considered. This is a significant weakness, as hydrodynamic forces often give a significant contribution to the total ice resistance.

In the DEM model and its applications as described in this thesis, hydrodynamics is considered by form drag and skin friction coefficients. This method is described in Tsarau (2015). The applied drag coefficients are partly based on the values determined by Tsarau et al. (2017). The values as determined by Tsarau et al. (2017) are modified based on the modelled conditions.

2.3.2 Contact properties

A local contact model that considers the mechanical properties of sea ice is essential for DEM models that consider ice failure and for models aimed at predicting load statistics. The contact behaviour in DEM models usually consists of a method to define the force-penetration behaviour and a method that describes the frictional contact properties. For some of the interaction scenarios studied in this thesis, the

contact rafting behaviour is also important. This section describes the contact assumptions made in existing DEM models in order to define contact properties for the force-penetration behaviour, contact friction and the rafting behaviour.

Force-penetration behaviour

Most DEM models define a contact model based on the assumption that local contact crushing is the mechanism governing the contact force. Models using an assumption of local contact crushing define the contact properties based on a crushing pressure or crushing specific energy (CSE). Although it is generally recognized that these properties are geometry dependent, the geometry dependence is neglected in most DEM models.

In codes and standards, the crushing pressure that should be used in design calculations is dependent on the contact area and aspect ratio (ISO 19906, 2018). This assumption is also used in Nicolas et al. (2019). However, the crushing pressure obtained by this method is the *maximum* global crushing pressure. It can be questioned if this is a proper way of calculating the contact forces in a time-domain DEM simulation. Therefore, most methods instead define a constant crushing pressure which is more representative of the *average* global crushing pressure. For example, Hopkins (1992); Paavilainen et al. (2011); Keijdener and Metrikine (2014); van den Berg et al. (2018) assume a constant crushing pressure (or plastic limit stress) during indentation. Using a constant crushing pressure is supported by Kim and Høyland (2014) and Kim and Gagnon (2016). Kim and Høyland (2014) suggest that the crushing specific energy (CSE) of ice might be a scale-independent parameter, at least for geometrically similar situations. Kinnunen et al. (2016) also suggest that the CSE value remains stable during an impact event. Daley (1999), on the other hand, assumes a crushing pressure that is dependent on the contact geometry and area.

Friction coefficients

Contact friction results from a combination of material properties and geometrical properties of the interacting bodies. All global models of ice-structure interaction use a greatly simplified friction model, where the frictional contact behaviour is often captured by a single or several coefficients. There is almost an order of magnitude difference between the friction values used in models. Friction coefficients used in discrete numerical modelling of ice-structure interaction range from 0.1 (Haase et al., 2010; Tsarau et al., 2017; Hocking, 1992) to 1.35 (Konno et al., 2011) for ice-ice friction (lower values have been used in sensitivity studies). For interaction between ice and non-ice (structure, tank wall, etc.), values range from 0.027 (Lu, Lubbad, Høyland and Løset, 2014) to 0.2 (Metrikin and Loset, 2013).

All models use a Coulomb model of friction, and assume that the friction is isotropic. Some models distinguish between wet, dry, static and dynamic friction, while other models do not make this distinction. The used friction values are justified based on:

- direct friction measurements,
- tuning of the numerical results to measured values,
- reference to friction values used by others.

Some numerical studies do not offer a justification for the friction values used. The differences between the used friction values can partly be explained by the environmental conditions that are modelled and the processes the friction coefficients are supposed to simplify. For instance, the scale of the modelled ice conditions in the analysed DEM studies ranges from model-scale broken ice to geospatial-scale simulations of interacting ice floes. Temperature differences and surface properties of the non-ice bodies (rough concrete to smooth steel) also explain part of the differences.

The friction coefficients used in discrete numerical models should often be seen as effective friction coefficients, that also account for the simplification of body geometries; edge asperities of ice floes are often smoothed in the numerical representation of the floes. Following this logic, a numerical model that simulates all ice floes as disk-shaped bodies should apply a higher friction coefficient than a model that allows for more angular ice floes.

A wide range of friction values can be justified based on the modelled scenarios and the other modelling assumptions that are made. However, the friction values used in numerical models are often insufficiently linked to the physical phenomena the value is supposed to capture. This is an area where improvement is possible. The following improvements are proposed:

- Ice tank tests in broken ice should measure friction between ice floes as part of the test campaign. The friction should be measured separately for ice floe sides and for ice floe top and bottom surfaces, because of possible differences in roughness.
- If numerical friction coefficients are determined by model tuning (i.e., matching the model result, often the structure load, to a measured value), this should be clearly stated. Tuning can be a valid approach, as long as the tuned model is subsequently validated against other cases that were not used for the tuning.

- Because of the wide range of justifiable friction values, a justification should always be provided for the friction values chosen.

Rafting

There is no generally accepted model or mechanism to describe the rafting behaviour of broken ice. A mechanical model of sea ice rafting behaviour was presented by Parmerter (1975). This model is based on the assumption that the sides of the ice floes are non-vertical and that there is no friction between two interacting ice sheets. However, data on the 'non verticality' of the sides of broken ice is not known to the authors. Additionally, the zero-friction assumption is questionable. Broken ice rafting experiments were done in the 1990's, by Tuhkuri and Lensu (1997); Tuhkuri (2002). Numerical modelling of these experiments is described by Hopkins and Tuhkuri (1999). Hopkins and Tuhkuri (1999) modelled circular ice floes with hemispherical edges. To match the rafting behaviour as observed in the experiments, Hopkins and Tuhkuri (1999) introduced and tuned a 'circular edge friction coefficient' that varied with the ice thickness. This method relies on experimental data to determine appropriate values, and the values used in Hopkins and Tuhkuri (1999) cannot be simply translated to appropriate values for other ice floe sizes or thicknesses or to the appropriate full-scale values.

In the numerical model described in this thesis, rafting can occur as a result of the contact assumptions, even if the edges of interacting ice floes are completely vertical. The rafting mainly occurs as a numerical phenomenon, and does not necessarily resembles the rafting mechanisms as occur in reality. However, the rafting behaviour can be quantified well, and can be tuned to match observed rafting behaviour by changing the ice-ice friction coefficient. The rafting mechanism in the model described in this thesis is further explained in Section 3.3.2.

2.3.3 Ice material properties and ice failure

In most ice-structure interaction scenarios, ice failure cannot be neglected when modelling the ice-structure interaction process. Ice material properties must be specified for an accurate representation of ice failure. The most used source of sea ice material properties in engineering applications is the literature review published by Timco and Weeks (2010). This review provides full-scale engineering values for most mechanical properties of sea ice.

The material properties of ice-tank ice are often measured as part of a test campaign. However, the measured properties often do not include all properties needed for the numerical reproduction of the tests. For instance, the ice-ice and ice-structure friction coefficients and the fracture toughness of model-scale ice are often not measured. Dempsey et al. (1986) gives fracture toughness values of

model scale ice. However, this study is limited to the ice in a single ice tank. In addition, it is unclear what the intended model ice properties were in this study. The applied scaling factor is not reported.

The combination of numerical modelling and ice tank tests can offer far more insight in the occurring processes than either tests or numerical modelling alone. However, the accurate representation of ice tank test conditions in a numerical model necessitates that the relevant ice mechanical properties are accurately measured. Therefore it is recommended that fracture toughness and friction measurements are added to the measurements performed as part of an ice tank test campaign.

2.3.4 Parameter values used in the studies included in this thesis

In the studies included in this thesis, the model input parameters are based on measured values where possible. If measured values were not available, the input parameters were determined based on values used by others, or by tuning the model parameters to match the results to test data. The parameter values used are listed where relevant.

In some of the earlier publications included in this thesis, the procedure used to determine certain model input parameters is, in hindsight, insufficiently explained. In accordance with the opinions expressed in this section, the author will aim to provide a more clear explanation of input parameters in future publications.

Chapter 3

Implicit discrete element modelling of ice-structure interaction

In this chapter, a novel implicit discrete element time-stepping scheme is derived starting from the Newmark-Beta method for differential equations (Newmark, 1959). The new formulations are valid for compliant continuous and discontinuous contacts. The position and velocity update rules of the Newmark-Beta method are rewritten, and limits are introduced in order to enable discontinuous contact modelling. The derived scheme can be classified as a non-smooth discrete element method (NDEM). Compared to previously applied NDEM methods in ice-structure interaction modelling, where only an upper limit for the contact force was defined based on the current contact area, this new method takes the current contact area as well as the expected change in the contact area into account in determining the contact response, leading to a higher accuracy of the predicted contact force for the same time step size. The main properties of the NDEM method are maintained in the new method, i.e., a mixed linear complementarity problem (MLCP) is solved in each time step, and large time steps can be used without affecting the stability. In addition, the new method can handle compliant as well as rigid contacts. Since the method can handle both rigid (non-smooth) as well as compliant (smooth) contacts, the method is described as implicit DEM rather than as a non-smooth method. The term implicit is a better description of the distinguishing feature of the method than the term *non-smooth*.

Section 3.1 derives the implicit time stepping scheme. Section 3.2 provides some background on how the MLCP resulting from the time-discetization method is solved. The procedure used to derive the contact parameters of discontinuous ice-ice and ice-structure contacts is described in Section 3.3. Section 3.5 describes how ice failure is implemented in the model. Section 3.6 describes a random lattice model that can be combined with the implicit time stepping scheme. It also summarizes a partial verification of the lattice model. Finally, Section 3.7 summarizes the key properties of the DEM model presented in this Chapter.

3.1 An implicit DEM time-stepping scheme

The derivations in this section were published in van den Berg et al. (2018). This publication is included in Appendix A. Figure 3.1 shows the 1-DOF example case used for the derivations in this section. In this example case, a generalized Kelvin-Voight unit is used as the contact model, in which the parallel spring and dashpot element can be linear or nonlinear. The method can also be applied to other rheological elements, such as a Maxwell unit, following a similar procedure as described in this section. In Figure 3.1, m stands for the mass of the body, δ for the penetration depth, $\dot{\delta}$ for the penetration velocity, $F_{\text{cont}}(\delta, \dot{\delta})$ for the contact force as a function of the penetration and the penetration velocity, and F_{ext} stands for an external (non-contact) force acting on the body during time step $\Delta t = t_{n+1} - t_n$, where t_n is the current time and t_{n+1} is the time at the end of the time step. u, $\dot{u}$ and $\ddot{u}$ are the body position, velocity and acceleration, respectively. For convenience, the axis system is chosen such that $\delta = u$ if $\delta \geq 0$. In the derivations in this section, it is assumed that $\delta \geq 0$, and thus $F_{\text{cont}}(\delta, \dot{\delta}) = F_{\text{cont}}(u, \dot{u})$. This is expanded to a case in which $u \in \mathbb{R}$ in Section 3.1.1.

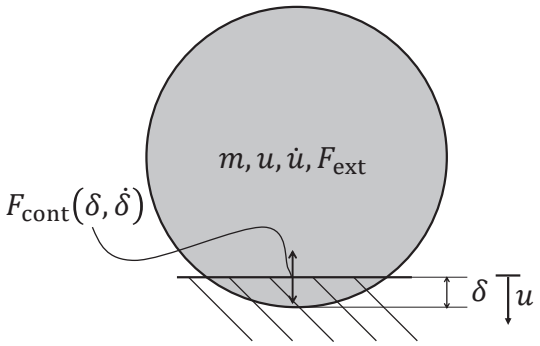

Figure 3.1: General single DOF contact case.

The equation of motion of the example case is:

$$m\ddot{u} + F_{\text{cont}}(u, \dot{u}) = F_{\text{ext}} \tag{3.1}$$

Assuming constant average acceleration within each time step, the equation of motion can be discretized, and body positions and velocities are updated according to Equations 3.2 and 3.3, which are the time-stepping equations as used in the constant average acceleration method:

$$u_{n+1} = u_n + \dot{u}_n \Delta t + \frac{1}{2}\left(\Delta \dot{u}_{\text{cont}} + F_{\text{ext}} m^{-1} \Delta t\right) \Delta t \tag{3.2}$$

$$\dot{u}_{n+1} = \dot{u}_n + \Delta \dot{u}_{\text{cont}} + F_{\text{ext}} m^{-1} \Delta t \tag{3.3}$$

Subscripts n indicate the body position and velocity at the beginning of the time step, subscripts $n+1$ indicate the body position and velocity at the end of the time step, Δt is the time step size and $\Delta \dot{u}_{\text{cont}}$ is the change in body velocity due to the contact force F_{cont}. The contact force at the beginning and end of the time step can be written as:

$$F_{\text{cont}}^{n} = F_{\text{cont}}\left(u_n, \dot{u}_n\right) \qquad \text{and} \qquad F_{\text{cont}}^{n+1} = F_{\text{cont}}\left(u_{n+1}, \dot{u}_{n+1}\right) \tag{3.4}$$

The partial derivatives of F_{cont} with respect to the penetration and the penetration velocity at the beginning of the time step are used to estimate the change of the contact force during a time step:

$$k_n = \left.\frac{\partial F_{\text{cont}}^{n}}{\partial u}\right|_{u=u_n} \qquad \text{and} \qquad c_n = \left.\frac{\partial F_{\text{cont}}^{n}}{\partial \dot{u}}\right|_{\dot{u}=\dot{u}_n} \tag{3.5}$$

Using these partial derivatives and the body propagation Equations 3.2 and 3.3, F_{cont}^{n+1} can be estimated as:

$$\begin{aligned} F_{\text{cont}}^{n+1} = F_{\text{cont}}^{n} + k_n \left(\dot{u}_n \Delta t + \frac{1}{2}\left(\Delta \dot{u}_{\text{cont}} + F_{\text{ext}} m^{-1} \Delta t\right) \Delta t \right) \\ + c_n \left(\Delta \dot{u}_{\text{cont}} + F_{\text{ext}} m^{-1} \Delta t\right) \end{aligned} \tag{3.6}$$

This equation is rewritten and a system of equations is formulated in which the contact impulse λ_{cont} and the velocity change $\Delta \dot{u}_{\text{cont}}$ are the unknowns. The contact impulse should be seen in this context as the integral of a finite force over the time step with a non-zero duration, rather than as an instantaneous momentum change. The contact impulse is equal to:

$$\lambda_{\text{cont}} = F_{\text{cont}}^{\text{av}} \cdot \Delta t \tag{3.7}$$

The average contact force over a time step $F_{\text{cont}}^{\text{av}}$ is defined as:

$$F_{\text{cont}}^{\text{av}} = \frac{F_{\text{cont}}^{n} + F_{\text{cont}}^{n+1}}{2} \tag{3.8}$$

Combining and rearranging Equations 3.6, 3.7 and 3.8 results in:

$$\begin{aligned} \lambda_{\text{cont}} = F_{\text{cont}}^{n} \Delta t + \frac{1}{2}\left(\dot{u}_n + \frac{1}{2} F_{\text{ext}} m^{-1} \Delta t \right) \Delta t^2 k_n + \frac{1}{4} \Delta \dot{u}_{\text{cont}} \Delta t^2 k_n + \\ \frac{1}{2} F_{\text{ext}} m^{-1} \Delta t^2 \, c_n + \frac{1}{2} \Delta \dot{u}_{\text{cont}} \Delta t \, c_n \end{aligned} \tag{3.9}$$

This can be rewritten as:

$$-\Delta\dot{u}_{\text{cont}} + \frac{\lambda_{\text{cont}}}{\left(\frac{1}{4}k_n\Delta t^2 + \frac{1}{2}c_n\Delta t\right)} = \frac{F^n_{\text{cont}}}{\left(\frac{1}{4}k_n\Delta t + \frac{1}{2}c_n\right)} + \\ \frac{\frac{1}{2}\left(\dot{u}_n + \frac{1}{2}F_{\text{ext}}m^{-1}\Delta t\right)\Delta t^2 k_n}{\left(\frac{1}{4}k_n\Delta t^2 + \frac{1}{2}c_n\Delta t\right)} + \frac{\frac{1}{2}F_{\text{ext}}m^{-1}\Delta t^2\, c_n}{\left(\frac{1}{4}k_n\Delta t^2 + \frac{1}{2}c_n\Delta t\right)} \tag{3.10}$$

By using the relation:

$$\lambda_{\text{cont}} = -\Delta\dot{u}_{\text{cont}}\, m \tag{3.11}$$

a system of equations can be formulated as:

$$\begin{bmatrix} m & 1 \\ -1 & \Sigma \end{bmatrix} \begin{bmatrix} \Delta\dot{u}_{\text{cont}} \\ \lambda_{\text{cont}} \end{bmatrix} = \begin{bmatrix} 0 \\ \Upsilon \end{bmatrix} \tag{3.12}$$

in which Σ and Υ are defined as:

$$\Sigma = \frac{1}{\left(\frac{1}{4}k_n\Delta t^2 + \frac{1}{2}c_n\Delta t\right)} \tag{3.13}$$

$$\Upsilon = \frac{F^n_{\text{cont}}}{\frac{1}{4}k_n\Delta t + \frac{1}{2}c_n} + \frac{\frac{1}{2}\left(\dot{u}_n + \frac{1}{2}F_{\text{ext}}m^{-1}\Delta t\right)\Delta t^2 k_n}{\frac{1}{4}k_n\Delta t^2 + \frac{1}{2}c_n\Delta t} + \\ \frac{\frac{1}{2}F_{\text{ext}}m^{-1}\Delta t^2\, c_n}{\frac{1}{4}k_n\Delta t^2 + \frac{1}{2}c_n\Delta t} \tag{3.14}$$

The solution of this system gives the impulse λ_{cont} and the body velocity change due to the contact impulse $\Delta\dot{u}_{\text{cont}}$.

Equations 3.12, 3.13 and 3.14 provide a general description of a compliant continuous 1-DOF contact. A special case occurs when the stiffness and damping parameters, k and c, respectively, are constant. In this case, $F^n_{\text{cont}} = u_n k + \dot{u}_n c$, so Σ and Υ can be simplified to:

$$\Sigma_{\text{lin}} = \frac{1}{\left(\frac{1}{4}k\Delta t^2 + \frac{1}{2}c\Delta t\right)} \tag{3.15}$$

$$\Upsilon_{\text{lin}} = \frac{u_n\, k}{\frac{1}{4}k\Delta t + \frac{1}{2}c} + 2\left(\dot{u}_n + \frac{1}{2}F_{\text{ext}}m^{-1}\Delta t\right) \tag{3.16}$$

This form occurs when the time-stepping scheme is combined with a lattice model to represent the material properties of intact ice. The Σ and Υ values then represent the spring-dashpot elements that form the lattice. A random lattice model which can be combined with the time-stepping scheme to model floe deformation and fracture is discussed in Section 3.6.

The Newmark-Beta method, on which this derivation is based, is only valid for continuously differentiable functions. In the case of ice-ice or ice-structure contacts, the contact force as a function of time is discontinuous in the time step in which the contact is initiated and in the time step in which local ice crushing stops (i.e., the relative contact velocity becomes zero). However, the method can still be used in this case by applying appropriate lower and upper limits to the calculated contact impulse.

The time-stepping scheme as derived in this section may be applied to continuous contacts, as occurs between the different elements of a lattice representation of the ice, and to discontinuous contacts, such as ice-ice or ice-structure contacts. Figure 3.2 clarifies where both types of contacts occur in an ice-structure interaction simulation.

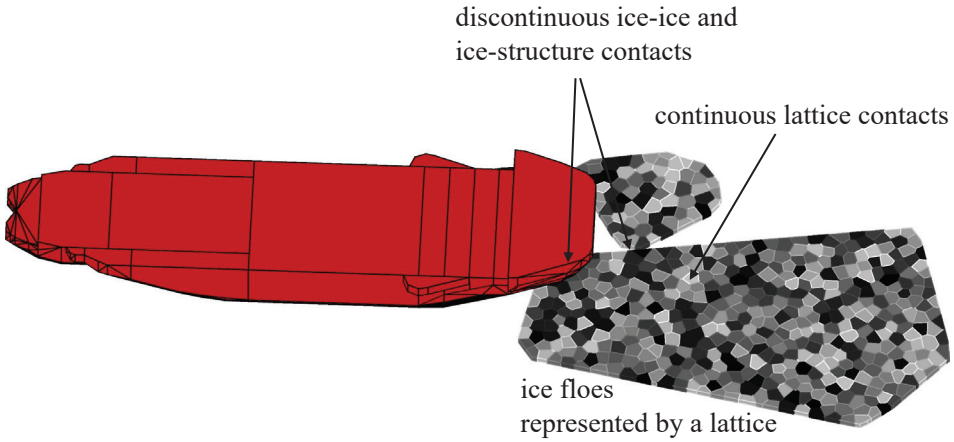

Figure 3.2: Continuous and discontinuous contacts in an ice-structure interaction simulation.

3.1.1 Extension of the time-stepping scheme to discontinuous contacts

The forces at ice-ice or ice-structure contacts are bounded by upper and lower limits, leading to a discontinuous contact behaviour. The limits follow from the local physical processes occurring at the contacts. Simplifying assumptions are used regarding the local contact processes to formulate the upper and lower limits

of the contact forces. The physical reasoning behind these limits will be further discussed in Section 3.3. The current section focusses on how these limits are enforced within the time-stepping scheme.

The discontinuous contact assumptions made in this thesis lead to a contact force that is only dependent on the contact penetration, not on the relative penetration velocity. If the contact force is only dependent on the penetration, and not on the penetration velocity, Equations 3.13 and 3.14 can be significantly simplified. All terms related to c_n can be dropped, leading to the simplified form of Σ and Υ:

$$\Sigma_{\text{pen}} = \frac{1}{\left(\frac{1}{4}k_n \Delta t^2\right)} \tag{3.17}$$

$$\Upsilon_{\text{pen}} = \frac{F^n_{\text{cont}}}{\frac{1}{4}k_n \Delta t} + 2\left(\dot{u}_n + \frac{1}{2}F_{\text{ext}} m^{-1} \Delta t\right) \tag{3.18}$$

Note that a velocity term still appears in Equation 3.18. This term appears because the change in position within a time step is taken into account, which is a function of velocity $\dot{u}_n$.

The following limits to the contact parameters are enforced in the case of discontinuous ice-ice and ice-structure contacts:

$$k_n \geq 0 \tag{3.19}$$

$$F^n_{\text{cont}} \geq 0 \tag{3.20}$$

$$F^n_{\text{cont}} = 0 \quad \text{if} \quad \delta \leq 0 \tag{3.21}$$

Equation 3.19 states that the contact force may not decrease as the contact penetration increases. Equations 3.20 and 3.21 state that the contact force may not be negative and that there may only be a contact force if there is a contact between bodies (penetration $\delta \geq 0$).

The contact impulse, which is part of the solution of the system expressed by Equation 3.12, is subject to the following limits:

$$\lambda_{\text{cont}} \geq 0 \tag{3.22}$$

$$\lambda_{\text{cont}} \leq \lambda_{\text{res}=0} \tag{3.23}$$

Equation 3.22 states that there may not be tensional impulses (and forces) at a contact, and Equation 3.23 states that the applied impulse may not be higher than the impulse needed to achieve a relative contact velocity of zero (the zero-restitution impulse $\lambda_{\text{res}=0}$).

Limits to the contact parameters (Equations 3.19, 3.20 and 3.21) are enforced in the formulation of the system of equations and usually follow naturally from the contact assumptions that are made. The limits to the solution (Equations 3.22 and 3.23) are taken into account in the system as formulated in Equation 3.12 by introducing complementarity conditions. This leads to the following mixed linear complementarity problem:

$$\begin{bmatrix} m & 1 & 0 \\ -1 & \Sigma_{\mathrm{cr}} & 1 \\ 1 & \Sigma_{\mathrm{cr}} & 1 \end{bmatrix} \begin{bmatrix} \Delta \dot{u}_{\mathrm{cont}} \\ \lambda_{\mathrm{cont}} \\ v_{\mathrm{cor}} \end{bmatrix} + \begin{bmatrix} 0 \\ -\Upsilon_{\mathrm{cr}} \\ -\frac{F_{\mathrm{cr}}}{\frac{1}{4}\frac{\Delta F_{\mathrm{cr}}}{\Delta \delta}\Delta t} \end{bmatrix} = \begin{bmatrix} 0 \\ \alpha_{\mathrm{r}} \\ \beta_{\mathrm{r}} \end{bmatrix} \tag{3.24}$$
$$0 \leq \begin{bmatrix} \lambda_{\mathrm{cont}} & v_{\mathrm{cor}} \end{bmatrix}^T \perp \begin{bmatrix} \alpha_{\mathrm{r}} & \beta_{\mathrm{r}} \end{bmatrix}^T \geq 0$$

in which v_{cor} is the correctional velocity needed to satisfy the zero restitution requirement, and α_{r} and β_{r} are residuals that have no physical meaning. Σ_{cr} and Υ_{cr} are defined as:

$$\Sigma_{\mathrm{cr}} = \frac{1}{\left(\frac{1}{4}\frac{\Delta F_{\mathrm{cr}}}{\Delta \delta}\Delta t^2\right)} \tag{3.25}$$

$$\Upsilon_{\mathrm{cr}} = \frac{F_{\mathrm{cr}}}{\frac{1}{4}\frac{\Delta F_{\mathrm{cr}}}{\Delta \delta}\Delta t} + 2\left(\dot{u}_n + \frac{1}{2}F_{\mathrm{ext}} m^{-1}\Delta t\right) \tag{3.26}$$

Note the difference between this formulation and the continuous contact formulation of Υ_{pen} in Equation 3.18. The contact force F^n_{cont} is replaced by the force F_{cr}. This is the force at which contact crushing would be initiated for this contact. This change follows from the fact that the contact force is no longer uniquely related to a specific penetration depth δ. The force penetration gradient k_n from Equation 3.18 is replaced by a discretized version $\frac{\Delta F_{\mathrm{cr}}}{\Delta \delta}$ because the analytical expression of the force-penetration curve $F_{\mathrm{cont}}(\delta)$ is not explicitly calculated for each contact.

The MLCP in Equation 3.24 fully describes the desired discontinuous contact behaviour. It is not immediately obvious how the MLCP enforces the limits expressed in Equations 3.22 and 3.23. Therefore the problem statement is further clarified and proven to be correct in Appendix A of the paper appended to this thesis in Appendix A.

3.1.2 Extension of the time-stepping scheme to multiple degrees of freedom

In order to apply this time-stepping scheme in a useful manner to ice-structure interaction, it must be expanded to a 3-D system with multiple degrees of freedom and friction. This expansion is similar to the procedures followed in previously applied methods and it is explained in Appendix B of the paper appended to this thesis in Appendix A. It leads to the following system:

$$\begin{bmatrix} \boldsymbol{M} & -\boldsymbol{J}_h & -\boldsymbol{J}_c \\ \boldsymbol{J}_h^T & \boldsymbol{\Sigma}_h & \mathbf{0} \\ \boldsymbol{J}_c^T & \mathbf{0} & \boldsymbol{\Sigma}_c \end{bmatrix} \begin{bmatrix} \boldsymbol{\Delta \dot{u}} \\ \boldsymbol{\lambda_h} \\ \boldsymbol{\lambda_c} \end{bmatrix} + \begin{bmatrix} \mathbf{0} \\ \boldsymbol{\Upsilon_h} \\ \boldsymbol{\Upsilon_c} \end{bmatrix} = \begin{bmatrix} \mathbf{0} \\ \mathbf{0} \\ \boldsymbol{\alpha_r} \end{bmatrix} \tag{3.27}$$
$$0 \leq \boldsymbol{\lambda}_c^T \perp \boldsymbol{\alpha}^T \geq 0$$

where $\boldsymbol{M}$ is a diagonal mass matrix containing the inertial properties of all bodies within the simulation; $\boldsymbol{J}_h$ and $\boldsymbol{J}_c$ are matrices containing constraint Jacobians, which express the influence of contact impulses on body velocities; $\boldsymbol{\Delta \dot{u}}$ is a vector containing the velocity change (both linear and rotational) of each body in the simulation domain; $\boldsymbol{\lambda_h}$ and $\boldsymbol{\lambda_c}$ are vectors containing the constraint impulses, which express the time-integrated contact forces within one time step; $\boldsymbol{\Sigma}_h$ and $\boldsymbol{\Sigma}_c$ are matrices containing the compliance factors with unit kg^{-1}; $\boldsymbol{\Upsilon_h}$ and $\boldsymbol{\Upsilon_c}$ contain the compliance factors with unit $\mathrm{m\,s}^{-1}$; and $\boldsymbol{\alpha_r}$ is a vector of residuals with no physical meaning. The difference between the variables with subscripts h and the variables with subscripts c is that the variables with subscripts h contain the holonomic constraints, i.e., the constraints with no upper or lower limits to the impulses, while the variables with subscripts c contain the non-holonomic constraints, i.e., the constraints for which the impulses are bound by upper and lower limits. Holonomic constraints are used to model connections between lattice elements when using a lattice model for the ice. Holonomic constraints can also be used to resemble a mooring system or towing carriage, connecting a structure to a fixed or moving reference point in the simulated domain.

3.2 Solving the formulated MLCP

The MLCP formulated in Section 3.1.2 is solved using a block Gauss-Seidel solver, similar to the methods applied in, for example, Servin et al. (2014); Jean (1999); Lacoursiere (2003). The block Gauss-Seidel solver is an iterative solver. Iterations can be stopped when a user-defined accuracy threshold is met. An advantage of using an iterative solver is that the solution from the previous time step can be used as an initial guess for the next time step, reducing the needed number of iterations. Contact compliance improves the convergence rate of the solver significantly compared to a similar system with infinitely stiff contacts. High mass ratios of interacting bodies, in combination with stiff contacts, can lead to an ill-conditioned system. The convergence will be slow in such a case.

Absolute convergence criteria are specified both for the velocity change of the bodies $\boldsymbol{\Delta \dot{u}}$ as well as for the contact impulses $\boldsymbol{\lambda_h}$ and $\boldsymbol{\lambda_c}$. Because of the difference in units and magnitudes of both parts of the solution, a different convergence criterion

is used for the body velocities and the contact impulses. Appropriate convergence criteria for the velocity change of bodies and the contact impulses depend on the physical characteristics of the modelled scenario.

3.3 Contact model

A contact model is defined based on the assumption that local ice crushing will occur at ice-ice and ice-structure contacts. The contact parameters are derived based on an assumption of constant energy dissipation per crushed volume of ice, or *crushing specific energy* (CSE) (Kim and Gagnon, 2016). The CSE is the amount of energy needed to crush a unit volume of ice (unit: $\mathrm{J/m^3}$). Ice contact models based on energy dissipation are similar to contact models based on ice crushing pressure and contact area. A certain assumed energy dissipation function can easily be converted to an equivalent crushing pressure, and vice versa.

The assumption of a constant CSE, as used in the contact model described in this thesis, is equivalent to a constant crushing pressure. This assumption is considered justifiable in light of other simplifications, such as geometrical simplifications of the floe shapes. The intended use of this contact model is for local crushing only. In cases where continuous crushing at the ice-structure interface is the governing failure mode, the assumption of a constant crushing pressure is no longer sufficient.

Referring to the contact parameters as described in Section 3.1.1, the discontinuous contact model needs to provide values for the contact force when crushing is initiated (F_{cr}) and the increase in contact force with penetration ($\frac{\Delta F}{\Delta \delta}$), as occur in Equations 3.24, 3.25 and 3.26. In addition, the contact point in global coordinates $\boldsymbol{o}_{\mathrm{c}}$ and the contact axis system $\boldsymbol{B}_{\mathrm{c}}$ need to be defined in order to generalize the time-stepping scheme to multiple contacts and three dimensions. The contact point and contact axis system are used in Appendix A. The contact axis system $\boldsymbol{B}_{\mathrm{c}}$ consists of a normal axis $\boldsymbol{n}_{\mathrm{c}}$ and two friction axes $\boldsymbol{t}_{\mathrm{c1}}$ and $\boldsymbol{t}_{\mathrm{c2}}$.

A distinction is made between ice-ice and ice-structure contacts. In ice-ice contacts, it is assumed that both contacting bodies will experience local crushing. In ice-structure contacts, only the ice body will experience local contact crushing. For clarity, 2-D sketches are used in this section, but the algorithm is implemented fully in 3-D.

3.3.1 Contact detection

Contacts between discrete bodies must be detected before the contact parameters can be derived and the contact response can be resolved. The detection and geometry processing of contacts is divided in three phases:

1. Broad-phase collision detection; dynamic axis-aligned bounding box (AABB) tree.

2. Mid-phase collision detection; the Gilbert-Johnson-Keerthi (GJK) distance algorithm (Gilbert et al., 1988).

3. Narrow-phase collision processing; accurate contact geometry determination based on plane intersections.

For the broad-phase and mid-phase collision detection, open-source algorithms from Bullet Physics are used (*Bullet Physics*, 2017). The narrow-phase collision processing code is developed as part of the PhD work.

An AABB tree is one of the most common algorithms for broad-phase collision detection. It approximates each body by a bounding box, and checks for overlaps between these boxes. The algorithm is robust: It is guaranteed to find all overlapping bounding boxes. The bounding boxes are updated in each time step to reflect the updated body positions. Bounding box sizes are increased by a fixed margin, such that the broad-phase algorithm also finds almost collisions; bodies that are currently not in contact, but may come in contact within the time step. If a potential overlap is found in the broad-phase, the mid-phase will further process the potential contact.

The GJK distance algorithm is used in the mid-phase. If it follows from the mid-phase that the bodies are in contact, a third processing phase is applied to find the exact contact geometry of the contacting bodies. The contact geometry is determined based on the intersection points of body planes.

Once the contact geometry is known, the geometry information is used in combination with ice material properties to determine the contact parameters. The procedures used to derive the contact parameters from the geometry information and material properties are different for ice-ice and for ice-structure contact.

3.3.2 Ice-ice contacts

As stated, ice-ice contact parameters are derived based on the assumption that local ice crushing will occur. Ice crushing is represented by body overlap in the numerical simulation. The overlap volume that occurs in the numerical simulation represents crushed ice. Figure 3.3 helps to illustrate this assumption.

The contact point (o_c) is defined as the centre of the overlap volume. This is the point at which the contact forces will be applied to the contacting bodies. The contact normal direction is defined as the weighted average of the normal directions

of the sub-contact areas related to one of the bodies:

$$\boldsymbol{n}_{\mathrm{c}} = \frac{\sum_{s=1}^{s=\mathrm{ns}} A_{j,s}\boldsymbol{n}_{j,s}}{\|\sum_{s=1}^{s=\mathrm{ns}} A_{j,s}\boldsymbol{n}_{j,s}\|} \tag{3.28}$$

in which ns is the number of surfaces related to one of the bodies in the overlap volume, $A_{j,s}$ are the areas of these surfaces, and $\boldsymbol{n}_{j,s}$ are unit length vectors perpendicular to these surfaces. The parameters are illustrated in Figure 3.3. The contact normal may also be defined using the surfaces related to body i, resulting in an opposite contact normal. This gives the same final result, as long as the normal direction definition is applied consistently throughout the calculations.

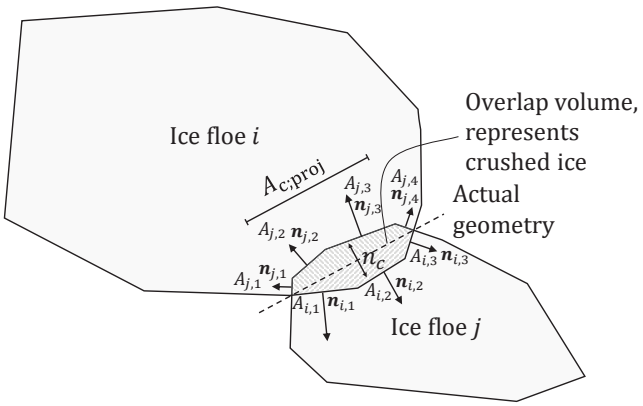

Figure 3.3: Top-view of two interacting ice floes. Ice-ice contacts are resolved using the contact projected area and normal direction.

The contact friction direction t_{c1} is chosen opposite to the tangential component of the contact velocity:

$$\boldsymbol{t}_{c1} = -\frac{\dot{\boldsymbol{u}}_{\mathrm{c}} - \boldsymbol{n}_{\mathrm{c}}\left(\boldsymbol{n}_{\mathrm{c}} \cdot \dot{\boldsymbol{u}}_{\mathrm{c}}\right)}{\|\dot{\boldsymbol{u}}_{\mathrm{c}} - \boldsymbol{n}_{\mathrm{c}}\left(\boldsymbol{n}_{\mathrm{c}} \cdot \dot{\boldsymbol{u}}_{\mathrm{c}}\right)\|} \tag{3.29}$$

The contact friction direction t_{c2} is chosen to complete the axis system:

$$\boldsymbol{t}_{c2} = \boldsymbol{t}_{c1} \times \boldsymbol{n}_{\mathrm{c}} \tag{3.30}$$

A second friction direction is needed because the change in the contact velocity within the time step is taken into account in the MLCP. Therefore, the resulting friction force is not necessarily opposite to the contact velocity at the beginning of the time step.

The contact force where crushing starts F_{cr} is determined based on the projected contact area and an assumed crushing specific energy of the ice:

$$F_{\mathrm{cr}} = A_{\mathrm{proj}} \cdot \mathrm{CSE} \tag{3.31}$$

in which the contact projected area is the area that results when projecting the contact polyhedron on the contact normal:

$$A_{\mathrm{proj}} = \sum_{s=1}^{s=\mathrm{ns}} A_{j,s} \boldsymbol{n}_{j,s} \cdot \boldsymbol{n}_{\mathrm{c}} \tag{3.32}$$

The gradient $\frac{\Delta F}{\Delta \delta}$ is determined such that the kinetic energy dissipated in the contact matches the energy absorbed in ice crushing. The gradient is determined by calculating the contact projected area in the current body positions and the contact projected area when the contacting bodies are propagated with their current velocity. This is clarified in Figure 3.4, where $\Delta\delta$ is the change in penetration:

$$\Delta\delta = \dot{u}_{\mathrm{cont}} \Delta t + \frac{1}{2} F_{\mathrm{ext}} m^{-1} \Delta t^2 \tag{3.33}$$

and $A_{\mathrm{proj}}^{\mathrm{prop}}$ is the contact projected area when the contacting bodies are propagated with their current velocity. If there is a zero or negative penetration velocity, one of the bodies is propagated with a user-defined distance in the contact normal direction.

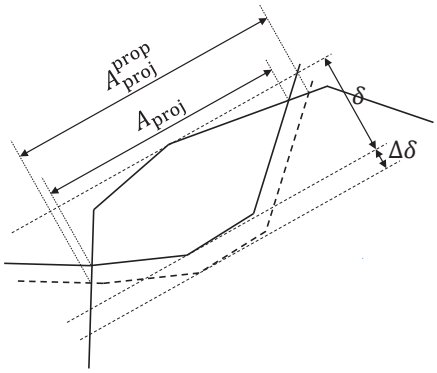

Figure 3.4: Projected contact area and propagated projected contact area.

The gradient $\frac{\Delta F}{\Delta \delta}$ is determined as:

$$\frac{\Delta F}{\Delta \delta} = \frac{\left(A_{\mathrm{proj}}^{\mathrm{prop}} - A_{\mathrm{proj}}\right) \mathrm{CSE}}{\Delta \delta} \tag{3.34}$$

In the case of decreasing contact penetration, the load will drop to zero. This follows from the assumption that the overlap volume between bodies represents crushed material.

This type of contact behaviour can be viewed as hysteretic damping, in which the loading/unloading curve will be similar to Figure 3.5. Three types of discontinuous contact behaviour can be distinguished:

- *crushing contact*: The contact force needed to prevent further penetration is higher than the bearing capacity of the current contact area. Ice crushes and body penetration increases.
- *resting contact*: The contact force needed to prevent further penetration is lower than the bearing capacity of the current contact area. Penetration remains the same, and the contact force is calculated such that the contact relative velocity in the contact normal direction remains zero.
- *separating contact*: Due to external forces or forces at other contacts, the relative contact velocity is negative (the contact separates). This results in decreasing penetration, and the contact force drops to zero.

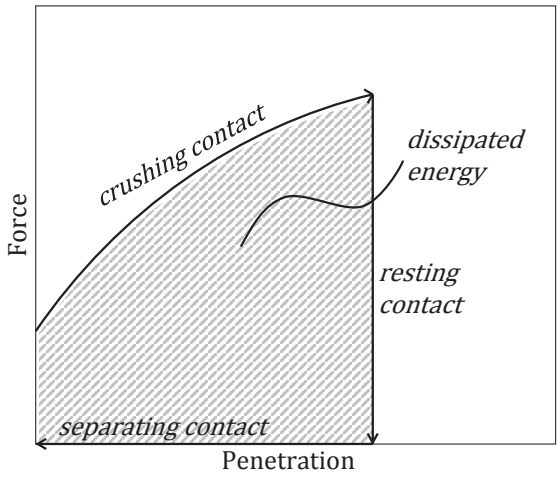

Figure 3.5: Contact crushing implementation as hysteretic damping.

The type of discontinuous contact behaviour is not determined at the beginning of the time step; it is an outcome of the MLCP, and its implementation in the time-stepping scheme is described in Section 3.1.

Since we assume that all available kinetic energy is dissipated by local crushing, this discontinuous contact algorithm results in a contact restitution of zero in the case of non-deformable floes. When floes are modelled using a lattice model or other material model, some of the available kinetic energy will be transformed to potential energy in the form of elastic deformation in the ice floe. This potential energy can be recovered to give a restitution > 0.

Ice floe rafting

Ice floe rafting may occur as a result of the assumptions made in the contact model, even if all bodies in the simulation domain have completely vertical sides. Rafting occurs if the ice-ice frictional force is insufficient to counteract the vertical component of the contact normal force:

$$F_{nc;z} > -F_{tc;z} \tag{3.35}$$

where $F_{nc;z}$ is the vertical component of the contact normal force and $F_{tc;z}$ is the vertical component of the contact friction force. The direction of the contact normal force $\boldsymbol{n}_{\mathrm{c}}$ in the numerical model follows from the contact geometry as specified in Equation 3.28. When two ice floes interact, overlap may occur because of the contact compliance which represents local crushing. If the ice floes are of equal thickness and are both in their hydrostatic equilibrium buoyancy position, then the top and bottom planes of the overlapping floes are coplanar. If this situation occurs, the contact algorithm uses the top plane of one ice floe and the bottom plane of the other ice floe in the determination of the local contact geometry, resulting in a vertical component in the contact normal direction. This is clarified in Figure 3.6.

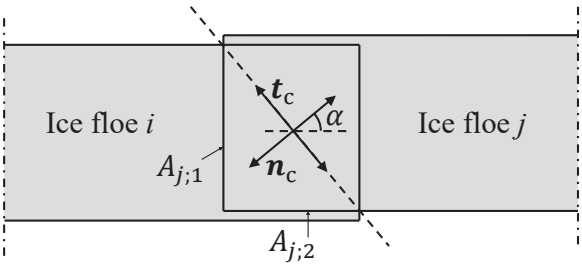

Figure 3.6: Side-view of two interacting ice floes, clarifying the rafting mechanism in the numerical model. The contact algorithm uses only the bottom plane of ice floe *j* in determining the contact normal direction.

The onset of rafting in the DEM model occurs mainly for numerical reasons and does not necessarily resemble the physical mechanisms that lead to rafting in model or full-scale broken ice conditions. This is taken into account in the application of the model in Chapter 4. In the assessment of the floe shape effects, simulations were performed in 2D, disabling rafting entirely. In the study on ice tank test variability, the ice-ice friction coefficient was calibrated in order to match the experimental results for a single test case. This resulted in a visually similar rafting behaviour in the ice tank test recordings and the numerical simulations.

As discussed in Section 2.3.2, The physical mechanisms responsible for the onset of rafting in model- or full-scale broken ice fields are currently not well understood. Therefore the current implementation of rafting behaviour in the numerical model is considered to be sufficient.

3.3.3 Ice-structure contacts

In ice-structure contacts, local crushing only occurs in the ice body, whereas the structure is assumed to be rigid. The contact geometry is defined by the structure geometry in contact with the ice. This is illustrated in Figure 3.7.

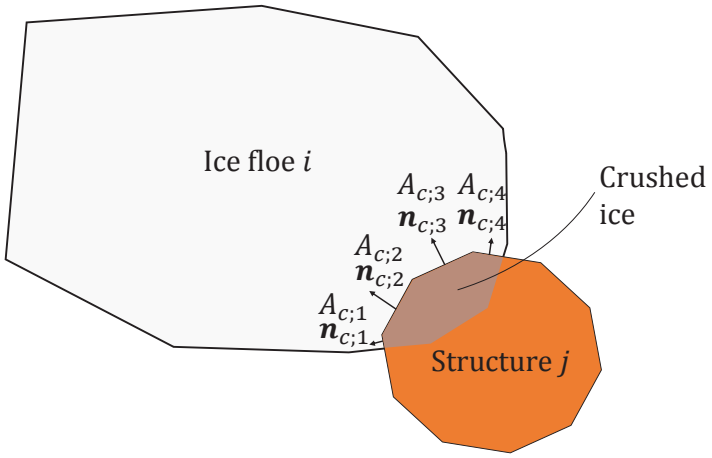

Figure 3.7: Ice-structure contacts are resolved using the sub-contact areas of each structure panel (partly) in contact with an ice sheet.

The actual contact geometry cannot be approximated by a single plane, as is done for ice-ice contacts. To obtain an estimate of the contact forces along the ice-structure contact interface, a contact 'point' is defined for every panel of the structure in contact with the ice. The contact force when crushing is initiated (F_{cr}) and

the increase in contact force with penetration ($\frac{\Delta F}{\Delta \delta}$) are determined similar to the method applied for ice-ice contacts, but now the area in contact with ice of each structure panel is used, instead of the total projected contact area.

3.4 Hydrodynamic forces

In broken ice-structure interaction, hydrostatic and hydrodynamic forces on the ice floes often give a significant contribution to the total ice resistance. In the numerical model applied in Chapter 4, hydrodynamics forces on ice floes are approximated using form drag and skin friction coefficients.

Hydrodynamic drag forces resulting from skin friction and form drag are applied to the ice floes according to their triangulated geometry and the local velocity vector and position of each triangle. An example of the triangulated body geometry of an ice floe is shown in Figure 3.8. This method is developed and implemented in

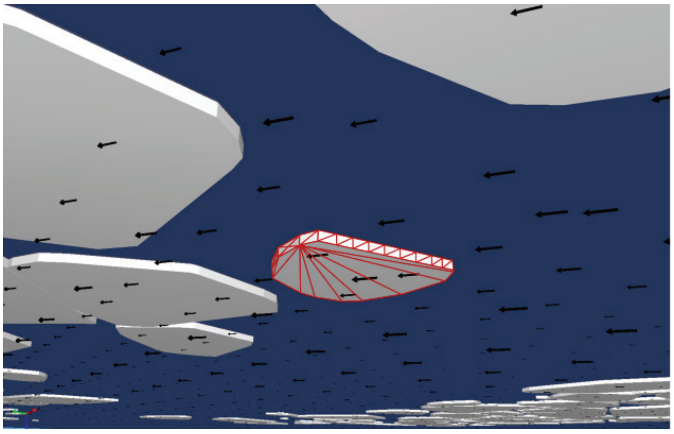

Figure 3.8: Triangulation of outer body geometry for the calculation of hydrodynamic forces.

the global numerical model by Andrei Tsarau. The method is described by Tsarau (2015). The total drag force on an ice body is calculated as follows:

$$\mathbf{F}_{\text{drag}} = \sum_{k=1}^{M} \left[\rho_{\text{w}} C_{\text{p}} A^k \left| \dot{\mathbf{U}}_{\parallel}^k \right| \dot{\mathbf{U}}_{\parallel}^k - \left(\rho_{\text{w}} C_{\text{d}} A^k \left[\left(\dot{\mathbf{U}}^k \cdot \mathbf{n}^k \right) \right]^2 \mathbf{n}^k \right) \Big|_{\left(\dot{\mathbf{U}}^k \mathbf{n}^k \right) < 0} \right] \tag{3.36}$$

in which $\mathbf{F}_{\text{drag}}$ is the total linear drag force on an ice body, M is the number of completely submerged triangles, ρ_{w} is the water density, C_{p} is the skin friction drag coefficient, A^k is the area of triangle k, $\dot{\mathbf{U}}_{\parallel}^k$ is the relative fluid velocity parallel to the triangle, $\mathbf{n}^k$ is the outward normal direction of the body geometry at the

triangle center point, and C_{d} is the form drag coefficient. Torsional drag forces are calculated similarly as:

$$\mathbf{T}_{\mathrm{drag}} = \sum_{k=1}^{M} \mathbf{r}^k \times \left[\rho_{\mathrm{w}} C_{\mathrm{p}} A^k \left| \dot{\mathbf{U}}_{\parallel}^k \right| \dot{\mathbf{U}}_{\parallel}^k - \left(\rho_{\mathrm{w}} C_{\mathrm{d}} A^k \left[\left(\dot{\mathbf{U}}^k \cdot \mathbf{n}^k \right) \right]^2 \mathbf{n}^k \right) \Big|_{(\dot{\mathbf{U}}^k \mathbf{n}^k) < 0} \right] \tag{3.37}$$

in which $\mathbf{r}^k$ is a vector from the body's COG to the center point of triangle k. Hydrostatic restoring forces are calculated based on the exact submerged body geometry and the water density.

3.5 Ice failure

In most interaction scenarios of a structure with broken ice, it is essential to consider ice failure when modelling the ice-structure interaction process. Ice failure is often one of the governing load releasing mechanisms.

Ice failure can be considered by discretizing the intact ice floes using lattice or FEM modelling techniques. A lattice model of ice, including selected verification results, is presented in Section 3.6. Computational modelling of ice failure with lattice or FEM models is time consuming because of the many degrees of freedom of the discretized ice features and the nonlinear nature of the fracture process. However, computational modelling of fracture by discretizing intact ice floes is the most accurate method of considering fracture. As an alternative to computational modelling, ice floe failure may be considered by applying analytical solutions, or pre-computed solutions for a range of cases from a computational model. In the remainder of this thesis, this method is referred to as semi-analytical ice failure.

In semi-analytical ice failure, the floe geometry and the contact forces resulting from the DEM model are mapped to a geometry and load case for which an analytical or pre-computed computational solution is known. Subsequently, this solution and the occurring contact forces are used to determine if and how ice failure will occur. The accuracy of the mapping procedure depends on the amount and the variety of the analytical/pre-computed solutions included in the model. Figure 3.9 gives an example of one of the most simplifying mapping procedures. Here, an ice floe with an irregular geometry is approximated by a rectangular bounding box, for which an analytical fracture solution is available.

Semi-analytical failure is used in the modelling results presented in Chapter 4. The analytical and pre-computed computational solutions used in the modelling preformed for these studies include:

- Off-centre splitting of a rectangular plate.

- Consideration of all contact forces, some of which cause confinement and some of which result in a splitting load.
- Bending failure assuming an infinite plate, taking into account speed effects and the local contact geometry.

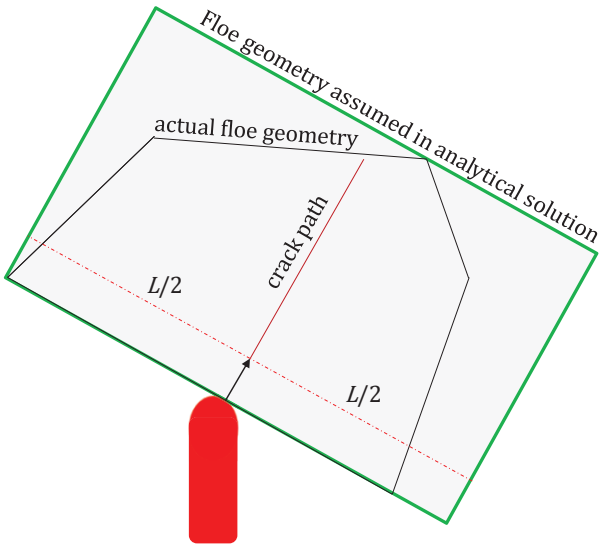

Figure 3.9: An irregular ice floe is approximated by a rectangular bounding box, for which an analytical fracture solution is known.

The development of the analytical and pre-computed computational solutions, and the mapping procedures used to link the load conditions as they occur in the simulation to the analytical and pre-computed solutions, were mainly developed by Wenjun Lu (PhD), and are partly described in Lu et al. (2015*a*,*b*, 2016); Lu, Lubbad, Shestov and Løset (2018); Lu, Lubbad and Løset (2018).

The current implementation of semi-analytical failure has the following limitations:

- The effect of ice floe elastic deformation on the contact force occurring in the DEM model is not taken into account.
- The semi-analytical solutions only consider statics, with the exception of the velocity-dependent bending failure.
- Crack propagation is instantaneous; the interaction between crack propagation and contact force is not considered.

- The number of analytical and pre-computed computational solutions is limited. The accuracy of the applied solution depends on how well the actual floe geometry and contact forces can be mapped to one of the pre-computed or analytical solutions.

The accuracy of the semi-analytical failure implementation should be considered against the current understanding of ice failure processes and the current modelling capabilities. In the context of the conditions for which the model is intended (a structure interacting with a high number of discrete ice floes), it is doubtful if a more accurate failure model would lead to numerical modelling results closer to reality. The results of performed verification studies indicate that the uncertainty in the choice of model parameters (friction coefficients, drag coefficients, ice mechanical properties, etc.) has a much greater influence on the modelling results than the simplifying model assumptions made in the contact and failure model. Therefore, research efforts should first focus on a more accurate determination of these values (either by experiments or detailed numerical analysis). Only when the most important model parameters can be established with reasonable accuracy, a more accurate fracture model will be of benefit. The limited gains in model accuracy, and the time consuming nature of computational fracture, are the main reasons for using a semi-analytical failure implementation in the model applications presented in Chapter 4.

3.6 Lattice modelling of ice floes

As a more accurate alternative to the semi-analytical failure procedures that are currently implemented, ice floe deformation and failure could be modelled using a lattice model. Lattice models, or spring network models, represent a material as a collection of discrete masses, connected with a network of springs and dashpots. Lattice models are principally based on the atomic lattice structure of materials, but lattice-type models can also be used to represent the continuum properties of a material by a much courser mesh (Ostoja-Starzewski, 2002). Compared to continuum models, lattice models offer advantages in the modelling of fracture, since no stress singularities will occur at the crack tips (van Vliet and Metrikine, 2018). Lattice models have been applied to ice modelling by a number of authors: Hocking (1992); Jirasek and Bazant (1995); Sayed and Timco (1999); Dorival et al. (2008); Paavilainen et al. (2009); Lilja et al. (2017); van Vliet and Metrikine (2018, 2019). The work by van Vliet and Metrikine (2018, 2019) shows that lattice models can accurately represent the continuum properties of ice, including the failure behaviour. van Vliet and Metrikine (2018) derive the lattice parameters of a structured (regular) lattice for out-of plane deformation of a plate based on the Mindlin-Reissner plate theory.

In contrast to the work by van Vliet and Metrikine (2018), the lattice method presented in this section represents the ice as an unstructured (irregular) lattice. There exist no lattice models that derive the lattice parameters of an unstructured lattice based on a classical plate theory. Instead, irregular lattice models use simplifying approximations to define the element properties. The lattice models thus constructed can capture some continuum properties relatively well, but have a limited accuracy for other properties. The lattice model presented in this section is primarily based on a lattice model originally described by Kawai (1978), and further developed by Bolander and Saito (1998) and Yip et al. (2005). The lattice model defined by Kawai (1978); Bolander and Saito (1998); Yip et al. (2005) is modified based on the results of verification tests and on a matching of the theoretical scaling behaviour of the out-of-plane plate stiffness with thickness.

The discrete nature of lattice models makes them well suited for the modelling of ice, in combination with the presented time-stepping scheme. When applying the time-stepping scheme to the continuous linear contacts as occur in a lattice model, energy conservation is assured, following from the use of the Newmark-Beta method. Applications of a combined lattice model and time-stepping scheme have been published in van den Berg (2016) and van den Berg et al. (2017). These publications are included in this thesis in Appendices B and C. A structured lattice model, like the model described by van Vliet and Metrikine (2018), can be combined equally well with the time stepping scheme as the unstructured lattice model described here.

The work on lattice modelling as described in this section is mainly related to verification of the presented model. The lattice model itself (i.e., the definition of the element properties) is mostly based on existing methods. The performed verification studies show the capabilities as well as some of the limitations of the random lattice model used. The verification studies presented here are limited to the natural frequencies of out-of-plane vibrations of a lattice plate, the static out-of-plane deformation in response to a point load, and static linear elastic mode I fracture of a symmetric rectangular plate. It is intended to serve as a basis for further verification studies and the future application of the lattice model in ice-structure interaction modelling.

3.6.1 Meshing and the determination of element properties

The lattice model described in this section determines the lattice geometry and properties based on Voronoi tessellation. Voronoi tessellation is a partitioning of space into polyhedral bodies around seed points. Random seed points are picked in a pre-defined 2-D or 3-D domain, which represents the geometry of the body to be discretized by the lattice. A relatively uniform distribution of seed points

is achieved by defining a minimum distance between seed points, and filling the domain with points until no new seed points fit in the domain while satisfying the minimum distance requirement. The procedure is visualized in Figure 3.10. A

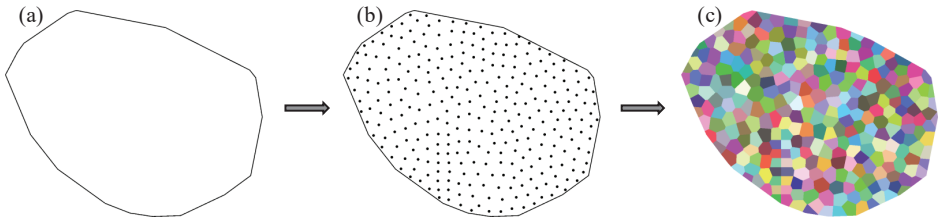

Figure 3.10: Mesh creation procedure. Define the outer geometry (a), fill the geometry with random points, under the condition of a minimum distance (b) and perform Voronoi tesselation based on the specified random points(c).

polyhedron around a point contains the region that is closer to that specific seed point than to any other point. Each surface of a polyhedron represents a lattice element. The lattice element consists of springs in 6 DOF: three translational and three rotational springs. The springs have zero length, and are connected to the discrete bodies at the centroids of the contact surfaces. The spring properties are determined based on the distance between the seed points, and on the properties of the contact surface. The connection between two seed points, and the contact surface determining the connection properties, are shown in Figure 3.11. The dis-

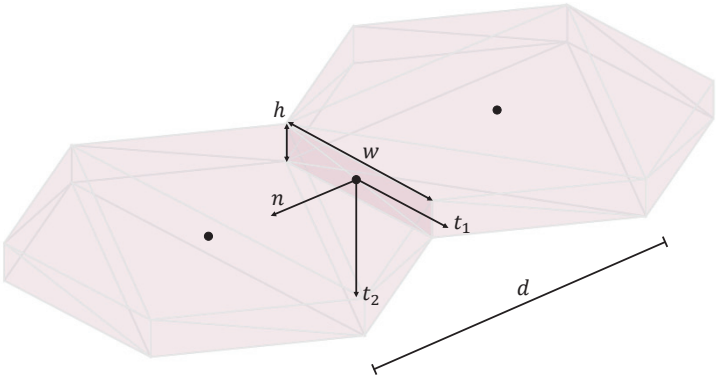

Figure 3.11: Lattice properties based on the shape and area of the contact surface and the distance between two elements.

tance d is the distance between the two connected seed points. Vectors n, t_1 and t_2 are normal to the contact surface, horizontal in-plane with the contact surface, and

vertical in-plane with the contact surface. h and w denote the height and width of the contact surface. In the lattices used for the verifications presented in this section, the spring constants for this contact surface are defined as:

$$k_n = \frac{EA}{d}, \qquad k_{t1} = k_{t2} = \frac{GA}{d}, \qquad k_{\phi n} = \frac{2 \cdot G \cdot I_{t1}}{d}$$
$$k_{\phi t1} = \frac{EI_{t1}}{d}, \qquad k_{\phi t2} = \frac{EI_{t2}}{d} \tag{3.38}$$

in which E is the Young's modulus, $G = \frac{E}{2}$ is the shear modulus, $A = wh$ is the contact area, and I_{t1} and I_{t2} are the second moments of area around axes t_1 and t_2. Note that the Poison's ratio does not appear in this definition of spring constants.

The spring constants defined in Equation 3.38 are somewhat different from the spring constants proposed in Yip et al. (2005). The difference is the use of the shear modulus G for the shear springs (whereas Yip et al. (2005) uses the Young's modulus for both the normal and the shear springs) and the second moment of area I_{t1} for the torsional spring (whereas Yip et al. (2005) uses the second moment of area around axis n). The second moment of area I_{t1} is used in the definition of the torsional spring stiffness because this results in a scaling of the plate stiffness proportional to h^3, in accordance with the analytical solution of out-of-plane plate deformation.

The definition of damping properties is not needed for the verifications performed in the remainder of this section. However, it is advisable to add damping when using the lattice model in a time-domain simulation of ice-structure interaction. For out-of-plane vibrations, the most important damping contribution is the hydrodynamic damping. For in-plane vibrations, ice material damping should be defined in order to prevent unrealistic dynamics. The material damping can be approximated by Rayleigh damping, in which the damping matrix $\boldsymbol{C}$ is defined as a function of the mass matrix $\boldsymbol{M}$ and the stiffness matrix $\boldsymbol{K}$:

$$\boldsymbol{C} = \zeta \boldsymbol{M} + \xi \boldsymbol{K} \tag{3.39}$$

where ζ is the mass-proportional damping coefficient and ξ is the stiffness-proportional damping coefficient. Appropriate values for these damping coefficients for ice are not described in existing literature.

3.6.2 Verification of the lattice model

The lattice model described in Section 3.6.1 is verified against analytical solutions for three cases:

1. Out-of-plane deformation of a semi-infinite plate loaded by a point load on the edge.
2. Natural frequencies and mode shapes of a finite, simply supported plate on a Winkler foundation.
3. Mode I splitting of a linear elastic rectangular plate.

The verification results are described in the following sections.

Out-of-plane deformation of a semi-infinite plate loaded by a point load on the edge

The lattice model is verified by comparison to an analytical solution of a semi-infinite Kirchoff – Love plate on an elastic foundation, subject to a point load on a free edge. The analytical solution is obtained as described in Kerr and Kwak (1993). The lattice plate that is compared to the analytical solution has finite dimensions, but the dimensions are chosen such that the side boundaries no longer influence the solution. All side boundaries are free. The lattice plate is supported by an elastic foundation. The model parameters used for verification are shown in Table 3.1.

Table 3.1: Parameters used in the edge load verification study.

parameter	**symbol**	**value**
Young's modulus [GPa]	E	5.0
Shear modulus [GPa]	G	2.5
Water density [$\mathrm{kg/m^3}$]	ρ_w	1025.0
Point load [kN]	F_p	10.0
Ice thickness [m]	h_i	1.0
Poisson's ratio [-]	ν	0.0

A Voronoi mesh is generated by picking random points within the sheet outer boundaries, and creating polyhedral bodies around the points, as described in the previous section. For each additional point, the minimum distance between the point and all other points is specified based on the position of the point within the sheet. If the point is too close to another point, it is discarded. Using this technique, the mesh can be refined around the point of interest by specifying a lower minimum point-to-point distance close to the loaded point. In this verification study, the minimum distance between points is specified as:

$$D_\mathrm{min;p} = \frac{D_f}{40} + D_\mathrm{min;t} \tag{3.40}$$

in which $D_{\mathrm{min;p}}$ is the minimum distance between the seed point and any other point, D_f is the distance between the loading point and the seed point, and $D_{\mathrm{min;t}}$ is the mesh size in the direct vicinity of the loading point. Figure 3.12 shows a sketch of the modelled situation.

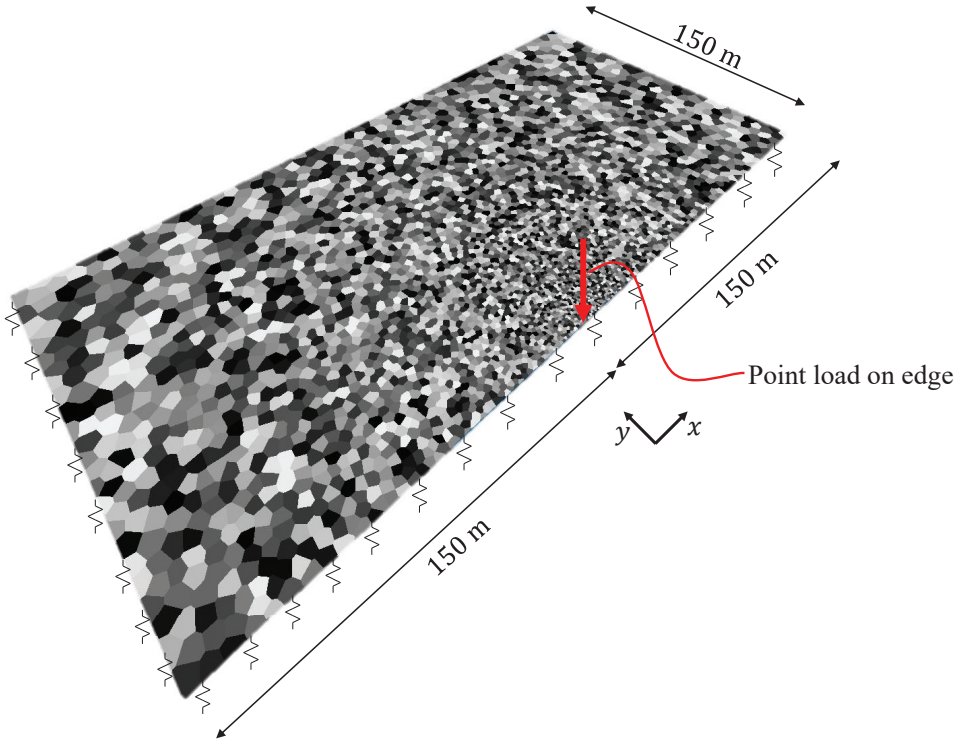

Figure 3.12: Verification of plate deformation when loaded by a point load on a plate edge.

Figure 3.13 shows the edge deformation of the loaded edge of the plate for different mesh sizes, in comparison to the analytical solution of a semi-infinite sheet loaded by a point load on its edge. It shows that the lattice solution converges to the analytical solution for a fine mesh. The error between the lattice solution and the analytical solution is 18.3% for a minimum mesh size $D_{\mathrm{min;t}}$ of 5.0 m, 9.0% for a minimum mesh size of 2.0 m, and 1.9% for a minimum mesh size of 0.5 m. The increase in error with mesh size can be partly explained by the absence of bending deformation close to the loading point in the case of coarser meshes. The deformation in the direct vicinity of the loaded point gives a large contribution to the total deformation.

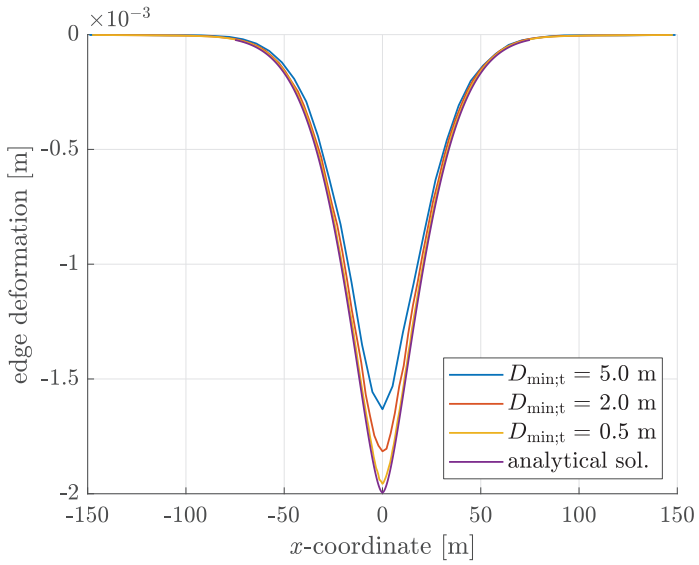

Figure 3.13: Edge deformation for different mesh sizes, compared to the analytical solution.

Natural frequencies and mode shapes of a finite simply supported plate on a Winkler foundation

The dynamic lattice properties are verified by comparing the out-of-plane natural frequencies and mode shapes as predicted by the lattice model to an analytical solution of a rectangular plate on a Winkler foundation that is simply supported at the edges. The analytical solution which is used for the verification is described by van Vliet and Metrikine (2018). The natural frequencies and mode shapes of the lattice plate are obtained by calculating the eigenvalues and eigenvectors of the stiffness matrix.

In order to compare the accuracy of the irregular lattice presented in this section to the accuracy of the regular lattice derived in van Vliet and Metrikine (2018), the plate dimensions are chosen to match the plate dimensions used for model verification in van Vliet and Metrikine (2018); 60 x 100 m. The other parameters are equal to the values used in the edge load validation case, as listed in Table 3.1. Figure 3.14 shows a comparison between the mode shapes predicted by the lattice model and the mode shapes resulting from the analytical solution. The mode shapes of the first 9 modes as predicted by the lattice model match well with the analytical mode shapes. The natural frequencies of the lattice plate have been compared against the natural frequencies given by the analytical solution. Table 3.2 shows the natural frequencies of the first 20 modes as given by the analytical

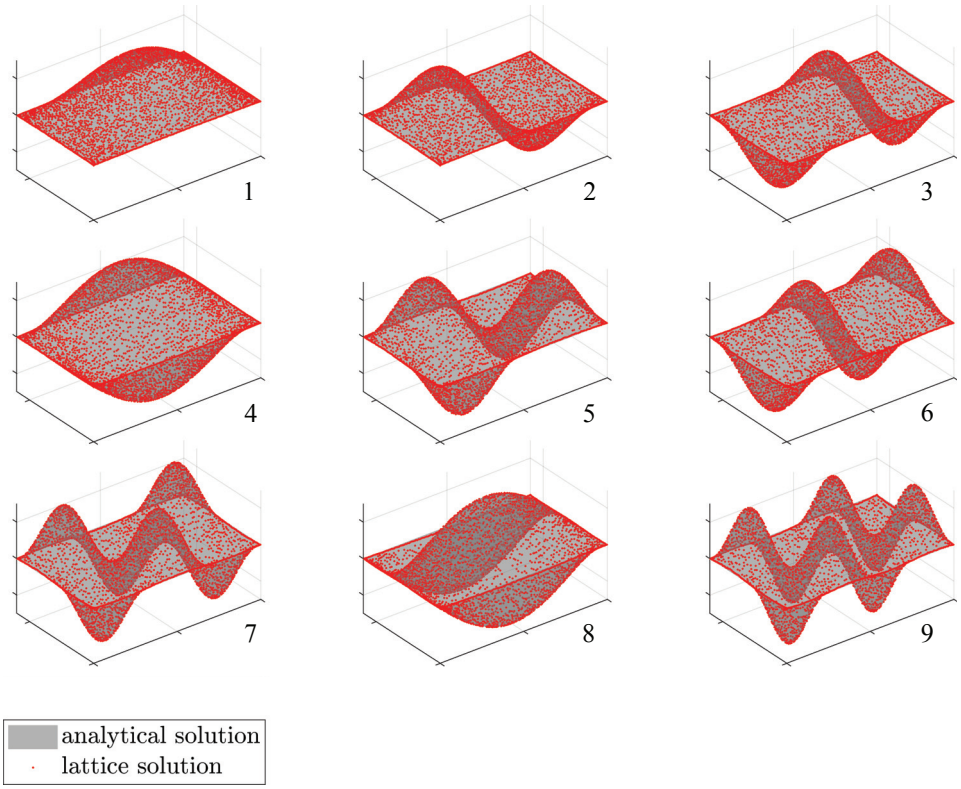

Figure 3.14: The first nine mode shapes of a 60 x 100 m plate on a Winkler foundation, simply supported at the edges.

solution, and the error percentages (e) between the natural frequencies predicted by the lattice model and the analytical solution, for three different mesh densities, expressed by the number of elements used to discretize the plate (N_b).

The error percentages consistently decrease with the mesh size. However, the error percentages are higher than the error predicted by the structured lattice model derived in van Vliet and Metrikine (2018), which gives an error percentage between 0.0 and 0.15% (for the first 20 modes) for a mesh with 6161 elements.

Mode I splitting of a linear elastic rectangular plate

The lattice model is verified against the analytical solution for static mode I splitting of a rectangular plate. The verification is performed against the analytical solution according to linear elastic fracture mechanics (LEFM) (Dempsey et al., 1994; Lu et al., 2015*a*). Two cases are modelled: in case *a*, the lattice is constructed such that there is a straight crack path from the crack initiation point to the

Table 3.2: Error percentages in the natural frequencies of out-of-plane vibration modes as a function of mesh size.

mode	**frequency [Hz]**	$\mathbf{e}$ [%] $N_\mathrm{b} = 582$	$\mathbf{e}$ [%] $N_\mathrm{b} = 1243$	$\mathbf{e}$ [%] $N_\mathrm{b} = 4768$
1	0.66	2.3	0.66	0.2
2	0.89	4.3	1.5	0.42
3	1.4	4.7	1.4	0.48
4	1.4	2.8	0.6	0.35
5	1.7	5.3	1.7	0.53
6	2.1	3.5	1.1	0.46
7	2.2	7.1	2.1	0.63
8	2.8	2.2	0.42	0.37
9	2.9	5.5	2.1	0.64
10	3.0	4.1	0.83	0.43
11	3.1	4.0	1.2	0.49
12	3.6	6.1	1.8	0.59
13	3.9	6.3	1.8	0.61
14	4.1	2.9	0.68	0.42
15	4.4	6.3	2.2	0.66
16	4.8	2.0	0.29	0.37
17	5.0	5.1	1.6	0.59
18	5.1	3.8	0.82	0.45
19	5.3	6.0	2.2	0.68
20	5.5	3.8	0.55	0.42

other end of the plate. In case *b*, the lattice is random. Verification is performed for both cases in order to distinguish between the effects of the irregular crack path and the effect of the plate deformation. The normalized splitting load as a function of the crack length is constructed for the lattice plate by the following procedure:

1. Load the crack tip with a unit load.
2. Store the crack opening displacement.
3. Remove the lattice element with the highest strain.
4. Load the lattice with the propagated crack with a unit load, and repeat the procedure.

The outcome of this procedure is the crack opening displacement (COD) as a function of crack length. From the COD and the crack length, the strain energy release rate G_f can be derived as described in Lu et al. (2015*b*):

$$G_f = \frac{F_Y}{h} \frac{du_0(L_{\text{cr}})}{dL_{\text{cr}}} \tag{3.41}$$

in which F_Y is the splitting load, h is the ice thickness, $u_0(L_{\text{cr}})$ is the conjugate deformation to each of the splitting loads and L_{cr} is the crack length as defined in Figure 3.15. The stress intensity factor can be derived from the energy release rate using the relationship:

$$K_I = \sqrt{G_f E} \tag{3.42}$$

Figure 3.16 shows the non-dimensional splitting load as a function of the (non-dimensional) crack length. for a straight crack path (a) and an irregular crack path (b), for mesh sizes of 10 m , 4 m and 2 m.

The lattice model is close to the analytical solution when the crack path is straight for all tested mesh sizes. This essentially means that the COD is predicted well by the lattice model. In the case of an irregular crack path, the lattice results follow the trend of the analytical solution, but there is substantial deviation at some points. The deviation is related to the deviation of the irregular crack from the straight crack path, according to which the analytical solution is constructed.

In the verification as performed above, the COD caused by a unit splitting load was used to reproduce the analytical non-dimensionalized splitting load curves. However, in more complicated scenarios, one would typically use the maximum strain in combination with a failure criterion to check whether a crack propagates.

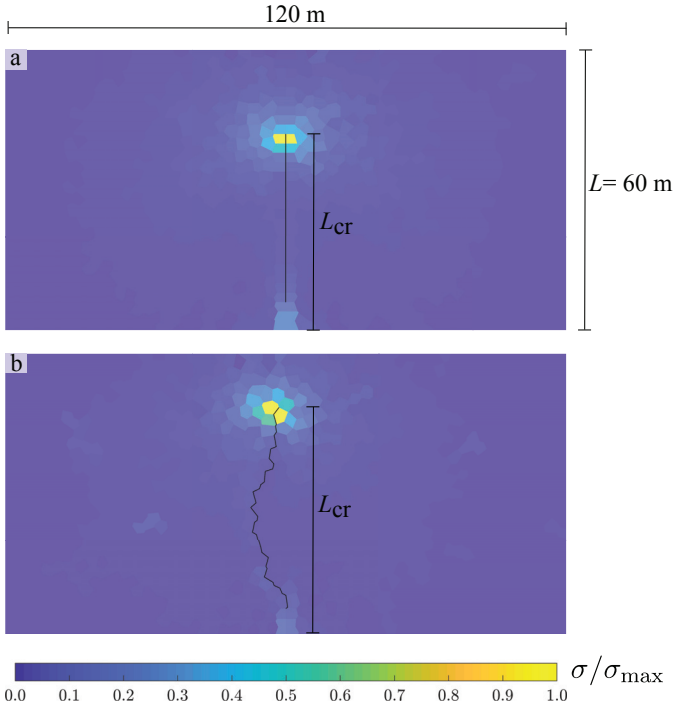

Figure 3.15: Visualization of the stress state within the plates during the splitting verification for a straight crack path (a) and for a irregular crack path (b).

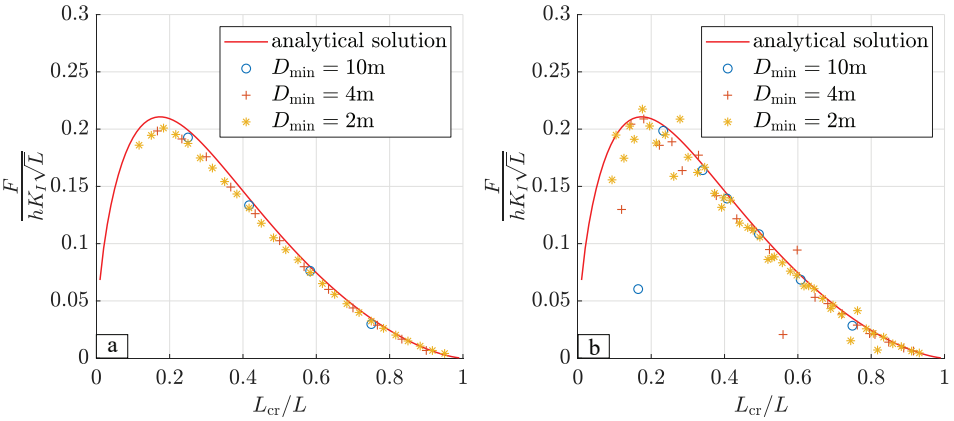

Figure 3.16: Non-dimensional splitting load as a function of the non-dimensional crack length for a straight crack path (a) and an irregular crack path (b).

Although the COD is largely mesh size independent, the strain at the crack tip is not. Therefore, a mesh-size dependent scaling factor should be applied to the stress at the crack tip.

In accordance with LEFM, the current implementation of the lattice model would predict a strain going to infinity for a mesh size approaching 0. The stress at the crack tip is proportional to one over the square root of the mesh size. This scaling behaviour is in accordance with theory, as derived below.

In LEFM, the stress near a crack tip is proportional to one over to the square root of the distance to the crack tip:

$$\sigma_{\mathrm{t}} \propto \frac{1}{\sqrt{r}} \tag{3.43}$$

The stress in a discrete lattice element representing a crack length δ would be the mean stress over the element length. For an element at the crack tip, this results in a stress that is proportional to:

$$\sigma_{\delta} \propto \frac{\int_0^{\delta} \frac{1}{\sqrt{r}} dr}{\delta} = \frac{1}{\sqrt{\delta}} \tag{3.44}$$

which gives the relationship between mesh size and crack tip stress. This relationship necessitates that the stresses near the crack tip be multiplied by $C\sqrt{\delta}$, in which C is a constant whose value depends on the critical stress intensity factor and the failure stress.

This approach effectively removes the mesh dependence from the crack propagation problem. However, it is not straightforward to determine when the scaling should be applied. After all, scaling should only be applied to the stresses at crack tips, and not to all stresses within the lattice plate. In principle, a numerical scheme can be conceived that keeps track of crack tips, and applies the stress scaling only where needed. However, such a scheme has not yet been implemented.

3.6.3 Summary of lattice verification

The presented verification studies show that the relatively simple random lattice model described in this section is capable of capturing the plate deformation under a point load on the edge; the out-of-plane eigen modes and vibration frequencies of a plate on a Winkler foundation and simply supported at the edges; and the force needed to split a rectangular plate according to LEFM. The accuracy of the lattice model is compared to analytical solutions. In two of the performed verification studies, the lattice model converges to the analytical solution for an increasing mesh density. In the splitting verification study, a small deviation remains present.

The unstructured nature of the lattice model leads to larger deviations between the lattice solutions and the analytical solutions compared to a structured lattice with a similar mesh size. These deviations can be partly attributed to the mesh random-

ness directly, such as the fact that the crack path must deviate from the straight crack path as predicted by the analytical solution. Another source of the deviation results from the simplified definitions of spring properties. Unlike a structured lattice, the spring properties for an unstructured lattice have not been derived from continuum theory. This explains the higher deviation between the natural frequencies of the plate discretized with the irregular lattice model compared to the regular lattice model plate frequencies as derived by van Vliet and Metrikine (2018). One of the predominant shortcomings of the presented unstructured lattice model is the inability to properly capture the Poisson effect. The verifications in this section are all performed against analytical solutions using a Poisson's ratio of 0. If a Poisson's ratio more common to sea ice would have been used, the deviations between the lattice result and the analytical solutions would be larger (as the Poisson effect is not captured in the lattice model).

In judging the applicability of this lattice model, the result inaccuracy caused by the irregular nature of the lattice should be compared against the irregularities in actual sea ice. In this perspective, the scatter in the results of the irregular lattice model is smaller than the scatter resulting from tests on sea ice. As the natural variability of sea ice is higher than the result variability caused by the lattice irregularity, the lattice model is considered sufficiently accurate. However, since more accurate structured lattice models are available, the benefits of an unstructured lattice compared to a structured lattice should be weighted against the downsides of result scatter and the lack of Poison effects. Which lattice model is most suitable (regular of irregular) depends on the modelled scenario. Some benefits of the irregular lattice model compared to the regular lattice model are:

- The mesh can be refined around a point of interest, as is done in the point-load-on-edge verification case.
- The dependence of crack paths on the mesh geometry is reduced. There are no pre-defined crack directions along which a crack can propagate more easily than other directions. Note, however, that the crack path is not mesh independent in the irregular lattice, since the crack can still only propagate along the failure surfaces between elements as defined by the discretization procedure.
- The effects of the irregular mesh may capture the inhomogeneous nature of actual sea ice. In fact, regular lattice meshes are often randomized in order to capture the inhomogeneous nature of materials, thereby intentionally introducing errors compared to the (homogeneous) continuum behaviour. This is done by, among others, van Vliet and Metrikine (2017).

3.7 Summary

This chapter describes a novel implicit discrete element time stepping scheme. The scheme can be used to model continuous as well as discontinuous contacts, using a unified approach. The time stepping scheme formulates and solves an MLCP in each time step. The MLCP is formulated using the constant average acceleration method. Continuous contacts occur when the time stepping scheme is combined with a lattice discretization of ice floes. Discontinuous contacts are used to model the interactions between ice floes and between the ice and the structure. Ice failure can be considered by discretizing the ice floes, or by applying semi-analytical failure criteria. When applying semi-analytical ice failure, the ice floe geometry and loading conditions are mapped to a case for which the failure loads can be obtained analytically or are pre-computed. The developed discrete element method is applied to investigate floe shape effects and the variability in ice tank test results in Chapter 4. Semi-analytical ice failure is used in the simulations performed for these studies

Chapter 4

Floe-shape effects and variability in the results of ice tank tests with broken ice

The discrete element time stepping scheme described in Chapter 3 is applied to investigate interaction phenomena in the interaction between structures and broken ice. Two studies are described in this section. The first study investigates the effect of floe shape on the load experienced by vertical-sided structures interacting with a broken ice field. The second study assesses the variability that may occur in the results of ice tank tests with broken ice. In both studies, the contact model and time stepping scheme are used in combination with a semi-analytical ice failure model. The floe-shape effect was studied using a 2-D implementation of the described model, while the ice tank test variability was studied with a 3-D model.

4.1 The effect of ice floe shape on the load experienced by vertical-sided structures interacting with a broken ice field

The effect of floe shape on the load experienced by vertical sided structures interacting with a broken ice field is investigated in van den Berg et al. (2019*b*). This publication is included in Appendix D. This section contains a summary of this study. The study is limited to low to medium ice areal coverage conditions (30-70%). The influence of the floe shape is most relevant in these conditions because the ice clearing process often governs the ice resistance. Furthermore, the study is limited to vertical-sided structures. Sloping sides promote bending failure and floe rafting, thereby significantly reducing the effect of the floe shape.

There are several scenarios in which the load from low- to medium-areal-coverage broken ice on vertical-sided structures is of interest. Three examples are:

1. *Constructions in the light Arctic.* The light Arctic is defined as regions where sea ice may occur as a statistical possibility, but which are normally ice-free throughout the year. Most recent Arctic offshore developments are in these regions. Structures for these regions are not usually designed for heavy ice conditions, and may have a vertical-sided waterline. Loads from low- to medium-areal-coverage broken ice may be the operational design load for such structures.

2. *Operations in the 'ice-free' season.* This includes drilling, towing or construction operations, possibly using jack-ups or other vertical-sided structures. Low- to medium-areal-coverage broken ice load estimates are needed to determine the operating window.

3. *Structures supported by ice management.* Structures can be supported by ice management operations, in which an ice breaker reduces the size of incoming ice floes in order to decrease the loads on a protected structure. Loads from broken ice may be the design load of the protected structure.

Floe-shape effects are especially relevant to ice tank tests or numerical simulations that may be performed in the design phases for the above mentioned scenarios. In ice tank tests, broken ice is created by manually or mechanically breaking up an intact ice sheet. Therefore, the resulting ice floe shapes can be controlled to some extent. Ice tank tests with broken ice are often performed with ice floes that have square or rectangular shapes (e.g., Hoving et al. (2013); Haase et al. (2012)), which may have a major effect on the resulting broken ice load.

The effect of the floe shape in DEM modelling of ice has been studied by Hopkins et al. (1991); Tuhkuri and Polojärvi (2005); Konno et al. (2011); Rheem et al. (1997); Yamaguchi et al. (1997). Hopkins et al. (1991) and Tuhkuri and Polojärvi (2005) studied the effects of rubble shape on the ridge formation process and on ridge keel punch through tests. Konno et al. (2011) studied the effect of rubble shape on the resistance of ships in rubble channels. These studies showed a clear shape effect. However, the modelled scenarios in these studies are different from the scenarios modelled in the current study, because the studied scenarios concern ice rubble only. This study investigates the effect of floe shape in level broken ice varying in size from $20\ \mathrm{m}^2$ to $4832\ \mathrm{m}^2$. Such broken ice fields typically occur when ice is broken by environmental forces, such as ocean gravity waves. To the authors' knowledge, Rheem et al. (1997) and Yamaguchi et al. (1997) are the only researchers that studied the effect of the floe shape in similar broken ice-structure interaction scenarios. However, the scenarios tested by Rheem et al. (1997) were primarily designed for the validation of a numerical model; therefore, they are not sufficiently realistic to conclude anything on floe shape effects in actual broken

ice-structure interactions, other than that the effect is present. Yamaguchi et al. (1997) proposed a method to take the floe shape effect into account using a parameter described as the C-angle. However, the tested scenarios are limited and the numerical model is greatly simplified. For example, no floe rotation is taken into account.

The floe-shape effect was studied in confined conditions (as would occur in ice-tank testing, due to the tank walls) and in unconfined conditions. The floe-shape effect in unconfined conditions is presented in this section. For an analysis of the floe-shape effect in confined conditions, the reader is referred to Appendix D.

A sensitivity study is conducted in which the floe shape and other parameters whose effect may be correlated with the floe-shape effect are systematically varied. The mean load and the standard deviation of the surge load on the structure are used as the primary comparison parameters in analysing the effect of the floe shape. The investigated parameters are the structure shape, the ice areal coverage, the confinement conditions and the friction coefficient. In the sensitivity study, random numerical broken ice fields with different floe shapes are created. All broken ice fields have the same properties, except for the difference in floe shape. The floe size distributions of the numerically created floe fields is obtained from a digitization of a top-view photograph of a full-scale broken ice field, which is broken under environmental loading (i.e., not by ice management). The floe field is digitized following the procedure described in Zhang and Skjetne (2015). Eight different floe shapes were tested; 3-8 corner regular shapes, circular floes, and real floe shapes. The real floe shapes are the shapes of the floes in the digitized top-view photograph. Figure 4.1 shows the floe fields with different floe shapes. Note that the initial positions of similar-sized floes are largely the same. The investigated parameter combinations are listed in Table 4.1.

4.1.1 Results of the sensitivity study

The results from the sensitivity study show there is a strong effect of the ice floe shape on the mean and on the standard deviation of the ice load in the surge direction. The mean ice loads in surge direction for the different floe shapes are shown in Figure 4.2. The coloured bars represent the results of the low friction simulations ($\mu = 0.1$). The square markers represent the results of the high friction simulations ($\mu = 0.5$). For the low-friction simulations, the results for circular and square structures are grouped in the coloured bars, in which the minimum of the bar is the lowest mean load and the maximum of the bar is the highest mean load from both tested structure shapes. In all simulations, the circular structure

Table 4.1: Investigated parameter combinations.

Constant parameters	
ice thickness	1.0 [m]
crushing specific energy (CSE)	2.0 $[\mathrm{MJ/m^3}]$
structure width	40.0 [m]
structure velocity	1.0 [m/s]
ice form drag coefficient	0.5 [-]
ice skin friction drag coefficient	0.005 [-]
floe area distribution	from top view photo
Varying parameters	
structure shape	square circular
ice areal coverage	30% 50% 70%
floe shape	digitized real floes 3 - 8 corner regular circular
friction coefficient	0.1 [-] 0.5 [-]

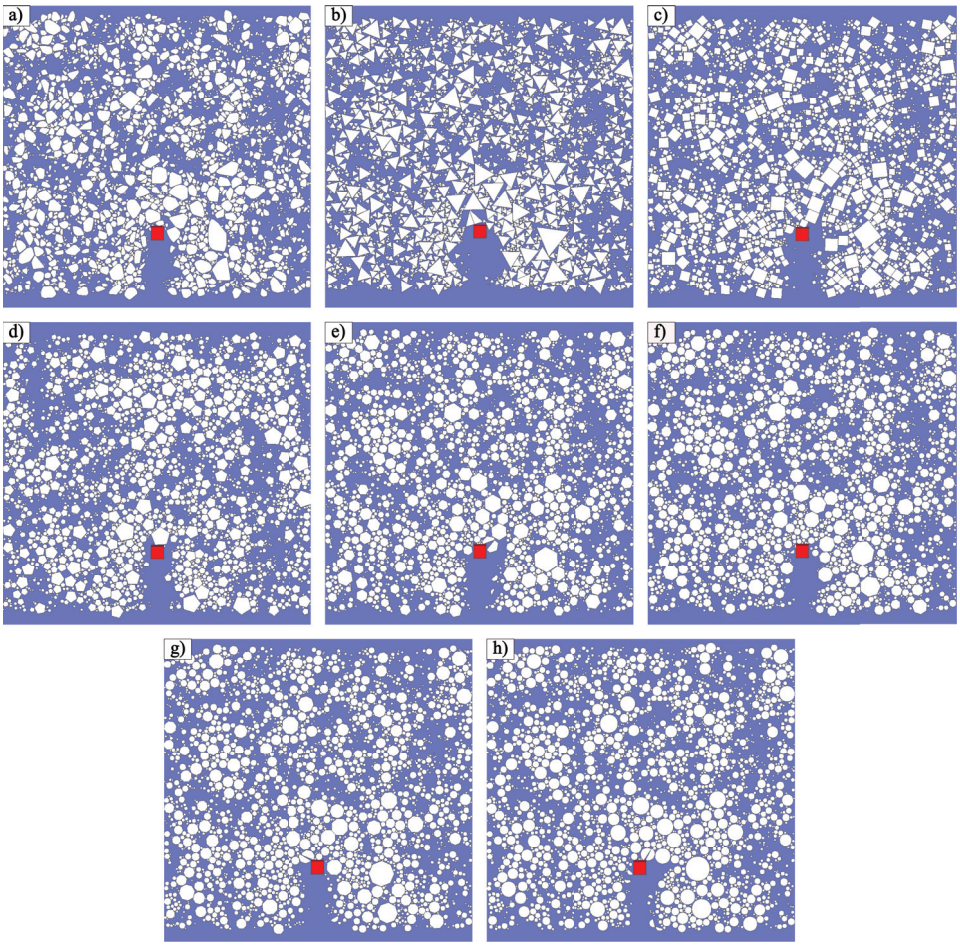

Figure 4.1: Floe fields with different floe shapes, but otherwise identical properties.

resulted in loads with a lower mean and standard deviation than the loads from the square structure. The high-friction simulations were only performed with the square structure geometry. The data in Figure 4.2 show the following:

- Square ice floes result in higher mean ice loads in the surge direction.
- Other regular shapes with 'parallel opposite edges', i.e., the hexagonal and octagonal floes, also result in higher mean ice loads in the surge direction than other floe shapes; however, the effect is not as strong as with square floe shapes.

- The floe-shape effect is stronger for a circular structure geometry than for a square structure geometry.

- The floe 'roundness' appears to play a role in the high-friction simulations, but not in the low-friction simulations.

- The influence of floe shape is inversely related to the friction coefficient. The higher the friction coefficient, the lower the effect of the floe shape.

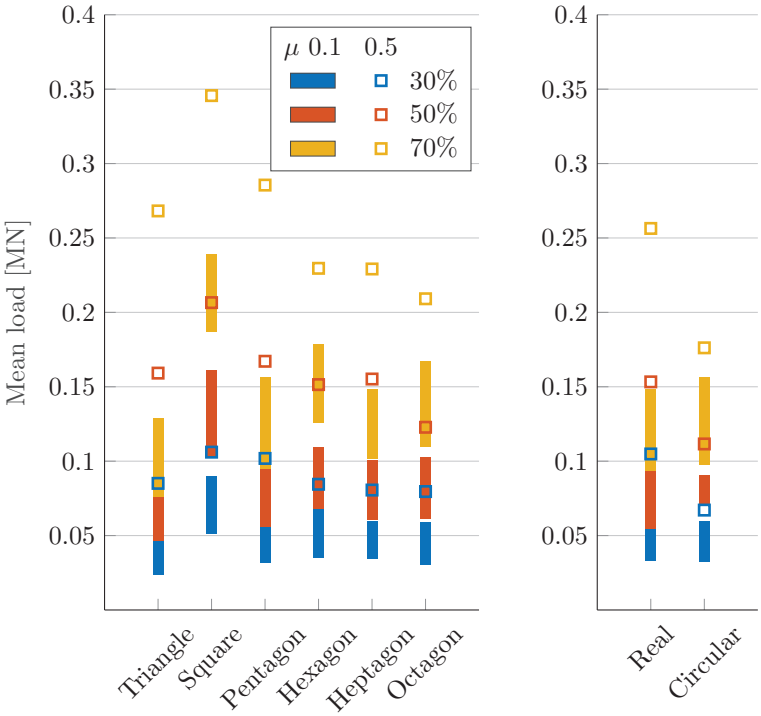

Figure 4.2: The effect of floe shape on the mean ice load in unconfined conditions.

Parallel opposite edges are defined as edges of the floe that have a parallel edge perpendicularly opposite to the edge across the floe. This is clarified in Fig. 4.3. Floe roundness is a measure for how closely a body approaches a disk geometry (in 2-D). Different definitions are used in the literature to define floe roundness; however, the exact definition is not relevant in this study. Floe roundness is a common way to classify ice floe geometry and is used, for example, by Toyota et al. (2011).

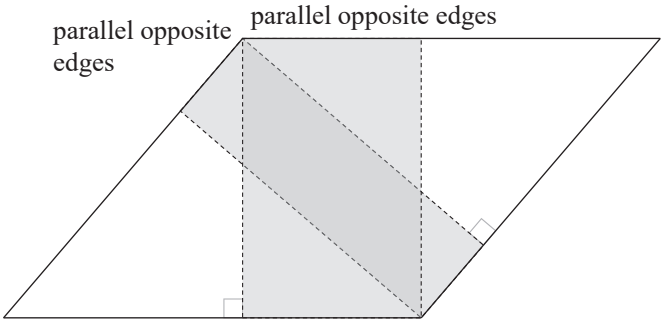

Figure 4.3: Parallel opposite edges enable the formation of larger force networks.

4.1.2 Mechanisms responsible for the floe-shape effect

The most important phenomenon responsible for the floe-shape effect is the greater extend of force networks in the broken ice field when floes have parallel opposite edges. The analyses presented in this section are published in van den Berg et al. (2019*a*). This publication is included in this thesis in Appendix E. The parameters used to generate the results in this section were equal to the constant parameters listed in Table 4.1. In addition, the following parameters were used:

structure shape:	circular
ice areal coverage:	70%
floe shape:	digitized real floes and square floes
friction coefficient:	0.15 [-]

A scalar loading value is assigned to each ice floe in order to study the difference in force propagation and dissipation in the broken ice field as a result of the different floe shapes. The loading value is defined similar to the value used to visualize force chains in Paavilainen and Tuhkuri (2013), as the maximum eigenvalue of the load tensor $\hat{\alpha}_{ij}$:

$$\hat{\alpha}_{\mathrm{ij}} = \sum_{c=1}^{N_c} F_i^c r_j^c \tag{4.1}$$

in which N_c is the number of contacts of each floe, F_i^c are the contact force vectors, and r_j^c are normalized vectors from the body's COG to the contact point. Differences in force propagation between the floe fields with real and square floe shapes are quantified by comparing the mean combined floe area of all floes with a loading value above a range of threshold load values:

$$\overline{A}\left(F_{\mathrm{thr}}\right) = \frac{\sum_{t=1}^{N_t} A_{\lambda_{\max} > F_{\mathrm{thr}}}\left(t\right)}{N_t} \tag{4.2}$$

in which $\overline{A}$ is the mean broken ice area with a loading value above threshold load value F_{thr}, N_t is the number of time steps, and $A_{\lambda_{\max}>F_{\text{thr}}}(t)$ is the broken ice area with a loading value above load value F_{thr} in each time step. Figure 4.4 shows a visual comparison of the force networks occurring in the square floe simulations and the force networks occurring in the real floe simulations. The area of the floes with a load level above a threshold load value at a time instance is the summation of the top areas of all coloured floes. A threshold load value of 5 kN is used in the left figures and a threshold load value of 0.25 MN is used in the right figures.

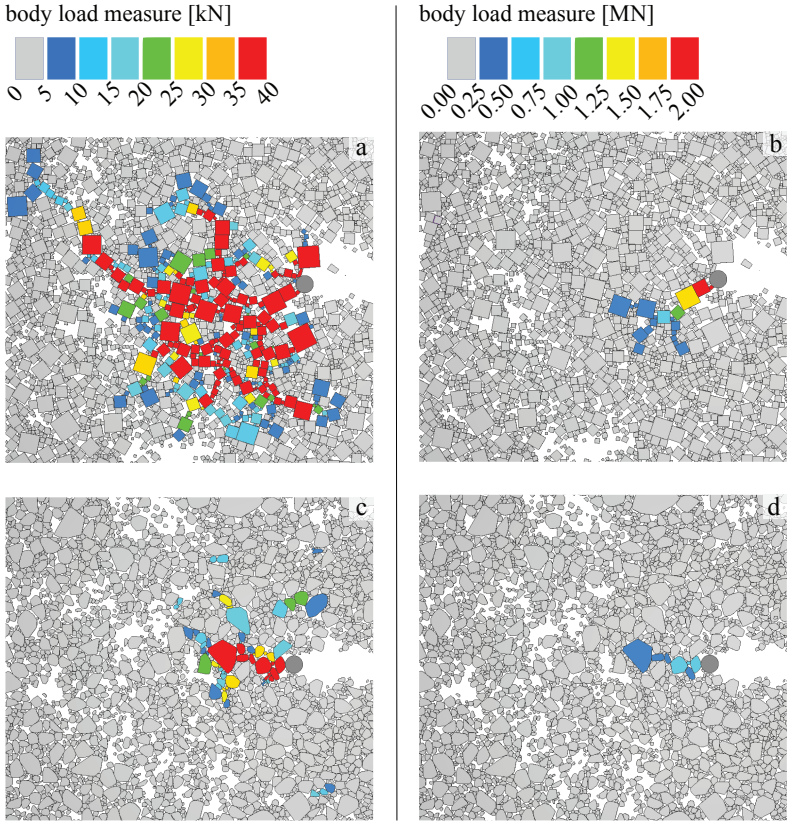

Figure 4.4: Floes with a load value exceeding a threshold level (coloured floes) for the simulations with square floes (top) and the simulations with real floe shapes (bottom), and for different threshold levels (left and right).

The resulting load-area curve is shown in Figure 4.5. Figure 4.5 shows that the force network is larger in the square floe simulations. Depending on the threshold load level, the mean floe area with a load value higher than the threshold load is 2.15 to 3.13 times higher in the square floe simulations.

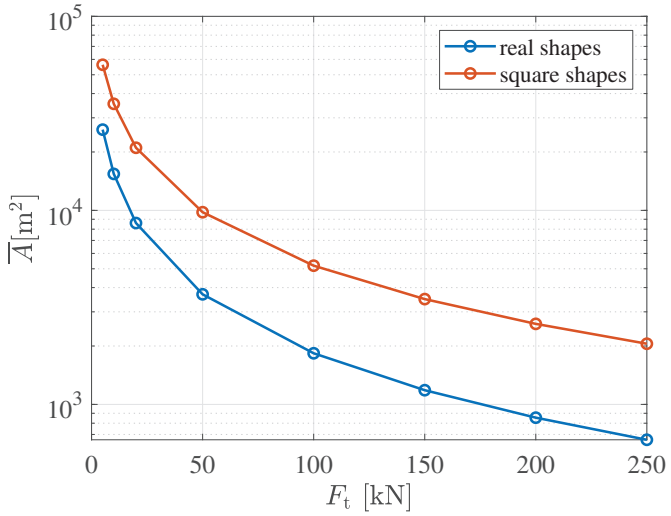

Figure 4.5: Mean total floe area of the floes exceeding a threshold load level.

In order to gain insight in the differences in force propagation and dissipation, the area-load curves are normalized by scaling the load thresholds with the mean structure load value. The mean area-over-load-threshold as a function of the normalized load thresholds can be described by a power function of the form:

$$\overline{A}\left(F_\mathrm{thr}\right) = a\left(\frac{F_\mathrm{thr}}{\overline{F}_\mathrm{thr;s}} + b\right)^c + d \tag{4.3}$$

in which $\overline{F}_\mathrm{thr;s}$ is the mean load value of the structure, constants b and c have no units and constants a and d have the unit of m^2. The normalized area-load curves are shown in Figure 4.6.

The normalized area-load curve of the square floe shape simulation can be scaled to match the area-load curve of the real floe shape simulation by applying a scaling factor of 0.7:

$$\overline{A}_\mathrm{nat} \approx 0.7\overline{A}_\mathrm{sq} \tag{4.4}$$

The scaled results, as well as a power law fit of the real and scaled results, are shown in Figure 4.6. The normalized area-load curve of the real floe shape simulation and the scaled area-load curve of the square floe simulation can be accurately approximated by the power law function given in Equation 4.3 with the coefficients $a = 2034\ \mathrm{m}^2$, $b = 0.0127$, $c = -0.891$ and $d = -359.5\ \mathrm{m}^2$. The exact values of coefficient a, b, c and d are not so relevant since they depend on the chosen simulation parameters such as drag and friction coefficients. However, it is an important finding that the normalized area-load curves of both the real and square floe shape

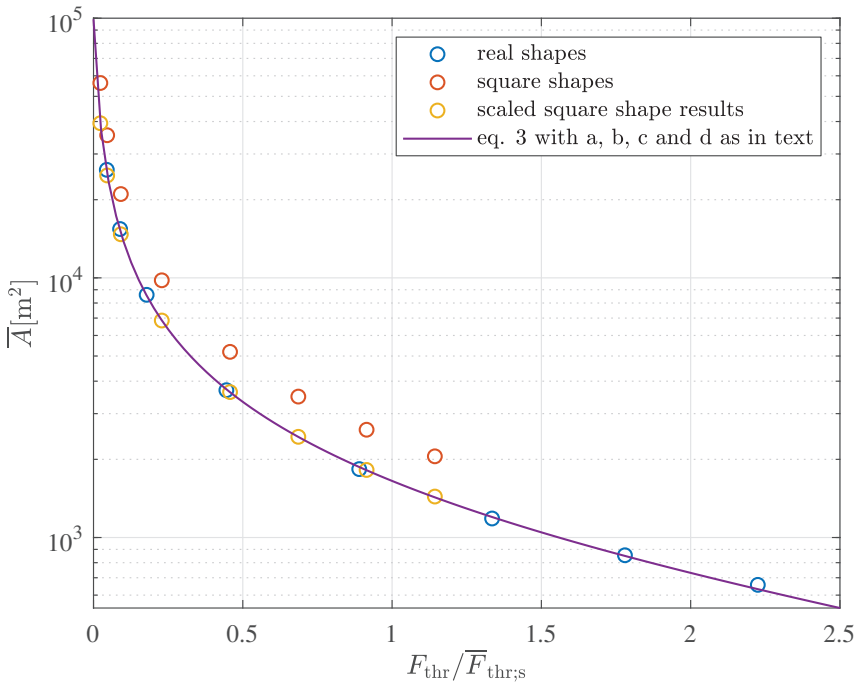

Figure 4.6: Mean total floe area of the floes exceeding a normalized threshold value, including the scaled square floe results and a power law fit to the real floe shape and scaled results.

simulations can be approximated with the same power $c = -0.891$. This indicates that the propagation and dissipation processes are similar in the real and square floe simulations. The force network in the square floe simulations can be seen as a scaled-up version of the force network in the real floe simulations.

4.1.3 Model limitations and result validity

As any numerical model, the model used in this study is a simplification of reality. The simplifications that were made may influence the modelling results. In the context of the study on floe-shape effects, the most important limitation is the 2-D nature of the numerical simulations and the lack of 3-D effects like ice floe rafting. However, the contact forces and ice areal coverage in the tested cases described in this section were such that it is not expected that ice floe rafting and/or rubbling would have a large effect on the study results.

In addition to the model simplifications, there is also a significant uncertainty in the chosen physical parameters. Parameters which may have a significant influence on the results, such as the friction coefficients and the hydrodynamic drag coefficients,

have a high uncertainty. There is no agreement in the ice modelling community on what values are most appropriate. As an example, there is a wide range of friction values being applied in discrete ice-structure interaction simulations, as described in Section 2.3.2. This uncertainty is partly alleviated by assessing the floe-shape effects at two friction values which represent the approximate lower and upper bounds of friction values used in other numerical ice modelling studies with conditions similar to the study performed in this section. For both friction values, the floe-shape effect is significantly present.

4.1.4 Conclusions and recommendations

The numerical simulations show that there is a strong floe-shape effect on the mean ice load in the surge direction in all tested broken ice conditions. The results from the sensitivity study show that the square floe simulations predict a mean ice load that is between 19% and 88% higher than the mean ice load predicted by the real floe shape simulations. The effect of floe shape is correlated to all of the investigated parameters. For instance, a circular structure results in a higher floe-shape effect than a square structure, a higher friction coefficient reduces the floe-shape effect and the floe-shape effect is stronger for a higher ice areal coverage. The greater extend of force networks is the primary mechanism responsible for the floe-shape effect.

The extend of force networks is related to the presence and length of parallel opposite edges. The presence and length of parallel opposite edges as a description of floe shape is novel and distinctly different from the often used roundness or (equivalent but opposite) angularity parameter. A quantification of the effect of parallel opposite edges is not provided. The high number of parameters that may influence the floe-shape effect and the complexity of the phenomena leading to the shape effect, make such a quantification infeasible. Currently, numerical simulation appears the best tool to assess the influence of floe shape in a particular interaction scenario, possibly in combination with ice-tank tests. The results of this study lead to two recommendations:

- DEM simulations of broken ice should attempt to approximate the expected real floe shape. If the floe shape is not known, several floe shapes should be modelled to assess the influence of floe shape in the scenario of interest. Approximating the broken ice with square floe shapes will lead to conservative results, but the results may be overly conservative, resulting, in some conditions, in loads that are almost two times greater than if real floe shapes would have been used. Approximating the ice floes with circular floe shapes may lead to an under-prediction of broken ice loads.

- Ice-tank tests of broken-ice-structure interaction should be performed using broken ice with shapes that resemble the floe shapes of the ice condition one intends to model. It is left to the ice tanks to define a realistic 'real-equivalent' floe shape.

4.2 Variability in the results of ice-tank tests with broken ice

During the numerical study on floe-shape effects, it was observed that changes in the initial (random) floe positions could have a large effect on the simulation results. An interaction length of 10 000 m was needed before the mean load was converged to a stable value (i.e, a longer simulation would not lead to a change in mean load) that was independent from the initial floe positions. The interaction length that was needed to get a converged mean load was much longer than the (full-scale equivalent) length of most ice tank tests in broken ice. Based on these results, the question arose if and how the result variability caused by a change in initial floe positions would affect ice tank test results. This led to the study described in this section. This study is submitted to *Marine Structures*. The submitted manuscript is included in Appendix F.

Ice-tank test campaigns are often designed to investigate the influence of several parameters that may affect the ice-structure interaction process, such as the floe size, the floe shape, the interaction velocity, the ice thickness, the ice concentration and the structure orientation. To analyse the influence of these parameters, each parameter must be varied separately compared to a base case, while keeping the other parameters constant. Ice-tank test campaigns generally do not perform multiple repetitions of tests with the same parameter combinations, mainly due to the cost and efforts involved in each single test case. Therefore, the variability and repeatability of tests in broken ice with the same initial parameters is not well understood.

In this study, selected test cases from two test campaigns were analysed. Both test campaigns were conducted at the Hamburg Ship Model Basin (HSVA). The first test campaign studied the interaction between a 4-legged structure with a vertical waterline and several broken and level ice conditions. This campaign is described in Hoving et al. (2013). The second test campaign studied the interaction between two ship-shaped structures and several level and broken ice conditions with the primary aim of testing the dynamic positioning capabilities of ships in ice. This campaign is described in, among others, Kjerstad et al. (2015); Haase et al. (2012); Haase and Jochmann (2013). In this section, only the ice tank test and numerical modelling results of the multi-leg structure tests are described. The results of the ship-shaped structure tests are described in Appendix F.

For the selected test cases, The measured structure load is analysed and the ice tank test is reproduced numerically. Each analysed test case is simulated 20 times. In each numerical simulation run, the initial position of the ice floes is slightly different. Otherwise the conditions are identical and equal to the ice-tank test conditions. Using the numerical simulation results, the variability in the ice load statistics caused by the difference in the initial floe positions is assessed.

The analysed multi-leg structure tests were performed in 2014 at HSVA as part of the Hydralab IV project. The primary objective of the tests was to investigate the loads from broken ice on a jack-up structure, and establish relationships between the level ice load and the load from broken ice with the same thickness and mechanical properties. A description of the tests and a preliminary evaluation of the ice loads can be found in Hoving et al. (2013). The structure that was used in the tests had 4 cylindrical legs, which were vertical at the waterline. The waterline dimensions of the test structure are shown in Figure 4.7. A scaling factor of 32 was applied in the ice tank tests, leading to an equivalent full-scale structure with a leg center-to-center spacing of 50 m and a leg diameter of 7 m.

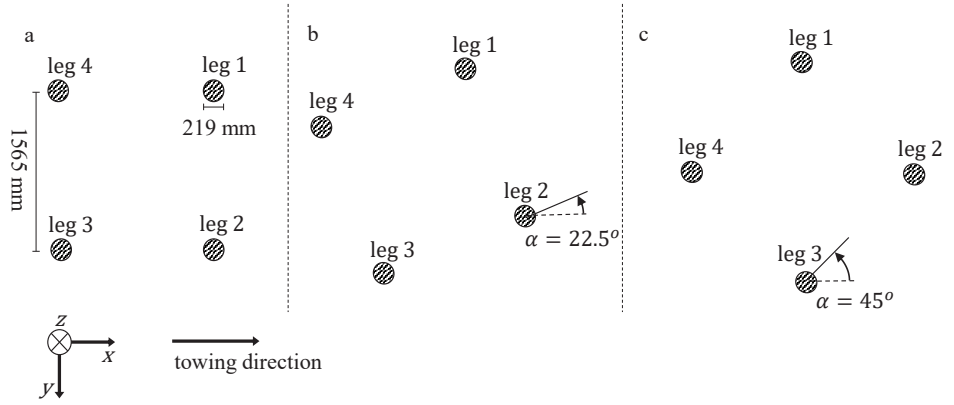

Figure 4.7: Planar view of the waterline geometry of the multi-leg test structure. Not rotated (a), rotated with $\alpha = 22.5^o$ (b) and rotated with $\alpha = 45^o$ (c).

Seven test cases were selected for the analysis in this study. The test cases were selected based on 1) the availability of complete top-view photographs of the broken ice field for accurate numerical reproduction and 2) the reliability of the measured structure loads. In some test cases, there were clear errors in the measured loads, which could not easily be corrected. These cases are not included in this study. The tests in level ice are also not considered. The analysed test cases are listed in Table 4.2. In the analysed tests, the ice thickness (h_i), the ice concentration (c_i) and the structure orientation (α) were varied. Table 4.3 lists the parameters

Table 4.2: Analysed test cases for the multi-leg structure. The case name includes the structure type (ML), the ice thickness, the ice concentration and the structure orientation.

case	h_i [m]	c_i [%]	α [°]
ML_33_80_000	0.033	80	0
ML_33_80_225	0.033	80	22.5
ML_33_60_225	0.033	60	22.5
ML_16_80_225	0.016	80	22.5
ML_16_60_225	0.016	60	22.5
ML_33_60_450	0.033	60	45
ML_16_80_000	0.016	80	0

Table 4.3: Constant simulation parameters, multi-leg structure tests.

structure velocity [m/s]	$v_\mathrm{s;l}$, $v_\mathrm{s;h}$	0.09-0.18 (first half, second half)
friction coefficient ice-ice [-]	μ_ii	0.25
friction coefficient ice-structure [-]	μ_is	0.12
ice form drag coefficient [-]	C_d	0.1, 0.5 (horizontal, vertical)
ice skin friction drag coefficient [-]	C_p	0.005
fracture toughness [$\mathrm{kPa}\sqrt{\mathrm{m}}$]	K_ic	6.0
crushing specific energy [kPa]	CSE	30.0
flexural strength [kPa]	σ_f	60.0
water density [$\mathrm{kg/m^3}$]	ρ_w	1020.0
ice density [$\mathrm{kg/m^3}$]	ρ_i	900.0

used in the numerical reproduction of the ice-tank tests. The structure velocity, flexural strength, water density and ice density are based on measured test values. The fracture toughness is based on measured values for model-scale ice reported in Dempsey et al. (1986) (not specifically for the ice used in the analysed tests). The crushing specific energy is derived from the measured loads in the level ice tests. It is equivalent to the mean crushing pressure and is approximately half of the maximum compressive strength. The ice-ice friction coefficient is determined by tuning the numerical model results to match the ice-tank test results of the ML_33_80_000 test case. The resulting ice-ice friction coefficient of 0.25 is similar to the value used in Metrikin et al. (2013). After tuning this parameter to match the ice-tank test results for this single case, the parameters are kept constant while modelling all other test cases.

The numerical broken ice fields were created from top-view photographs of the fields used in the ice-tank tests. The fields were digitized using an adapted version of the algorithm described in Zhang and Skjetne (2015). Figure 4.8 shows an

example of the stitched top-view photographs of test case ML_33_80_000 and the digital reproduction of the broken ice field. This figure also shows the tank dimensions, the coordinate system and the boundary conditions.

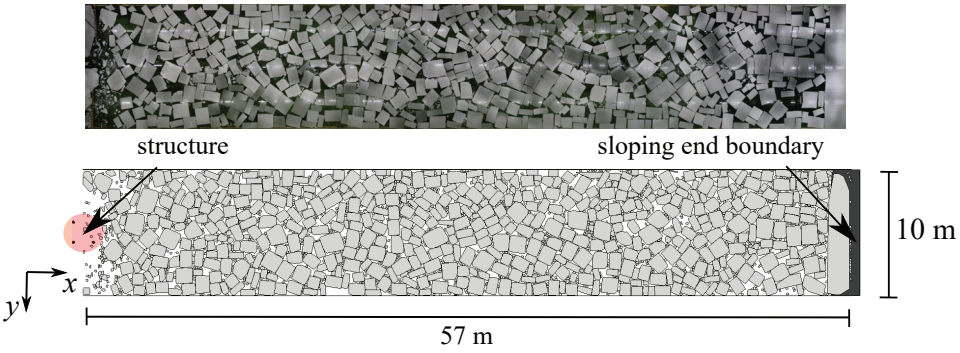

Figure 4.8: Stitched top-view photograph of the broken ice field of case ML_33_80_000 (top) and the digitized version of the broken ice field (bottom).

4.2.1 Comparison of the results from ice-tank tests and numerical simulations

To visualize the results of all the numerical simulations and to compare the results against the results of the 7 selected ice-tank test cases, 5 representative load properties are compared for each test case. The compared parameters are the autocorrelation of the load-time signal in the x-direction (ρ_{ac}), the absolute mean load in the x-direction ($|\overline{F}_x|$), the load standard deviation (σ_F), the maximum of the absolute load in the x-direction ($\max\left(|F_x|\right)$) and the sheltering effect. The sheltering effect is assessed by considering the ratio between the mean load in the x-direction on the most sheltered leg (leg 4) and the least sheltered leg (leg 2):

$$\gamma = \frac{\overline{F}_{\mathrm{l};4}}{\overline{F}_{\mathrm{l};2}} \tag{4.5}$$

in which γ is a parameter describing the sheltering effect. The autocorrelation is the correlation of the load-time signal with a delayed copy of itself. The autocorrelation can be viewed as a measure of the fluctuation of the load-time signal. It is calculated as in Box et al. (2016):

$$\rho_{ac;n} = \frac{\mathrm{E}\left[\left(F_{x;t} - \overline{F}_x\right)\left(F_{x;t+n} - \overline{F}_x\right)\right]}{\sigma_F^2} \tag{4.6}$$

where $\rho_{ac;n}$ is the autocorrelation at time lag n, E is the expected value operator, $F_{x;t}$ is the load in the x-direction at time t, $\overline{F}_x$ is the mean load in the x-direction and σ_F^2 is the variance of the load.

Figure 4.9 shows a comparison of the properties of the simulated and measured loads for the multi-leg ice tank test cases. The properties are separately shown for the low-velocity segment of the ice-tank tests and numerical simulations (the first half of the run) and for the high-velocity segment (the second half of the run).

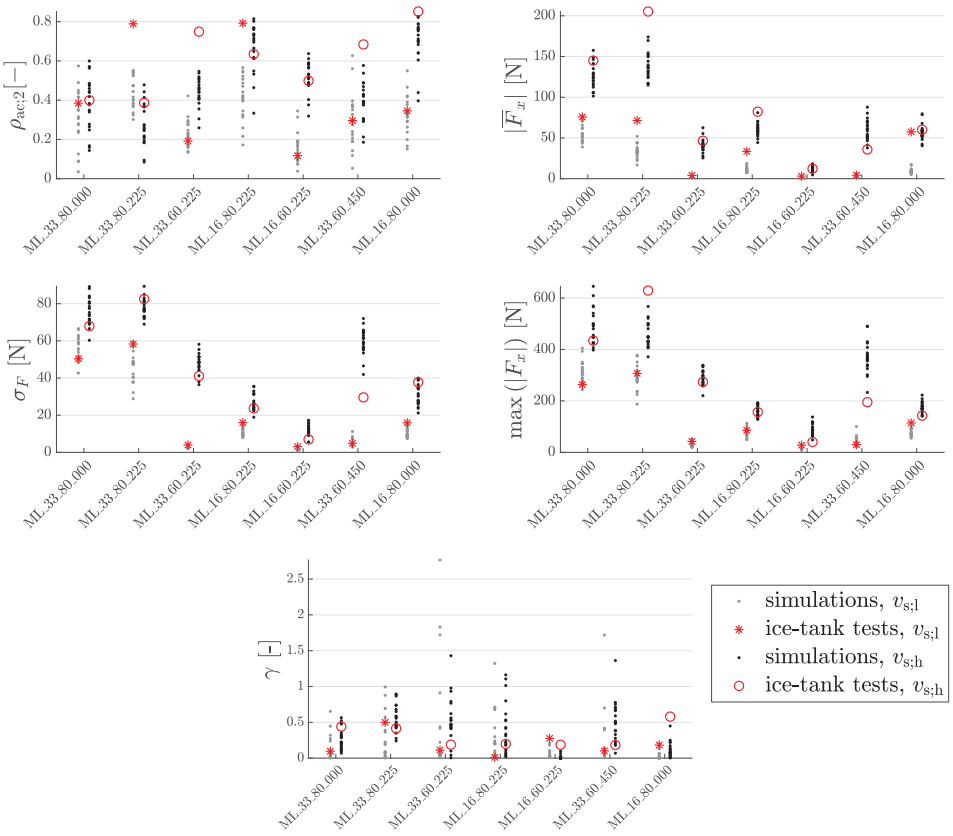

Figure 4.9: Properties of the simulated loads compared to the properties of the measured loads on the multi-leg structure. Values are shown separately for the low-velocity segments of the tests ($v_{s;l}$) and the high-velocity segments of the tests ($v_{s;h}$).

The influence of structure velocity, ice concentration and ice thickness as was observed in the ice-tank tests is captured well in the numerical simulations. For most cases and for most properties, the value resulting from the ice-tank tests falls within the range predicted by the 20 numerical simulations for each case. For each property, there is a minority of cases where the ice-tank test result falls outside of the range predicted by the 20 numerical simulations. Several reasons for the observed discrepancies are discussed in Section 4.2.4.

4.2.2 Variability in the results of the ice-tank tests and in the numerical simulations

All representative properties used for the result comparison are strongly influenced by the initial floe positions. The variation can, in some cases, be attributed to specific interaction events. This section examines one of the interaction events responsible for the result variability in more detail.

Bridging of a force chain between the tank wall and the structure occurs in one of the numerical simulations for case ML_33_60_225. This results in the highest mean load of the 20 numerical simulations performed for this case. Figure 4.10 shows the load-time signals of the simulation with the highest and lowest mean loads for case ML_33_60_225. Only the high-velocity segment of the time series is analysed.

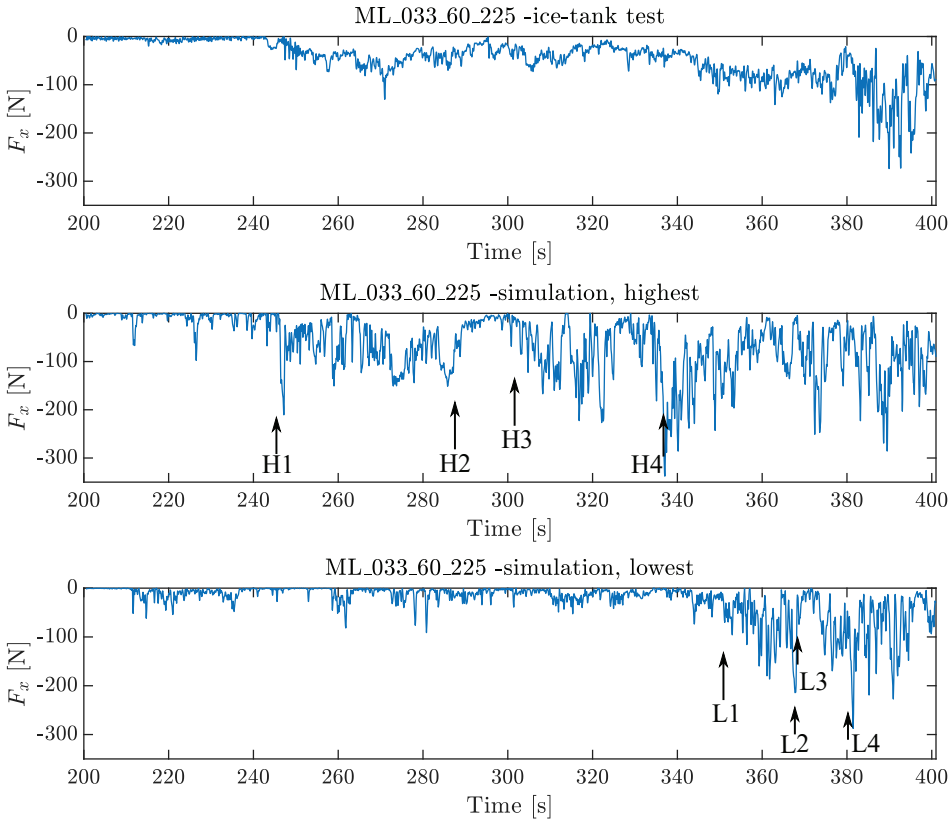

Figure 4.10: Comparison between the load-time signals of the total load in the x-direction of the ice-tank test result, the numerical simulation result with the highest mean load and the numerical simulation result with the lowest mean load.

The floe positions and the stress state within the ice sheet at several instances during the simulation is examined. The analysed intances are indicated by H1-H4 (for the simulation with the highest mean load) and L1-L4 (for the simulation with the lowest mean load). The stress state in the ice sheet is visualized by assigning a load value to each floe. The load value is defined as the maximum eigenvalue of the load tensor defined in Equation 4.1. The floe positions and stress states are visualized in Figure 4.11.

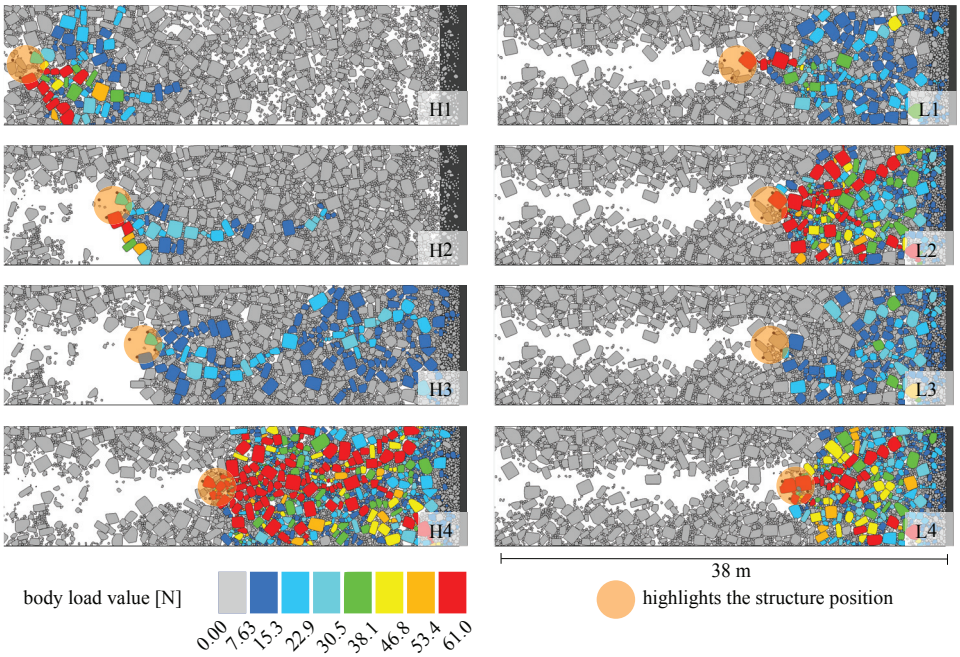

Figure 4.11: Differences in interaction between the simulation with the highest mean load (H1 - H4) and the simulation with the lowest mean load (L1 - L4), visualized by the force networks.

In the simulation with the highest mean load, bridging of a force chain between the structure and the tank wall occurs at H1. The force chain is clearly visible, and the occurrence of the bridging event leads to a peak in the ice load. At H2, the bridging is cleared, leading to a drop in the ice load. Because of the occurrence of bridging, a lead has formed behind the bridging event. Ice floes have accumulated ahead of the structure and ice floe bridge, leading to a higher ice concentration ahead of the structure. Because of the higher concentration, the force networks within the broken ice can extend to the end of the ice tank at H3, leading to a build-up of the ice load. At H4, the remaining ice ahead of the structure is under a

high pressure. In summary, the bridging event that occurs at H1 leads to a higher ice concentration ahead of the structure for the remainder of the test, leading to substantially higher ice loads even after the bridging event has cleared.

In the simulation with the lowest mean ice load, on the other hand, no bridging occurs; therefore, the ice concentration ahead of the structure remains lower for a longer period of time. No significant force networks are formed until L1, much later than in the simulation with the highest load. After L1, the load-time signal is comparable to that of the high-load simulation, and the interaction process is governed by the formation and release of force networks.

A bridging event as the one described above does not occur in the ice-tank test of case ML_33_60_225. This is not surprising, because the ice-tank test only represents one realization of many possible interaction scenarios. However, a similar bridging event is observed in one of the other analysed test cases; case ML_16_80_225. Figure 4.12 shows the bridging event observed in the ice-tank test ML_16_80_225. In the 20 numerical simulations of case ML_16_80_225, a similar bridging event did not occur. This may be the reason why all numerical simulations of case ML_16_80_225 result in a lower mean load than the mean of the measured load.

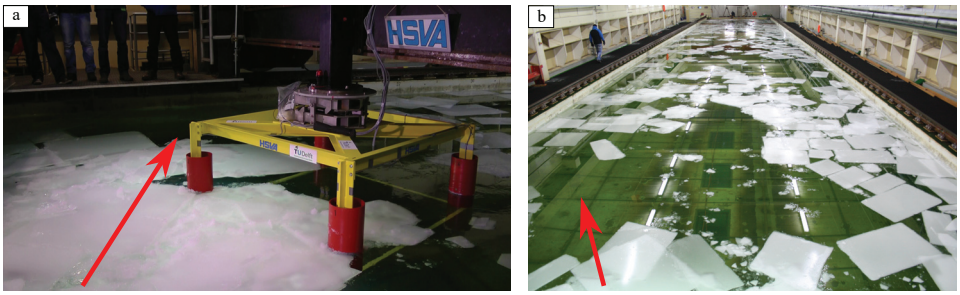

Open lead appears due to bridging of ice between the structure and the tank wall.

Open lead due to bridging of ice between the structure and the tank wall.

Figure 4.12: Bridging event in ice-tank test - case ML_16_80_225

4.2.3 Interpretation of results from ice-tank tests with broken ice

The high variability observed in the numerical reproductions of the ice-tank tests can be related to specific interaction events. The occurrence of these events is also observed in the ice-tank tests. This result indicates that the mechanisms leading to the result variability are not merely a numerical phenomenon. Therefore, it is expected that a variability similar to the variability in the numerical simulation

results would also occur if a single case (i.e., with the same parameters) would be repeated several times in the ice tank. This should be considered in the interpretation of results from ice-tank tests with broken ice.

A possible solution to the issue of result variability, is the processing of ice loads as a function of ice concentration. As discussed, the variability of ice-tank test results can be partly attributed to changes in the concentration of the broken ice field ahead of the structure. The numerical simulation data produced in this study provides several cases that can be used to analyse the influence of concentration, and the change in concentration, on the loads.

The ice concentration ahead of the structure was analysed over several regions for all simulated cases. The results of this analysis show that the concentration from the centre of gravity (COG) of the structure to the end of the ice tank correlated best with the ice load in the x-direction.

Figure 4.13 shows a binned scatter plot of the load as a function of the concentration of the 20 simulations performed for the cases ML_33_80_225 and ML_33_60_225. Only the high-velocity segments of the simulations were analysed. The brightness is a measure of the number of data points in each bin. At each concentration interval, the mean load at that concentration, denoted as $\mu(c_\mathrm{i})$, is calculated and displayed in the figure. The mean load at each concentration interval is calculated as follows:

$$S = c_i^l < c_i < c_i^h \tag{4.7}$$

$$\mu(c_i) = \frac{\sum F_{x|c_i \in S}}{N_s} \tag{4.8}$$

in which S is the concentration interval between c_i^l and c_i^h, where c_i^l and c_i^h are the lower and upper limits of the concentration interval; F_x is a vector containing all loads in the x-direction of the 20 simulation runs performed for each case; and N_s is the number of load data points in the concentration interval.

Figure 4.13 shows a clear jump in load at an ice concentration of 83%. Until a concentration of 83%, the load is almost unaffected by the concentration. When the concentration exceeds 83%, the load increases sharply as a function of concentration. There is some disagreement between the mean loads as a function of concentration resulting from the 80% initial concentration case ML_33_80_225 and the 60% initial concentration case ML_33_60_225. A possible explanation for this disagreement is the higher amount of ice rubble (as a percentage of the total ice cover) in the ML_33_60_225 case.

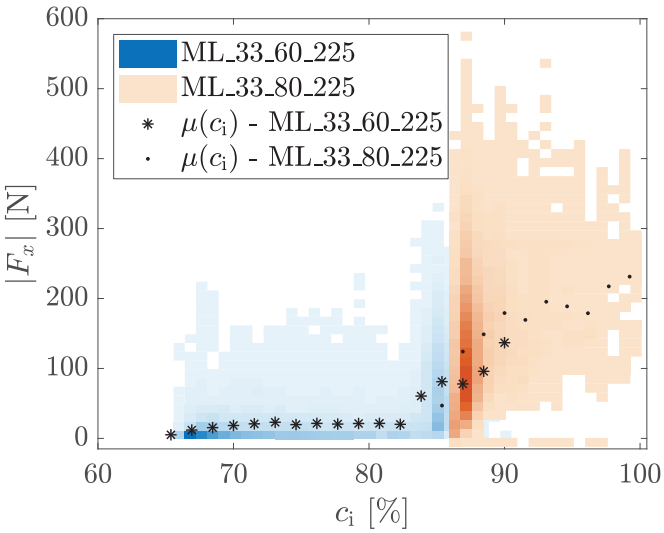

Figure 4.13: Binned scatter plot of the total load in the x-direction versus the ice concentration ahead of the structure, for the cases ML_33_80_225 and ML_33_60_225.

van der Werff et al. (2012) described an earlier study in which the relationship between the ice concentration and the ice load was analysed. van der Werff et al. (2012) found that the concentration correlated well with the ice load in some cases, but not in others. In the current study the ice concentration correlated well with the ice load in all analysed simulation results. A possible reason for this discrepancy is that the concentration was only analysed in the direct vicinity of the structure in van der Werff et al. (2012), whereas in the current study the ice concentration is assessed over a larger region (from the structure COG to the end of the ice tank).

4.2.4 Discussion of the discrepancy between ice-tank test and numerical simulation results

This section discusses possible reasons for the discrepancy, for some cases and parameters, between the numerical simulation results and the ice tank test results, as shown in Figure 4.9.

Of the 5 load parameters used to compare the simulation results to the ice tank test results, most discrepancy between the numerical and ice tank test results can be observed in the autocorrelation. Specifically in the high-velocity segments of the time series, the autocorrelation of the ice tank test signal is often higher than the maximum value resulting from the numerical simulations. A comparison of the video images and the visual simulation results indicates that this may be caused by the discrete nature of the rubble in the numerical simulations. In the cases

where the autocorrelation is significantly higher in the ice-tank tests, there is often a significant amount of crushed ice present, which possibly smooths out the load peaks. In the numerical simulations, on the other hand, ice rubble is approximated by small ice bodies, but crushed ice, which appears more like slush in the physical tests, is not simulated.

For each of the other load parameters, there are one or two ice tank test results that fall outside of the range predicted by the numerical simulations. This can be partly explained by the natural variability in results. The result variability of the 20 performed simulation does not necessarily capture the maxima and minima of that particular property, and thus the ice tank test result may fall outside of the range predicted by the numerical simulations.

In addition, it should be noted that there is a high uncertainty in some of the assumed numerical simulation parameters and model properties. Although both the visual model results and the simulated loads indicate that the model captures the observed interaction phenomena well, there are inherently differences between the assumptions made in the model and reality. The most important model properties that may influence the numerical model results are the rafting behaviour, the constant friction coefficient (no distinction between static, dynamic, wet or dry friction), the lack of roughness on the edges of ice floes and the simplified crushing model (constant crushing pressure). The current knowledge and measured data on these factors is such that a more advanced numerical model is not warranted. There is a high uncertainty in some of the parameters used in the numerical model, such as the drag coefficients, friction coefficients and fracture toughness of ice.

4.2.5 Conclusions and recommendations

In this study, 7 ice-tank test cases were analysed. Each test case was simulated 20 times using a numerical model based on the non-smooth discrete element method. In the 20 simulations performed for each case, the ice floes had different initial positions. Otherwise, the simulations were identical. The goal was to study the variability that may occur in the statistical properties of the ice loads due to uncontrollable conditions, such as the initial floe positions. The results of this study support the following conclusions:

- Uncontrollable properties of tests in broken ice (the initial positions of ice floes) can cause significant differences in the statistical properties of the ice load in numerical simulations.
- The development of floe accumulation ahead of a structure is often strongly influenced by specific interaction events, such as the bridging of a force chain between the structure and the tank wall.

- The events responsible for the variability in load statistics as observed in the numerical simulations also occur in the analysed physical ice-tank tests. This indicates that the variability observed in the numerical simulation results would also occur in physical tests if a single test case would be repeated multiple times.

This study shows, using numerical simulations, to what extent representative load properties such as the autocorrelation, mean, standard deviation and maximum can be affected by changes in the initial floe positions. The variability in the results of ice-tank tests with broken ice should be considered when interpreting the results from ice-tank tests. The effects of differences in the floe accumulation process can be partly accounted for by considering the ice load as a function of the ice concentration ahead of the structure. It is recommended that this measure be used in the post processing of results from ice-tank tests with broken ice. To enable this, ice tanks should be equipped with a camera system that accurately captures the ice field ahead of the structure throughout the test duration.

In addition, this study shows that numerical modelling can be used in combination with ice-tank tests to investigate and account for phenomena such as the result variability caused by a difference in initial floe positions and the change in ice concentration during a test run.

Chapter 5

Discussion

Numerical modelling is a valuable tool that can be used to better understand and predict the phenomena that will occur in ice-structure interaction. The role of numerical models is to:

- *Clarify* the mechanisms and phenomena that lead to a certain outcome, as is done in the study on the floe shape effect in this thesis.
- *Predict* what would happen in an interaction scenario for which no model- or full-scale data are available, as is done in the study on result variability in this thesis.

When applying numerical models for these purposes, three central questions come to mind:

1. How can numerical models of ice-structure interaction be validated?
2. How can the input parameters of a numerical model be determined in a consistent and justifiable way?
3. Can numerical models ever replace, rather than support, ice tank tests and/or full-scale measurements?

The answers to these questions are interlinked and often no definitive answer can be given. In the remainder of this chapter, potential answers to these questions are discussed both from a general perspective and specifically focussing on the model presented in this thesis.

5.1 How can numerical models of ice-structure interaction be validated?

There is currently no agreement within the ice-structure modelling community on how model validation should be performed. There is no standardized approach for model validation, and, given the wide range of possible interaction scenarios, it is

questionable if a standardized approach would even be possible. The judgement of whether a model is sufficiently validated for its intended area of application currently mostly falls on reviewers, editors and the model developers when applied in scientific studies and on certifying authorities, clients and the model developers when applied in industrial practice.

Journal editors and reviewers are often relatively lenient with regard to model validation, and usually operate from the assumption that validation results are reported honestly and completely. Certifying authorities, on the other hand, require a more thorough validation process and documentation.

In other areas where numerical modelling is applied, validation is also an ongoing topic of discussion. Tinoco (2008) describes the model validation process well in the context of CFD modelling:

"CFD validation cannot consist of the comparison of the results of one code to those of one experiment. Rather, it is the agglomeration of comparisons at multiple conditions, code-to-code comparisons, an understanding of the wind tunnel corrections, etc., that leads to the understanding of the CFD uncertainty and validation of its use as an engineering tool. Examples include comparisons of predictive CFD to subsequently acquired test data. The question is not can CFD give a great answer for one or two test cases, but can the CFD "processes" give good answers for a range of cases when run by a competent engineer? This is what validation for an intended purpose is all about."

In summary:

- Rather than a single comparison, validation is the agglomeration of comparisons of multiple test cases.
- Model validation should include tests of the predictive value of the model by comparison of pre-computed model results to subsequently acquired test data.

This validation philosophy can be directly applied to numerical models of ice-structure interaction as well. It is proposed that the validation of ice-structure interaction models be performed in two phases:

1. *Validation of sub-models.* In the validation of sub models, specific model assumptions and simplifications can be tested. The validation tests should be simplified as much as possible, such that a single model assumption can be tested in isolation. In the context of the model developed in this thesis,

an example of a validation test that could be performed for a sub model is a test of the edge friction of model- or full-scale ice floes, or a test of the drag experienced by an ice floe in model- or full-scale.

2. *Global validation.* Successful validation of sub-models does not automatically mean that the global model captures all important phenomena correctly. For instance, it may be that an important phenomenon is simply overlooked in the model development. There is no sub-model for this phenomenon, thus the sub-model cannot be validated. Therefore global validation is a necessary additional validation step.

   The simulations performed for the result variability study (Section 4.2) presented in this thesis can be seen as a global validation of the presented numerical model for the specific application area of the reproduction of ice tank tests with broken ice. In the assessment of result variability, the numerical model was tuned using the results of one test case, after which the predictive value of the model was tested by applying the model with the same parameter set to all other test cases. The model results indicate that the presented numerical method has clarifying and predictive capabilities for the modelled interaction scenarios. For other scenarios, such as the resistance of ships in level ice, the predictive value of the model is still being investigated. An example is the sensitivity study performed by Raza et al. (2019).

   Although the global model validation gives promising results, the validation of sub-models has yet to be performed for the presented method. Therefore it can not be excluded that the error in one sub-model is offset by the error in another sub-model, leading to global model results that seem correct, although the underlying processes are different from reality. It is the author's intention to continue performing validation of sub-models in the near future.

5.2 How can the input parameters of a numerical model be determined in a consistent and justifiable way?

The determination of model input parameters is interlinked with the model validation. As discussed in Chapter 2, model input parameters can be determined by direct measurements, by tuning of the model results, or by copying values used by others.

Direct measurements are considered the most accurate and justifiable way of determining model input parameters. However, this approach is not always an option because is it not always feasible to directly measure all required model input parameters. Determination of model input parameters by direct measurement can be combined with the validation of sub-models.

When determining model parameters by tuning, there is a risk that the parameter values may be incorrectly determined if the underlying model assumptions are incorrect, or if other model parameters or assumptions are not correct. In this case, the tuning of the model parameters may indirectly correct for an error introduced by other assumptions or parameters. The resulting (incorrect) model may not have predictive value for cases other than the case(s) used for tuning. The determination of model input parameters by tuning may be combined with the global model validation.

When basing model parameters on values used in other models, one should consider the source of the values used in the other model. If the values are determined by direct measurements, then this approach is equivalent to using values from direct measurements. If the parameter values are determined by tuning, the assumptions made in the other model may have an influence on the parameter values that best capture the underlying physics. For instance, a discrete ice-structure interaction model that assumes circular floe shapes may find that a higher friction coefficient is needed to capture phenomena observed in physical tests than a model that uses more realistic floe shapes. If the friction coefficient from the model with circular floe shapes is used in the model with realistic floe shapes, then this may lead to incorrect interaction phenomena.

Ultimately, model development, parameter determination and validation is an interlinked and iterative, rather than a linear process. Figure 5.1 shows the model development and validation process as envisioned here. As discussed, validation can be split up in validation of sub-models and validation of the global model. The global model should be validated and adapted based on comparisons against multiple data sets. After each model adaptation, the model performance in previous validation cases should be re-evaluated.

It should be noted that there is often substantial uncertainty in measured data as well. This uncertainty should be taken into account when comparing numerical modelling results to full-scale or ice-tank test data. In addition, it is important to consider that model-scale tests (i.e., ice tank tests) are also 'models', and that the mechanisms and results from model-scale tests are not necessarily representative of full-scale interaction.

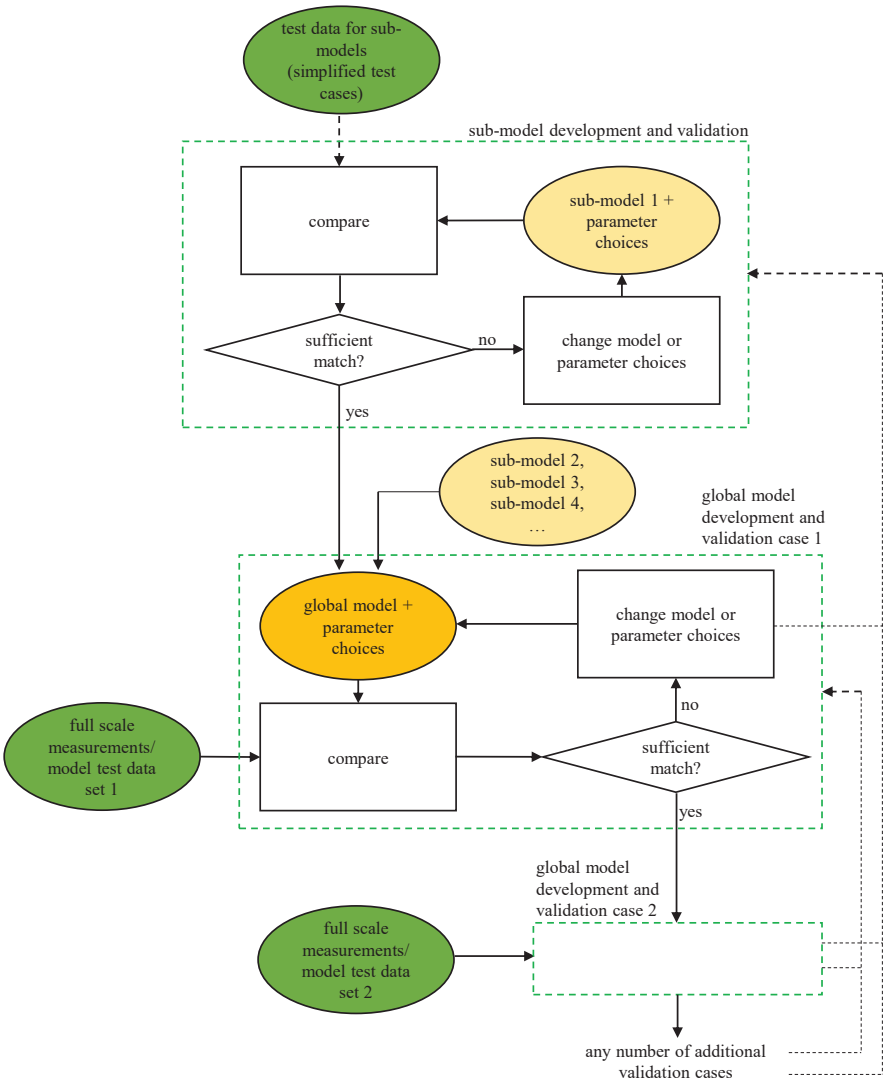

Figure 5.1: The process of model development, parameter determination and validation.

5.3 Can numerical models ever replace, rather than support, ice tank tests and/or full-scale measurements?

The capabilities of numerical ice-structure interaction models are continuously increasing. At the same time, both ice-tank testing and full-scale measurements have various shortcomings, as listed in the introduction of this thesis. This raises the question if there will ever be a time when numerical modelling will completely replace ice-tank tests and/or full-scale measurements.

The many physical processes that play a role in ice-structure interaction (multi-body interaction, dynamic fracture and failure, fluid dynamics, material modelling) make that even current state-of-the-art ice-structure interaction models must greatly simplify many of the interaction-processes. Scale-model tests and full-scale measurements are still needed to determine if the simplifications that are made are sufficiently valid. Even in fields where the numerical modelling capabilities are arguably more advanced, and where the underlying assumptions are better validated, numerical modelling has not yet replaced model-scale testing and measurements. An example is CFD models and wind tunnel testing Kraft (2010). Therefore it is expected that numerical simulations will not replace scale-model testing any time soon. Full-scale measurements will always be needed to validate the assumptions made in models. Thus, it is expected that full-scale tests will never be replaced by numerical modelling.

In the near future, the only cases in which numerical modelling may replace model-scale testing are the cases for which very similar model-scale tests have already been performed. If the data from previous similar tests is available, and it has been shown that a numerical model is capable of accurately capturing the test results, then there is no practical reason to perform another model-scale test campaign. However, this stage of model accuracy and validation has probably not been reached yet.

A final consideration is that certifying and regulating authorities, as well as industrial clients, should approve the use of numerical modelling instead of model-scale tests.

5.4 Summary

Numerical models of ice-structure interaction can clarify observed phenomena, and can be used to predict what would happen in interaction cases for which no physical measurements are available. The implicit DEM model developed in this thesis has been used to *clarify* phenomena leading to floe shape effects, and to *predict* what would happen to the results of ice tank tests if the initial positions of ice floes would be different. The model is partly validated against the results of ice tank tests. However, validation of sub-models has yet to be performed. The validation and development of numerical models is an interlinked and iterative process, which is still ongoing for the model presented in this thesis.

Chapter 6

Conclusions and recommendations

In this thesis, a novel implicit discrete element method is developed. The method follows similar procedures as other non-smooth discrete element methods. However, the contact parameters are derived such that the method can capture both non-smooth as well as smooth contacts. The method is capable of modelling the interaction between discrete polyhedral bodies in 3-D. In the calculation of contact forces between bodies, contact compliance is taken into account. The contact compliance parameters are derived based on the assumption that local contact crushing will occur. The compliance parameters are derived using the exact contact geometry and the material properties of the interacting bodies. Specifically, the crushing specific energy of ice is used to derive the contact compliance properties. The combination of model properties; implicit time integration, and a compliant contact model which uses the exact contact geometry and material properties in calculating the contact forces, is novel and offers expanded capabilities and improved accuracy compared to other DEM models applied in ice-structure interaction. A notable capability of the method is the ability to model ice floes as lattices. This is not possible in other NDEM methods used in ice-structure interaction. The developed method was applied to investigate specific aspects of the interaction between structures and broken ice fields.

First, the method was used to investigate the effect of floe shape on the load experienced by vertical-sided structures interacting with broken ice. A sensitivity study was performed that assessed the influence of structure shape, confinement conditions, friction coefficients, and ice areal coverage on the floe shape effect.

Second, the model was used to study the variability in the results of ice tank tests with broken ice. 7 ice tank test runs were analysed. Each test run was simulated 20 times with the numerical model. In each simulation, the initial floe positions were slightly different, while all other model parameters were constant. The numerical modelling results were studied and compared to the ice tank test results in order to identify sources of result variability. These studies lead to the following conclusions:

- There is a clear and strong effect of floe shape in the interaction between broken ice and vertical-sided structures. This floe-shape effect should be taken into account in the numerical modelling of interaction between broken ice and structures, and in the design and interpretation of ice tank tests with broken ice. In clearance-dominated interaction regimes, the mechanism responsible for the floe shape effect is the increased ability of floes with parallel opposite edges to form force networks. This results in a larger ice area that is loaded and displaced by the structure.

- There is a high variability in the results of ice tank tests in broken ice. The mean load, load standard deviation and the maximum load in the surge direction are all strongly influenced by uncontrollable test properties such as the initial positions of ice floes. The result variability should be considered when interpreting results from ice tank tests in broken ice. It is shown that the mechanisms that lead to the results variability occur both in the numerical simulations as well as in the physical ice tank tests. This indicates that the result variability is not merely a numerical phenomenon. As an example, the formation of a force chain between the structure and the tank wall is highlighted. This event occurred both in the numerical simulations as well as in the ice tank tests. In both cases, the formation of the force chain led to an increase in ice concentration ahead of the structure for the remainder of the test. This, in turn, led to an increased surge load on the structure.

  It is shown that there is a correlation between the ice concentration ahead of the structure and the ice load in surge direction. The ice concentration ahead of the structure can be used to correct for the effects of floe accumulation. Currently, ice tank tests often only film the ice field in the direct vicinity of the structure. The analysis results show that the broken ice over a larger aerial domain influences the structure load. Therefore it is recommended that ice tanks be equipped with a camera system that captures the ice field in the complete tank during a test. This would allow post-processing of the test data while taking into account the changes in ice concentration.

- The studies on floe shape effects and result variability show that valuable insights in ice-structure interaction processes can be obtained by combining ice tank tests with numerical modelling. Numerical reproductions of tests can be used to assess the influence of modelling choices such as the used floe sizes and shapes, and to study the variability in the test results due to uncontrollable test conditions. In addition, numerical modelling can be used to assess the influence of scaling effects.

However, there are also challenges in the numerical reproduction of ice tank tests with numerical models. The correct determination of model parameters and the implementation in the model of all phenomena that occur in the tests are the two main challenges.

For the conditions studied in this thesis, the friction and drag coefficients are the model parameters that have a high uncertainty and a large influence on the simulation results. Ice floe rafting is the interaction phenomenon that is least understood in the scenarios studied in this thesis, while the rafting behaviour has a large influence on the model results. These uncertainties can be partly alleviated by a series of simple tests, which can help in further identifying the parameters and phenomena needed for the numerical model:

- The floe rafting behaviour in model-scale can be tested by compressing a series of free floating ice floes.
- Ice floe edge, top and bottom friction coefficients can be measured in a similar fashion.
- Ice floe drag can be tested by dragging a single ice floe through the tank with a constant velocity.

In the review process of the publications that are part of this thesis, a criticism was that the results of the floe shape and test variability studies were self-evident. Although the shape effects and results variability may seem self-evident to the experienced ice expert, the consequences of these effects are currently not properly accounted for in the preparation of ice tank tests and the interpretation of test results. This demonstrates the relevance of the studies performed in this thesis.

Further development of the model presented in this thesis will focus on the validation of sub-model components, the further implementation and validation of a lattice model for ice failure, and the implementation of a more realistic hydrodynamics model based on potential theory.

Chapter 7

Bibliography

Alawneh, S., Dragt, R., Peters, D., Daley, C. and Bruneau, S. (2015), 'Hyper-Real-Time Ice Simulation and Modeling Using GPGPU', *IEEE Transactions on Computers* **64**(12), 3475–3487.

Anitescu, M. and Potra, F. (1997), 'Formulating dynamic multi-rigid-body contact problems with friction as solvable linear complementarity problems', *Nonlinear Dynamics* **14**(93), 231–247.

Baraff, D. (1989), 'Analythical Methods for Dynamic Simulation of Non-penetrating Rigid Bodies', *Computer Graphics* **23**(3), 223–232.

Baraff, D. (1993), 'Issues in Computing Contact Forces for Non-Penetrating Rigid Bodies', *Algorithmica* **10**, 292–352.

Bolander, J. E. and Saito, S. (1998), 'Fracture analyses using spring networks with random geometry', *Engineering Fracture Mechanics* **61**, 569–591.

Box, G. E. P., Jenkins, G. M., Reinsel, G. C. and Ljung, G. M. (2016), *Time Series Analysis: Forecasting and Control*, fifth edit edn, John Wiley & Sons. Inc.

Bullet Physics (2017).
URL: *http://bulletphysics.org*

Cundall, P. a. and Strack, O. D. L. (1979), 'A discrete numerical model for granular assemblies', *Géotechnique* **29**(1), 47–65.

Daley, C. (1999), Energy Based Ice Collision Forces, *in* 'Proceedings of the 15th International Conference on Port and Ocean Engineering under Arctic Conditions', Helsinki, Finland.

Daley, C., Alawneh, S., Peters, D. and Colbourne, B. (2014), GPU-Event-Mechanics Evaluation of Ice Impact Load Statistics, *in* 'Arctic Technology Conference', Houston, Texas.

Daley, C., Alawneh, S., Peters, D., Quinton, B. and Colbourne, B. (2012), GPU modeling of ship operations in pack ice, *in* 'International Conference and Exhibition on Performance of Ships and Structures in Ice', Banff Alberta, Canada, pp. 20–23.

Dempsey, J., Bentley, D. and Sodhi, D. (1986), Fracture toughness of model ice, *in* 'Proceedings 8th IAHR Symposium on Ice', Iowa City, Iowa, pp. 365–376.

Dempsey, J. P., DeFranco, S. J., Blanchet, D. and Prodanovic, A. (1994), 'Mechanisms of fracture of sea ice', *Hydrotechnical Construction* **28**(3), 164–168.

Dorival, O., Metrikine, A. V. and Simone, A. (2008), A Lattice Model to Simulate Ice-Structure Interaction, *in* 'Proceedings of the ASME International Conference on Offshore Mechanics and Arctic Engineering', Estoril, Portugal.

Erleben, K. (2005), Stable , Robust , and Versatile Multibody Dynamics Animation, PhD thesis, University of Copenhagen.

Gilbert, E. G., Johnson, D. W. and Keerthi, S. S. (1988), 'A Fast Procedure for Computing the Distance Between Complex Objects in Three-Dimensional Space', *IEEE Journal of Robotics and Automation* **4**(2), 193–203.

Gong, H., Tuhkuri, J. and Box, P. O. (2019), The effect of ship bow shape on ridge resistance in a narrow ridge, *in* 'Proceedings of the 25th International Conference on Port and Ocean Engineering under Arctic Conditions', Delft, The Netherlands.

Haase, A. and Jochmann, P. (2013), DYPIC - Dynamic Positioning in Ice - Second Phase of Model Testing, *in* 'Proceedings of the ASME 2013 32nd International Conference on Ocean, Offshore and Arctic Engineering', Nantes, France.

Haase, A., Polojärvi, A. and Tuhkuri, J. (2010), 3D Discrete Numerical Modelling of Conical Structure-Ice Rubble Interaction, *in* '20 th IAHR International Symposium on Ice', Lahti, Finland.

Haase, A., van der Werff, S. and Jochmann, P. (2012), DYPIC - Dynamic Positioning in Ice - First Phase of Model Testing, *in* 'Proceedings of the ASME 2012 31st International Conference on Ocean, Offshore and Arctic Engineering', Rio de Janeiro.

Hocking, G. (1992), 'The discrete element method for analysis of fragmentation of discontinua', *Engineering Computations* **9**, 145–155.

Hocking, G., Mustoe, G. and Williams, J. (1985), Validation of the CICE code for ice ride-up and ice ridge cone interaction, *in* 'Proc. of the Conf. Arctic'85' Civil Engineering in the Arctic Offshore', San Francisco, California, USA, pp. 962–970.

Hopkins, M. A. (1992), 'Numerical Simulation of Systems of Multitudinous Polygonal Blocks', *Technical Report 92-22 Cold Regions Research and Engineering Laboratory, CRREL* p. 69.

Hopkins, M. A. and Hibler III, W. D. (1991*a*), 'Numerical simulations of a compact convergent system of ice floes', *Annals of glaciology* **15**, 26–30.

Hopkins, M. A. and Hibler III, W. D. (1991*b*), 'On the shear strength of geophysical scale ice rubble', *Cold Regions Science and Technology* **19**(2), 201–212.

Hopkins, M. A., Hibler, W. D. and Flato, G. M. (1991), 'On the Numerical Simulation of the Sea Ice Ridging Process', *Journal of Geophysical Research* **96**(C), 4809–4820.

Hopkins, M. a. and Tuhkuri, J. (1999), 'Compression of floating ice fields', *Journal of Geophysical Research* **104**(C7), 15815–15825.

Hopkins, M. and Hibler III, W. D. (1991*c*), 'On the ridging of a thin sheet of lead ice', *Annals of glaciology* **15**, 81–86.

Hoving, J. S., Vermeulen, R., Mesu, A. W. and Cammaert, G. (2013), Experiment-Based Relations between Level Ice Loads and Managed Ice Loads on an Arctic Jack-Up Structure, *in* 'Proceedings of the 22nd International Conference on Port and Ocean Engineering under Arctic Conditions', Espoo, Finland.

Islam, S., Watson, D., Brown, J. and Sayed, M. (2019), Modeling of a Full Scale DP in Ice Scenario using an Advanced Ice Dynamics Model, *in* 'Proceedings of the 25th International Conference on Port and Ocean Engineering under Arctic Conditions', Delft, The Netherlands.

ISO 19906 (2018), 'Petroleum and natural gas industries: Arctic offshore structures', *International Organization for Standardization, Geneva, Switzerland* .

Janßen, C. F., Mierke, D. and Rung, T. (2017), 'On the development of an efficient numerical ice tank for the simulation of fluid-ship-rigid-ice interactions on graphics processing units', *Computers and Fluids* **155**, 22–32.

Jean, M. (1999), 'The non-smooth contact dynamics method', *Computer Methods in Applied Mechanics and Engineering* **177**(3-4), 235–257.

Ji, S., Di, S. and Liu, S. (2015), 'Analysis of ice load on conical structure with discrete element method', *Engineering Computations* **32**(4), 1121–1134.

Jirasek, M. and Bazant, Z. P. (1995), 'Particle Model for Quasibrittle Fracture and Application to Sea Ice', *Journal of Engineering Mechanics* **121**(9).

Karulin, E. B. and Karulina, M. M. (2017), Environmental Effects on Dynamic Behavior of Moored Turret Ship Based on Numerical Simulations, *in* 'Proceedings of the 24th International Conference on Port and Ocean Engineering under Arctic Conditions', Busan, Korea.

Kawai, T. (1978), 'New Discrete Models and their Application to Seismic Response Analysis of Structures', *Nuclear Engineering and Design* **48**(1978), 207–229.

Keijdener, C. and Metrikine, A. V. (2014), The effect of ice velocity on the breaking length of level ice failing in downward bending, *in* 'Proceedings of the 22nd IAHR International Symposium on Ice', Singapore, pp. 396–403.

Kerr, A. D. and Kwak, S. S. (1993), 'The semi-infinite plate on a Winkler base, free along the edge, and subjected to a vertical force', *Archive of Applied Mechanics* **63**(3), 210–218.

Kim, E. and Gagnon, R. E. (2016), A Preliminary Analysis of the Crushing Specific Energy of Iceberg Ice under Rapid Compressive Loading, *in* 'Proceedings of the 23rd IAHR International Symposium on Ice', Ann Arbor, Michigan, USA.

Kim, E. and Høyland, K. V. (2014), Experimental Investigations of the Energy Absorption Capacity of Ice During Crushing: Is the Specific Energy Scale Independent?, *in* 'Proceedings of the 22nd IAHR International Symposium on Ice', Singapore, pp. 163–170.

Kinnunen, A., Tikanmäki, M. and Heinonen, J. (2016), An energy model for ice crushing in ice-structure impact, *in* 'Proceedings of the 23rd IAHR International Symposium on Ice', Ann Arbor, Michigan, USA.

Kjerstad, Ø. K., Metrikin, I., Løset, S. and Skjetne, R. (2015), 'Experimental and phenomenological investigation of dynamic positioning in managed ice', *Cold Regions Science and Technology* **111**, 67–79.

Konno, A. and Mizuki, T. (2006), Numerical Simulation of Pre-sawn Ice Test of Model Icebreaker Using Physically Based Modeling, *in* '18th IAHR International Symposium on Ice', Sapporo, Japan.

Konno, A., Saitoh, O. and Watanabe, Y. (2011), Numerical Investigation of Effect of Channel Condition Against Ship Resistance in Brash Ice Channels, *in* 'Proceedings of the 21st International Conference on Port and Ocean Engineering under Arctic Conditions', Montreal, Canada.

Koperski, J. (2019), 'Internet Encyclopedia of Philosophy'.
URL: *https://www.iep.utm.edu/models/*

Krabbenhoft, K., Huang, J., Da Silva, M. V. and Lyamin, A. V. (2012), 'Granular contact dynamics with particle elasticity', *Granular Matter* **14**(5), 607–619.

Kraft, E. M. (2010), 'After 40 Years Why Hasn't the Computer Replaced the Wind Tunnel?', *International Test and Evaluation Journal* **31**, 329–346.

Lacoursiere, C. (2003), Splitting Methods for Dry Frictional Contact Problems in Rigid Multibody Systems : Preliminary Performance Results, *in* 'Conference Proceedings from SIGRAD2003', pp. 11–16.

Lacoursière, C. (2007), Regularized, stabilized, variational methods for multibodies, *in* 'Proceedings of the 48th Scandinavian Conference on Simulation and Modelling', pp. 40–48.

Lilja, V.-P., Polojärvi, A., Tuhkuri, J. and Paavilainen, J. (2017), A Three-Dimensional FEM-DEM Model of an Ice Sheet, *in* 'Proceedings of the 24th International Conference on Port and Ocean Engineering under Arctic Conditions', Busan, Korea.

Liu, L. and Ji, S. (2018), 'Ice load on floating structure simulated with dilated polyhedral discrete element method in broken ice field', *Applied Ocean Research* **75**, 53–65.

Liu, R. W., Xue, Y. Z., Lu, X. K. and Cheng, W. X. (2018), 'Simulation of ship navigation in ice rubble based on peridynamics', *Ocean Engineering* **148**, 286–298.

Løset, S. (1994*a*), 'Discrete element modelling of a broken ice field - Part I : model development', *Cold Regions Science and Technology* **22**(4), 339–347.

Løset, S. (1994*b*), 'Discrete element modelling of a broken ice field — Part II: simulation of ice loads on a boom', *Cold Regions Science and Technology* **22**(4), 349–360.

Lötstedt, P. (1982), 'Mechanical Systems of Rigid Bodies Subject to Unilateral Constraints', *SIAM Journal on Applied Mathematics, Society for Industrial and Applied Mathematics* **42**(2), 281–296.

Lu, W. and Amdahl, J. (2019), Glacial Ice and Offshore Structure Impacts under Wave and Current Excitation, *in* 'Proceedings of the 25th International Conference on Port and Ocean Engineering under Arctic Conditions', Delft, The Netherlands.

Lu, W., Lubbad, R., Høyland, K. and Løset, S. (2014), 'Physical model and theoretical model study of level ice and wide sloping structure interactions', *Cold Regions Science and Technology* **101**, 40–72.

Lu, W., Lubbad, R. and Løset, S. (2014), 'Simulating Ice-Sloping Structure Interactions With the Cohesive Element Method', *Journal of Offshore Mechanics and Arctic Engineering* **136**(3), 31501.

Lu, W., Lubbad, R. and Løset, S. (2015*a*), 'In-plane fracture of an ice floe: A theoretical study on the splitting failure mode', *Cold Regions Science and Technology* **110**, 77–101.

Lu, W., Lubbad, R. and Løset, S. (2015*b*), 'Out-of-plane failure of an ice floe: Radial-crack-initiation-controlled fracture', *Cold Regions Science and Technology* **119**, 183–203.

Lu, W., Lubbad, R. and Løset, S. (2018), 'Parallel channels' fracturing mechanism during ice management operations. Part II: Experiment', *Cold Regions Science and Technology* **156**, 117–133.

Lu, W., Lubbad, R., Løset, S. and Kashafutdinov, M. (2016), 'Fracture of an ice floe: Local out-of-plane flexural failures versus global in-plane splitting failure', *Cold Regions Science and Technology* **123**, 1–13.

Lu, W., Lubbad, R., Shestov, A. and Løset, S. (2018), 'Parallel channels' fracturing mechanism during ice management operations. Part I: Theory', *Cold Regions Science and Technology* .

Lubbad, R. and Løset, S. (2011), 'A numerical model for real-time simulation of ship-ice interaction', *Cold Regions Science and Technology* **65**(2), 111–127.

Lubbad, R., Løset, S., Lu, W., Tsarau, A. and van den Berg, M. (2018*a*), 'An overview of the Oden Arctic Technology Research Cruise 2015 (OATRC2015) and numerical simulations performed with SAMS driven by data collected during the cruise', *Cold Regions Science and Technology* **156**, 1–22.

Lubbad, R., Løset, S., Lu, W., Tsarau, A. and van den Berg, M. (2018*b*), Simulator for Arctic Marine Structures (SAMS), *in* 'Proceedings of the ASME 2018 37th International Conference on Ocean, Offshore and Arctic Engineering', American Society of Mechanical Engineers.

Matlock, H., Dawkins, W. P. and Panak, J. J. (1969), A Model for the Prediction of Ice-Structure Interaction, *in* 'Offshore Technology Conference', Dallas, Texas.

Metrikin, I. (2014), 'A software framework for simulating stationkeeping of a vessel in discontinuous ice', *Modeling, Identification and Control* **35**(4), 211–248.

Metrikin, I., Gürtner, A., Bonnemaire, B., Tan, X., Fredriksen, A. and Sapelnikov, D. (2015), SIBIS : A Numerical Environment for Simulating Offshore Operations in Discontinuous Ice, *in* 'Proceedings of the 23rd International Conference on Port and Ocean Engineering under Arctic Conditions', Trondheim, Norway.

Metrikin, I., Kerkeni, S., Jochmann, P. and Løset, S. (2013), Experimental and Numerical Investigation of Dynamic Positioning in Level Ice, *in* 'ASME 2013 32nd International Conference on Ocean, Offshore and Arctic Engineering', American Society of Mechanical Engineers, Nantes, France.

Metrikin, I. and Loset, S. (2013), Nonsmooth 3D Discrete Element Simulation of a drillship in discontinuous ice, *in* 'Proceedings of the 22nd International Conference on Port and Ocean Engineering under Arctic Conditions, POAC'13', Espoo, Finland.

Mirtich, B. V. (1996), Impulse-based Dynamic Simulation of Rigid Body Systems, PhD thesis, University of California at Berkeley.

Moreau, J. J. (1988), Unilateral Contact and Dry Friction in Finite Freedom Dynamics, *in* 'Moreau J.J.; Panagiotopoulos P.D. Nonsmooth Mechanics and Applications', Springer, International Centre for Mechanical Sciences (Courses and Lectures), chapter 302, pp. 1–82.

Moreau, J. J. (1999), 'Numerical aspects of the sweeping process', *Computer Methods in Applied Mechanics and Engineering* **177**(3-4), 329–349.

Morgan, D. (2016), An Improved Three-Dimensional Discrete Element Model for Ice-Structure Interaction, *in* '23 rd IAHR International Symposium on Ice', Ann Arbor, Michigan, USA.

Newmark, N. M. (1959), 'A Method of Computation for Structural Dynamics', *Journal of the Engineering Mechanics Division* **85**(3), 67–94.

Nicolas, S., Sofien, K., Charles, P., Matthias, R., Dmitry, S. and Åse, E. (2019), Numerical simulation of broken ice interaction with offshore structures : validation exercises, *in* 'Proceedings of the 25th International Conference on Port and Ocean Engineering under Arctic Conditions', Delft, The Netherlands.

Ostoja-Starzewski, M. (2002), 'Lattice models in micromechanics', *Applied Mechanics Reviews* **55**(1), 35.

Paavilainen, J. and Tuhkuri, J. (2013), 'Pressure distributions and force chains during simulated ice rubbling against sloped structures', *Cold Regions Science and Technology* **85**, 157–174.

Paavilainen, J., Tuhkuri, J. and Polojärvi, A. (2009), '2D combined finite-discrete element method to model multi-fracture of beam structures', *Engineering Computations* **26**(6), 578–598.

Paavilainen, J., Tuhkuri, J. and Polojärvi, A. (2011), '2D numerical simulations of ice rubble formation process against an inclined structure', *Cold Regions Science and Technology* **68**(1-2), 20–34.

Parmerter, R. R. (1975), 'A Model of Simple Rafting in Sea Ice', *Journal of Geophysical Research* **80**(5), 1948 – 1952.

Polojärvi, A. and Tuhkuri, J. (2009), '3D discrete numerical modelling of ridge keel punch through tests', *Cold Regions Science and Technology* **56**(1), 18–29.

Polojärvi, A., Tuhkuri, J. and Pustogvar, A. (2015), 'DEM simulations of direct shear box experiments of ice rubble : Force chains and peak loads', *Cold Regions Science and Technology* **116**, 12–23.

Rabatel, M., Labbé, S. and Weiss, J. (2015), 'Dynamics of an assembly of rigid ice floes', *Journal of Geophysical Research: Oceans* **120**, 5887–5909.

Ranta, J., Polojärvi, A. and Tuhkuri, J. (2017), 'The statistical analysis of peak ice loads in a simulated ice-structure interaction process', *Cold Regions Science and Technology* **133**, 46–55.

Ranta, J., Polojärvi, A. and Tuhkuri, J. (2018*a*), 'Ice Loads on Inclined Marine Structures - Virtual Experiments on Ice Failure Process Evolution', *Marine Structures* **57**, 72–86.

Ranta, J., Polojärvi, A. and Tuhkuri, J. (2018*b*), 'Limit mechanisms for ice loads on inclined structures : Buckling', *Cold Regions Science and Technology* **147**, 34–44.

Ranta, J., Polojärvi, A. and Tuhkuri, J. (2018*c*), 'Scatter and error estimates in ice loads – Results from virtual experiments', *Cold Regions Science and Technology* **148**, 1–12.

Raza, N., van den Berg, M., Lu, W. and Lubbad, R. (2019), Analysis of Oden Icebreaker Performance in Level Ice using Simulator for Arctic Marine Structures (SAMS), *in* 'Proceedings of the 25th International Conference on Port and Ocean Engineering under Arctic Conditions', Delft, The Netherlands.

Rheem, C. K., Yamaguchi, H. and Kato, H. (1997), 'Distributed mass/discrete floe model for pack ice rheology computation', *Journal of Marine Science and Technology* **2**(2), 101–121.

Sayed, M. and Barker, A. (2011), Numerical Simulations of Ice Interaction with a Moored Structure, *in* 'OTC Arctic Technology Conference', Houston, Texas.

Sayed, M. and Kubat, I. (2011), 'Forces on ships transiting pressured ice covers', *Proceedings of the International Offshore and Polar Engineering Conference* **8**, 1087–1092.

Sayed, M. and Timco, G. (1999), A lattice model of ice failure, *in* 'Proceedings of the Ninth International Offshore and Polar Engineering Conference', Vol. II, Brest, France, pp. 528 – 534.

Servin, M., Wang, D., Lacoursière, C. and Bodin, K. (2014), 'Examining the smooth and nonsmooth discrete element approaches to granular matter', *International Journal for Numerical Methods in Engineering* **97**, 878–902.

Stewart, D. E. and Trikle, J. C. (1996), 'An Implicit Time Stepping Scheme for Rigid Body Dynamics with Inelastic Collisions and Coulomb Friction', *International Journal for Numerical Methods in Engineering* **39**, 2673–2691.

Su, B., Aarsæther, K. G. and Kristiansen, D. (2019), 'Numerical Study of a Moored Structure in Moving Broken Ice Driven by Current and Wave', *Journal of Offshore Mechanics and Arctic Engineering* **141**.

Tasora, A., Anitescu, M., Negrini, S. and Negrut, D. (2013), 'A compliant viscoplastic particle contact model based on differential variational inequalities', *International Journal of Non-Linear Mechanics* **53**, 2–12.

Timco, G. W. and Weeks, W. F. (2010), 'A review of the engineering properties of sea ice', *Cold Regions Science and Technology* **60**(2), 107–129.

Tinoco, E. N. (2008), Validation and Minimizing CFD Uncertainty for Commercial Aircraft Applications, *in* '26th AIAA Applied Aerodynamics Conference', Honolulu, Hawaii, USA.

Toyota, T., Haas, C. and Tamura, T. (2011), 'Size distribution and shape properties of relatively small sea-ice floes in the Antarctic marginal ice zone in late winter', *Deep-Sea Research Part II: Topical Studies in Oceanography* **58**(9-10), 1182–1193.

Tsarau, A. (2015), Numerical Modelling of the Hydrodynamic Effects of Marine Operations in Broken Ice, Doctoral thesis, Norwegian University of Science and Technology.

Tsarau, A., Lubbad, R. and Løset, S. (2017), 'A numerical model for simulating the effect of propeller flow in ice management', *Cold Regions Science and Technology* **142**, 139–152.

Tsarau, A., van den Berg, M., Lu, W., Lubbad, R. and Løset, S. (2018), Modelling Results With a New Simulator for Arctic Marine Structures-SAMS, *in* 'ASME 2018 37th International Conference on Ocean, Offshore and Arctic Engineering', ASME.

Tuhkuri, J. (2002), 'Laboratory tests on ridging and rafting of ice sheets', *Journal of Geophysical Research* **107**(C9), 1–14.

Tuhkuri, J. and Lensu, M. (1997), Ice Tank Tests on Rafting of a Broken Ice Field, Technical report, Helsinki University of Technology Ship Laboratory - Arctic Offshore Research Centre.

Tuhkuri, J. and Polojärvi, A. (2005), Effect of Particle Shape in 2D Ridge Keel Deformation Simulations, *in* 'Proceedings of the 18th International Conference on Port and Ocean Engineering Under Arctic Conditions', Vol. 2, pp. 939–948.

van den Berg, M. (2016), A 3-D Random Lattice Model of Sea Ice, *in* 'Arctic Technology Conference. St. Johns, Newfoundland and Labrador'.

van den Berg, M., Lubbad, R. and Løset, S. (2017), Accuracy of a Non-Smooth Time Stepping Scheme with Non-Rigid Contacts for Ice-Structure Interaction, *in* 'Proceedings of the 24th International Conference on Port and Ocean Engineering under Arctic Conditions', Busan, Korea.

van den Berg, M., Lubbad, R. and Løset, S. (2018), 'An Implicit Time-Stepping Scheme and an Improved Contact Model for Ice-Structure Interaction Simulations', *Cold Regions Science and Technology* **155**, 193–213.

van den Berg, M., Lubbad, R. and Løset, S. (2019*a*), The effect of floe shape on the interaction of vertical-sided structures with broken ice, *in* 'Proceedings of the 25th International Conference on Port and Ocean Engineering under Arctic Conditions', Delft, The Netherlands.

van den Berg, M., Lubbad, R. and Løset, S. (2019*b*), 'The effect of ice floe shape on the load experienced by vertical- sided structures interacting with a broken ice field', *Marine Structures* **65**, 229–248.

van den Berg, M., Lubbad, R., van den Berg, M. and Lubbad, R. (2015), The application of a non-smooth discrete element method in ice rubble modeling, *in* 'Proceedings of the 23rd International Conference on Port and Ocean Engineering under Arctic Conditions', Trondheim, Norway.

van der Werff, S., Haase, A., Huijsmans, R. and Zhang, Q. (2012), Influence of the Ice Concentration on the Ice Loads on the Hull of a Ship in a Managed Ice Field, *in* 'Proceedings of the ASME 2012 31st International Conference on Ocean, Offshore and Arctic Engineering', Rio de Janeiro, Brazil.

van Vliet, R. and Metrikine, A. V. (2017), Simulating Interaction Between Level Ice and Conical Structures with a 2D Lattice Model, *in* 'Proceedings of the 24th International Confrence on Port and Ocean Engineering under Arctic Conditions', Busan, Korea.

van Vliet, R. and Metrikine, A. V. (2018), 'Derivation and verification of a lattice model for bending vibration of a plate', *ZAMM Zeitschrift fur Angewandte Mathematik und Mechanik* **98**(3), 367–387.

van Vliet, R. and Metrikine, A. V. (2019), 'Failure criteria for a numerical model of sea ice in multi-directional tension , compression , bending and splitting', *Cold Regions Science and Technology* **159**, 123–141.

Yamaguchi, H., Rheem, C. K., Toyada, M., Matsuzawa, T., Nakayama, H., Kato, H., Kato, K. and Adachi, M. (1997), Influence of Floe Shape on Behaviour of Ice Floes around a Structure, *in* 'OMAE - Volume IV, Arctic/Polar Technology ASME', pp. 461–468.

Yip, M., Mohle, J. and Bolander, J. E. (2005), 'Automated Modeling of Three-Dimensional Structural Components Using Irregular Lattices', *Computer-Aided Civil and Infrastructure Engineering* **20**, 393–407.

Yulmetov, R., Bailey, E. and Ralph, F. (2017), A Discrete Element Model of Ice Ridge Interaction with a Conical Structure, *in* 'Proceedings of the 24th Inernational Confrence on Port and Ocean Engineering under Arctic Conditions', Busan, Korea.

Yulmetov, R., Lubbad, R. and Løset, S. (2016), 'Planar multi-body model of iceberg free drift and towing in broken ice', *Cold Regions Science and Technology* **121**, 154–166.

Zhang, J., Feng, D. and Pang, S. D. (2019), Bulk constitutive law and its importance in CEM simulations of ice-structure interaction, *in* 'Proceedings of the 25th International Conference on Port and Ocean Engineering under Arctic Conditions', Delft, The Netherlands.

Zhang, Q. and Skjetne, R. (2015), 'Image processing for identification of sea-ice floes and the floe size distributions', *IEEE Transactions on Geoscience and Remote Sensing* **53**(5), 2913–2924.

Appendix A

An implicit time-stepping scheme and an improved contact model for ice-structure interaction simulations

This paper was published in Cold Regions Science and Technology, issue 155 (2018).

Cold Regions Science and Technology 155 (2018) 193–213

Contents lists available at ScienceDirect

Cold Regions Science and Technology

journal homepage: www.elsevier.com/locate/coldregions

An implicit time-stepping scheme and an improved contact model for ice-structure interaction simulations

Marnix van den Berg*, Raed Lubbad, Sveinung Løset

SAMCoT, Department of Civil and Transport Engineering, NTNU, NO-7491 Trondheim, Norway

ARTICLE INFO

Keywords:
Non-smooth discrete element method
Contact model
Ice-structure interaction

ABSTRACT

This paper presents a novel time-stepping scheme for the modelling of discrete ice-structure interaction. The scheme extends the *non-smooth* discrete element modelling (NDEM) technique to enable compliant continuous and discontinuous contacts. This increases the accuracy and expands the applicability range of the NDEM technique related to ice-structure interaction problems. We derive the parameters representing the compliant behaviour of contacts. The accuracy of the presented scheme for discontinuous contacts is compared to an existing, simpler scheme that limits the contact force based on a maximum force assumption. The comparison shows that the derived scheme results in more accurate contact forces, for the same time step size, as previously applied NDEM schemes in ice-structure interaction. An example simulation is compared against ice tank tests of a 4-legged, vertical-walled structure moving through a broken ice field.

1. Introduction

The reduction of the areal extent and thinning of the Arctic sea ice cover will increase activity in waters where sea ice may occur. The accurate prediction of the loads and resistance caused by sea ice is important for safe and economical operations in these waters. Existing calculation methods for loads from sea ice on structures often rely on empirical formulas based on a limited range of full-scale data. Full-scale data are limited to existing structures and the regions where they are located. On top of this, the data are often incomplete and there is a high uncertainty in the measured loads. Ice tank tests can be used to obtain load data for specific types of structures or ice conditions. However, it is often uncertain if and how the loads measured in the ice tank can be scaled to full-scale equivalent loads. This is especially challenging for load cases other than continuous level ice, such as floe ice or ice ridges. Numerical modelling of ice-structure interaction can help, in combination with full-scale and model test data, to increase the understanding of occurring phenomena and ice failure modes, and can lead to a more accurate prediction of the sea ice loads that may be encountered.

Interaction between sea ice and structures is a complicated process. There are many factors that may contribute to the load and resistance experienced by a structure interacting with sea ice, and that pose challenges to the accurate numerical representation of the occurring processes. For example:

- many simultaneously contacting ice bodies
- complicated, and (seemingly) random body geometries
- difficult to estimate and highly variable ice material properties
- complicated hydrodynamic effects
- complicated and continuous dynamic fractures and failures

This combination of factors makes ice-structure interaction different from any other engineering problem. A numerical model will need to simplify some or all of the above-mentioned factors. To what extent the parameters can (and need to) be simplified depends on the processes to be investigated and limiting factors such as the available computing power and computation time, as well as the availability and accuracy of input parameters. The broad range of occurring processes and the different requirements that may be put upon numerical models, has led to a broad range of models and modelling types.

Numerical models for sea ice load estimation can broadly be divided in continuum and discrete models, although there are also several models that combine both modelling types. Among discrete ice-structure interaction models, a further distinction can be made based on the time-stepping scheme that is used. This difference is often described as *smooth* discrete element modelling (SDEM) versus *non-smooth* discrete element modelling (NDEM). The difference between NDEM and SDEM can be seen as the difference between implicit and explicit time integration (Servin et al. (2014)), allowing for much larger time steps, while maintaining stable simulations, when using NDEM. The time

* Corresponding author.
E-mail address: marnix.berg@ntnu.no (M. van den Berg).

https://doi.org/10.1016/j.coldregions.2018.07.001
Received 31 October 2017; Received in revised form 3 May 2018; Accepted 1 July 2018
Available online 22 August 2018
0165-232X/

steps can often be several orders of magnitude larger than those in SDEM, but the processing of each time step is more computationally expensive. NDEM requires the solution of a linear complementarity problem (LCP) or a mixed linear complementarity problem (MLCP) at each time step. Nevertheless, NDEM simulations are often considered more efficient and are mostly chosen when real-time or near-real-time simulations are required.

There are many publications describing SDEM models and modelling results of ice-structure interaction, going back to the early 90s. Some examples can be found in Hopkins et al. (1991); Hocking (1992); Løset (1994*a*,b); Tuhkuri and Polojärvi (2005); Polojärvi and Tuhkuri (2009); Paavilainen et al. (2009); Liu et al. (2017). The application of NDEM in ice-structure interaction has been more recent, and so far it has been mostly applied to global broken ice-structure simulations. Application examples of NDEM in ice-structure interaction can be found in Konno and Mizuki (2006); Lubbad and Løset (2011); Metrikin (2014); Alawneh et al. (2015); Yulmetov et al. (2016). In NDEM, contacts between interacting bodies are often assumed to be infinitely rigid. Therefore, contact forces cannot be defined in a physically correct manner. This limitation can be remedied to some extent by introducing an upper limit for the contact force based on a combination of contact area and crushing pressure, as is done in Lubbad and Løset (2011) and Metrikin (2014), where both papers use a slightly different method to apply the upper limit.

In this paper, we derive a novel NDEM time-stepping scheme starting from the Newmark-Beta method for differential equations (Newmark (1959)). The new formulations are valid for compliant continuous and discontinuous contacts. The position and velocity update rules of the Newmark-Beta method are rewritten, and limits are introduced in order to enable discontinuous contact modelling. Compared to previously applied NDEM methods in ice-structure interaction modelling, where only an upper limit for the contact force was defined based on the current contact area, our new method takes the current contact area as well as the expected change in the contact area into account in determining the contact response, leading to a higher accuracy of the predicted contact force for the same time step size. The main properties of the NDEM time-stepping scheme are maintained in the new method, i.e., an MLCP is solved in each time step, and large time steps can be taken without affecting the stability. In addition, the new method can now handle compliant as well as infinitely stiff contacts. The method is implemented in the *Simulator of Arctic Marine Structures* (SAMS), the product of *Arctic Integrated Solutions* (ArcISo); see *ArcISo* (2018); Lubbad et al. (2018).

To the authors' knowledge, this is the first time such a time-stepping scheme has been applied to ice-structure interaction modelling. In other fields, such as soil modelling and physics simulations, similar methods have been described and used Jean (1999); Moreau (1999); Lacoursière (2007); Krabbenhoft et al. (2012); Tasora et al. (2013); Servin et al. (2014). The difference between these methods and the method described in this paper is that the current model assures energy conservation for continuous linear contacts. This is a property of the Newmark-Beta method. The other methods are derived from an implicit Euler or similar schemes, and therefore result in numerical damping.

In Section 2, we first derive a generalized form of the time-stepping scheme that applies to rigid, compliant, continuous and discontinuous contacts. Sections 3 and 4 describe how the needed contact parameters can be obtained for continuous contacts, as would occur in a lattice model, and discontinuous contacts, such as ice-ice and ice-structure contacts. The accuracy of the derived scheme for discontinuous contacts is compared against an existing scheme in Section 5. In Section 6 we provide an application example, in which we compare the results from the numerical model against data obtained in an ice tank test. Section 7 discusses some features of the numerical model and the application example. Finally, Section 8 concludes the paper.

2. An implicit DEM time-stepping scheme

The proposed implicit time stepping-scheme expands the traditional NDEM formulation to include compliant contact behaviour, which is needed for the accurate simulation of ice-structure interactions. Similar to the traditional NDEM formulation, the stability of the simulations is independent of the time step size when using the proposed scheme, and it is capable of efficiently solving a large network of simultaneous contacts.

The following sections derive the MLCP, which needs to be solved at each time step. The central assumption in the derivations is a constant average acceleration within a time step. More particularly, this means that we use the average force occurring within a time step in body propagation. It does not mean, however, that the contact force itself is assumed constant. This corresponds to a Newmark-Beta method (Newmark (1959)) with parameters $\gamma = \frac{1}{2}$ and $\beta = \frac{1}{4}$, yielding the constant average acceleration method. We start by deriving some terms for a continuous 1 degree of freedom (DOF) case, then add constraints to the contact force to enable discontinuous contact modelling, and finally compare the resulting formulation to previously used formulations. The expansion to multiple degrees of freedom and frictional contacts is explained in Appendix B, since this part is similar to previously applied methods.

2.1. Derivation of the time-stepping scheme for a continuous 1-DOF case

Fig. 1 shows the 1-DOF example case used for the derivations in this section. In this example case, we use a generalized Kelvin-Voigt unit as the contact model, in which the parallel spring and dashpot element can be linear or nonlinear. The method can also be applied to other rheological elements, such as a Maxwell unit, following a similar procedure as described in this section. In Fig. 1, m stands for the mass of the body, δ for the penetration depth, $\dot{\delta}$ for the penetration velocity, $F_{\text{cont}}(\delta, \dot{\delta})$ for the contact force as a function of the penetration and the penetration velocity, and F_{ext} stands for an external (non-contact) force acting on the body during time step $\Delta t = t_{n+1} - t_n$, where t_n is the current time and t_{n+1} is the time at the end of the time step. u, $\dot{u}$ and $\ddot{u}$ are the body position, velocity and acceleration, respectively. For convenience, we choose the axis system such that $\delta = u$ if $\delta \geq 0$. In the derivation in this section, we assume $\delta \geq 0$, and thus $F_{\text{cont}}(\delta, \dot{\delta}) = F_{\text{cont}}(u, \dot{u})$. This is expanded to a case in which $u \in \mathbb{R}$ in Section 2.2. The equation of motion of this system is:

$$m\ddot{u} + F_{\text{cont}}(u, \dot{u}) = F_{\text{ext}} \tag{1}$$

Assuming constant average acceleration within each time step, the equation of motion can be discretized, and body positions and velocities are updated according to Eqs. (2) and (3), which are the time-stepping equations as used in the constant average acceleration method:

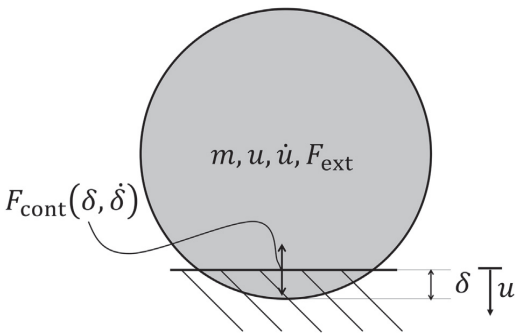

Fig. 1. General single DOF contact case.

$$u_{n+1} = u_n + \dot{u}_n \Delta t + \frac{1}{2}(\Delta \dot{u}_{\text{cont}} + F_{\text{ext}} m^{-1} \Delta t)\Delta t \tag{2}$$

$$\dot{u}_{n+1} = \dot{u}_n + \Delta \dot{u}_{\text{cont}} + F_{\text{ext}} m^{-1} \Delta t \tag{3}$$

Subscripts n indicate the body position and velocity at the beginning of the time step, subscripts $n + 1$ indicate the body position and velocity at the end of the time step, Δt is the time step size and $\Delta \dot{u}_{\text{cont}}$ is the change in body velocity due to the contact force F_{cont}. We write the contact force at the beginning and end of the time step as:

$$F^n_{\text{cont}} = F_{\text{cont}}(u_n, \dot{u}_n) \quad \text{and} \quad F^{n+1}_{\text{cont}} = F_{\text{cont}}(u_{n+1}, \dot{u}_{n+1}) \tag{4}$$

The partial derivatives of F_{cont} with respect to the penetration and the penetration velocity at the beginning of the time step are used to estimate the change of he contact force during a time step:

$$k_n = \frac{\partial F^n_{\text{cont}}}{\partial u} \Big|_{u=u_n} \quad \text{and} \quad c_n = \frac{\partial F^n_{\text{cont}}}{\partial \dot{u}} \Big|_{\dot{u}=\dot{u}_n} \tag{5}$$

Using these partial derivatives and the body propagation Eqs. (2) and (3), we estimate F^{n+1}_{cont} as:

$$F^{n+1}_{\text{cont}} = F^n_{\text{cont}} + k_n\left(\dot{u}_n \Delta t + \frac{1}{2}(\Delta \dot{u}_{\text{cont}} + F_{\text{ext}} m^{-1} \Delta t)\Delta t\right) + c_n(\Delta \dot{u}_{\text{cont}} + F_{\text{ext}} m^{-1} \Delta t) \tag{6}$$

We rewrite this equation and formulate a system of equations in which the contact impulse λ_{cont}, as in Eq. (7), and the velocity change $\Delta \dot{u}_{\text{cont}}$ are the unknowns:

$$\lambda_{\text{cont}} = F^{\text{av}}_{\text{cont}} \cdot \Delta t \tag{7}$$

The average contact force over a time step $F_{\text{cont}}{}^{\text{av}}$ is defined as:

$$F^{\text{av}}_{\text{cont}} = \frac{F^n_{\text{cont}} + F^{n+1}_{\text{cont}}}{2} \tag{8}$$

Combining and rearranging Eqs. (6), (7) and (8), we obtain:

$$\lambda_{\text{cont}} = F^n_{\text{cont}} \Delta t + \tfrac{1}{2}\left(\dot{u}_n + \tfrac{1}{2} F_{ext} m^{-1} \Delta t\right)\Delta t^2 k_n + \tfrac{1}{4}\Delta \dot{u}_{\text{cont}} \Delta t^2 k_n + \tfrac{1}{2} F_{ext} m^{-1} \Delta t^2 \;\; c_n + \tfrac{1}{2}\Delta \dot{u}_{\text{cont}} \Delta t \;\; c_n \tag{9}$$

This can be rewritten as:

$$-\Delta \dot{u}_{\text{cont}} + \frac{\lambda_{\text{cont}}}{\left(\frac{1}{4}k_n \Delta t^2 + \frac{1}{2}c_n \Delta t\right)} = \frac{F^n_{\text{cont}}}{\left(\frac{1}{4}k_n \Delta t + \frac{1}{2}c_n\right)} + \frac{\frac{1}{2}\left(\dot{u}_n + \frac{1}{2}F_{\text{ext}} m^{-1}\Delta t\right)\Delta t^2 k_n}{\left(\frac{1}{4}k_n \Delta t^2 + \frac{1}{2}c_n \Delta t\right)} + \frac{\frac{1}{2}F_{\text{ext}} m^{-1}\Delta t^2 \;\; c_n}{\left(\frac{1}{4}k_n \Delta t^2 + \frac{1}{2}c_n \Delta t\right)} \tag{10}$$

Using the relation:

$$\lambda_{\text{cont}} = -\Delta \dot{u}_{\text{cont}} \;\; m \tag{11}$$

we can formulate a system of equations:

$$\begin{bmatrix} m & 1 \\ -1 & \Sigma \end{bmatrix}\begin{bmatrix} \Delta \dot{u}_{\text{cont}} \\ \lambda_{\text{cont}} \end{bmatrix} = \begin{bmatrix} 0 \\ \Upsilon \end{bmatrix} \tag{12}$$

in which Σ and Υ are defined as:

$$\Sigma = \frac{1}{\left(\frac{1}{4}k_n \Delta t^2 + \frac{1}{2}c_n \Delta t\right)} \tag{13}$$

$$\Upsilon = \frac{F^n_{\text{cont}}}{\frac{1}{4}k_n \Delta t + \frac{1}{2}c_n} + \frac{\frac{1}{2}\left(\dot{u}_n + \frac{1}{2}F_{\text{ext}} m^{-1}\Delta t\right)\Delta t^2 k_n}{\frac{1}{4}k_n \Delta t^2 + \frac{1}{2}c_n \Delta t} + \frac{\frac{1}{2}F_{\text{ext}} m^{-1}\Delta t^2 \;\; c_n}{\frac{1}{4}k_n \Delta t^2 + \frac{1}{2}c_n \Delta t} \tag{14}$$

The solution of this system gives the impulse λ_{cont} and the body velocity change due to the contact impulse $\Delta \dot{u}_{\text{cont}}$.

Eqs. (12), (13) and (14) provide a general description of a compliant continuous 1-DOF contact. A special case occurs when the stiffness and damping parameters, k and c, respectively, are constant. In this case, $F^n_{\text{cont}} = u_n k + \dot{u}_n c$, so Σ and Υ can be simplified to:

$$\Sigma_{\text{lin}} = \frac{1}{\left(\frac{1}{4}k\Delta t^2 + \frac{1}{2}c\Delta t\right)} \tag{15}$$

$$\Upsilon_{\text{lin}} = \frac{u_n \;\; k}{\frac{1}{4}k\Delta t + \frac{1}{2}c} + 2\left(\dot{u}_n + \frac{1}{2}F_{\text{ext}} m^{-1}\Delta t\right) \tag{16}$$

This form occurs when the time-stepping scheme is combined with a lattice model to represent the material properties of intact ice. The Σ and Υ values then represent the spring-dashpot elements that form the lattice. The application of this scheme to lattice modelling is further explained in Section 3.

Note that the Newmark-Beta method, on which this derivation is based, is only valid for continuously differentiable functions. In the case of ice-ice or ice-structure contacts, the contact force as a function of time is discontinuous in the time step in which the contact is initiated and in the time step in which the crushing stops. However, the method can still be used in this case by applying appropriate lower and upper limits to the calculated contact impulse.

2.2. Extension of the time-stepping scheme for discontinuous 1-DOF contacts

The forces at ice-ice or ice-structure contacts are bounded by upper and lower limits, leading to a discontinuous contact behaviour. The limits follow from the local physical processes occurring at the contacts. In this paper, we use simplifying assumptions regarding the local contact processes to formulate the upper and lower limits of the contact forces. The physical reasoning behind these limits will be further elaborated in Section 4. The current section focusses on how these limits are enforced within the time-stepping scheme.

Our discontinuous contact assumptions lead to a contact force that is only dependent on the contact penetration, not on the relative penetration velocity. If the contact force is only dependent on the penetration, and not on the penetration velocity, Eqs. (13) and (14) can be significantly simplified. All terms related to c_n can be dropped, leading to the simplified form of Σ and Υ:

$$\Sigma_{\text{pen}} = \frac{1}{\left(\frac{1}{4}k_n \Delta t^2\right)} \tag{17}$$

$$\Upsilon_{\text{pen}} = \frac{F^n_{\text{cont}}}{\frac{1}{4}k_n \Delta t} + 2\left(\dot{u}_n + \frac{1}{2}F_{\text{ext}} m^{-1}\Delta t\right) \tag{18}$$

Note that a velocity term still appears in Eq. (18). This term appears because the change in position within a time step is taken into account, which is a function of velocity $\dot{u}_n$.

The following limits to the contact parameters are enforced in the case of discontinuous ice-ice and ice-structure contacts:

$$k_n \geq 0 \tag{19}$$

$$F^n_{\text{cont}} \geq 0 \tag{20}$$

$$F^n_{\text{cont}} = 0 \quad \textit{if} \quad \delta \leq 0 \tag{21}$$

Eq. (19) states that the contact force may not decrease as the contact penetration increases. Eqs. (20) and (21) state that the contact force may not be negative and that there may only be a contact force if there is a contact between bodies (penetration $\delta \geq 0$).

The contact impulse, which is part of the solution of the system expressed by Eq. (12), is subject to the following limits:

$$\lambda_{\text{cont}} \geq 0 \tag{22}$$

$$\lambda_{\text{cont}} \leq \lambda_{\text{res}=0} \tag{23}$$

Eq. (22) states that there may not be tensional impulses (and forces) at a contact, and Eq. (23) states that the applied impulse may not be higher

than the impulse needed to achieve a relative contact velocity of zero (the zero-restitution impulse $\lambda_{res=0}$).

Limits to the contact parameters (Eqs. (19), (20) and (21)) are enforced in the formulation of the system of equations and usually follow naturally from the contact assumptions that are made. The limits to the solution (Eqs. (22) and (23)) are taken into account in the system as formulated in Eq. (12) by introducing complementarity conditions. This leads to the following mixed linear complementarity problem:

$$\begin{bmatrix} m & 1 & 0 \\ -1 & \Sigma_{cr} & 1 \\ 1 & \Sigma_{cr} & 1 \end{bmatrix} \begin{bmatrix} \Delta\dot{u}_{cont} \\ \lambda_{cont} \\ v_{cor} \end{bmatrix} + \begin{bmatrix} 0 \\ -\Upsilon_{cr} \\ -\frac{F_{cr}}{\frac{1}{4}\frac{\Delta F_{cr}}{\Delta\delta}\Delta t} \end{bmatrix} = \begin{bmatrix} 0 \\ \alpha_r \\ \beta_r \end{bmatrix}$$
$$0 \le [\lambda_{cont} \;\; v_{cor}]^T \perp [\alpha_r \;\; \beta_r]^T \ge 0 \tag{24}$$

in which v_{cor} is the correctional velocity needed to satisfy the zero restitution requirement, and α_r and β_r are residuals that have no physical meaning. Σ_{cr} and Υ_{cr} are defined as:

$$\Sigma_{cr} = \frac{1}{\left(\frac{1}{4}\frac{\Delta F_{cr}}{\Delta\delta}\Delta t^2\right)} \tag{25}$$

$$\Upsilon_{cr} = \frac{F_{cr}}{\frac{1}{4}\frac{\Delta F_{cr}}{\Delta\delta}\Delta t} + 2\left(\dot{u}_n + \frac{1}{2}F_{ext}m^{-1}\Delta t\right) \tag{26}$$

Note the difference between this formulation and the continuous contact formulation of Υ_{pen} in Eq. (18). The contact force ${F_{cont}}^n$ is replaced by the force F_{cr}. This is the force at which contact crushing would be initiated for this contact. This change follows from the fact that the contact force is no longer uniquely related to a specific penetration depth δ. The force penetration gradient k_n from Eq. (18) is replaced by a discretized version $\frac{\Delta F_{cr}}{\Delta\delta}$ because the analytical expression of the force-penetration curve $F_{cont}(\delta)$ is not explicitly calculated for each contact.

The MLCP in Eq. (24) fully describes the desired discontinuous contact behaviour. It is not immediately obvious how the MLCP enforces the limits expressed in Eqs. (22) and (23). Therefore the problem statement is further clarified and proven to be correct in AppendixA.

To highlight the difference between the derived MLCP (Eqs. (24), (25) and (26)) and the corresponding MLCP used in other schemes, a direct comparison is made in Section 2.3.

2.3. Comparison of the new time-stepping scheme to the rigid contact method

In this section we present the MLCP for the 1 DOF example case according to previously used formulations and compare these to the derived formulation in Eqs. (24), (25) and (26).

Most NDEM formulations assume that contacts between bodies are rigid. The rigid contact NDEM formulation does not take the contact force evolution $F_{cont}(\delta, \dot{\delta})$ into account. Instead, when a contact is detected, an impulse is applied such that the relative contact velocity changes according to a certain restitution factor γ_{rf}:

$$\Delta\dot{u}_{cont} = (1 + \gamma_{rf})(\dot{u}_n + F_{ext}m^{-1}\Delta t) \tag{27}$$

Combining this with Eq. (11) and Condition 22, leads to the following MLCP for the 1 DOF example in Section 2.2:

$$\begin{bmatrix} m & 1 \\ -1 & 0 \end{bmatrix} \begin{bmatrix} \Delta\dot{u}_{cont} \\ \lambda_{cont} \end{bmatrix} + \begin{bmatrix} 0 \\ (1 + \gamma_{rf})(\dot{u}_n + F_{ext}m^{-1}\Delta t) \end{bmatrix} = \begin{bmatrix} 0 \\ \alpha_r \end{bmatrix}$$
$$0 \le \lambda_{cont} \perp \alpha_r \ge 0 \tag{28}$$

The restitution factor γ_{rf} specifies the extent to which the contact dissipates energy. A restitution factor of zero results in a contact that dissipates all kinetic energy (the relative contact velocity becomes zero), and a restitution factor of 1 would result in a fully 'elastic' contact: the relative velocity after contact resolution is opposite and equal in value to the relative velocity before the contact resolution.

Since no contact properties are included in the formulation as shown in Eq. (28), it is not possible to find a physically correct contact force using this method. Only the contact impulse is defined, but the impulse cannot be translated in a physically meaningful way to an equivalent force. This is problematic for ice-structure interaction simulations, since most simulation methods use contact forces to determine whether ice failure should occur.

As mentioned in the introduction, some existing papers work around this limitation by introducing an upper limit to the contact impulse based on contact properties. The upper limit is determined based on a certain assumed upper limit force F_{lim}. If the impulse resulting from the MLCP is equal to the upper limit, it can be assumed that the contact force is equal to the limit force, multiplied by the time step. The way this upper limit is enforced differs between methods. For instance, Metrikin (2014) enforces an upper limit contact force in the MLCP framework in the following manner:

$$\begin{bmatrix} m & 1 & 0 \\ -1 & 0 & 1 \\ 0 & -1 & 0 \end{bmatrix} \begin{bmatrix} \Delta\dot{u}_{cont} \\ \lambda_{cont} \\ v_{cor} \end{bmatrix} + \begin{bmatrix} 0 \\ -(1 + \gamma_{rf})(\dot{u}_n + F_{ext}m^{-1}\Delta t) \\ F_{lim}\Delta t \end{bmatrix} = \begin{bmatrix} 0 \\ \alpha_r \\ \beta_r \end{bmatrix}$$
$$0 \le [\lambda_{cont} \;\; v_{cor}]^T \perp [\alpha_r \;\; \beta_r]^T \ge 0 \tag{29}$$

Comparing this formulation to the new MLCP formulation in Eq. (24) as presented in this paper, this formulation is clearly different. The difference can be most easily understood by considering that the approach using an upper limit force only uses the geometry information at the beginning of the time step, while the approach presented in this paper uses the current contact geometry as well as the expected change in contact geometry to define a force penetration gradient $\frac{\Delta F_{cr}}{\Delta\delta}$, resulting in the higher accuracy of this scheme. An accuracy comparison is provided for a simplified test case in Section 5.

2.4. Expansion of the time-stepping scheme to a multi-contact three-dimensional case with friction

To apply this time-stepping scheme in a useful manner to ice-structure interaction, it must be expanded to a three dimensional (3-D) system with multiple degrees of freedom and friction. This expansion is similar to the procedures followed in previously applied methods and it is explained in AppendixB. It leads to the following system:

$$\mathbf{Az} + \mathbf{b} = \mathbf{w}$$
$$0 \le [\boldsymbol{\lambda}_n^T \;\; \boldsymbol{\lambda}_t^T \;\; \boldsymbol{\lambda}_\phi^T \;\; (\boldsymbol{\lambda}_n^{cor})^T \;\; (\boldsymbol{\lambda}_t^{cor})^T \;\; (\boldsymbol{\lambda}_\phi^{cor})^T]^T$$
$$\perp [\boldsymbol{\alpha}_r^T \;\; \boldsymbol{\beta}_r^T \;\; \boldsymbol{\gamma}_r^T \;\; \boldsymbol{\zeta}_r^T \;\; \boldsymbol{\eta}_r^T \;\; \boldsymbol{\theta}_r^T]^T \ge 0 \tag{30}$$

in which:

$$\mathbf{A} = \begin{bmatrix} \mathbf{M} & -\mathbf{J}_h & -\mathbf{J}_n & -\mathbf{J}_t & -\mathbf{J}_\phi & \mathbf{0} & \mathbf{0} & \mathbf{0} \\ \mathbf{J}_h^T & \boldsymbol{\Sigma}_h & \mathbf{0} & \mathbf{0} & \mathbf{0} & \mathbf{0} & \mathbf{0} & \mathbf{0} \\ \mathbf{J}_n^T & \mathbf{0} & \boldsymbol{\Sigma}_n & \mathbf{0} & \mathbf{0} & \mathbf{E}_n & \mathbf{0} & \mathbf{0} \\ \mathbf{J}_t^T & \mathbf{0} & \mathbf{0} & \mathbf{0} & \mathbf{0} & \mathbf{0} & \mathbf{E}_{fr} & \mathbf{0} \\ \mathbf{J}_\phi^T & \mathbf{0} & \mathbf{0} & \mathbf{0} & \mathbf{0} & \mathbf{0} & \mathbf{0} & \mathbf{E}_{rot} \\ -\mathbf{J}_n^T & \mathbf{0} & \boldsymbol{\Sigma}_n & \mathbf{0} & \mathbf{0} & \mathbf{E}_n & \mathbf{0} & \mathbf{0} \\ \mathbf{0} & \mathbf{0} & \mathbf{U}_{fr} & -\mathbf{E}_{fr}^T & \mathbf{0} & \mathbf{0} & \mathbf{0} & \mathbf{0} \\ \mathbf{0} & \mathbf{0} & \mathbf{U}_{rot} & \mathbf{0} & -\mathbf{E}_{rot}^T & \mathbf{0} & \mathbf{0} & \mathbf{0} \end{bmatrix}, \quad \mathbf{z} = \begin{bmatrix} \Delta\dot{\mathbf{u}} \\ \boldsymbol{\lambda}_h \\ \boldsymbol{\lambda}_n \\ \boldsymbol{\lambda}_t \\ \boldsymbol{\lambda}_\phi \\ \boldsymbol{\lambda}_n^{cor} \\ \boldsymbol{\lambda}_t^{cor} \\ \boldsymbol{\lambda}_\phi^{cor} \end{bmatrix} \tag{31}$$

$$\mathbf{b} = \begin{bmatrix} \mathbf{0} \\ \mathbf{Y}_h \\ \mathbf{Y}_n \\ \dot{\mathbf{u}}_i^c + \frac{1}{2}\Delta\dot{\mathbf{u}}_{i;ext}^c \\ \dot{\phi}^c + \frac{1}{2}\Delta\dot{\phi}_{ext}^c \\ \mathbf{S}_n \\ \mathbf{0} \\ \mathbf{0} \end{bmatrix}, \quad \mathbf{w} = \begin{bmatrix} \mathbf{0} \\ \mathbf{0} \\ \alpha_r \\ \beta_r \\ \gamma_r \\ \zeta_r \\ \eta_r \\ \theta_r \end{bmatrix} \tag{32}$$

and S_n is:

$$\mathbf{S}_n = \begin{bmatrix} \frac{F_{cr;1}}{\frac{1}{4}\frac{\Delta F_{cr;1}}{\Delta\delta_1 \Delta t}} \\ \vdots \\ \frac{F_{cr;nc}}{\frac{1}{4}\frac{\Delta F_{cr;nc}}{\Delta\delta_{nc} \Delta t}} \end{bmatrix} \tag{33}$$

The terms in this system are derived and explained in Appendix B.

2.5. Solving the formulated MLCP

The MLCP is solved using a block Gauss-Seidel solver, similar to the methods applied in, for example, Servin et al. (2014); Jean (1999); Lacoursiere (2003). The block Gauss-Seidel solver is an iterative solver. Iterations can be stopped when a user defined accuracy threshold is met. An advantage of using an iterative solver is that the solution from the previous time step can be used as an initial guess for the next time step, reducing the needed number of iterations. The inclusion of the parameters Σ improves the convergence rate of the solver significantly compared to a similar system with infinitely stiff contacts.

The time-stepping scheme as derived in this section may be applied to continuous contacts, as occurs between the different elements of a lattice representation of the ice, and to discontinuous contacts, such as ice-ice or ice-structure contacts. Fig. 2 clarifies where both types of contacts occur in an ice-structure interaction simulation. The following sections will explain in further detail how the scheme may be applied to both scenarios.

3. Application of time stepping-scheme to lattice modelling

Lattice models represent a material as a collection of discrete masses, connected with a network of springs and dashpots. Compared to continuum models, lattice models offer advantages in the modelling of fracture, since no stress singularities will occur at the crack tips (van Vliet and Metrikine (2018)). Therefore, lattice models have been applied to ice modelling by a number of authors: Hocking (1992); Jirasek and Bazant (1995); Sayed and Timco (1999); Dorival et al. (2008); Paavilainen et al. (2009); Lilja et al. (2017). The discrete nature of lattice models makes them well suited for the modelling of ice, in combination with the presented time-stepping scheme. When applying the time-stepping scheme to the continuous linear contacts as occur in a lattice model, energy conservation is assured, following from the use of the Newmark-Beta method. Applications of a combined lattice model and time-stepping scheme have been presented by the authors in van den Berg (2016) and van den Berg et al. (2017). In these papers, the spring stiffness of connections between masses are defined as:

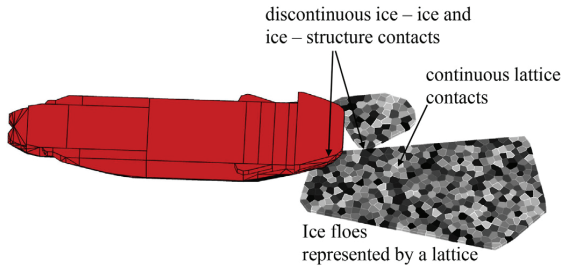

Fig. 2. Continuous and discontinuous contacts in an ice-structure interaction simulation.

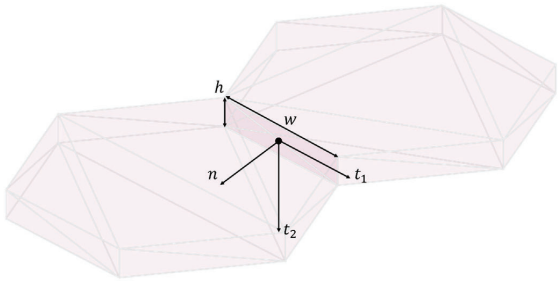

Fig. 3. Local axis system of lattice connection in an ice plate (from van den Berg (2016)).

$$k_n = \frac{EA}{d}, \qquad k_{t1} = k_{t2} = \frac{GA}{d}, \qquad k_{\phi n} = \frac{2 \cdot G \cdot min(I_{t1}, I_{t2})}{d} \tag{34}$$

$$k_{\phi t1} = \frac{EI_{t1}}{d}, \qquad k_{\phi t2} = \frac{EI_{t2}}{d} \tag{35}$$

where E is the Young's modulus of the ice, $A = wh$ is the area between the mass elements and w and h as defined in Fig. 3, G is the shear modulus of ice, d is the distance between the centres of gravity of both mass elements, and I_{t1} and I_{t2} are the second moments of area around axes t_1 and t_2, respectively. n is the axis perpendicular to the contact plane, and t_1 and t_2 are the principal axes or the contact area as defined in the contact plane. This is clarified in Fig. 3.

The spring-dashpot connections between the masses in a lattice representation of ice are treated similar to discontinuous contacts in the time-stepping scheme, and appear in the linear complementarity problem as shown in Eqs. (15) and (16). The main difference between the continuous lattice contacts and the discontinuous contacts such as ice - ice or ice - structure contacts is that the connection properties within the lattice remain constant and that no upper and lower limits are applied if ice failure is not considered.

In the remainder of this paper, we focus on the application and validation of the time-stepping scheme to discontinuous contacts, as would occur in ice-ice or ice-structure interaction. For the application to lattice modelling, the reader is referred to van den Berg (2016) and van den Berg et al. (2017).

4. Application of the time-stepping scheme to discontinuous ice-ice and ice-structure contact modelling

This section derives the parameters of discontinuous ice-ice and ice-structure contacts. The parameters of these discontinuous contacts between the ice and/or structure bodies are derived based on an assumption of constant energy dissipation per crushed volume or *crushing specific energy* (CSE) (Kim and Gagnon (2016)). The CSE is the amount of energy needed to crush a unit volume of ice (unit: J/m^3). Ice contact models based on energy dissipation are similar to contact models based on ice crushing pressure and contact area. A certain assumed energy dissipation function can easily be converted to an equivalent crushing pressure, and vice versa. The main difference between existing contact models for ice is whether they assume a constant crushing pressure/energy dissipation or a crushing pressure that is dependent on the contact area. For example, Hopkins (1992); Paavilainen et al. (2011); Keijdener and Metrikine (2014) assume a constant crushing pressure (or plastic limit stress) during indentation. Using a constant crushing pressure is supported by Kim and Høyland (2014) and Kim and Gagnon

(2016). Kim and Høyland (2014) suggest that the crushing specific energy (CSE) of ice might be a scale-independent parameter, at least for geometrically similar situations. Kinnunen et al. (2016) also suggests that the CSE value remains stable during an impact event. Daley (1999), on the other hand, assumes a crushing pressure that is dependent on the contact area.

The assumption of a constant CSE is equivalent to a constant crushing pressure. We consider this assumption justifiable in light of other simplifications, such as geometrical simplifications of the floe shapes. The intended use of this contact model is for local crushing only. In cases where continuous crushing at the ice-structure interface is the governing failure mode, the assumption of a constant crushing pressure is no longer sufficient.

For the detection of contacts between bodies, we use an open-source algorithm which is part of the Bullet Physics library *Bullet Physics* (2017). After a contact is detected, we use the assumption of constant energy absorption during crushing to derive the discontinuous contact parameters that are needed in our new time-stepping scheme. The parameters are derived using the contact geometry. Referring to the contact parameters as described in Section 2, the discontinuous contact model needs to provide values for the contact force when crushing is initiated (F_{cr}) and the increase in contact force with penetration ($\frac{\Delta F}{\Delta \delta}$), as occur in Eqs. (24), (25) and (26). In addition, we need to define the contact point in global coordinates o_{c} and the contact axis system B_{c} to generalize the time-stepping scheme to multiple contacts and three dimensions. The contact point and contact axis system are used in Appendix B. The contact axis system B_{c} consists of a normal axis n_{c} and two friction axes t_{c1} and t_{c2}.

For clarity, 2-D sketches are used in this section, but the algorithm is implemented fully in 3-D.

Contact crushing is represented by body overlap in the numerical simulation, under the assumption that the overlap volume that occurs in the numerical simulation represents crushed ice. Fig. 4 helps to illustrate this assumption.

The contact point (o_{c}) is defined as the centre of the overlap volume. The contact normal direction is defined as the weighted average of the normal directions of the sub contact areas related to one of the bodies:

$$\mathbf{n}_{\mathrm{c}} = \frac{\sum_{s=1}^{s=\mathrm{ns}} A_{j,s}\mathbf{n}_{j,s}}{\left\| \sum_{s=1}^{s=\mathrm{ns}} A_{j,s}\mathbf{n}_{j,s} \right\|} \tag{36}$$

in which ns is the number of surfaces related to the one of the bodies in the overlap volume, $A_{j,\,s}$ are the areas of these surfaces, and $n_{j,\,s}$ are unit length vectors perpendicular to these surfaces. The parameters are illustrated in Fig. 5. The contact normal may also be defined using the surfaces related to body i, resulting in an opposite contact normal. This gives the same final result, as long as the normal direction definition is applied consistently throughout the calculations.

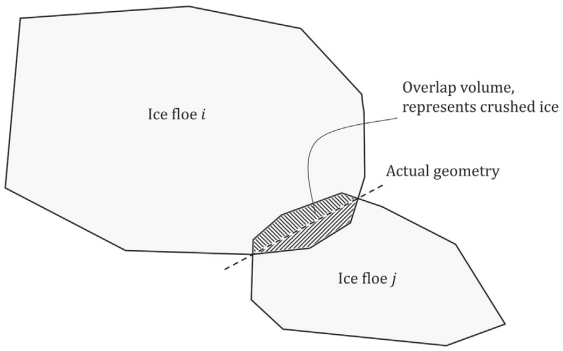

Fig. 4. The overlap volume of two interacting bodies represents crushed ice.

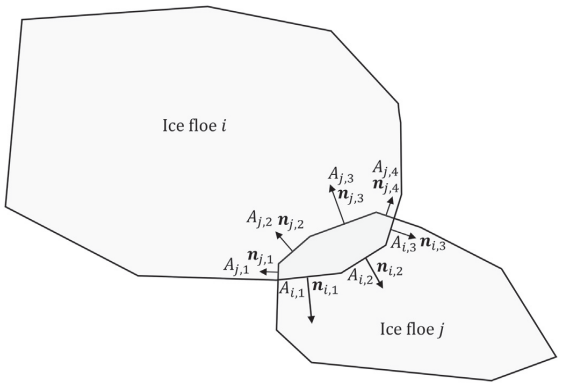

Fig. 5. Clarification of sub contact areas and normals.

The contact friction direction t_{c1} is chosen opposite to the tangential component of the contact velocity:

$$\mathbf{t}_{c1} = -\frac{\dot{\mathbf{u}}_{\mathrm{c}} - \mathbf{n}_{\mathrm{c}}(\mathbf{n}_{\mathrm{c}}\cdot\dot{\mathbf{u}}_{\mathrm{c}})}{\|\dot{\mathbf{u}}_{\mathrm{c}} - \mathbf{n}_{\mathrm{c}}(\mathbf{n}_{\mathrm{c}}\cdot\dot{\mathbf{u}}_{\mathrm{c}})\|} \tag{37}$$

The contact friction direction t_{c2} is chosen to complete the axis system:

$$\mathbf{t}_{c2} = \mathbf{t}_{c1} \times \mathbf{n}_{\mathrm{c}} \tag{38}$$

A second friction direction is needed because the change in the contact velocity within the time step is taken into account in the MLCP. Therefore, the resulting friction force is not necessarily opposite to the contact velocity at the beginning of the time step.

The contact force where crushing starts F_{cr} is determined based on the projected contact area and an assumed crushing specific energy of the ice:

$$F_{\mathrm{cr}} = A_{\mathrm{proj}}\cdot\mathrm{CSE} \tag{39}$$

in which the contact projected area is the area that results when projecting the contact polyhedron on the contact normal:

$$A_{\mathrm{proj}} = \sum_{s=1}^{s=\mathrm{ns}} A_{j,s}\mathbf{n}_{j,s}\cdot\mathbf{n}_{\mathrm{c}} \tag{40}$$

We determine the gradient $\frac{\Delta F}{\Delta \delta}$ such that the kinetic energy dissipated in the contact matches the energy absorbed in ice crushing. The gradient is determined by calculating the contact projected area in the current body positions and the contact projected area when the contacting bodies are propagated with their current velocity. This is clarified in Fig. 6, where $\Delta\delta$ is the change in penetration:

$$\Delta\delta = \dot{u}_{\mathrm{cont}}\Delta t + \frac{1}{2}F_{\mathrm{ext}}m^{-1}\Delta t^2 \tag{41}$$

and $A_{\mathrm{proj}}^{\mathrm{prop}}$ is the contact projected area when the contacting bodies are propagated with their current velocity. If there is a zero or negative penetration velocity, one of the bodies is propagated with a user-defined distance in the contact normal direction. The gradient $\frac{\Delta F}{\Delta \delta}$ is determined as:

$$\frac{\Delta F}{\Delta \delta} = \frac{(A_{\mathrm{proj}}^{\mathrm{prop}} - A_{\mathrm{proj}})\mathrm{CSE}}{\Delta\delta} \tag{42}$$

In the case of decreasing contact penetration, the load will drop to zero. This follows from the assumption that the overlap volume between bodies represents crushed material. This type of contact behaviour can be viewed as hysteretic damping, in which the loading/unloading curve will be similar to Fig. 7. Three types of discontinuous contact behaviour can be distinguished:

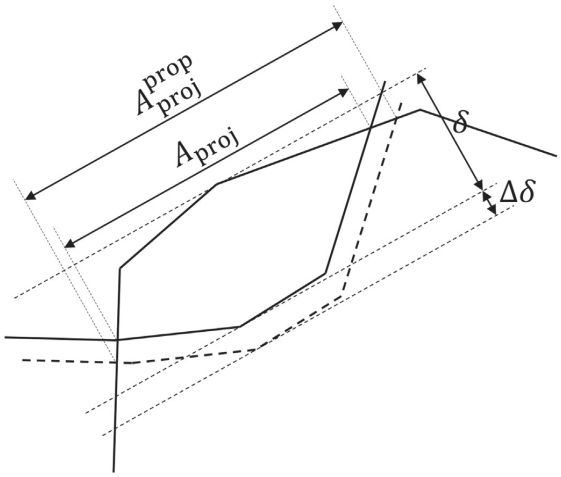

Fig. 6. Projected contact area and propagated projected contact area.

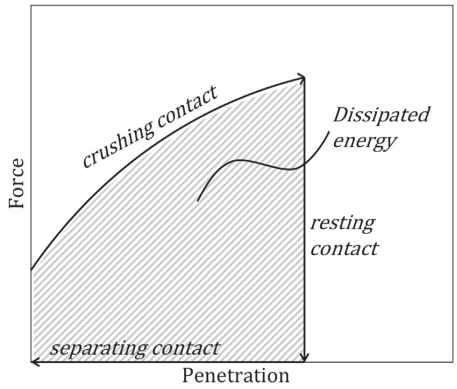

Fig. 7. Contact crushing implementation as hysteretic damping.

- *crushing contact* The contact force needed to prevent further penetration is higher than the bearing capacity of the current contact area. Ice crushes and body penetration increases.
- *resting contact* The contact force needed to prevent further penetration is lower than the bearing capacity of the current contact area. Penetration remains the same, and the contact force is calculated such that the contact relative velocity in the contact normal direction remains zero.
- *separating contact* Due to external forces or forces at other contacts, the relative contact velocity is negative (the contact separates). This results in decreasing penetration, and the contact force drops to zero.

The type of discontinuous contact behaviour is not determined at the beginning of the time step; it is an outcome of the MLCP, and its implementation in the time-stepping scheme is explained in Section 2.

Since we assume that all available kinetic energy is dissipated by local crushing, this discontinuous contact algorithm results in a contact restitution of zero in the case of non-deformable floes. When floes are modelled using a lattice model or other material model, some of the available kinetic energy will be transformed to potential energy in the form of elastic deformation in the ice floe. This potential energy can be recovered to give some restitution > 0.

In time steps in which contact is initiated and in time steps in which contact crushing stops, the assumed continuity of the time-stepping scheme longer holds, causing a numerical error. This error is reduced by treating the contact somewhat differently in these cases. This is explained in Sections 4.1 and 4.2.

4.1. Discontinuous contact treatment when contact is initiated

The assumption of constant average acceleration as made in the time-stepping scheme is not valid in a time step in which the contact is initiated. Therefore, a numerical error is introduced in this time step. In practice, this means that the contacting bodies will overlap less than they should at the end of such a time step, reducing the amount of overlap volume, which is assumed to be crushed. This leads to the following energy imbalance:

$$E_{\text{kin}}^{\text{dissip}} > \Delta V_{\text{overlap}} \cdot \text{CSE} \tag{43}$$

in which $\Delta V_{\text{overlap}}$ is the change of overlap volume of two contacting bodies and $E_{\text{kin}}^{\text{dissip}}$ is the dissipated kinetic energy. We find that this error can be minimized by calculating the $\frac{\Delta F}{\Delta \delta}$ value for this time step as:

$$\frac{\Delta F}{\Delta \delta} = \frac{\delta_{\text{prop}}}{\dot{u}_{\text{cont}} \Delta t} \frac{A_{\text{proj}}^{\text{prop}} \cdot \text{CSE}}{\dot{u}_{\text{cont}} \Delta t} \tag{44}$$

in which δ_{prop} is the contact penetration after the contacting bodies are propagated with their current velocity, and $\dot{u}_{\text{cont}}$ is the relative contact velocity at the beginning of the time step. This effectively reduces the gradient $\frac{\Delta F}{\Delta \delta}$, causing a lower dissipated kinetic energy and a higher overlap volume at the end of the time step.

4.2. Discontinuous contact treatment when crushing stops

In a time step in which crushing stops, the contact will penetrate further than it should because the constant average acceleration assumption is not valid. This causes the following energy imbalance:

$$E_{\text{kin}}^{\text{dissip}} < \Delta V_{\text{overlap}} \cdot \text{CSE} \tag{45}$$

A positional error will be introduced in the contacting bodies, causing too much penetration. This is most problematic when one wants to determine the peak force during a time step, for instance, to determine whether or not a threshold value is reached such as for the initiation of splitting or bending failure of an ice floe. Usually, the force-time curve during such a time step will look similar to Fig. 8.

The F_{peak} force is the exact peak force we want to extract from our numerical results. There are several ways of computing the peak force:

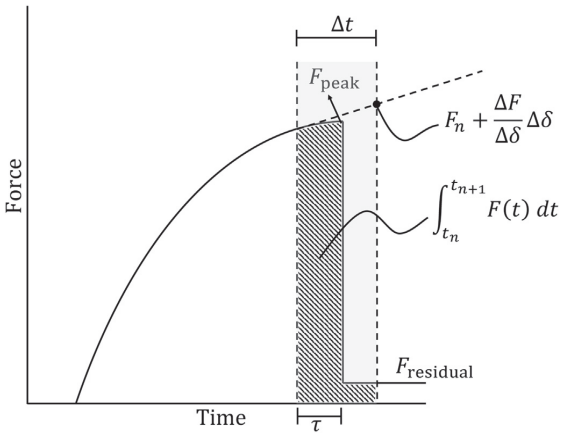

Fig. 8. Peak force determination in time steps where crushing stops.

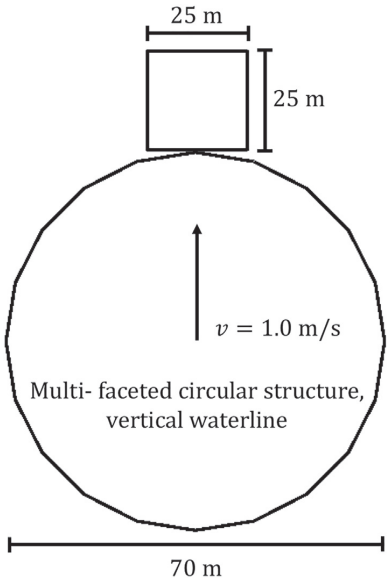

Fig. 9. Contact implementation comparison case, overview.

- Assume the force is constant during the time step, and approximate the peak force as:

$$F_{\text{peak}} \approx \frac{\int_{t_n}^{t_{n+1}} F(t)dt}{\Delta t} \tag{46}$$

- Another option is to use the initial contact force and the change in penetration to approximate the peak force:

$$F_{\text{peak}} \approx F_n + \frac{\Delta F}{\Delta \delta}\Delta\delta \tag{47}$$

Both methods will introduce an error, as demonstrated in Fig. 8. This error can be reduced to a minimum by considering the difference between an unconstrained impulse and the impulse resulting in zero restitution:

$$\frac{\tau}{\Delta t} = \frac{\lambda_{\text{cont}}}{\lambda_{\text{cont}} + \frac{v_{\text{cor}}}{\frac{1}{m} + \Sigma_{\text{cr}}}}$$

$$F_{\text{cont}}^{\text{peak}} = F_{\text{cont}}^{n} + \frac{\tau}{\Delta t}\frac{\Delta F}{\Delta \delta}\Delta\delta \tag{48}$$

in which τ is a measure for the moment within the time step where the peak force occurs, as visualized in Fig. 8. Using this approximation of the peak force, we find we can get an accurate peak force prediction even for large time steps, provided that the contact force does not increase step-wise. A step-wise increase may occur if the initial contact area between bodies (penetration $\delta_C = 0$) is higher than zero. In practice, this rarely occurs.

The next section compares the accuracy of our new time-stepping scheme to an existing method for discontinuous contacts.

5. Accuracy comparison to an existing algorithm

We compare the numerical accuracy of the proposed time-stepping scheme against a time-stepping scheme that only considers the current contact area for discontinuous contacts. We use the error percentage of the peak force as predicted by both numerical methods as a measure for the method accuracy. The peak force is chosen as a measure of accuracy because this is often one of the main parameters of interest in ice-structure interaction scenarios. The error percentage is calculated as:

$$e = \frac{F_{\text{peak}}^{\text{analytical}} - F_{\text{peak}}^{\text{numerical}}}{F_{\text{peak}}^{\text{analytical}}} \cdot 100 \tag{49}$$

The time -tepping scheme presented in this paper is referred to as *force gradient method* in the remainder of this section. The existing time-stepping scheme that only takes the current contact area into account is referred to as the *limit force method*. The limit force method is applied in, among others, Metrikin (2014). Note that there are further differences between the contact model as applied in Metrikin (2014) and the contact model as applied in the current paper. Therefore the accuracy comparison between both methods only applies to the used time-stepping scheme, and not directly to the predicted loads. For instance, Metrikin (2014) introduces randomness in the contact algorithm, making a direct load comparison irrelevant.

The time-stepping schemes are compared for two cases: one in which the contact force increases linearly with penetration and one in which the contact force jumps to an initial value as soon as contact is initiated, after which it has a limited further increase with penetration. These cases can both be linked to a physical situation in which a multi-faceted circular structure is in contact with an ice floe. Both situations are sketched in Figs. 9 and 10.

We choose a simple case for the accuracy comparison because it is not straightforward to define a good error measure in more complicated scenarios. Because of the non-linear nature of discrete element simulations, the results are often highly sensitive to initial conditions or changes in the solution procedure. As a consequence, the results will inevitably diverge after a number of discrete interactions. Therefore, model accuracy and validity in more complicated scenarios can only be assessed by comparing the statistical properties of the outcomes, and since the 'correct' solution is not necessarily known in a more complicated case, it would be difficult to determine which method gives the most accurate solution. The parameters of the example case are listed in

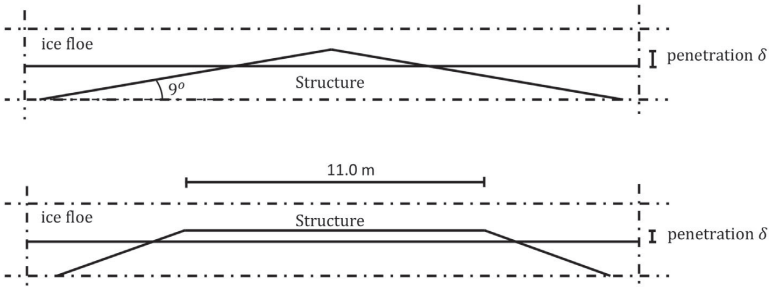

Fig. 10. Contact implementation comparison case, detail. The upper figure shows the linearly increasing contact force situation and the lower figure shows the situation in which there is an initial jump in the contact force.

Table 1
Parameters used in accuracy comparison.

Ice thickness (m)	1.0
CSE (MJ/m^2)	2.0
Diameter of structure (m)	70.0
Mass of structure (kg)	$28 \cdot 10^6$
Mass of ice floe (kg)	$5.69 \cdot 10^5$
Initial velocity difference (m/s)	1.0

Table 1.

For this test case, the exact force-time curves, using the assumption of constant energy absorption per crushed volume, will look like the curves shown in Figs. 11 and 12.

The force gradient and the limit force methods both formulate a different MLCP to solve for the contact impulse (or equivalent average contact force) at each time step. The MLCP of the force gradient method is equal to the formulation presented Eq. (24). The formulation using the limit force method is equal to the formulation presented in Eq. (29), in which F_{lim} is calculated using the contact projected area and the crushing pressure and the restitution coefficient $\gamma_{\text{rf}} = 0$.

Figs. 13 and 14 show an accuracy comparison of the limit force method against the force gradient method for a linearly increasing contact force and an initial jump in the contact force, respectively. In the case of a linearly increasing contact force, the error in the peak force in the force gradient method scales proportional to Δt^4. This shows that second-order accuracy is maintained in the case of a constant force-penetration gradient, even when the discontinuities at contact initiation and at the end of contact crushing are included. The error in peak force using the limit force method scales proportional to

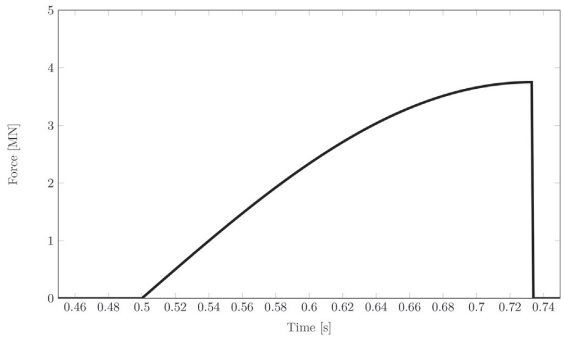

Fig. 11. Exact force-time curve in the case of a contact force that increases linearly with penetration.

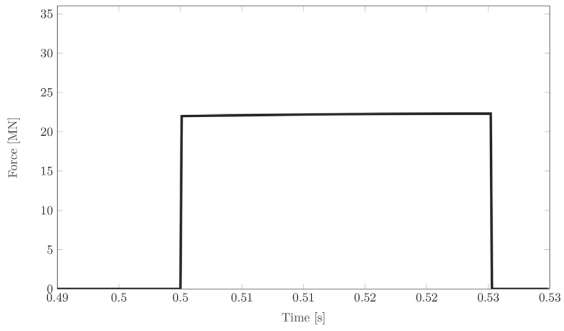

Fig. 12. Exact force-time curve in the case of initial non-zero contact area.

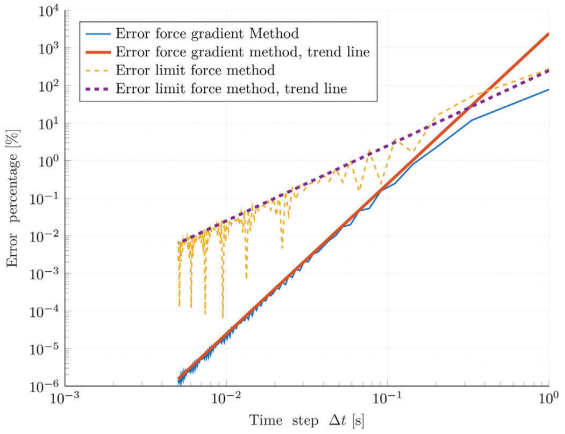

Fig. 13. Error in peak force prediction, contact force increasing linear with penetration.

Δt^2, which is consistent with the first-order accuracy of the limit force method. Over the complete range of tested time-step sizes, the force gradient method gives a more accurate prediction of the occurring peak force than the limit force method for a linear increase in contact force with penetration.

A generalized analytical expression for the numerical error in the peak force predicted by both methods can be found by considering the duration of the contact resolution relative to the time step size. In the case of a constant gradient $\frac{\Delta F}{\Delta \delta}$, and assuming there are no external forces or other contacts influencing the interacting bodies, the crushing duration can be calculated as:

$$T = \frac{\frac{1}{2}\pi}{\sqrt{\frac{\frac{\Delta F}{\Delta \delta}}{m_{\text{eff}}}}} \tag{50}$$

in which T is the time duration from contact initiation until the end of the crushing phase. In this example case, the effective mass of the contact m_{eff} (in contact normal direction) is equal to:

$$m_{\text{eff}} = \frac{1}{\frac{1}{m_{\text{struc}}} + \frac{1}{m_{\text{ice}}}} \tag{51}$$

The effective mass of the contact is a measure of the impulse that is

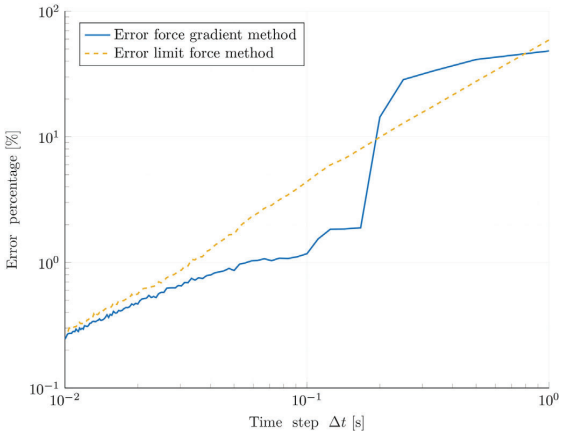

Fig. 14. Error in peak force prediction, initial jump in contact force.

needed to change the relative contact velocity. The numerical error percentage is then a factor of the time step size relative to the crushing duration:

$$e_{\mathrm{fg}} = C_1\left(\frac{\Delta t}{T}\right)^4$$
$$e_{\mathrm{lf}} = C_2\left(\frac{\Delta t}{T}\right)^2 \tag{52}$$

in which e_{fg} is the numerical error percentage of the peak force predicted by the force gradient method and e_{lf} is the numerical error percentage in the peak force predicted by the limit force method. C_1 and C_2 are constants that need to be determined from our calculation example.

We found the following expressions for the error percentage by fitting to the outcome of the calculation example:

$$e_{fg} = 1.18\Delta t^4\left(\frac{\frac{\Delta F}{\Delta \delta}}{m_{eff}}\right)^2$$
$$e_{lf} = 5.5\Delta t^2\frac{\frac{\Delta F}{\Delta \delta}}{m_{eff}} \tag{53}$$

Note that this error definition is independent from the the interaction velocity. It only depends on the time needed to resolve the contact, T, relative to the time-step size, Δt.

In the case of an initial jump in the force-time curve, as is the case when the contact area at zero penetration is non-zero, the accuracy of both methods is comparable, as shown in Fig. 14. This is in accordance with expectation, since the higher order of the force gradient method degenerates in this case, giving results comparable to the limit force method. A generalized analytical approximation of the error percentage is more difficult to define in this case, since it depends on the ratio between the initial crushing threshold and the linearly increasing component of the contact force as well as on the ratio between both force components and the contact effective mass.

6. Application example: comparison to ice tank test data

Numerical results from the proposed time-stepping scheme and the discontinuous contact model are compared to ice tank test results for a 4-legged, vertical-walled structure moving through broken ice with an areal coverage of 60%. The ice tank tests were performed in 2012 at the Hamburg Ship Model Basin (HSVA) as part of the European Community's HYDRALAB-IV project. More details can be found in Hoving et al. (2013). We chose a comparison case in which ice failure did not have a major influence on the results for the majority of the experiment, since ice failure modelling is not part of the current paper.

The experimental parameters of the ice tank test are shown in Table 2. The towing velocity was changed during the experiment, from the lower value in Table 2 for the first 1/3 of the tank, to the higher value for the other 2/3, resulting in an equal test duration at the lower and at the higher velocity. The loads on the structure were measured on each leg separately and the load on the complete structure was measured using a separate measuring device. The back wall of the tank is upward-sloping under a 30° angle, to allow ice floes to raft and reduce the effect of confinement.

Table 2
Measured experimental parameters.

Ice thickness (mean value)(m)	0.035
Ice areal coverage (as reported)	6/10th
Compressive strength (kPa)	57.7
Carriage velocity (m/s)	0.09–0.18
Tank width (m)	10
Tank length (as used in experiments) (m)	57

The time-stepping scheme as described in Section 2 and the discontinuous contact model as described in Section 4 are used in this application example. Lattice modelling is not applied in this example, because we do not predict it to have a noticeable effect on the accuracy of the final results. In addition to the presented time-stepping scheme and contact model, a hydrodynamic model is needed to obtain numerical results that can be compared to the experimental data. Buoyancy and hydrodynamic damping in the form of form drag and skin friction are included as external forces. The form drag and skin friction are calculated as described in Tsarau (2015).

The ice tank floe field was replicated by the numerical processing of the top view photos of the actual ice field. The following steps were taken in the image processing procedure:

1. Top view photos are stitched together using Image Composite Editor (*Image Composite Editor 2.0* (2017)).
2. The image is converted to monochrome black and white using GIMP 2 (*GIMP 2.8.22* (2017)).
3. Some distortion is removed using the *Cage Transform* tool in GIMP 2.
4. The tank walls are removed from the image using the *Intelligent Scissors* tool in GIMP 2, to prevent the tank walls from being recognized as ice floes.
5. Ice floes are detected using the GVF snake algorithm as described in Zhang and Skjetne (2015).
6. Convex ice floe polygons are created from the ice floe pixels using the *convexhull* algorithm in MATLAB.
7. The geometry of large ice floes (area $> 0.5\,\mathrm{m}^2$) is approximated by a similar-sized rectangle, in order to better represent the observed ice floe shapes.

A top view of the actual and numerical floe fields is shown in Fig. 15. The waterline geometry of the structure is shown in Fig. 16.

The areal coverage of the numerical floe field that was produced using image processing is similar to the reported coverage of 60% at 62.9%. The tank walls and the slope at the far end of the tank were included in the numerical model.

Some input parameters that are needed in the numerical model were not measured during the ice tank tests. These parameters are estimated based on reported values in other experiments and based on engineering judgement. The most important parameters not measured during the tests are the friction coefficients, the CSE value, and the hydrodynamic skin friction and form drag coefficients.

The skin friction and form drag coefficients are taken from measured values in full scale as reported by Tsarau et al. (2017). The CSE value is chosen based on the assumption that during crushing, the average crushing pressure is half the maximum crushing pressure, taking the maximum crushing pressure as reported in Table 2. The friction coefficients were chosen similar to Haase et al. (2010). Table 3 lists the used experimental parameters.

The loads on all four legs in the x and y directions from the numerical simulation are compared against the loads on the legs as measured in the tests in Figs. 17 and 18. From 0 to 200 s the structure moves at a velocity of 0.09 m/s, and from 200 to 400 s the structure moves at a velocity of 0.18 m/s. In comparing the data, we should note that the results are significantly influenced by specific events within the simulation. For instance, whether jamming of floes between the legs occurs or not can significantly influence the results for a major portion of the resulting signal. From a qualitative comparison of the measured data and the numerical results, we observe the following:

- Similar to the measured data, the numerically predicted ice load increases in the second half of the test. The increase in load corresponds to the increase in towing velocity.
- The loads as predicted by the numerical model are of the same order of magnitude as the measured experimental loads.
- Jamming of ice floes between the two front legs is observed both in

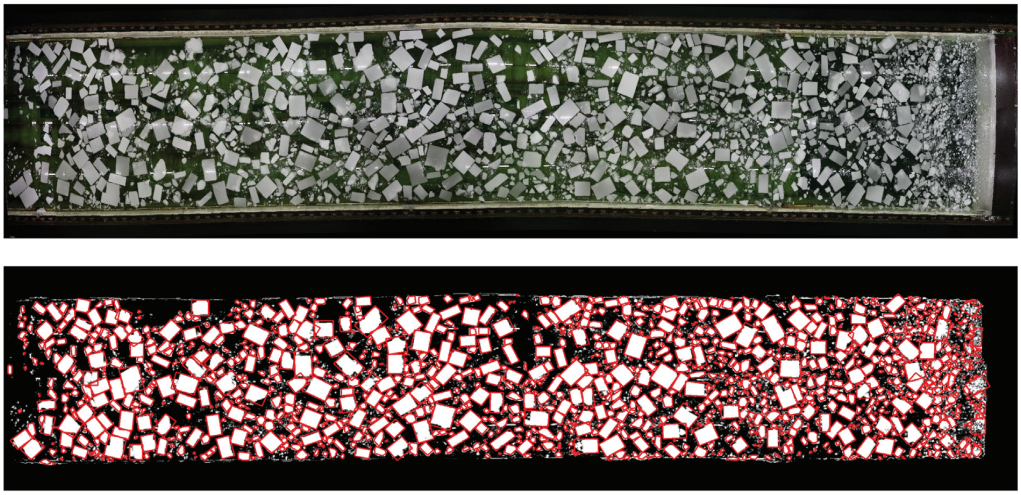

Fig. 15. Ice tank floe field stitched top view image (top) and processed floe field (bottom). Structure moves from left to right.

the numerical simulation as well as in the tests. Figs. 19 and 20 show a snapshot of the jamming events.

- The directionality of the ice loads in the numerical simulation is similar to the directionality of the ice loads in the experiment.
- Sheltering of leg 4 is apparent both in the experimental as well as in the numerical results

A statistical comparison between the measured loads and the simulated loads is not appropriate in this case because the loads are influenced too much by specific events within the simulation, and the measured load signal is too short to say anything significant about the statistical properties of the signal.

In general, we conclude that the loads predicted by the numerical simulation are of the same order of magnitude as the measured results.

Table 3
Parameters used in numerical simulation.

Ice thickness (m)	0.0346
Ice-ice friction coefficient (−)	0.12
Ice-structure friction coefficient (−)	0.12
Ice areal coverage (based on image analysis) (%)	62.9
CSE (kJ/m^3)	29
Carriage velocity (m/s)	0.09–0.18
Skin friction drag coefficient (−)	0.005
Form drag coefficient (−)	0.5
Water density (kg/m^3)	1005
Ice density (kg/m^3)	900
Gravity acceleration (m/s^2)	9.81

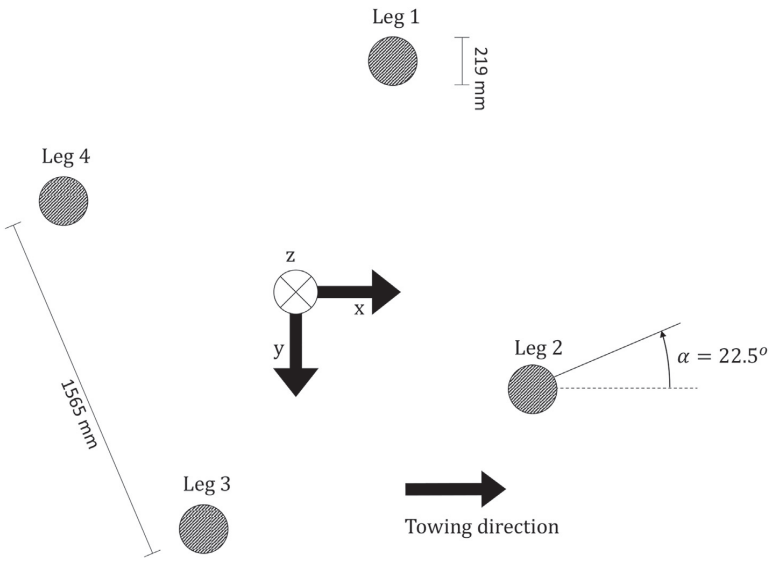

Fig. 16. Waterline geometry of the test structure.

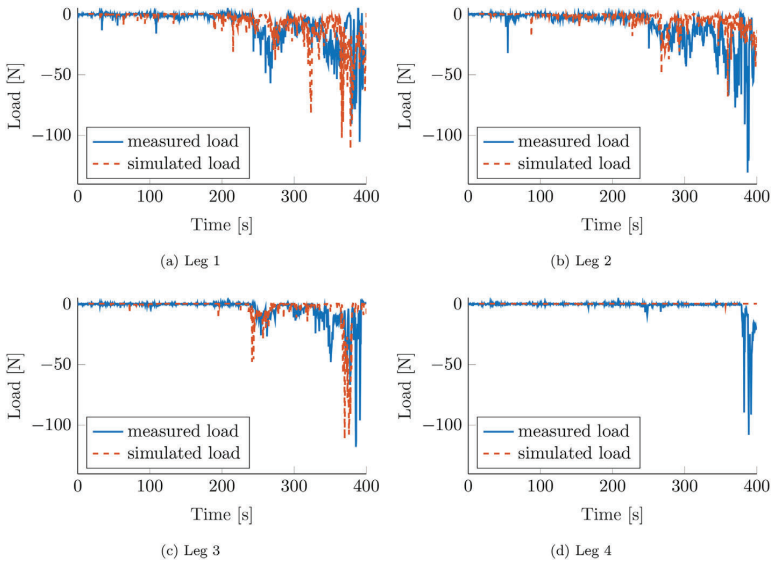

(a) Leg 1 (b) Leg 2

(c) Leg 3 (d) Leg 4

Fig. 17. Numerical results compared to experimental results: loads in x-direction.

7. Discussion

The discussion section is divided into three parts. First, we discuss the time-stepping scheme, then we discuss the discontinuous contact model, and lastly, we discuss the application example.

7.1. Time-stepping scheme

We derive a time-stepping scheme based on the second-order Newmark-Beta method. As mentioned in the introduction, other models introducing contact compliance in an NDEM scheme often derive the compliance parameters based on first-order methods, such as the implicit Euler scheme. One may wonder why a higher-order method is not used by others.

A possible reason for the use of lower-order methods in other fields of application is that a higher-order method will not lead to more accurate results in discrete modelling of many materials other than ice. Referring to the accuracy comparison in Section 5, we see that as the time step Δt increases compared to the period needed for contact resolution T, the accuracy gained by using a higher-order method diminishes. In many application areas, individual contacts are resolved within one time step due to a combination of particle size, contact stiffness and the relatively large time steps (compared to explicit DEM modelling) that are used in NDEM. Therefore, a higher-order method

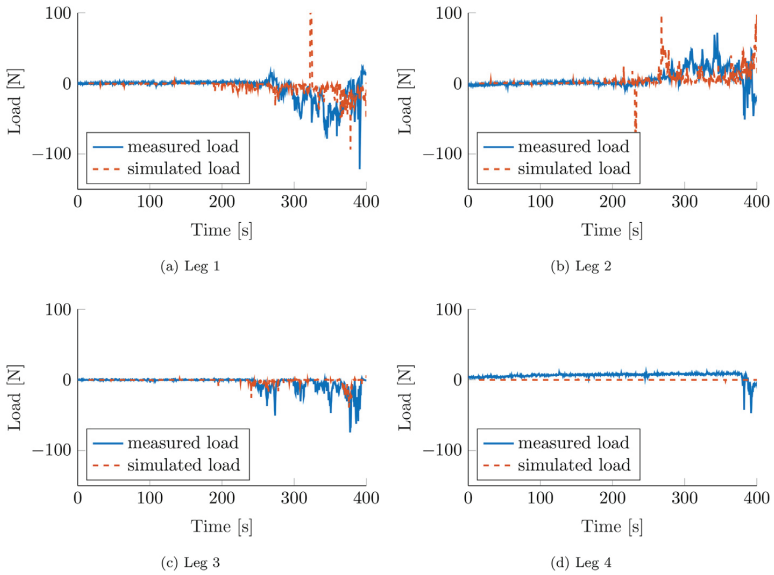

(a) Leg 1 (b) Leg 2

(c) Leg 3 (d) Leg 4

Fig. 18. Numerical results compared to experimental results: load in y-direction.

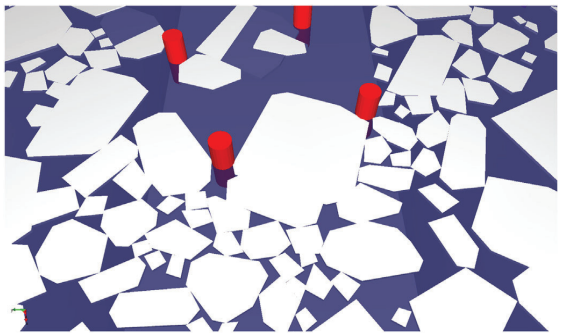

Fig. 19. Jamming of an ice floe between the two front legs in the simulation.

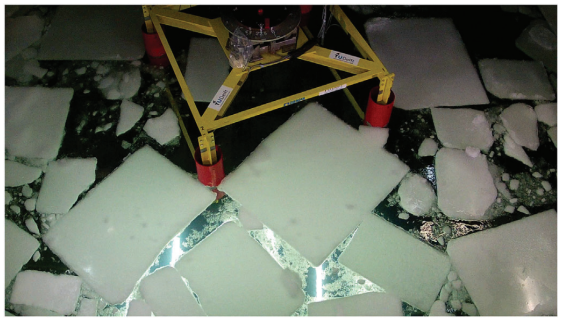

Fig. 20. Jamming of an ice floe between the two front legs in the experiment.

will not lead to more accurate contact force predictions. In ice-structure interaction, on the other hand, the build-up of contact forces often takes place over multiple time steps. This is especially true for contacts between larger ice floes and a structure, where local crushing often occurs before other failure modes might occur. The higher-order method is more accurate for these types of contacts, while its accuracy is similar to the accuracy of lower-order methods in the case of more stiff contacts.

7.2. Ice-ice and ice-structure contact model (discontinuous contacts)

The presented discontinuous contact model is based on the assumption of constant CSE, which is equivalent to a constant crushing pressure. This assumption has a limited validity. Other contact models assume a crushing pressure that is dependent on the contact area (pressure-area relationship). We acknowledge that the assumption of constant CSE is a simplification of reality. Whether the crushing pressure is related to the contact area or not, it will certainly fluctuate over time, even within very short time scales, due to the mechanical processes in the ice such as spalling events. However, a more detailed crushing model would not fit within the computational framework of this paper and is better suited for detailed simulations of a single contact with a structure.

As explained in Section 4, the assumption of constant crushing specific energy, or a constant crushing pressure, is not new in itself. Similar assumptions have been used in other studies. The novelty of our contact algorithm is how the assumption of constant CSE is subsequently used to derive the contact parameters as needed for the time-stepping scheme.

7.3. Application example results

The comparison of discrete element simulation results to experimental data is not straightforward. The numerical simulation results are strongly dependent on the initial conditions: a minor change in initial ice floe positions may lead to completely different results later in the simulation. Similarly, a minor change in the model input parameters may also lead to different results. This is similar to what is observed in Ranta and Tuhkuri (2017). Due to the strong dependence of the results on the initial conditions and the input parameters, a direct match between the numerical and experimental results should not be expected. Moreover, measurement and processing errors in the experimental data give another source of discrepancy. Some factors that may cause additional discrepancies between the experimental and numerical data are further discussed below.

- Capturing the floe field. From the comparison of the experiment recordings and the top view photos of the floe field, we observe that the floe field at the moment the experiment is started is actually a bit different from the floe field in the top view images. Probably, the floe field was not completely static at the moment that the photos were taken. In Fig. 21, the initial position of a group of floes from the experiment recordings is compared to the initial position of the same group of floes as captured in the top view photo.One can clearly recognize the same floes in the experiment recording and the top view photo, and see that the floe positions are significantly different.
- Digitizing the floe field. The digitization process of top view images is not perfect. Discrepancies between the observed and digitized floe fields occur regularly. These are mostly related to distinguishing separate ice floes. Sometimes, two floes are digitized as one floe, or one floe is digitized as several floes. Examples are given in Fig. 22. Similar errors occur in about 10% of the discretized floes.
- Uncertainty in model input parameters. Some parameters, which are required as inputs for the numerical model were not measured directly during the experiments. Most importantly, the ice-ice and ice-structure friction coefficients, the crushing specific energy during crushing and the form and skin friction drag coefficients were not measured during the experiments but can have a significant influence on the numerical model outcome. Because of the high

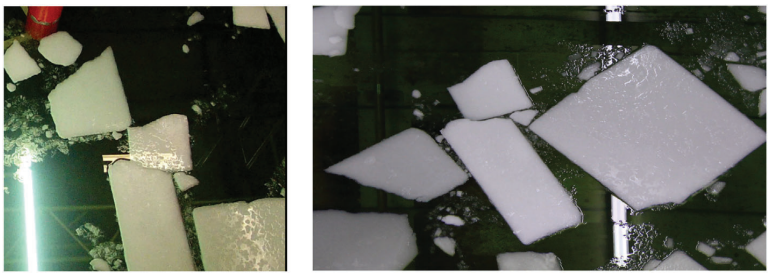

Fig. 21. Floe positions in experiment recording, start of experiment (left) compared to top view photo of floe field (right).

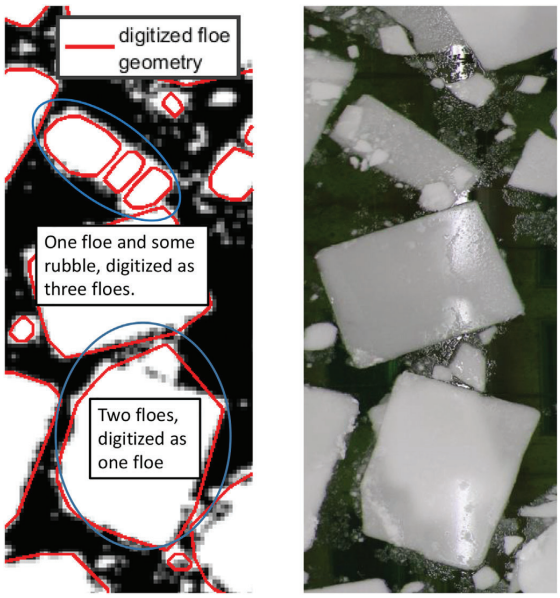

Fig. 22. Discretization (left) compared to actual floe field (right).

sensitivity of the results to input parameters, a minor change in input parameters will lead to completely different results later in the simulation, and the only proper way to assess input parameter influence would be to study the influence on the statistical properties of the results. However, the duration of the experiments is too short to assess the statistical properties of occuring ice loads. Therefore, an assessment of statistical properties would require running a high number of simulations for each set of input parameters, similar to the analysis done in Ranta et al. (2018). Such an analysis is not performed in the current paper, since this paper mainly focusses on the introduction of a novel time-stepping scheme and contact model, and the experimental comparison is merely introduced as an application example. A more detailed analysis of the model parameter influence on the results will be provided in future work.

- Neglection of splitting failure. Near the end of the ice tank test, it appears that the ice is more confined by the walls and the end of the tank, and several splitting failure events occurred in the experiment. This splitting failure is not captured in the presented numerical model. Based on this, one may expect that the numerical simulation would give higher loads near the end of the simulation. However, this is not apparent in the presented simulation results. We attribute this to other, largely random processes that are inherently different in the numerical simulation compared to the physical experiments. In the numerical simulation, it appears that the accumulation of ice that forms in front of the structure clears right before the end of the tank is reached, while this in not the case in the physical experiments.

8. Conclusions

Numerical modelling can help to increase the understanding of the processes occurring during ice-structure interactions. The presented implicit DEM time-stepping scheme expands the previously applied NDEM modelling framework to allow for compliant contact behaviour. This enables modelling of continuous compliant contacts, as would occur in a lattice representation of ice, as well as modelling of discontinuous ice-ice and ice-structure contacts. The discontinuous contact model formulates contact parameters based on the assumption that ice crushing will occur when a crushing pressure is exceeded, using the exact contact geometry and expected change of contact geometry. To the authors' knowledge, this is the first time such a time-stepping scheme is applied to ice-structure interaction scenarios. The time-stepping scheme presented in this paper enables accurate large time step simulations, which may lead to increased numerical efficiency in a range of cases. Comparison with ice tank test data shows that the new time-stepping scheme and discontinuous contact model manages to capture some important phenomena that were also observed in ice tank tests. It predicts well the sheltering effects, directionality, and order of magnitude of ice loads on a 4-legged, vertical-walled structure in ice tank tests.

Referring to the factors mentioned in the introduction that make ice-structure interaction modelling challenging, the presented model addresses the first two points, one directly and the other indirectly. Regarding the first mentioned factor, the modelling of many simultaneously interacting bodies, the presented time stepping scheme enables more accurate numerical simulations, which enables possible efficiency improvements by using a larger time-step size. The second factor, complicated body geometries, is partly alleviated as a result of the higher numerical efficiency. The efficiency gains can be used to implement more accurate geometrical representations of actual ice floes.

Further development of the presented time-stepping scheme and contact model will mainly focus on the inclusion of ice failure. Ice failure may be included in several ways:

- *Combination with a lattice model.* As shortly discussed in this paper, the presented time-stepping scheme is well suited for the modelling of dynamic lattices in combination with discontinuous ice-ice and ice structure contacts. The combined latttice-NDEM model will be further developed and validated, mainly focussing on accurate fracture behaviour of the ice lattice.
- *Combination with analytical ice failure calculations.* Using the contact forces resulting from the contact model and time-stepping scheme, analytical approximations can be used to represent ice failure behaviour. A comprehensive set of analytical solutions for ice fracture have been developed in Lu et al. (2015*a*,b, 2016). Combinations of NDEM models with analytical ice failure have been published earlier by Lubbad and Løset (2011) and Metrikin (2014), and lead to efficient numerical simulations.

The authors intend to compare the model results to more challenging model scale and full scale experimental results for further validation of the model. These will include the following cases:

- Higher-concentration broken ice fields.
- Tests in which ice failure plays a significant role, both bending and splitting failure.
- A comparison with experimental results of ice ridge-structure interaction, using the presented time-stepping scheme in combination with a lattice material model representing the consolidated part of the ice ridge.

One of the envisioned usages of the model is for pre-testing of concept structures and configurations. This testing stage before real-life ice tank tests are commenced can help designers to narrow down the range of to be tested ice conditions to the most challenging ones, and reduce the needed amount of ice tank testing. This can lead to a more efficient design cycle, and to more efficient and robust designs.

Acknowledgements

The authors would like to acknowledge the support of the SAMCoT CRI through the Research Council of Norway and all of the SAMCoT Partners.

Appendix A. Clarification of MLCP behaviour

This appendix will demonstrate that the used MLCP will satisfy the assumptions made for ice-ice or ice-structure contacts. Consider the 1-DOF MLCP statement as given in Section 2.2:

$$\begin{bmatrix} m & 1 & 0 \\ -1 & \Sigma & 1 \\ 1 & \Sigma & 1 \end{bmatrix} \begin{bmatrix} \Delta \dot{u}_{\text{cont}} \\ \lambda_{\text{cont}} \\ v_{\text{cor}} \end{bmatrix} + \begin{bmatrix} 0 \\ -\text{Y}_{\text{cr}} \\ -\frac{F_{\text{cr}}}{\frac{1}{4}\frac{\Delta F_{\text{cr}}}{\Delta \delta}\Delta t} \end{bmatrix} = \begin{bmatrix} 0 \\ \alpha_{\text{r}} \\ \beta_{\text{r}} \end{bmatrix}$$

$$0 \leq [\lambda_{\text{cont}} \quad v_{\text{cor}}]^T \perp [\alpha_{\text{r}} \quad \beta_{\text{r}}]^T \geq 0 \tag{A1}$$

For which the parameters are explained in Sections 2.1 and 2.2. This MLCP can be rewritten in the following form:

$$\frac{\lambda_{\text{cont}}}{m} + \Sigma\lambda_{\text{cont}} + v_{\text{cor}} - X - Y = \alpha_{\text{r}} \quad 0 \leq \alpha_{\text{r}} \perp \lambda_{\text{cont}} \geq 0 \tag{A2}$$

$$-\frac{\lambda_{\text{cont}}}{m} + \Sigma\lambda_{\text{cont}} + v_{\text{cor}} - X = \beta_{\text{r}} \quad 0 \leq \beta_{\text{r}} \perp v_{\text{cor}} \geq 0 \tag{A3}$$

in which, for crushing contacts:

$$X = \frac{F_{\text{cr}}}{\frac{1}{4}\frac{\Delta F_{\text{cr}}}{\Delta \delta}\Delta t}$$
$$Y = 2\left(\dot{u}_n + \frac{1}{2}F_{\text{ext}}m^{-1}\Delta t\right) \tag{A4}$$

Under the assumption that:

$$\frac{\Delta F_{\text{cr}}}{\Delta \delta} \geq 0$$
$$F_{\text{cr}} = 0 \quad \text{if} \quad \delta \leq 0$$
$$\Sigma \geq 0 \tag{A5}$$

this MLCP full describes the desired contact behaviour. It enforces the limits to the contact impulse as stated in Eqs. (22) and (23). To clarify the problem statement, we distinguish two cases:

- Negative contact velocity: $X \geq 0$ and $Y \leq 0$
- Positive contact velocity: $X \geq 0$ and $Y > 0$

We consider all solution options for both cases, and show that there is only one correct solution in each case.
In the case of a negative contact velocity, we first assume that $v_{\text{cor}} > 0$. Using Eq. (A3) and Conditions expressed in Eq. (A5), this results in:

$$v_{\text{cor}} = \frac{\lambda_{\text{cont}}}{m} - \Sigma\lambda_{\text{cont}} + X \tag{A6}$$

Substituting A6 in Eq. (A2), we obtain:

$$2\frac{\lambda_{\text{cont}}}{m} - Y = \alpha_{\text{r}} \quad 0 \leq \alpha_{\text{r}} \perp \lambda_{\text{cont}} \geq 0 \tag{A7}$$

Since Y in this case is ≤ 0, $\lambda_{\text{cont}} = 0$ in order to satisfy the condition, resulting in $v_{\text{cor}} = X$.
If we assume that $v_{\text{cor}} = 0$, we find that $\lambda_{\text{cont}} = 0$ since, if $\lambda_{\text{cont}} > 0$, in order to satisfy Eq. (A2):

$$\lambda_{\text{cont}} = \frac{X + Y}{\frac{1}{m} + \Sigma} \tag{A8}$$

substituting Eq. (A8) in Eq. (A3), we obtain:

$$\frac{-\frac{1}{m} + \Sigma}{\frac{1}{m} + \Sigma}(X + Y) - X \geq 0 \tag{A9}$$

Eqs. (A8) and (A9) cannot be satisfied simultaneously because $Y > 0$, and $X \geq -Y$, following from Eq. (A8). Thus, the only possible solution in the case of a negative contact velocity $Y > 0$, is $\lambda_{\text{cont}} = 0$ and $v_{\text{cor}} = X$.

In the case of a positive contact velocity, we follow the same procedure as for a negative contact velocity. If we assume that $v_{\text{cor}} > 0$, and use Eq. (A3) and the conditions expressed in Eq. (A5), we again obtain:

$$v_{\text{cor}} = \frac{\lambda_{\text{cont}}}{m} - \Sigma\lambda_{\text{cont}} + X \tag{A10}$$

Substituting this in Eq. (A2), we obtain:

$$2\frac{\lambda_{\text{cont}}}{m} - Y = \alpha_{\text{r}} \quad 0 \leq \alpha_{\text{r}} \perp \lambda_{\text{cont}} \geq 0 \tag{A11}$$

resulting in:

$$\lambda_{\text{cont}} = m\frac{Y}{2} \rightarrow \lambda_{\text{cont}} = m\left(\dot{u}_n + \frac{1}{2}F_{\text{ext}}m^{-1}\Delta t\right) \tag{A12}$$

This is the impulse resulting in zero restitution. The correctional velocity becomes:

$$v_{\text{cor}} = \frac{1-\Sigma m}{2}Y + X \tag{A13}$$

If $v_{\text{cor}} = 0$ it follows from Eq. (A2) that:

$$\lambda_{\text{cont}} = \frac{X+Y}{\frac{1}{m}+\Sigma} \tag{A14}$$

This is the impulse that results if there is continuous crushing at a contact. Substituting this in Eq. (A3) gives:

$$\frac{-\frac{1}{m}+\Sigma}{\frac{1}{m}+\Sigma}(X+Y) - X \geq 0 \tag{A15}$$

If this condition is met, there is continuous crushing. Otherwise the contact impulse is calculated such that the zero restitution requirement is enforced, or the contact velocity is negative, resulting in a zero contact impulse.

This shows that there is a unique solution to the MLCP for a contact that satisfies the conditions expressed in Eq. (A5). Fig. A23 gives an overview of the possible solutions.

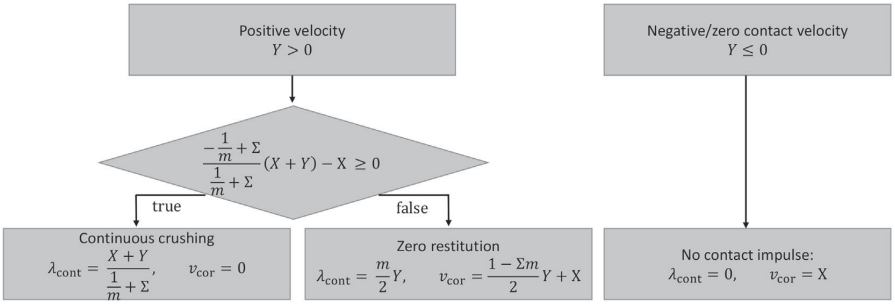

Fig. A23. Solution diagram of MLCP.

Appendix B. Multiple degrees of freedom, rotation and friction

In this section we derive the MLCP for the general case in which a 3-D ice body interacts with a fixed plane. The body has 6 DOF, three translational and three rotational. In addition to the derivation in Section 2, three new concepts are introduced: The contact Jacobian, the addition of Gyroscopic forces and frictional contact constraints.

We define a body fixed coordinate system such that its origin is at the body centre of gravity (COG), and the axes coincide with the principal axes of rotation, making the body inertia tensor diagonal. We define a mass matrix for the body in Eq. (B1), which represents the body's inertial properties in the body fixed coordinate system:

$$\mathbf{M} = \begin{bmatrix} m & 0 & 0 & 0 & 0 & 0 \\ 0 & m & 0 & 0 & 0 & 0 \\ 0 & 0 & m & 0 & 0 & 0 \\ 0 & 0 & 0 & I_{xx} & 0 & 0 \\ 0 & 0 & 0 & 0 & I_{yy} & 0 \\ 0 & 0 & 0 & 0 & 0 & I_{zz} \end{bmatrix} \tag{B1}$$

The basis of the body fixed coordinate system is described by the 3×3 matrix B_{b}, in which the columns of B_{b} are unit length vectors describing the axis directions defined according to a right-handed coordinate system and the COG of the body is described in a global coordinate system by the vector o_{b}. The basis of the contact coordinate system is described by the 3×3 matrix B_{c}, and the contact 'point' is described in global coordinates by vector o_{c}. The determination of the contact point is further explained in Section 4. The axes of the contact coordinate system coincide with the contact normal direction and two perpendicular frictional directions, one of which is opposite to the perpendicular contact velocity and the other completing the axis system according to the right-hand-rule. The determination of the contact normal direction is further explained in Section 4.

We define the basis of the contact coordinate system in body coordinates, obtaining Eq. (B2):

$$\mathbf{B}_{\text{cb}} = \mathbf{B}_{\text{b}}^T B_{\text{c}} \tag{B2}$$

and we define a vector r_{b} in the body coordinate system from the contact point to the body COG as in Eq, (B3):

$$\mathbf{r}_{\text{b}} = \mathbf{B}_{\text{b}}^T(\mathbf{o}_{\text{c}} - \mathbf{o}_{\text{b}}) \tag{B4}$$

The influence of contact impulses in the contact coordinate system on the body velocity change in the body coordinate system are described by Jacobian Matrix J. The matrix J is formulated as:

$$\mathbf{J} = \begin{bmatrix} \mathbf{B}_{cb} & \mathbf{0} \\ \mathbf{Q}_{cb} & \mathbf{B}_{cb} \end{bmatrix} \tag{B5}$$

in which:

$$\mathbf{Q}_{cb} = \begin{bmatrix} (\mathbf{r}_b \times \mathbf{B}_{cb,*1})_1 & (\mathbf{r}_b \times \mathbf{B}_{cb,*2})_1 & (\mathbf{r}_b \times \mathbf{B}_{cb,*3})_1 \\ (\mathbf{r}_b \times \mathbf{B}_{cb,*1})_2 & (\mathbf{r}_b \times \mathbf{B}_{cb,*2})_2 & (\mathbf{r}_b \times \mathbf{B}_{cb,*3})_2 \\ (\mathbf{r}_b \times \mathbf{B}_{cb,*1})_3 & (\mathbf{r}_b \times \mathbf{B}_{cb,*2})_3 & (\mathbf{r}_b \times \mathbf{B}_{cb,*3})_3 \end{bmatrix} \tag{B6}$$

The translational and rotational velocity of the body at the contact point in contact coordinates is described by Eq. (B7):

$$\dot{\mathbf{u}}_c = \mathbf{J}^T \dot{\mathbf{u}}_b \tag{B7}$$

In which $\dot{\mathbf{u}}_c$ and $\dot{\mathbf{u}}_b$ are vectors describing the body velocity (in the body coordinate system) and contact velocity (in the contact coordinate system) in 6DOF as shown in Eq. (B8):

$$\dot{\mathbf{u}}_b = \begin{bmatrix} \dot{u}_{b1} \\ \dot{u}_{b2} \\ \dot{u}_{b3} \\ \dot{\phi}_{b1} \\ \dot{\phi}_{b2} \\ \dot{\phi}_{b3} \end{bmatrix} \qquad \dot{\mathbf{u}}_c = \begin{bmatrix} \dot{u}_n^c \\ \dot{u}_{t1}^c \\ \dot{u}_{t2}^c \\ \dot{\phi}_n^c \\ \dot{\phi}_{t1}^c \\ \dot{\phi}_{t2}^c \end{bmatrix} \tag{B8}$$

We take the gyroscopic forces into account in an implicit manner, similar to the implementation in the Bullet Physics engine *Bullet Physics* (2017). This is done by calculating the rotational velocity change due to gyroscopic forces over the time step. The velocity change is calculated using a time discretized version of Euler's rotation equation, shown in Eq. (B9):

$$\begin{gathered} \mathbf{I}(\phi)\frac{\Delta\dot{\phi}}{\Delta t} + \dot{\phi}_n \times (\mathbf{I}(\phi)\dot{\phi}_n) = \mathbf{P} \\ \downarrow \\ \mathbf{I}(\phi)\Delta\dot{\phi} + (\dot{\phi}_n \times (\mathbf{I}(\phi)\dot{\phi}_n))\Delta t = \mathbf{P}\Delta t \end{gathered} \tag{B9}$$

in which I is the inertia tensor of the body, $\dot{\phi}$ is the rotational velocity vector, and P is the momentum working on the body. Assuming there is no external momentum, $\Delta\dot{\phi}$ is solved using Newton's method, as shown in Eq. (B10):

$$\begin{aligned} \dot{\phi}_{n+1} &= \dot{\phi}_n - \frac{(\dot{\phi}_n \times (\mathbf{I}(\phi_n)\dot{\phi}_n))\Delta t}{\mathbf{I}(\phi_n) + (\mathbf{1} \times (\mathbf{I}(\phi_n\dot{\phi}_n) + \dot{\phi}_n \times \mathbf{I}(\phi_n))\Delta t} \\ \Delta\dot{\phi} &= \dot{\phi}_{n+1} - \dot{\phi}_n \end{aligned} \tag{B10}$$

We now incorporate the derived J matrix and gyroscopic velocity change in the MLCP of Eq. (24), in order to expand it to a multi degree of freedom system shown in Eq. (B11):

$$\begin{aligned} &\mathbf{Az} + \mathbf{b} = \mathbf{w} \\ &0 \le [\lambda_n \quad \lambda_{n,cor}]^T \perp [\alpha_r \quad \beta_r]^T \ge 0 \end{aligned} \tag{B11}$$

in which A and b are defined as in Eqs. (B12) and (B13):

$$\mathbf{A} = \begin{bmatrix} \mathbf{M} & -\mathbf{J}_n & -\mathbf{J}_t & -\mathbf{J}_\phi & \mathbf{0} \\ \mathbf{J}_n^T & \Sigma & \mathbf{0} & \mathbf{0} & 1 \\ \mathbf{J}_t^T & \mathbf{0} & \mathbf{0} & \mathbf{0} & \mathbf{0} \\ \mathbf{J}_\phi^T & \mathbf{0} & \mathbf{0} & \mathbf{0} & \mathbf{0} \\ -\mathbf{J}_n^T & \Sigma & \mathbf{0} & \mathbf{0} & 1 \end{bmatrix}, \quad \mathbf{z} = \begin{bmatrix} \Delta\dot{\mathbf{u}} \\ \lambda_n \\ \boldsymbol{\lambda}_t \\ \boldsymbol{\lambda}_\phi \\ \lambda_n^{cor} \end{bmatrix} \tag{B12}$$

$$\mathbf{b} = \begin{bmatrix} \mathbf{0} \\ Y_n \\ \dot{\mathbf{u}}_t^c + \frac{1}{2}\Delta\dot{\mathbf{u}}_{t;ext}^c \\ \dot{\phi}^c + \frac{1}{2}\Delta\dot{\phi}_{ext}^c \\ \frac{F_{cr}}{\frac{1}{4}\frac{\Delta F_{cr}}{\Delta\delta}\Delta t} \end{bmatrix}, \quad \mathbf{w} = \begin{bmatrix} \mathbf{0} \\ \alpha_r \\ \mathbf{0} \\ \mathbf{0} \\ \beta_r \end{bmatrix} \tag{B13}$$

$\boldsymbol{J_n}$ is the column of the Jacobian matrix related to the contact normal constraint (the first column), $\boldsymbol{J_t}$ are the columns of the Jacobian matrix related to the tangential constraints, and $\boldsymbol{J_\phi}$ are the columns of the Jacobian matrix related to the rotational constraints.

The contact velocity changes $\frac{1}{2}\Delta\dot{\mathbf{u}}_{t;ext}^c$ and $\frac{1}{2}\Delta\dot{\phi}_{ext}^c$ are half the velocity change caused by external (non-contact) forces within a time step.

In this system, the tangential and rotational constraint impulses are calculated such that the velocity at the contacts in these DOF's becomes zero. However, for ice-ice and ice-structure contacts, both the tangential and rotational contact constraints should be limited as a function of the normal impulse, because of the friction limit and the fact that there can not be tension in a contact. The next section explains how these limits are applied.

B.1. Friction constraints and constraints on contact rotational impulses

Both the frictional impulses and rotational impulses at ice-ice or ice-structure contacts are limited by the contact normal impulse. This is taken into account in the MLCP in the form of complementarity conditions. According to the Coulomb friction law, the frictional impulses λ_{t1} and λ_{t2} are limited according to:

$$\sqrt{\lambda_{t1}^2 + \lambda_{t2}^2} \leq \mu\lambda_n \tag{B14}$$

In which λ_{t1} is the frictional impulse in tangential direction $t1$, λ_{t2} is the frictional impulse in tangential direction $t2$, λ_n is the impulse in the contact normal direction, and μ is the friction coefficient. In order to enforce this limit within the framework of an MLCP, we approximate the resulting friction cone by a multi-faceted friction polyhedron, illustrated in Fig. B24. The number of facets can be altered based on the desired accuracy at each contact.

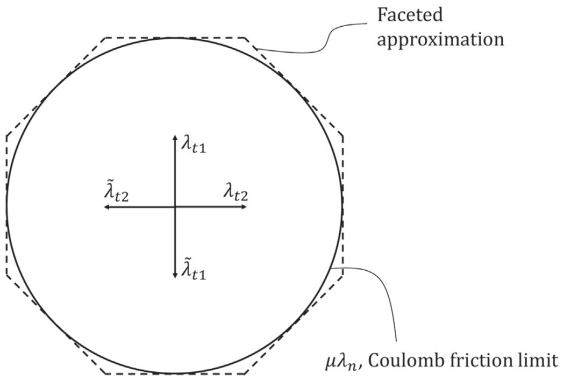

Fig. B24. Faceted approximation with 8 sides of Coulomb friction cone.

The direction of the resultant friction force during a time step should be opposite to the average tangential velocity vector during the time step. This average tangential velocity vector is a combination of the tangential velocity vector at time t_n, and the velocity change at the contact during the time step. The average sliding velocity during the time step is not known before the MLCP is solved. Therefore there should be enough tangential impulse directions such that a tangential friction impulse opposite to the average tangential velocity can result as a sum of impulses in the pre-defined frictional directions. Simultaneously, one of basic conditions of a LCP must be ensured, namely that all constraint impulses $\lambda_t \geq 0$. To achieve this, we define two friction impulse variables, t and $\tilde{t}$, for each friction direction, one opposite to the other.

Frictional impulses are limited by complementarity conditions for each face of the friction cone approximation. This is achieved using the matrices E_{fr} and U_{fr}, corresponding to the 8 faceted friction cone approximation shown in Fig. B24:

$$\mathbf{E}_{\text{fr}} = \begin{bmatrix} \cos\left(\frac{1}{4}\pi\right) & \cos\left(\frac{1}{2}\pi\right) & 0 & 0 & 0 & 0 & \cos\left(-\frac{1}{4}\pi\right) & \cos(0) \\ \cos\left(\frac{1}{4}\pi\right) & \sin\left(\frac{1}{2}\pi\right) & \sin\left(\frac{3}{4}\pi\right) & \sin(\pi) & 0 & 0 & 0 & 0 \\ 0 & 0 & \cos\left(-\frac{1}{4}\pi\right) & \cos(0) & \cos\left(\frac{1}{4}\pi\right) & \cos\left(\frac{1}{2}\pi\right) & 0 & 0 \\ 0 & 0 & 0 & 0 & \sin\left(\frac{1}{4}\pi\right) & \sin\left(\frac{1}{2}\pi\right) & \sin\left(\frac{3}{4}\pi\right) & \sin(\pi) \end{bmatrix}$$

$$\mathbf{E}_{\text{fr}} \in \mathbb{R}^{N_{\text{facets}} \times N_{\text{fric-directions}}} \tag{B15}$$

$$\mathbf{U}_{\text{fr}} = \begin{bmatrix} \mu \\ \mu \\ \mu \\ \mu \end{bmatrix} \tag{B16}$$

Adding the complementarity conditions for the frictional contacts to the MLCP of Eq. (B11), we obtain:

$$\mathbf{Az} + \mathbf{b} = \mathbf{w}$$
$$0 \leq [\lambda_n \;\; \boldsymbol{\lambda}_t^T \;\; \lambda_n^{\text{cor}} \;\; (\boldsymbol{\lambda}_t^{\text{cor}})^T]^T \perp [\alpha_{\text{r}} \;\; \boldsymbol{\beta}_{\text{r}}{}^T \;\; \gamma_{\text{r}} \;\; \boldsymbol{\zeta}_{\text{r}}{}^T]^T \geq 0 \tag{B17}$$

in which:

$$\mathbf{A} = \begin{bmatrix} \mathbf{M} & -\mathbf{J}_n & -\mathbf{J}_t & -\mathbf{J}_\phi & \mathbf{0} & \mathbf{0} \\ \mathbf{J}_n^T & \Sigma & \mathbf{0} & \mathbf{0} & 1 & \mathbf{0} \\ \mathbf{J}_t^T & \mathbf{0} & \mathbf{0} & \mathbf{0} & \mathbf{0} & \mathbf{E}_{\mathrm{fr}} \\ \mathbf{J}_\phi^T & \mathbf{0} & \mathbf{0} & \mathbf{0} & \mathbf{0} & \mathbf{0} \\ -\mathbf{J}_n^T & \Sigma & \mathbf{0} & \mathbf{0} & 1 & \mathbf{0} \\ \mathbf{0} & \mathbf{U}_{\mathrm{fr}} & -\mathbf{E}_{\mathrm{fr}}^T & \mathbf{0} & \mathbf{0} & \mathbf{0} \end{bmatrix}, \quad \mathbf{z} = \begin{bmatrix} \Delta\dot{\mathbf{u}} \\ \lambda_n \\ \boldsymbol{\lambda}_t \\ \boldsymbol{\lambda}_\phi \\ \lambda_n^{\mathrm{cor}} \\ \boldsymbol{\lambda}_t^{\mathrm{cor}} \end{bmatrix} \tag{B18}$$

$$\mathbf{b} = \begin{bmatrix} \mathbf{0} \\ \mathrm{Y}_n \\ \dot{\mathbf{u}}_t^{\mathrm{c}} + \frac{1}{2}\Delta\dot{\mathbf{u}}_{t;\mathrm{ext}}^{\mathrm{c}} \\ \dot{\phi}^{\mathrm{c}} + \frac{1}{2}\Delta\dot{\phi}_{\mathrm{ext}}^{\mathrm{c}} \\ \frac{F_{\mathrm{cr}}}{\frac{1}{4}\frac{\Delta F_{\mathrm{cr}}}{\Delta\delta}\Delta t} \\ \mathbf{0} \end{bmatrix}, \quad \mathbf{w} = \begin{bmatrix} \mathbf{0} \\ \alpha_{\mathrm{r}} \\ \boldsymbol{\beta}_{\mathrm{r}} \\ \mathbf{0} \\ \gamma_{\mathrm{r}} \\ \boldsymbol{\zeta}_{\mathrm{r}} \end{bmatrix} \tag{B19}$$

The rotational contact impulses should also be limited by the contact normal impulse. We limit the rotational impulses based on the outer points of the contact area and the normal impulse. The upper limits for rotational impulses are interlinked: one rotational impulse influences the maximum magnitude of the other. This link is neglected in the current formulation.

The limits to rotational impulses, based on the normal impulse and the outer points of the contact area, are taken into account by introducing matrices U_{rot} and E_{rot}:

$$\mathbf{U}_{\mathrm{rot}} = \begin{bmatrix} d_{t1}^{\max} \\ d_{\tilde{t}1}^{\max} \\ d_{t2}^{\max} \\ d_{\tilde{t}2}^{\max} \\ d_n^{\max} \\ d_{\tilde{n}}^{\max} \end{bmatrix} \tag{B20}$$

$$\mathbf{E}_{\mathrm{rot}} = \begin{bmatrix} 1 & 0 & 0 & 0 & 0 & 0 \\ 0 & 1 & 0 & 0 & 0 & 0 \\ 0 & 0 & 1 & 0 & 0 & 0 \\ 0 & 0 & 0 & 1 & 0 & 0 \\ 0 & 0 & 0 & 0 & 1 & 0 \\ 0 & 0 & 0 & 0 & 0 & 1 \end{bmatrix} \tag{B21}$$

in which the distances d are as shown in Fig. B25.

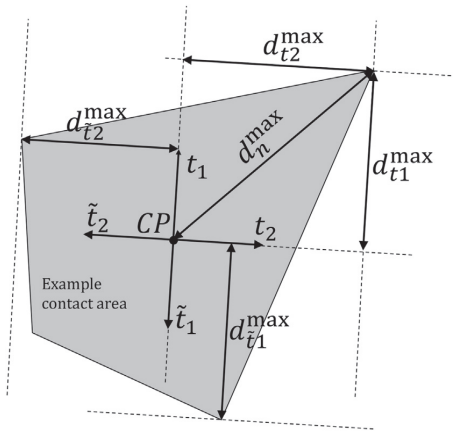

Fig. B25. Example contact area, demonstrating the maximum distance determination.

Adding these matrices to the MLCP of Eq. (B11), the MLCP becomes:

$$\mathbf{A}\mathbf{z} + \mathbf{b} = \mathbf{w}$$
$$0 \le [\lambda_n \;\; \boldsymbol{\lambda}_t^T \;\; \boldsymbol{\lambda}_\phi^T \;\; \lambda_n^{\mathrm{cor}} \;\; (\boldsymbol{\lambda}_t^{\mathrm{cor}})^T \;\; (\boldsymbol{\lambda}_\phi^{\mathrm{cor}})^T]^T \perp [\alpha_{\mathrm{r}} \;\; \boldsymbol{\beta}_{\mathrm{r}}{}^T \;\; \boldsymbol{\gamma}_{\mathrm{r}}{}^T \;\; \boldsymbol{\zeta}_{\mathrm{r}} \;\; \boldsymbol{\eta}_{\mathrm{r}}{}^T \;\; \boldsymbol{\theta}_{\mathrm{r}}{}^T]^T \ge 0 \tag{B22}$$

in which:

$$\mathbf{A} = \begin{bmatrix} \mathbf{M} & -\mathbf{J}_n & -\mathbf{J}_t & -\mathbf{J}_\phi & \mathbf{0} & \mathbf{0} & \mathbf{0} \\ \mathbf{J}_n^T & \Sigma & \mathbf{0} & \mathbf{0} & 1 & \mathbf{0} & \mathbf{0} \\ \mathbf{J}_t^T & \mathbf{0} & \mathbf{0} & \mathbf{0} & \mathbf{0} & \mathbf{E}_{\text{fr}} & \mathbf{0} \\ \mathbf{J}_\phi^T & \mathbf{0} & \mathbf{0} & \mathbf{0} & \mathbf{0} & \mathbf{0} & \mathbf{E}_{\text{rot}} \\ -\mathbf{J}_n^T & \Sigma & \mathbf{0} & \mathbf{0} & 1 & \mathbf{0} & \mathbf{0} \\ \mathbf{0} & \mathbf{U}_{\text{fr}} & -\mathbf{E}_{\text{fr}}^T & \mathbf{0} & \mathbf{0} & \mathbf{0} & \mathbf{0} \\ \mathbf{0} & \mathbf{U}_{\text{rot}} & \mathbf{0} & -\mathbf{E}_{\text{rot}}^T & \mathbf{0} & \mathbf{0} & \mathbf{0} \end{bmatrix}, \quad \mathbf{z} = \begin{bmatrix} \Delta\dot{\mathbf{u}} \\ \lambda_n \\ \boldsymbol{\lambda}_t \\ \boldsymbol{\lambda}_\phi \\ \lambda_n^{\text{cor}} \\ \boldsymbol{\lambda}_t^{\text{cor}} \\ \boldsymbol{\lambda}_\phi^{\text{cor}} \end{bmatrix} \tag{B23}$$

$$\mathbf{b} = \begin{bmatrix} \mathbf{0} \\ \mathrm{Y}_n \\ \dot{\mathbf{u}}_t^{\text{c}} + \frac{1}{2}\Delta\dot{\mathbf{u}}_{t;\text{ext}}^{\text{c}} \\ \dot{\phi}^{\text{c}} + \frac{1}{2}\Delta\dot{\phi}_{\text{ext}}^{\text{c}} \\ \frac{F_{\text{cr}}}{\frac{1}{4}\frac{\Delta F_{\text{cr}}}{\Delta\delta}\Delta t} \\ \mathbf{0} \\ \mathbf{0} \end{bmatrix}, \quad \mathbf{w} = \begin{bmatrix} \mathbf{0} \\ \alpha_{\text{r}} \\ \boldsymbol{\beta}_{\text{r}} \\ \gamma_{\text{r}} \\ \boldsymbol{\zeta}_{\text{r}} \\ \boldsymbol{\eta}_{\text{r}} \\ \theta_{\text{r}} \end{bmatrix} \tag{B24}$$

Finally, the MLCP from Eq. (B22) can be generalized to multi-contact case, in which some contacts have upper and lower limits as explained in previous section and some contacts (such as spring-damper contacts within a lattice) are holonomic. This generalized MLCP becomes:

$$\mathbf{A}\mathbf{z} + \mathbf{b} = \mathbf{w}$$
$$0 \leq [\boldsymbol{\lambda}_n^T \ \boldsymbol{\lambda}_t^T \ \boldsymbol{\lambda}_\phi^T \ (\boldsymbol{\lambda}_n^{\text{cor}})^T \ (\boldsymbol{\lambda}_t^{\text{cor}})^T \ (\boldsymbol{\lambda}_\phi^{\text{cor}})^T]^T \perp [\boldsymbol{\alpha}_{\text{r}}^T \ \boldsymbol{\beta}_{\text{r}}^T \ \boldsymbol{\gamma}_{\text{r}}^T \ \boldsymbol{\zeta}_{\text{r}}^T \ \boldsymbol{\eta}_{\text{r}}^T \ \theta_{\text{r}}^T]^T \geq 0 \tag{B25}$$

in which:

$$\mathbf{A} = \begin{bmatrix} \mathbf{M} & -\mathbf{J}_h & -\mathbf{J}_n & -\mathbf{J}_t & -\mathbf{J}_\phi & \mathbf{0} & \mathbf{0} & \mathbf{0} \\ \mathbf{J}_h^T & \boldsymbol{\Sigma}_{\text{h}} & \mathbf{0} & \mathbf{0} & \mathbf{0} & \mathbf{0} & \mathbf{0} & \mathbf{0} \\ \mathbf{J}_n^T & \mathbf{0} & \boldsymbol{\Sigma}_n & \mathbf{0} & \mathbf{0} & \mathbf{E}_n & \mathbf{0} & \mathbf{0} \\ \mathbf{J}_t^T & \mathbf{0} & \mathbf{0} & \mathbf{0} & \mathbf{0} & \mathbf{0} & \mathbf{E}_{\text{fr}} & \mathbf{0} \\ \mathbf{J}_\phi^T & \mathbf{0} & \mathbf{0} & \mathbf{0} & \mathbf{0} & \mathbf{0} & \mathbf{0} & \mathbf{E}_{\text{rot}} \\ -\mathbf{J}_n^T & \mathbf{0} & \boldsymbol{\Sigma}_n & \mathbf{0} & \mathbf{0} & \mathbf{E}_n & \mathbf{0} & \mathbf{0} \\ \mathbf{0} & \mathbf{0} & \mathbf{U}_{\text{fr}} & -\mathbf{E}_{\text{fr}}^T & \mathbf{0} & \mathbf{0} & \mathbf{0} & \mathbf{0} \\ \mathbf{0} & \mathbf{0} & \mathbf{U}_{\text{rot}} & \mathbf{0} & -\mathbf{E}_{\text{rot}}^T & \mathbf{0} & \mathbf{0} & \mathbf{0} \end{bmatrix}, \quad \mathbf{z} = \begin{bmatrix} \Delta\dot{\mathbf{u}} \\ \boldsymbol{\lambda}_h \\ \boldsymbol{\lambda}_n \\ \boldsymbol{\lambda}_t \\ \boldsymbol{\lambda}_\phi \\ \boldsymbol{\lambda}_n^{\text{cor}} \\ \boldsymbol{\lambda}_t^{\text{cor}} \\ \boldsymbol{\lambda}_\phi^{\text{cor}} \end{bmatrix} \tag{B26}$$

$$\mathbf{b} = \begin{bmatrix} \mathbf{0} \\ \mathbf{Y}_{\text{h}} \\ \mathbf{Y}_n \\ \dot{\mathbf{u}}_t^{\text{c}} + \frac{1}{2}\Delta\dot{\mathbf{u}}_{t;\text{ext}}^{\text{c}} \\ \dot{\phi}^{\text{c}} + \frac{1}{2}\Delta\dot{\phi}_{\text{ext}}^{\text{c}} \\ \mathbf{S}_n \\ \mathbf{0} \\ \mathbf{0} \end{bmatrix}, \quad \mathbf{w} = \begin{bmatrix} \mathbf{0} \\ \mathbf{0} \\ \boldsymbol{\alpha}_{\text{r}} \\ \boldsymbol{\beta}_{\text{r}} \\ \boldsymbol{\gamma}_{\text{r}} \\ \boldsymbol{\zeta}_{\text{r}} \\ \boldsymbol{\eta}_{\text{r}} \\ \theta\text{r} \end{bmatrix} \tag{B27}$$

and S_n is:

$$\mathbf{S}_n = \begin{bmatrix} \frac{F_{\text{cr};1}}{\frac{1}{4}\frac{\Delta F_{\text{cr};1}}{\Delta\delta_1\Delta t}} \\ \vdots \\ \frac{F_{\text{cr;nc}}}{\frac{1}{4}\frac{\Delta F_{\text{cr;nc}}}{\Delta\delta_1\Delta t}} \end{bmatrix} \tag{B28}$$

in which nc is the number of crushing contacts in the current time step.

References

Alawneh, S., Dragt, R., Peters, D., Daley, C., Bruneau, S., 2015. Hyper-real-time ice simulation and modeling using GPGPU. IEEE Trans. Comput. 64 (12), 3475–3487.

ArclSo, 2018. *arciso.com*.

Bullet Physics, 2017. *http://bulletphysics.org*.

Daley, C., 1999. Energy based ice collision forces. In: Proceedings of the 15th International Conference on Port and Ocean Engineering under Arctic Conditions', Helsinki, Finland.

Dorival, O., Metrikine, A.V., Simone, A., 2008. A lattice model to simulate ice-structure interaction. In: Proceedings of the ASME International Conference on Offshore Mechanics and Arctic Engineering.

GIMP 2.8.22, 2017. *http://www.gimp.org*.

Haase, A., Polojarvi, A., Tuhkuri, J., 2010. 3D discrete numerical modelling of conical structure-ice rubble interaction. In: '20th IAHR International Symposium on Ice', Lahti.

Hocking, G., 1992. The discrete element method for analysis of fragmentation of discontinua. Eng. Comput. 9, 145–155.

Hopkins, M.A., 1992. Numerical simulation of systems of multitudinous polygonal blocks. In: Technical Report 92-22 Cold Regions Research and Engineering Laboratory, CRREL. 69.

Hopkins, M.A., Hibler, W.D., Flato, G.M., 1991. On the numerical simulation of the sea ice ridging process. J. Geophys. Res. 96 (C), 4809–4820.

Hoving, J.S., Vermeulen, R., Mesu, A.W., Cammaert, G., 2013. Experiment-based relations between level ice loads and managed ice loads on an arctic jack-up structure. 'Proceedings of the 22nd International Conference on Port and Ocean Engineering under Arctic Conditions', Espoo, Finland.

Image Composite Editor 2.0, 2017. URL: *https://www.microsoft.com/en-us/research/product/computational-photography-applications/image-composite-editor/*.
Jean, M., 1999. The non-smooth contact dynamics method. Comput. Methods Appl. Mech. Eng. 177 (3–4), 235–257.
Jirasek, M., Bazant, Z.P., 1995. Particle model for Quasibrittle fracture and application to sea ice. J. Eng. Mech. 121 (9).
Keijdener, C., Metrikine, A.V., 2014. The effect of ice velocity on the breaking length of level ice failing in downward bending. In: 'Proceedings of the 22nd IAHR International Symposium on Ice', Singapore, pp. 396–403.
Kim, E., Gagnon, R.E., 2016. A preliminary analysis of the crushing specific energy of iceberg ice under rapid compressive loading. In: 'Proceedings of the 23rd IAHR International Symposium on Ice', Ann Arbor, Michigan, USA.
Kim, E., Hoyland, K.V., 2014. Experimental investigations of the energy absorption capacity of ice during crushing: is the specific energy scale independent? In: 'Proceedings of the 22nd IAHR International Symposium on Ice', Singapore, pp. 163–170.
Kinnunen, A., Tikanmäki, M., Heinonen, J., 2016. An energy model for ice crushing in ice-structure impact. 'Proceedings of the 23rd IAHR International Symposium on Ice', Ann Arbor, Michigan, USA.
Konno, A., Mizuki, T., 2006. Numerical simulation of pre-sawn ice test of model ice-breaker using physically based modeling. '18th IAHR Symposium on Ice', Sapporo, Japan.
Krabbenhoft, K., Huang, J., Da Silva, M.V., Lyamin, A.V., 2012. Granular contact dynamics with particle elasticity. Granul. Matter 14 (5), 607–619.
Lacoursiere, C., 2003. Splitting methods for dry frictional contact problems in rigid multibody systems: preliminary performance results. In: Conference Proceedings from SIGRAD2003, pp. 11–16.
Lacoursière, C., 2007. Regularized, stabilized, variational methods for multibodies. In: Proceedings of the 48th Scandinavian Conference on Simulation and Modelling. 027. pp. 40–48.
Lilja, V.-P., Polojärvi, A., Tuhkuri, J., Paavilainen, J., 2017. A three-dimensional FEM-DEM model of an ice sheet. In: 'Proceedings of the 24th International Conference on Port and Ocean Engineering under Arctic Conditions', Busan, Korea.
Liu, L., Sun, S., Ji, S., 2017. Interaction Between Floater and Sea Ice Simulated with Dilated Polyhedral DEM. Springer, Singapore, pp. 1065–1074.
Løset, S., 1994a. Discrete element modelling of a broken ice field - part I: model development. Cold Reg. Sci. Technol. 22 (4), 339–347.
Løset, S., 1994b. Discrete element modelling of a broken ice field — part II: simulation of ice loads on a boom. Cold Reg. Sci. Technol. 22 (4), 349–360.
Lu, W., Lubbad, R., Løset, S., 2015a. In-plane fracture of an ice floe: a theoretical study on the splitting failure mode. Cold Reg. Sci. Technol. 110, 77–101.
Lu, W., Lubbad, R., Løset, S., 2015b. Out-of-plane failure of an ice floe: radial-crack-initiation-controlled fracture. Cold Reg. Sci. Technol. 119, 183–203.
Lu, W., Lubbad, R., Løset, S., Kashafutdinov, M., 2016. Fracture of an ice floe: local out-of-plane flexural failures versus global in-plane splitting failure. Cold Reg. Sci. Technol. 123, 1–13.
Lubbad, R., Løset, S., 2011. A numerical model for real-time simulation of ship-ice interaction. Cold Reg. Sci. Technol. 65 (2), 111–127.
Lubbad, R., Løset, S., Lu, W., Tsarau, A., van den Berg, M., 2018. An overview of the Oden Arctic Technology Research Cruise 2015 (OATRC2015) and numerical simulations performed with SAMS driven by data collected during the cruise. Cold Reg. Sci. Technol. https://doi.org/10.1016/j.coldregions.2018.04.006. (in press).
Metrikin, I., 2014. A software framework for simulating stationkeeping of a vessel in discontinuous ice. Model. Identif. Control. 35 (4), 211–248.
Moreau, J.J., 1999. Numerical aspects of the sweeping process. Comput. Methods Appl. Mech. Eng. 177 (3–4), 329–349.
Newmark, N.M., 1959. A method of computation for structural dynamics. J. Eng. Mech. Div. 85 (3), 67–94.
Paavilainen, J., Tuhkuri, J., Polojärvi, A., 2009. 2D combined finite-discrete element method to model multi-fracture of beam structures. Eng. Comput. 26 (6), 578–598.
Paavilainen, J., Tuhkuri, J., Polojärvi, A., 2011. 2D numerical simulations of ice rubble formation process against an inclined structure. Cold Reg. Sci. Technol. 68 (1–2), 20–34.
Polojärvi, A., Tuhkuri, J., 2009. 3D discrete numerical modelling of ridge keel punch through tests. Cold Reg. Sci. Technol. 56 (1), 18–29.
Ranta, J., Tuhkuri, J., 2017. Sources of stochasticity in ice-structure interaction process. In: 'Proceedings of the 24th Inernational Confrence on Port and Ocean Engineering under Arctic Conditions', Busan, Korea.
Ranta, J., Polojärvi, A., Tuhkuri, J., 2018. Ice loads on inclined marine structures - virtual experiments on ice failure process evolution. Mar. Struct. 57, 72–86.
Sayed, M., Timco, G., 1999. A lattice model of ice failure. In: *Proceedings of the Ninth International Offshore and Polar Engineering Conference* II, pp. 1–28.
Servin, M., Wang, D., Lacoursière, C., Bodin, K., 2014. Examining the smooth and non-smooth discrete element approaches to granular matter. Int. J. Numer. Methods Eng. 97, 878–902.
Tasora, A., Anitescu, M., Negrini, S., Negrut, D., 2013. A compliant visco-plastic particle contact model based on differential variational inequalities. Int. J. Non-Linear Mech. 53, 2–12.
Tsarau, A., 2015. Numerical Modelling of the Hydrodynamic Effects of Marine Operations in Broken Ice. Doctoral thesis. Norwegian University of Science and Technology.
Tsarau, A., Lubbad, R., Løset, S., 2017. A numerical model for simulating the effect of propeller flow in ice management. Cold Reg. Sci. Technol. 142, 139–152.
Tuhkuri, J., Polojärvi, A., 2005. Effect of particle shape in 2D ridge keel deformation simulations. In: Proceedings of the 18th International Conference on Port and Ocean Engineering under Arctic Conditions. Vol. 2. pp. 939–948.
van den Berg, M., 2016. A 3-D random lattice model of sea ice. In: Arctic Technology Conference. St. Johns, Newfoundland and Labrador.
Berg, M., Lubbad, R., Løset, S., 2017. Accuracy of a non-smooth time stepping scheme with non-rigid contacts for ice-structure interaction. In: Proceedings of the 24th International Conference on Port and Ocean Engineering under Arctic Conditions. Busan, Korea (Busan, Korea).
van Vliet, R., Metrikine, A.V., 2018. Derivation and verification of a lattice model for bending vibration of a plate. ZAMM 98 (3), 367–387.
Yulmetov, R., Lubbad, R., Løset, S., 2016. Planar multi-body model of iceberg free drift and towing in broken ice. Cold Reg. Sci. Technol. 121, 154–166.
Zhang, Q., Skjetne, R., 2015. Image processing for identification of sea-ice floes and the floe size distributions. IEEE Trans. Geosci. Remote Sens. 53 (5), 2913–2924.

Appendix B

A 3-D random lattice model of sea ice

This paper was prepared for presentation at the Arctic Technology Conference held in St. John's, Newfoundland and Labrador, 24-26 October 2016.

Appendix C

Accuracy of a non-smooth time stepping scheme with non-rigid contacts for ice-structure interaction

This paper is published in the Proceeding of the 24th International Conference on Port and Ocean Engineering under Arctic Conditions, June 11-16, 2017, Busan, Korea.

POAC'17
Busan, KOREA

Proceedings of the 24th International Conference on
Port and Ocean Engineering under Arctic Conditions
June 11-16, 2017, Busan, Korea

Accuracy of a Non-Smooth Time Stepping Scheme with Non-Rigid Contacts for Ice-Structure Interaction

Marnix van den Berg[1], Raed Lubbad[1], Sveinung Løset[1]
[1] Sustainable Arctic Marine and Coastal Technology (SAMCoT), Centre for Research-based Innovation (CRI), Norwegian University of Science and Technology, Trondheim, Norway

ABSTRACT

Discrete element methods enable us to model the interactions between individual ice blocks and the structure of interest. This may give information on relevant processes in ice- structure or ice-ice interaction that cannot be captured by continuous methods. Discrete element methods can broadly be divided into two categories; smooth and non-smooth. While the former is known for high computational cost, the latter may significantly reduce the calculation time of discrete element simulations by enabling larger time steps. This paper investigates the applicability bounds of a novel non-smooth discrete element time stepping scheme that includes contact non-rigidity. Contact non-rigidity allows us to compute ice-structure or ice-ice contact forces based on crushing assumptions. Additionally, it enables the modelling of deformable ice features and failure. A major advantage of the applied method is that it maintains stability for a much wider range of time step sizes. This enables discrete element simulations with a much reduced calculation time compared to smooth methods. The accuracy of the applied method is investigated for two case studies. Results show that accurate results can be generated with significantly larger time steps than used in other methods.

KEY WORDS: Lattice model; Non-Smooth DEM; Ice-Structure interaction

INTRODUCTION

Full-scale ice-structure interaction is of interest in the design of structures and ships, and in the planning of ice management operations. Several numerical approaches are possible to model these interactions. A distinction can be made between continuum methods and discrete methods. The latter models the individual ice blocks as discrete bodies, while continuum methods take the influence of broken ice into account by approximating the bulk material properties of ice and ice rubble. Some phenomena can only be studied using discrete methods, such as the formation of force chains within broken ice. A downside of discrete methods is the computational demand.

Discrete element methods can broadly be divided into two categories; smooth and non-smooth. The difference between smooth and non-smooth discrete element methods can be understood as the difference between explicit and implicit time integration (Servin et al. 2014). Smooth- or explicit methods require only simple evaluations per time step, but need very small time steps to maintain stability. Non-smooth- or implicit methods, on the other hand, require the solution of a system of equations for each time step, but they maintain accuracy for larger time step sizes. The use of non-smooth discrete element methods may significantly reduce the calculation time of discrete ice-structure interaction simulations. A downside of many existing non-smooth discrete element methods is that contacts are assumed infinitely rigid. This makes the contact forces predicted by such methods unphysical for most ice structure interaction scenarios.

This paper presents a novel method that extends the 'classical' non-smooth formulation to account for contact non-rigidity. This results in a time stepping scheme that still has all advantages of the non-smooth methods, namely 1) the stability is independent of time step size, 2) it can handle rigid (infinitely stiff) contacts, and 3) it gives accurate results for larger time steps. In addition, the new method is capable of accounting for contact non-rigidity, and it predicts physically correct contact forces. With the proper choice of model parameters, the current scheme can be as accurate as smooth schemes. The time stepping scheme used in this paper differs from schemes published by others (Lacoursiere 2007; Servin et al. 2014; Krabbenhoft et al. 2012) in that it is derived based on the second-order accurate Newmark-Beta method. In contrast to other schemes, it does not introduce (artificial) numerical damping.

Although the proposed method maintains stability for a wide range of time step sizes, the accuracy of the results may be compromised before instability occurs. This paper investigates the influence of time step size, as well as mesh size on the accuracy of the results for two different interaction scenarios; the interaction between a free floating ship and a single square ice floe, and the interaction between a fixed, vertical walled cylindrical structure and a confined floe field.

The paper starts with a short description of the used model. Two case studies are presented. Thereafter, the results are described and discussed. Lastly, the results are summarized and conclusions are drawn.

MODEL DESCRIPTION

The proposed model consists of four parts:

- A *material model*, used to account for the influence of ice floe deformation on the results.
- A *contact model*, used to determine the contact parameters for in ice-ice and ice-structure interactions.
- A *time stepping scheme* used for stable and accurate time integration.
- A *hydrodynamic model*, which accounts for hydrostatic forces, form drag and skin friction.

Ice failure (except local crushing) is not taken into account in the model and results presented in this paper. Therefore, the results should be seen as describing trends in the contact behavior, and should not be perceived as loads that would occur in actual full-scale interaction.

Material model

A random lattice model based on Voronoi Tesselation is used as a material model for the ice. This model is presented in (van den Berg 2016). The model parameters are determined as described in (Yip et al. 2005) and are adapted to ice plates as described in (van den Berg 2016). Lattice models based on Voronoi tessellation give accurate results in fracture modelling of brittle, inhomogeneous, and/or polycrystalline materials such as concrete and rock.

Contact model

The contact model is used to derive contact parameters in ice-ice and ice-structure contacts. The model is based on the assumption that local crushing will occur at ice-ice or ice-structure contacts when a maximum crushing pressure is exceeded. Full-scale observations show that local crushing does indeed occur in most ice-ice and ice-structure interactions. An example of local crushing is shown in Figure 1.

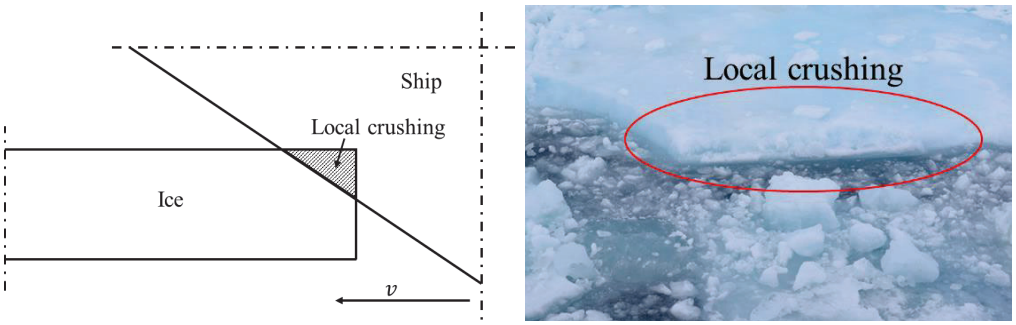

Figure 1. Local crushing at ship-ice contact. Sketch of interaction scenario (left) and full-scale observation (right, Oden 2016).

We find that it is essential to take this local crushing into account for an accurate contact force determination. The contact parameters are determined assuming constant energy dissipation per crushed volume. This is similar to (Kinnunen et al. 2016) and is supported by experiments described in (Kim & Høyland 2014). We note that the assumption of a constant energy absorption during crushing is a simplification of the actual phenomena that occur during crushing. Such a simplification is needed because of the large difference in scale between the phenomena that occur at the ice-structure contact and the global ice sheet behavior. To our knowledge, a similar simplification is made in any global ice structure interaction model, the only difference being the assumptions made in deriving the force-penetration curve. Models that attempt to physically model the crushing process are currently limited to small scales.

We derive an expression for the contact force as a function of penetration in the form:

$$F(\delta) = p_{cr1}\delta^2 + p_{cr2}\delta + p_{cr3} \tag{1}$$

In which the constants p_{cr1}, p_{cr2} and p_{cr3} are determined based on the contact geometry and the specific energy absorption during crushing. F is the contact force in the normal direction of the contact and δ is the crushing penetration in the normal direction. Crushing contacts are fully dissipative; the energy 'consumed' in the crushing process cannot be recovered.

Time stepping scheme

The time stepping scheme utilizes the contact parameters derived from the lattice model and the contact model to propagate the simulation in an implicit manner. The time stepping scheme used for the simulations in this paper is a relatively new way of modelling, and shows similarities with the methods described in (Lacoursiere 2007; Servin et al. 2014; Krabbenhoft et al. 2012). However, the derivation of the current method is based on a different implicit integration method, resulting in different integration factors and model properties. It is derived based on the second-order accurate Newmark-Beta method. In contrast to other schemes, it does not introduce (artificial) numerical damping.

Each time step, the velocity change of the bodies $\Delta \boldsymbol{v}$ and the contact force integral at each contact $\boldsymbol{\lambda}$ is calculated by solving the system of equations shown in formula 2:

$$\begin{bmatrix} \mathbf{M} & -\mathbf{J}^T \\ -\boldsymbol{J} & \boldsymbol{\Sigma} \end{bmatrix} \begin{bmatrix} \Delta \boldsymbol{v} \\ \boldsymbol{\lambda} \end{bmatrix} = \begin{bmatrix} \mathbf{0} \\ \mathbf{G} \end{bmatrix} \tag{2}$$

Here, $\mathbf{M}$ is the mass matrix, $\boldsymbol{J}$ is a matrix containing the constraint Jacobians, $\Delta \boldsymbol{v}$ contains the velocity change of each body and $\boldsymbol{\lambda}$ are the Lagrange multipliers at each contact, which have the dimension of impulse in this formulation. The diagonal matrices $\boldsymbol{\Sigma}$ and $\mathbf{G}$ describe the contact non-rigidity. The terms in $\boldsymbol{\Sigma}$ and $\mathbf{G}$ are derived by ensuring energy balance at each contact and utilizing an implicit integration scheme similar to the Newmark-Beta method. The terms in $\boldsymbol{\Sigma}$ and $\mathbf{G}$ can be used to represent elastic contacts, like the lattice elements representing the ice deformation, or they can represent dissipative contacts for contact between separate ice floes or between ice and structure, in which local crushing occurs.

At ice-ice or ice-structure contacts, there cannot be any tension and the frictional force is limited based on the normal force. Coulomb friction is assumed, resulting in the following constraints for loose contacts;

$$\lambda_n \geq 0 \text{ (no tension)} \tag{3}$$

$$\lambda_{t,i} \leq \mu \lambda_{n,i} \tag{4}$$

In which μ is the friction coefficient. λ_n is the integral of normal force over the time step and λ_t is the integral of frictional forces over a time step;

$$\lambda_n = \int_{t_n}^{t_{n+1}} F_n(t) dt \tag{5}$$

$$\lambda_t = \int_{t_n}^{t_{n+1}} F_t(t) dt \tag{6}$$

Hydrodynamic model

Hydrodynamic drag and hydrostatic forces are included in the model. The drag is calculated based on a quadratic drag equation and skin friction. More details can be found in (Tsarau 2015). The effect of added mass is not taken into account. This may influence the results at higher interaction velocities.

DESCRIPTION OF CASE STUDIES

We investigate the influence of time step, mesh size and interaction velocity on the contact force, contact area and sheet deformation in the time domain. The influence of these parameters is investigated for two cases:

- Case #1: Interaction between a ship-shaped structure (sloping at the waterline) and a single 100x100 m ice floe.
- Case #2: Interaction between a bottom-fixed circular-shaped structure (vertical at the waterline) and a confined floe field of 100 x 100 m. The floes are randomly generated according to the method described in (Yulmetov et al. 2014) and have areas between 100 and 400 m^2.

Figure 2 and Figure 3 show the two case studies. In Case #1, a ship interacts with a free-floating ice floe. In the initial condition, the ice has no velocity and the ship propagates in the direction indicated in the figure. The velocity of the ship is not constant, as it interacts with the ice, the ship slows down and the ice floe accelerates.

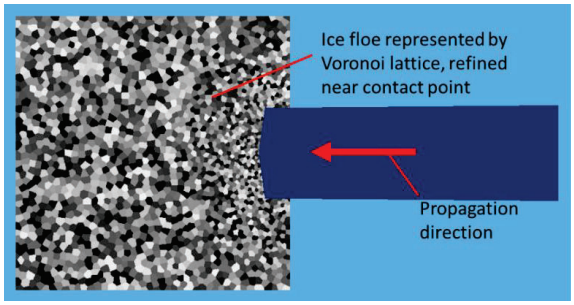

Figure 2. Ship-ice interaction scenario, top view.

In Case #2, the ice floes are confined by the domain boundaries, as they would be in an ice tank. In full-scale, the confinement could come from larger ice floes or ice pressure situations. The cylindrical structure is propagated with a constant velocity of 2.0 m/s in the direction indicated in the figure.

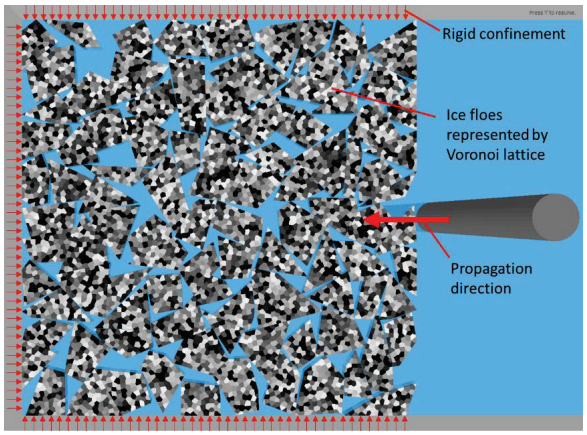

Figure 3. Fixed structure interaction scenario, top view.

Other simulation parameters are shown in Table 1.

Table 1. Simulation parameters

Parameter	Value
Ice thickness	$1.0\ m$
Time step	variable, see Table 2
Ice-structure friction coefficient	0.3
Water density	$1025\ kg/m^3$
Ice density	$910\ kg/m^3$
Young's modulus of ice	$5.0 \cdot 10^9\ N/m^2$
Poisson's ratio*	0
Specific energy absorption during crushing**	$2.0 \cdot 10^6\ J/m^3$
Mesh size	variable, see Table 2
Interaction velocity	variable, see Table 2

* The current method of lattice properties determination does not allow for accurate modelling of Poisson effects. Therefore, a value of 0 is used.
** This corresponds to a constant crushing pressure of 2.0 MPa.

The ship dimensions are roughly similar to that of existing icebreakers, however it does not match any existing icebreaker in particular. The ship has a stem angle of 33.7°. The middle of the ship bow protrudes compared to the sides of the bow. This ensures initial point contact between the ship hull and the ice, which makes the analysis of contact model behavior and sheet deformation more convenient. The diameter of the fixed cylindrical structure matches the diameter of the Nordstrømsgrund lighthouse. The geometry of the ship and the fixed structure are shown in Figure 4.

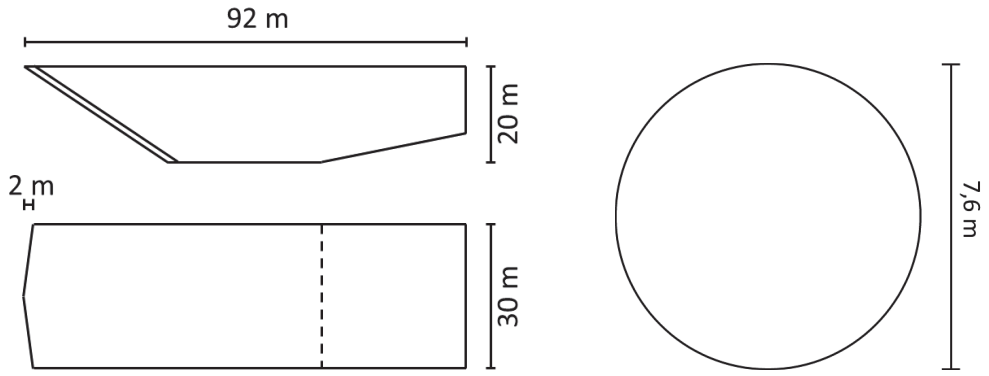

Figure 4. Geometry of ship and fixed cylindrical structure.

RESULTS

In all ice-structure interaction simulations presented below, the following phenomena occur:

- Ice and structure come in contact. Because of roughness of the ice surface area and/or the contact geometry, the contacting area at initial contact between the ice and the structure is close to zero.
- Local crushing occurs at the ice-structure contact, which results in a higher contact area. This higher contact area is needed to transfer a load from the structure to the ice.
- As the contact area and the total contact force between ice and structure increases, the ice sheet starts to deform. This deformation influences the temporal evolution of the contact force.

We consider the above described phenomena a reasonably good approximation of the phenomena that occur during actual ice- structure interaction. During the simulations, the stress distributions in the ice were similar to those displayed in Figure 5. Bending waves were observed in Case #1 (the ship interaction scenario) and force chains formed in Case #2 (the fixed structure scenario).

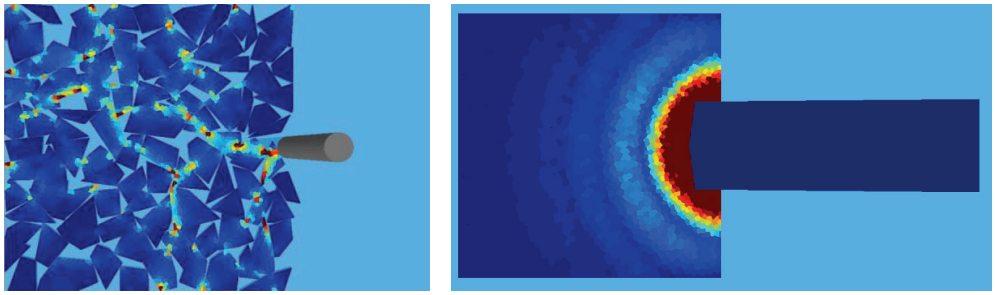

Figure 5. Stress in ice sheets during interaction with fixed structure and ship

We investigate the effect of mesh size (d_s), time step (dt), and interaction velocity (v) on the results of Case #1. For Case #2, we study the effect of mesh size and time step on the results. The combinations of the tested parameters are shown in Table 2.

Table 2. Numerical test matrix

Case number #	Time step (dt) [s]	Mesh size (d_s) [m]	Interaction velocity (v) [m/s]	Structure type
1.1	$1.0 \cdot 10^{-4}$, $5.0 \cdot 10^{-4}$, $1.0 \cdot 10^{-3}$, $5.0 \cdot 10^{-3}$, $1.0 \cdot 10^{-2}$, $5.0 \cdot 10^{-2}$, $1.0 \cdot 10^{-1}$	[0.5 / 2.0]*	5.0	Ship-shaped floater
1.2	$1.0 \cdot 10^{-4}$	[0.5 / 2.0], [1.0 / 4.0], [1.5 / 6.0], [2.0 / 8.0], [2.5 / 10.0], [3.0 / 12.0], [3.5 / 14.0]*	5.0	Ship-shaped floater
1.3	$1.0 \cdot 10^{-2}$	[0.5 / 2.0]*	0.05, 0.1, 0.5, 1.0, 5.0	Ship-shaped floater
2.1	$1.0 \cdot 10^{-3}$, $5.0 \cdot 10^{-3}$, $1.0 \cdot 10^{-2}$, $5.0 \cdot 10^{-2}$, $1.0 \cdot 10^{-1}$	1.0	2.0	Fixed cylindrical
2.2	$1 \cdot 10^{-2}$ s	1.0, 2.0, 5.0, 10.0, ∞	2.0	Fixed cylindrical

*[d_{smin} / d_{smax}] The mesh changes from fine near the contact to a coarser mesh further away.

In the following sections, selected results are presented. First, we present the results for ship-ice interaction. Then we present the results for the fixed structure scenario.

Case #1.1; influence of time step in ship-ice interaction

In the ship simulation case, the influence of time step size on the results is minimal for $dt \leq 0.01$ s, and is significant for the presented higher step sizes. The results are shown in Figure 6. An interesting observation in the below figures is that while the contact force is lower at $t = 0.1$ s for the large time step cases, the vertical sheet deformation at the contact point is higher at this time. This indicates that the sheet dynamics are no longer accurate at these time steps.

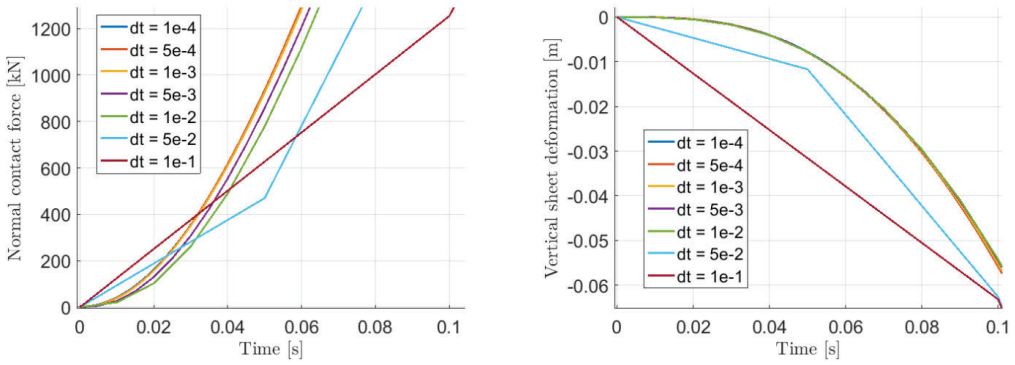

Figure 6. Contact force as a function of time (left) and vertical sheet deformation as a function of time (right), for a range of time step sizes *dt*.

Case #1.2; influence of mesh size on ship-ice interaction

The influence of mesh size on the contact force and the sheet deformation is shown in Figure 7. Note that the contact force is hardly effected by the mesh size in this simulation case. This may be explained by the result presented in Figure 9. At an interaction velocity $v = 5.0$ m/s, bending deformation is much smaller than the local crushing deformation. This reduces the effect of sheet deformation on contact force. Therefore, the inaccuracy in sheet deformation behavior that occurs for coarser meshes has little effect on the contact force build up. The right plot of Figure 7 shows that the local mesh deformation stiffness is increased as the mesh size increases. This is in line with the results presented in (ref ATC 2016) and can be attributed to the inability of coarse meshes to capture the local sheet deformation near the contact point.

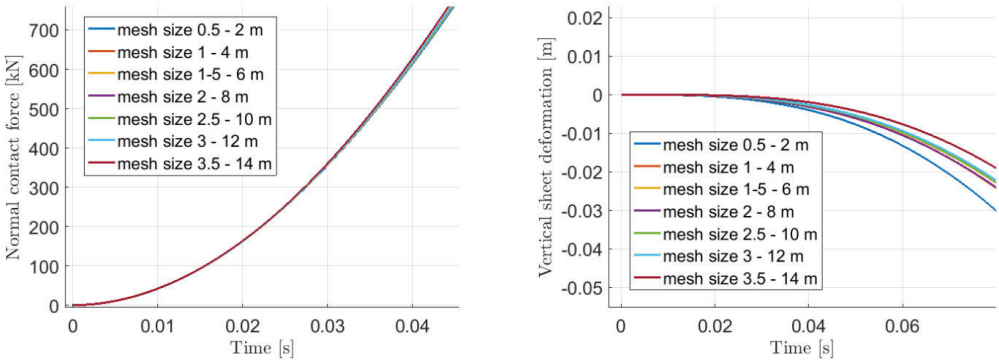

Figure 7. Contact force as a function of time (left) and vertical sheet deformation as a function of time (right), for a range of time step sizes.

Case #1.3; influence of interaction velocity in ship-ice interaction

In contrast to mesh size and time step, which are purely numerical features, the interaction velocity is a parameter of the actual interaction. We choose to investigate and demonstrate the influence of interaction velocity on the model results because it demonstrates the importance of sheet dynamics on the results. The influence of interaction velocity is apparent in Figure 8. Here, the vertical sheet deformation at the loading point is plotted against the contact normal force. At higher interaction velocities, the sheet deformation increases much slower with an increasing normal force. This can be attributed to ice sheet inertia and hydrodynamic damping. Since strain is often used as a failure criterion, different deformation behavior will also result in a different failure pattern. In case of bending failure, this will most likely mean a shorter failure length.

Note that the contact normal force is limited for the lowest interaction velocities, 0.05 m/s and 0.1 m/s. At these velocities, the sheet reaches the same velocity as the ship before the cut-off normal force is reached.

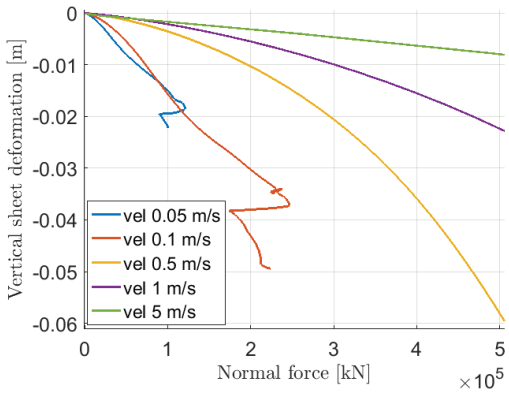

Figure 8. Contact force against sheet deformation for different interaction velocities

Another interesting observation can be made when looking at the difference between local crushing deformation and sheet bending deformation. This is shown in Figure 9. At lower interaction velocities, there is both bending deformation in the ice sheet and local crushing deformation. At high interaction velocities, the sheet deformation is much smaller compared to the crushing deformation, which may result in a steeper increase of the contact force.

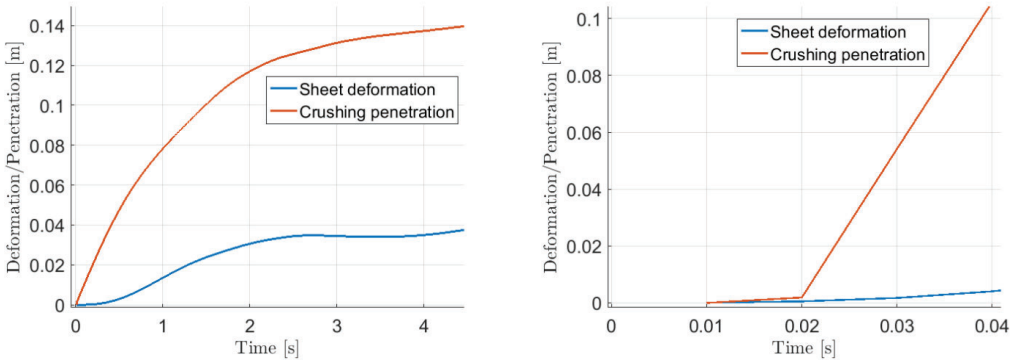

Figure 9. Sheet deformation and crushing penetration at an interaction velocity of 0.1 m/s (left) and 5.0 m/s (right).

Case #2.1; influence of time step on fixed structure – ice interaction

Figure 10 and Figure 11 shows the load from the ice on the fixed structure in the direction opposite to the propagation direction. Any change in time step causes a clear difference in the load signal. We may wonder if a complete correlation between load-time signals should be expected. Due to the nature of the modelled case, the load at any moment in time depends on the ice floe displacements in the previous simulation steps. Because of this, minimal (numerical) differences in the beginning of the simulation may lead to a completely different load signal later in the simulation. Therefore, the properties of the signals over the duration of the simulation should be compared, rather than comparing the exact load values at any moment in time. The current simulations are considered too short to say anything statistically significant about the load-time signals, but from visual comparison we conclude that the signals for time steps $5.0 \cdot 10^{-2}\,s$ to $1.0 \cdot 10^{-3}\,s$ show similar behavior. Even the load-time signal for $1.0 \cdot 10^{-1}$ s has peak loads and an average load value of comparable size.

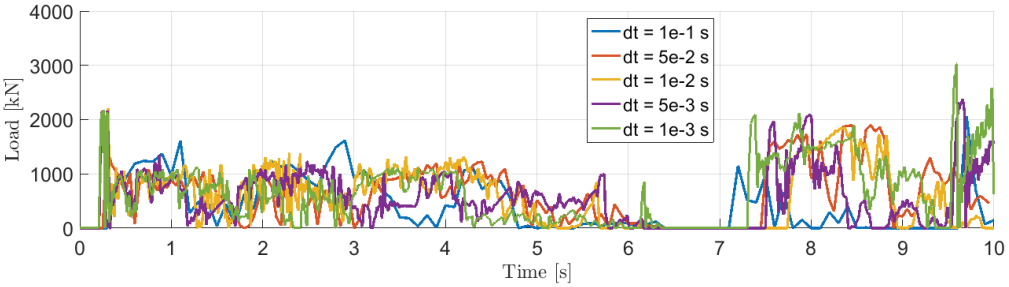

Figure 10 Unfiltered load-time signals, time steps $1 \cdot 10^{-3}\,s$ to $1 \cdot 10^{-1}$ s.

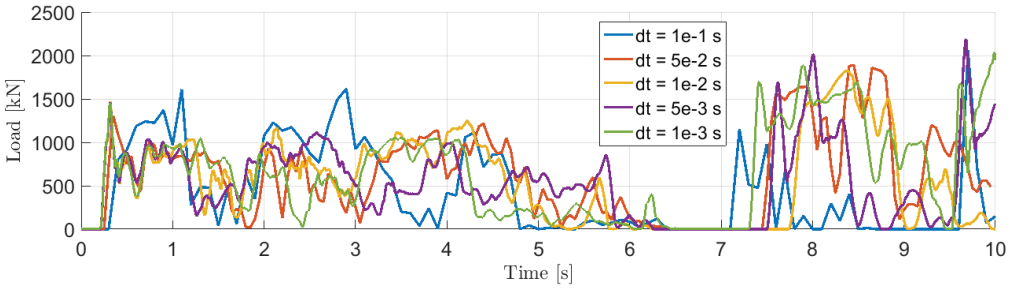

Figure 11. Filtered load-time signals, time steps $1 \cdot 10^{-3}\,s$ to $1 \cdot 10^{-1}\,s$.

Case #2.2; influence of mesh size on fixed structure – ice interaction

Figure 12 and Figure 13 shows the load from the ice on the fixed structure in propagation direction, in a comparison for different mesh sizes. As discussed in the previous section, we should not expect a correlation over the whole time signal because of the nonlinear nature of the simulation. The results are similar for the first second of the simulation, after which the results start to differ. Comparing the load-time signals over the complete duration, we see that the signals for mesh sizes 5.0 – 1.0 m have broadly similar characteristics. The load-time signals for no mesh and for a mesh size of 10.0 m are similar to each other, but are different from the signals obtained with finer mesh sizes.

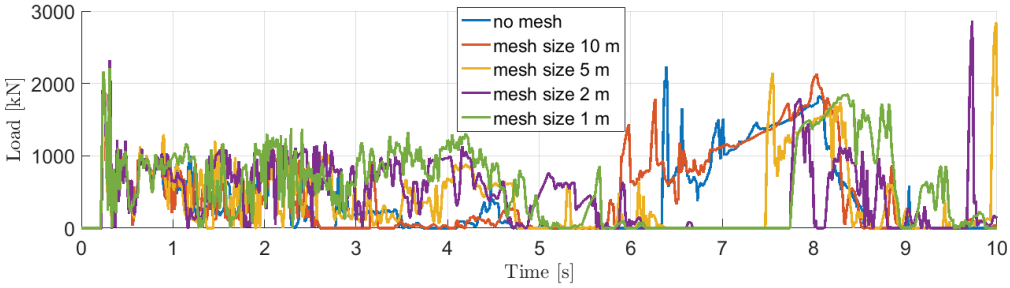

Figure 12 Unfiltered load-time signals, no mesh to mesh size 1 m.

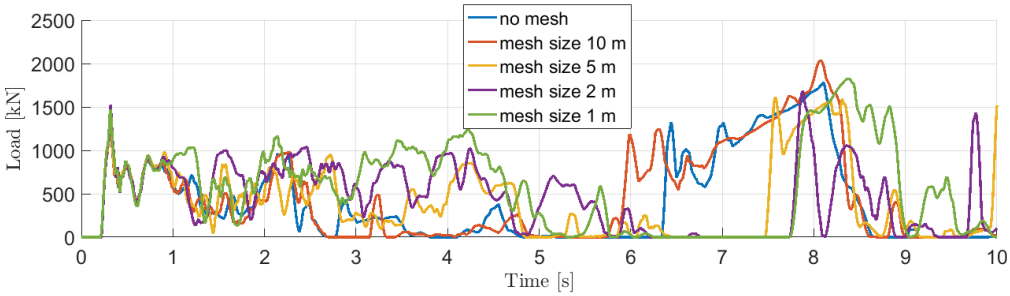

Figure 13. Filtered load-time signals, no mesh to mesh size 1 m.

CONCLUSIONS

The accuracy limits of a novel non-smooth discrete element time stepping scheme that includes contact non-rigidity were investigated. The sensitivity of model results to mesh density, time step and interaction velocity were compared. Based on the results of this analysis, we draw the following conclusions:

Case #1: Ship – single floe interaction

- The ship-ice interaction results can be considered accurate for time steps ≤ 0.01 s. For larger time steps, the model results start to differ significantly.
- The mesh size has little influence on the results in the performed simulations. This is due to the high interaction velocity, which reduces the effect of ice floe deformation on the results.
- At low velocity interaction, the ice floe deformation was significant compared to the local crushing deformation. For high interaction velocities, (> 1 m/s) the sheet deformation is much smaller than the local crushing deformation. Hydrodynamic damping and inertia of the ice floe cause the difference in deformation behavior. This will most likely result in a different failure pattern for high velocity interactions.

Case #2: Fixed structure floe field interaction

- Due to the nonlinear nature of the simulation, we should not expect a correlation between results over the full time signal. A minimal (numerical) difference in the beginning of the simulation may lead to completely different results later on.
- Comparing the load-time signals for different time step sizes, we find broadly similar results for time steps $5.0 \cdot 10^{-2}\ s$ to $1.0 \cdot 10^{-3}\ s$.
- Comparing the load-time signals for different mesh sizes, the results for mesh sizes 5.0 -1.0 m are broadly similar.

In the fixed structure simulation case #2, the local crushing at ice-ice and ice structure contacts is important for a correct contact force prediction, but the elastic ice floe deformation (taken into account by the lattice model) does not have much influence on the load signal. In the ship simulation case #1, the bending deformation of the ice floe influences the contact force at low interaction velocities. At higher interaction velocities, local crushing is much more important. Since the sheet deformation as a function of contact force is different at high ice velocities, we expect that the failure pattern will also change as a function of interaction velocities. These results were obtained while neglecting the added mass of the water. Including added mass will most likely exacerbate the velocity effects.

ACKNOWLEDGEMENTS

The authors would like to acknowledge the support from the SAMCoT CRI through the Research Council of Norway and all of the SAMCoT Partners.

REFERENCES

van den Berg, M., 2016. A 3-D Random Lattice Model of Sea Ice. In *Arctic Technology Conference. St. Johns, Newfoundland and Labrador*.

Kim, E. & Høyland, K. V., 2014. Experimental Investigations of the Energy Absorption Capacity of Ice During Crushing: Is the Specific Energy Scale Independent? *Proceedings of the 22nd IAHR International Symposium on Ice*, pp.163–170.

Kinnunen, A., Tikanmäki, M. & Heinonen, J., 2016. An energy model for ice crushing in ice-structure impact. In *23 r d IAHR International Symposium on Ice*. Ann Arbor, Michigan, USA, pp. 1–8.

Krabbenhoft, K. et al., 2012. Granular contact dynamics with particle elasticity. *Granular Matter*, 14(5), pp.607–619.

Lacoursiere, C., 2007. *Ghosts and machines: regularized variational methods for interactive simulations of multibodies with dry frictional contacts*. Umeå University.

Servin, M. et al., 2014. Examining the smooth and nonsmooth discrete element approaches to granular matter. *International Journal for Numerical Methods in Engineering*, (March), pp.1885–1891.

Tsarau, A., 2015. *Numerical Modelling of the Hydrodynamic Effects of Marine Operations in Broken Ice*. Norwegian University of Science and Technology.

Yip, M., Mohle, J. & Bolander, J.E., 2005. Automated Modeling of Three-Dimensional Structural Components Using Irregular Lattices. *Computer-Aided Civil and Infrastructure Engineering*, 20, pp.393–407.

Yulmetov, R., Løset, S. & Lubbad, R., 2014. An Effective Numerical Method for Generation of Broken Ice Fields, Consisting of a Large Number of Polygon-Shaped Distinct Floes. In *Proceedings of the 22nd IAHR International Symposium on Ice*.

Appendix D

The effect of ice floe shape on the load experienced by vertical-sided structures interacting with a broken ice field

This paper is Published in Marine Structures, issue 62 (2019).

Marine Structures 65 (2019) 229–248

Contents lists available at ScienceDirect

Marine Structures

journal homepage: www.elsevier.com/locate/marstruc

The effect of ice floe shape on the load experienced by vertical-sided structures interacting with a broken ice field

Marnix van den Berg*, Raed Lubbad, Sveinung Løset

SAMCoT, Department of Civil and Environmental Engineering, NTNU, NO-7491, Trondheim, Norway

ARTICLE INFO

Keywords:
Ice floe shape
Discrete element modelling
Broken ice

ABSTRACT

In this study, numerical experiments are conducted to investigate the effect of ice floe shape on the load experienced by vertical-sided structures interacting with a broken ice field. We create numerical ice fields with different floe shapes and otherwise identical properties. These fields are used to simulate ice-structure interaction with vertical-sided structures. First, we investigate the effect of floe shape in ice-tank tests by comparing the numerical results to the ice tank test results. Then, we conduct a sensitivity study to investigate the correlation between the floe shape effect and other parameters. The primary finding is that the ice floe shape has a large influence on the mean and standard deviation of the ice load in interaction scenarios dominated by ice accumulation and clearance around the structure. In particular, square floes, which are often used in ice tank tests, result in higher mean loads and standard deviations than other floe shapes. The simulation results show that the greater length and higher stability of force chains is the primary mechanism causing the floe shape effect. The floe shape effect is exacerbated in confined conditions, where the force chains may cause bridging between the structure and a rigid boundary. The presence and length of 'parallel opposite edges' is an important factor influencing the floe shape effect. This result is novel compared to earlier studies, which only consider body 'roundness' or 'angularity' in assessing shape effects. We demonstrate the importance of using accurate floe shapes in ice tank tests and in discrete element method (DEM) modelling of broken ice-structure interaction scenarios.

1. Introduction

The Arctic sea ice cover is decreasing both in areal coverage and thickness as a result of the long-term changes in the climate. Therefore, sea ice will be encountered more often in the form of broken ice, rather than intact level ice.

The prediction of broken ice loads on structures is complicated by many (often not well understood) phenomena that may influence the ice load. The contributing factors are the ice areal coverage; the ice thickness; the ice material properties and the floe size (including size distribution); the floe shape; the quantity of brash ice; the ice drift velocity; the wind and current conditions; and the confinement conditions (e.g., by a shoreline or other structures).

Of the above factors, the effects of the ice areal coverage, the ice thickness and the ice drift velocity are most studied. The ice areal coverage is found to have the largest influence on the ice load (Comfort et al. [1]. However, most studies of broken ice loads do not take the ice floe shape into account as a parameter. Therefore, its influence is currently not well understood.

In this study, the influence of ice floe shape on the load experienced by structures interacting with a broken ice field is

* Corresponding author.
E-mail address: marnix.berg@ntnu.no (M. van den Berg).

https://doi.org/10.1016/j.marstruc.2019.01.011
Received 24 September 2018; Received in revised form 12 December 2018; Accepted 24 January 2019

investigated. The study is limited to low to medium ice areal coverage conditions (30–70%). The effect of the floe shape is most relevant in these conditions because the ice clearing process often governs the ice resistance. Furthermore, we limit the study to vertical-sided structures. Sloping sides promotes bending failure and floe rafting, significantly reducing the effect of the floe shape.

There are several scenarios in which the load from low-to medium-areal-coverage broken ice on vertical-sided structures is of interest. Three examples are:

1. *Constructions in the light Arctic.* We define the light Arctic as regions where sea ice may occur as a statistical possibility, but which are normally ice-free throughout the year. Most recent Arctic offshore developments are in these regions. Structures for these regions are not usually designed for heavy ice conditions, and may have a vertical-sided waterline. Loads from low-to medium-areal-coverage broken ice may be the operational design load for such structures.
2. *Operations in the 'ice-free' season.* This includes drilling, towing or construction operations, possibly using jack-ups or other vertical-sided structures. Low-to medium-areal-coverage broken ice load estimates are needed to determine the operating window.
3. *Structures supported by ice management.* Structures can be supported by ice management operations, in which an ice breaker reduces the size of incoming ice floes in order to decrease the loads on a protected structure. Broken ice loads may be the design load of the protected structure.

Floe shape effects are especially relevant to ice tank tests or numerical simulations that may be performed in the design phases for the above mentioned scenarios. In ice tank tests, broken ice is created by manually or mechanically breaking up an intact ice sheet. Therefore, the resulting ice floe shapes can be controlled to some extent. Ice tank tests with broken ice are often performed with ice floes that have square or rectangular shapes (e.g., Hoving et al. [2]; Haase et al. [3], which may have a major effect on the resulting broken ice load.

The effect of floe shape on rafting of a broken ice field was studied by Tuhkuri and Lensu [4]. Tuhkuri and Lensu [4] found that the floe shape does not have a clear effect on the force. The effect of the floe shape in discrete element method (DEM) modelling of ice has been studied by Hopkins et al. [5]; Tuhkuri and Polojärvi [6]; Konno et al. [7]; Rheem et al. [8]; Yamaguchi et al. [9]. Hopkins et al. [5] and Tuhkuri and Polojärvi [6] studied the effects of rubble shape on the ridge formation process and on ridge keel punch through tests. Konno et al. [7] studied the effect of rubble shape on the resistance of ships in rubble channels. These studies showed a clear shape effect. However, the modelled scenarios in these studies are different from the scenarios modelled in the current study, because the studied scenarios concern ice rubble only. This paper investigates the effect of floe shape in broken ice varying in size from $20m^2$ to $4832m^2$. Such broken ice fields typically occur when ice is broken by environmental factors, such as ocean gravity waves. To the authors' knowledge, Rheem et al. [8] and Yamaguchi et al. [9] are the only researchers that studied the effect of the floe shape in similar broken ice-structure interaction scenarios. However, the scenarios tested by Rheem et al. [8] were primarily designed for the validation of a numerical model; therefore, they are not sufficiently realistic to conclude anything on floe shape effects in actual broken ice structure interactions, other than that the effect is present. Yamaguchi et al. [9] proposed a method to take the floe shape effect into account using a parameter described as the *C*-angle. However, the tested scenarios are limited and the numerical model is greatly simplified. For example, no floe rotation is taken into account.

In the DEM modelling community, there are many studies on the effect of body shape, of which Cleary and Sawley [10] is one of the most cited examples. The effect of body shape is mostly studied in relation to particle flow through a hopper (Cleary and Sawley [10], the stability and shear strength of packings (Azéma et al. [11], and the behaviour of bodies in a rotating drum (Höhner et al. [12]. Although a shape effect is observed in all situations, the results are not sufficiently generalized or comparable to broken ice-structure interaction to extrapolate their findings to the scenarios modelled in the current study.

The simulations for this study are performed with an adapted version of the *Simulator for Arctic Marine Structures* (SAMS), a product of *Arctic Integrated Solutions* (ArcISo); see *ArcISo* [13]; Lubbad et al. [14]. To study the effect of floe shape, first we numerically reproduce ice tank tests using different floe shapes to demonstrate that the floe shape had an influence in the described tests. Thereafter, we perform a parametric study in which the correlation of the floe shape effect with other parameters is investigated. The results show that the floe shape has a strong influence on the mean and standard deviation of the simulated ice loads in all studied parameter combinations.

2. Methodology

We study the effect of floe shape using DEM modelling. Ice-ice and ice-structure contacts are resolved using the non-smooth discrete element method (NDEM). Section 2.1 explains the used method in more detail. The study of floe shape effects is divided into two parts.

In Part 1, the presence and relevance of the floe shape effect is demonstrated by a comparison of ice tank test results to numerical simulation results. The ice tank tests used for the comparison were carried out as part of the Hydralab IV project (Hoving et al. [2]. The experiment is replicated numerically with the floe shapes used in the tank experiment, and additionally with triangular, square and circular floe shapes. The numerical replication of the ice tank tests is explained in further detail in Section 2.2.

In Part 2, we perform a sensitivity study in which the floe shape and other parameters whose effect may be correlated with the floe shape effect are systematically varied. The mean load and the standard deviation of the surge load on the structure are used as the primary comparison parameters in analysing the effect of the floe shape. The time series comparison methodology is further explained in Section 2.3. The investigated parameters are the structure shape, the ice areal coverage, the confinement conditions and the friction coefficient. This is further described in Section 2.4. In the sensitivity study, the broken ice fields are created randomly,

using a method that enables the generation of very large unique broken ice fields. The random ice field generation method is further explained in Section 2.5.

2.1. The discrete element method

The discrete element method which is used in the numerical simulations can be classified as a non-smooth discrete element method. Ice-ice, ice-structure and ice-wall contacts are compliant. The contact compliance parameters are determined based on the material properties and the geometrical properties of the contacts, under the assumption that local ice crushing will occur. The method used in the simulations is explained by van den Berg et al. [15].

In NDEM, a mixed linear complementarity problem (MLCP) is solved at each time step. For the simulations in this study, the MLCP is formulated as follows:

$$\begin{bmatrix} \boldsymbol{M} & -\boldsymbol{J}_h & -\boldsymbol{J}_c \\ \boldsymbol{J}_h^T & \boldsymbol{\Sigma}_h & 0 \\ \boldsymbol{J}_c^T & 0 & \boldsymbol{\Sigma}_c \end{bmatrix} \begin{bmatrix} \boldsymbol{\Delta \dot{u}} \\ \boldsymbol{\lambda_h} \\ \boldsymbol{\lambda_c} \end{bmatrix} + \begin{bmatrix} 0 \\ \boldsymbol{\Upsilon_h} \\ \boldsymbol{\Upsilon_c} \end{bmatrix} = \begin{bmatrix} 0 \\ 0 \\ \boldsymbol{\alpha} \end{bmatrix} \tag{1}$$

$$0 \leq \boldsymbol{\lambda}_c^T \perp \boldsymbol{\alpha}^T \geq 0 \tag{2}$$

where $\boldsymbol{M}$ is a diagonal mass matrix containing the inertial properties of all bodies within the simulation; $\boldsymbol{J}_h$ and $\boldsymbol{J}_c$ are matrices containing constraint Jacobians, which express the influence of contact impulses on body velocities; $\boldsymbol{\Delta \dot{u}}$ is a vector containing the velocity change (both linear and rotational) of each body in the simulation domain; $\boldsymbol{\lambda_h}$ and $\boldsymbol{\lambda_c}$ are vertices containing the constraint impulses, which express the time-integrated contact forces within one time step; $\boldsymbol{\Sigma}_h$ and $\boldsymbol{\Sigma}_c$ are matrices containing the impulse-dependent compliance factors; vertices $\boldsymbol{\Upsilon_h}$ and $\boldsymbol{\Upsilon_c}$ contain the compliance factors which are independent from the contact impulses; and $\boldsymbol{\alpha}$ is a vector of residuals with no physical meaning. The difference between the variables with subscripts h and the variables with subscripts c is that the variables with subscripts h contain the holonomic constraints, i.e., the constraints with no upper or lower limits to the impulses, while the variables with subscripts c contain the non-holonomic constraints, i.e., the constraints for which the impulses are bound by upper and lower limits. A holonomic constraint is used in the simulations for this study to propagate the structure with a constant velocity.

Upper and lower limits to the contact forces are enforced by the complementarity condition as specified in Eq. (2). The following limits are enforced:

$$\boldsymbol{\lambda_n} \geq 0 \tag{3}$$

$$\boldsymbol{\lambda_t} \leq \mu \boldsymbol{\lambda}_n \tag{4}$$

$$\boldsymbol{\lambda}_\phi \leq \frac{1}{2} \boldsymbol{l}_c \boldsymbol{\lambda}_n \tag{5}$$

where $\boldsymbol{\lambda}_n$ are the normal impulses, $\boldsymbol{\lambda}_t$ are the frictional impulses, $\boldsymbol{\lambda}_\phi$ are the rotational impulses that occur between interacting bodies, and $\boldsymbol{\lambda}_n$, $\boldsymbol{\lambda}_t$ and $\boldsymbol{\lambda}_\phi$ are part of the $\boldsymbol{\lambda_c}$ vector in Eq. (1). Eq. (3) states that there cannot be any tension at the ice-ice or ice-structure contacts. Eq. (4) states that the frictional impulses are limited by a friction coefficient μ and the normal impulse occurring at the same contact. Eq. (5) states that the rotational impulses are limited by the normal impulse at that contact and the contact length l_c. The contact length l_c is defined as follows:

$$\frac{A_c}{h} \tag{6}$$

where A_c is the contact area and h is the ice thickness. The variable A_c is defined as the contact projected area in the case of ice-ice

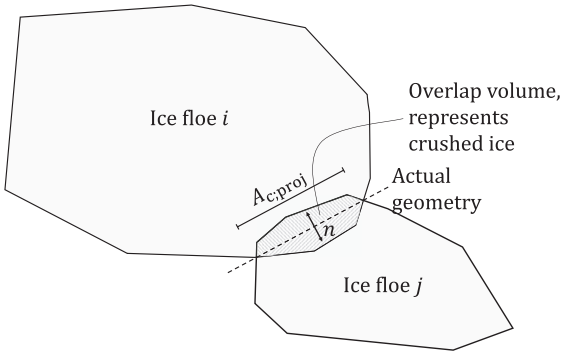

Fig. 1. Ice-ice contacts are resolved using the contact projected area and normal direction.

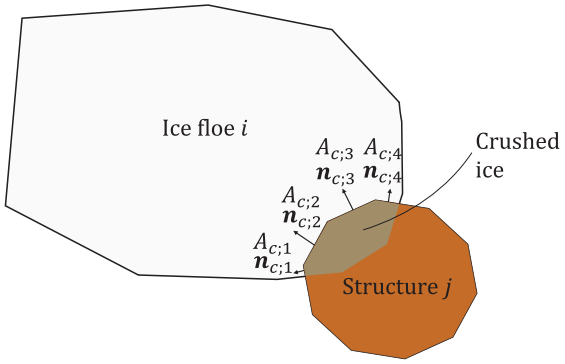

Fig. 2. Ice-structure contacts are resolved using the sub-contact areas of each structure panel (partly) in contact with an ice sheet.

contact. In the case of ice structure contact, it is defined as the area in contact with the ice of each individual structure panel, which is clarified in Figs. 1 and 2. For further details and explanation on how the limits expressed in Eqs. (3)–(5) lead to the MLCP as formulated in Eqs. (1) and (2), the reader is referred to van den Berg et al. [15].

The contact parameters representing compliance are determined based on an assumption of constant crushing specific energy (CSE) (Kim and Gagnon [16]. The CSE is the amount of energy needed to crush a unit volume of ice (unit: J/m^3). The CSE assumption is used in combination with the exact contact geometry to determine the compliance properties of each contact, such that the loss in kinetic energy matches the energy dissipated in local ice crushing:

$$\mathrm{CSE}\cdot\Delta V_o = -\Delta E_k \;\leftrightarrow\; \Delta V_o > 0 \tag{7}$$

in which ΔV_o is the change in overlap volume at the contact and ΔE_k is the change in kinetic energy of the contacting bodies. The contact geometry and overlap volume is determined by finding the intersection points of the lines that form the ice floe shapes, and composing the contact geometry from these points. The local crushing assumption results in a contact behaviour with zero restitution; all available kinetic energy is dissipated. This type of contact behaviour can be viewed as hysteratic damping. A detailed mathematical description of the contact model is provided by van den Berg et al. [15].

Using the contact forces occurring at the compliant contacts, ice floe splitting is implemented using closed-form analytical solutions as presented by Lu et al. [17]. Bending failure is not considered because we limit the study to vertical-sided structures. Form drag and skin friction on the ice floes are calculated as described by Tsarau [18].

The limitations of the model used in this study are clarified below.

Exclusion of rafting and ridging behaviour. Floe rafting is excluded because of a lack of a generally accepted model or mechanism to describe ice floe rafting. There is not much literature examining broken ice rafting behaviour. A mechanical model of sea ice rafting behaviour was presented by Parmerter [19]. This model is based on the assumption that the sides of the ice floes are non-vertical and that there is no friction between two interacting ice sheets. However, data on the 'non verticality' of the sides of broken ice is not known to the authors. Additionally, we question the validity of the zero friction assumption. Broken ice rafting experiments were done in the 1990's, by Tuhkuri and Lensu [4]; Tuhkuri [20]. Numerical modelling of these experiments is described by Hopkins and Tuhkuri [21]. Hopkins and Tuhkuri [21] modelled circular ice floes with hemispherical edges. To match the rafting behaviour as observed in the experiments, Hopkins and Tuhkuri [21] introduced and tuned a 'circular edge friction coefficient' that varied with the ice thickness. This method relies on experimental data to determine appropriate values, and the values used in Hopkins and Tuhkuri [21] cannot be simply translated to appropriate values for other ice floe sizes or thicknesses or to the appropriate full-scale values. Moreover, the numerical model used in the current paper assumes vertical floe edges; thus, the method of Hopkins and Tuhkuri cannot be directly applied.

Considering the modelled ice floe sizes, areal coverage and ice thickness of the broken ice floes used in the simulations presented in this paper, we would expect rafting to occur only when significant accumulation of ice occurs. In this case, rafting can be a load releasing mechanism capping the upper limit load that may occur. As rafting is considered the initial stage of ice ridging, excluding rafting behaviour also excludes ridging.

No ice rubble and no brash ice. Ice rubble and brash ice is not modelled primarily because of numerical reasons. The inclusion of rubble as a large number of small bodies would make the simulations too inefficient to generate the statistically significant results that are needed for the examinations done in this study. Additionally, ice rubble can occur in many forms; therefore, the size and size distribution as well as the quantity of rubble particles would be additional variables in the sensitivity analysis. In existing numerical models, rubble or brash is sometimes included as a viscous fluid (Løset [22]. However, the properties of this representative fluid are not quantified, and it is not clear that the inclusion of ice rubble or brash ice as a fluid will properly capture its influence on the discrete ice-structure interaction process. Because rubble is not included in the simulation, the presented results should be considered valid for no- or low-rubble broken ice conditions only.

Although our numerical model is capable of performing 3D simulations including bending, we choose to perform 2D simulations since 3D effects, such as bending failure and floe rafting, are not taken into account. Since the simulations are in 2D, each ice floe has

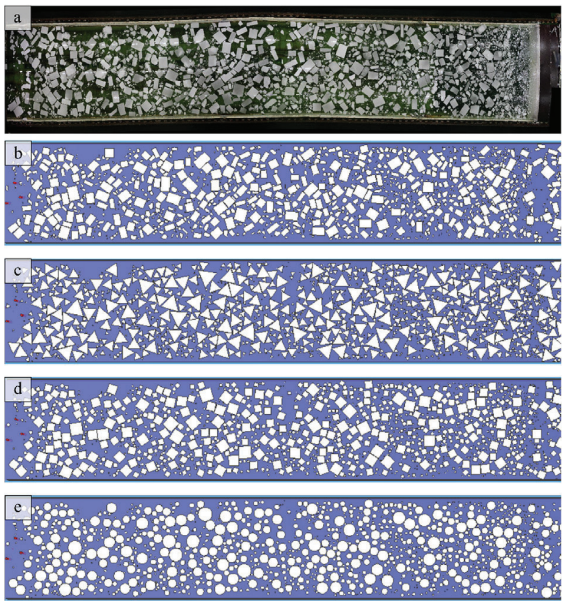

Fig. 3. Top view photo of the Hamburg Ship Model Basin (HSVA) ice field (a) and digitizations of the field using different ice floe shapes. From top to bottom; 'real' shapes (b), triangles (c), squares (d) and circles (e). Note that the numerical fields are extended with randomly placed ice floes, whereas the HSVA ice field ends with a sloping boundary.

three degrees of freedom; two translational and one rotational.

Given the limitations regarding ice rubble and floe rafting behaviour, the validity of the results must be carefully interpreted. For certain parameter combinations, phenomena occur that we would not expect to see in reality because floe rafting and ridging would occur as load limiting mechanisms. This finding is further discussed in Section 5.

2.2. Part 1: The effect of ice floe shape in ice-tank tests

The first part of this study examines the effect of floe shape on loads measured in an ice-tank test. The experiment we used as comparison involves a structure with four vertical-sided cylindrical legs at the waterline that moves through a broken ice field with a reported concentration of 60%. Most of the floes in this experiment are rectangular in shape. More details can be found in Hoving et al. [2]. These experimental results have been used previously for comparison to the results of a numerical model by van den Berg et al. [15]. We chose these experimental results as comparison case because it is the processing of these results which led to the current study of the floe shape effect.

The experimental results are compared to the results of numerical replications of the ice-tank test. The numerical replications are performed with 1) the digitized floe shapes (as used in the actual experiment), 2) triangular floe shapes, 3) square floe shapes and 4) circular floe shapes. The generated broken ice fields are shown in Fig. 3. All other broken ice properties except for the floe shape remain constant.

The structure geometry is shown in Fig. 4. Other parameters used in the simulations of the experiment are shown in Table 1. Note that there are two velocities listed in the table. During the experiment, the structure moved with the lower velocity for the first one-third of the experiment, while moving with the higher velocity for the last two-thirds of the experiment, resulting in an equal measurement duration for each velocity.

The Hamburg Ship Model Basin (HSVA) ice tank has a sloping boundary at the far end of the ice tank. Since the simulations were performed in 2D, the sloping boundary at the end of the ice tank was not included in the numerical simulation. Instead, the numerical ice field is extended by a random field with similar properties as the ice field used in the ice tank. This is clarified in Fig. 3.

The results of this type of experiment are very sensitive to the initial conditions. The initial conditions of the numerical experiments will always be slightly different from the actual experiment because of inaccuracies in the broken ice digitization and the uncertainty in the model parameters. Therefore, a direct time-series comparison between the numerical and experimental results is not very informative; the time series will always be different. Hence, we investigate the statistical properties of the numerical results, examining how these properties are influenced by the floe shape. Statistical properties are obtained by running 100 numerical simulations for each floe shape. In each simulation, a slight variation is introduced by giving the ice floes a low random initial velocity of 0.002 m/s. The initial velocity is quickly dissipated because of drag, but it results in slightly different initial floe positions. From the 100 data points obtained at each time step, the 5th lowest (P_5), the mean, and the 5th highest (P_{95}) simulation results are compared to the ice tank test results.

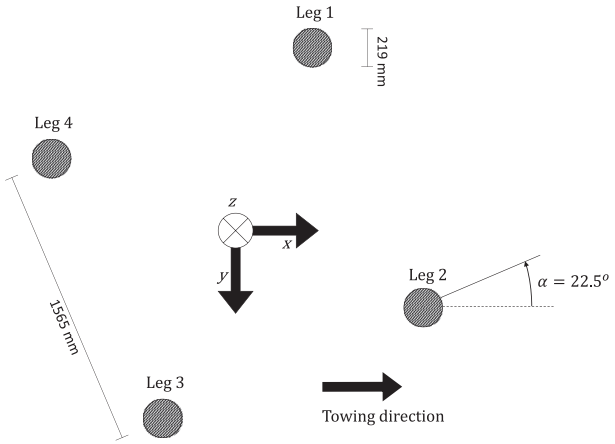

Fig. 4. Waterline geometry of the test structure (from van den Berg et al. [15].

Table 1
Parameters used in the numerical simulations (from van den Berg et al. [15].

Ice thickness [m]	0.0346
Ice-ice friction coefficient [−]	0.12
Ice-structure friction coefficient [−]	0.12
Ice areal coverage (from analysis) [%]	62.9
CSE [kJ/m^3]	29
Carriage velocity [m/s]	0.09–0.18
Skin friction drag coefficient [−]	0.005
Form drag coefficient [−]	0.5
Water density [kg/m^3]	1005
Ice density [kg/m^3]	900
Gravity acceleration [m/s^2]	9.81

2.3. Part 2: sensitivity study; time series comparison methodology

In the sensitivity study, time series for different parameter combinations are compared using the mean and standard deviation of the ice load in the surge direction. We ensure statistical homogeneity of the results by inspecting the cumulative mean load and standard deviation as a function of interaction length. If the results are statistically homogeneous, the cumulative mean and standard deviation should converge to constant values as the simulation progresses. The cumulative mean load is calculated as follows:

$$\bar{F}_{x;N}(l) = \frac{\sum_{i=1}^{N} F_{x;i}}{N(l)} \tag{8}$$

where $N(l)$ is the number of time steps until interaction length l and F_x is the total ice load on the structure in the surge direction. The cumulative standard deviation is calculated as follows:

$$\sigma_{Fx;N}(l) = \sqrt{\frac{\sum_{i=1}^{N} (F_{x;i} - \bar{F}_{x;N}(l))^2}{N(l) - 1}} \tag{9}$$

For all simulations, except for the case of triangular and square floes in the confined domain with the high friction coefficient $\mu = 0.5$, the data shows that the cumulative mean and the cumulative standard deviation converge to constant values. An interaction length of 10 000 m is needed to reach convergence of the mean and standard deviation in all simulations. The following convergence criterion was used:

$$\frac{\max(\bar{F}_{x;N}(l - 500{:}\ l)) - \min(\bar{F}_{x;N}(l - 500{:}\ l))}{\bar{F}_{x;N}(l)} \leq 0.03 \tag{10}$$

and similarly for the standard deviation:

$$\frac{\max(\sigma_{Fx;N}(l - 500{:}\ l)) - \min(\sigma_{Fx;N}(l - 500{:}\ l))}{\bar{F}_{x;N}(l)} \leq 0.03 \tag{11}$$

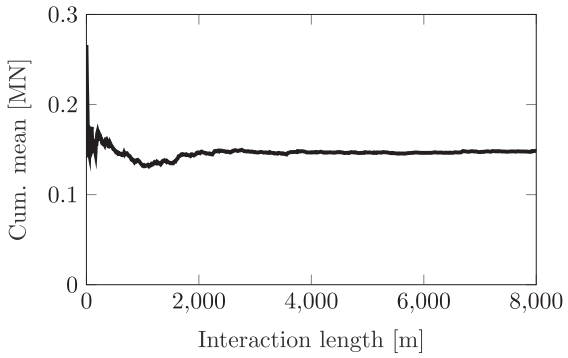

Fig. 5. Cumulative mean load, 70% areal ice coverage, no confinement, digitized real floes and friction coefficient $\mu = 0.1$.

The convergence criteria in Equations (10) and (11) state that the variance of the mean and standard deviation of the structure load in the last 500 m of the simulation must be less than 3%. Figs. 5 and 6 show examples of a converging cumulative mean and standard deviation for the simulation case of 70% areal ice coverage, no confinement, digitized real floes and friction coefficient $\mu = 0.1$. The first 2000 s of each simulation were discarded, since the load statistics are different in this start-up period because the processes affecting the ice load are developing. The non-converging results are further studied in Section 5.

2.4. Part 2: sensitivity study; investigated parameter combinations

In the sensitivity study, we investigate the correlation between the floe shape effect and other environmental and structural parameters to determine in which conditions the floe shape effect is (most) important. To investigate the correlation, we formulate a test matrix in which we systematically vary model parameters that may correlate with the floe shape effect. Because of the long duration of each individual simulation, we limit the test parameters to the ones that we expect to have the highest correlation with the floe shape effect. In addition, there are some practical considerations affecting our parameter choice. The chosen simulation parameters are shown in Table 2.

We discuss the chosen parameter combinations and explain why we chose to investigate the influence of these parameters in the following sections.

Structure shape. The correlation of the structure shape with the floe shape effect was expected to be especially important in combination with confinement. The shape of the structure may influence the formation of force chains and may encourage 'ice bridging' between the structure and ice tank walls. We test a square and a circular structure shape, in which the sides of the square structure are parallel and perpendicular to the propagation direction (i.e., the structure is not rotated).

Confinement conditions. The influence of confinement conditions is investigated because of their relevance to the ice tank tests. Earlier studies performed by the authors (van den Berg et al. [15] as well as earlier ice tank experiments (Hopkins and Tuhkuri [21] suggest that tank walls may influence ice tank test results under certain conditions. We expected that the influence of confinement by tank walls may be correlated to the ice floe shape effect.

Areal ice coverage. Ice areal coverage is one of the most important parameters determining the resistance of structures in broken ice (Comfort et al. [1]. We expected a strong correlation between the broken ice shape effect and the areal coverage. In former ice-tank tests and numerical simulations, the results showed that for high ice areal coverage (> 70%), ice clearance is no longer the predominant load limiting mechanism; therefore, the effect of floe shape becomes less important with high areal coverage. We test

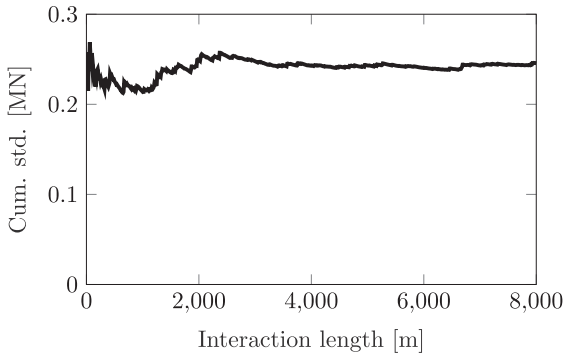

Fig. 6. Cumulative standard deviation, 70% areal ice coverage, no confinement, digitized real floes and friction coefficient $\mu = 0.1$.

Table 2
Investigated parameter combinations.

Constant parameters	
ice thickness	1.0 [m]
CSE	2.0 [MJ/m^3]
structure width	40.0 [m]
structure velocity	1.0 [m/s]
ice form drag coefficient	0.5 [-]
ice skin friction drag coefficient	0.005 [-]
floe area distribution	from top view photo
Varying parameters	
structure shape	square circular
confinement conditions	ice tank walls unconfined
ice areal coverage	30% 50% 70%
floe shape	digitized real floes 3–8 corner regular circular
friction coefficient	0.1 [-] 0.5 [-]

the floe shape effect in ice areal coverage ranging from 30% to 70%.

Friction coefficient. Frictional forces play an important role in the accumulation of broken ice. Therefore we expected a correlation between the assumed friction coefficient and the effect of the floe shape. We investigate the influence of floe shape at friction coefficients of 0.1 and 0.5. These values roughly coincide with the lower and upper values used in the literature for simulations of similar ice-structure interaction scenarios. The same friction coefficient is used for ice-ice and ice-structure interactions.

Floe shape. Because the floe shape is the primary parameter of interest in this study, we test several floe shapes to assess its influence. First, we run simulations with floe geometries obtained from a digitized top view photo of a broken ice field. These floe geometries are referred to as the 'real' floe geometries in the remainder of this paper. Second, we run simulations with regular shapes, ranging from triangular to octagonal. Third, we run simulations with circular floe shapes. The floe shapes used in this study are shown in Fig. 7, where the 'real' floe shape (upper left) is an example shape.

All possible combinations of structure shape, confinement conditions, ice areal coverage and floe shape are simulated with a friction coefficient of $\mu = 0.1$. To save calculation time, only the square structure geometry is used in combination with the friction coefficient $\mu = 0.5$. This results in 144 unique simulations of 10 000 m structure propagation each. To limit the number of simulations, certain simulation parameters are set to constant values. The constant parameters are included in Table 2. The constant simulation parameters may also be correlated with the floe shape effect, but their correlation is not investigated in this study.

2.5. Part 2: sensitivity study; broken ice definition and field creation

For the sensitivity study, random broken ice fields are created using the ice floe sizes, shapes and size distribution obtained from a top-view photo, which ensures that the randomly created broken ice fields resemble broken ice conditions as observed in nature. Fig. 8a shows the top view photo used for digital broken ice creation and Fig. 8b shows the digitized field. The photo was taken during the Oden Arctic Technology Research Cruise 2015 (OATRC2015) and was published and digitized by Lubbad et al. [14]. The ice field was digitized using the method described by Zhang and Skjetne [23]; using a minimum floe area of 20 m^2.

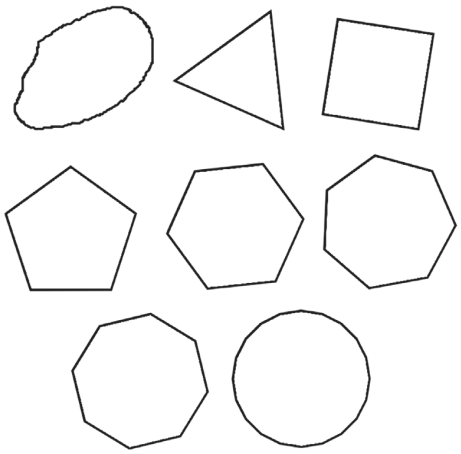

Fig. 7. Floe shapes used in the simulations. Left to right, top to bottom: 'Real' floe shapes (as observed in top view photo), 3–8 corner regular shapes and circular floes.

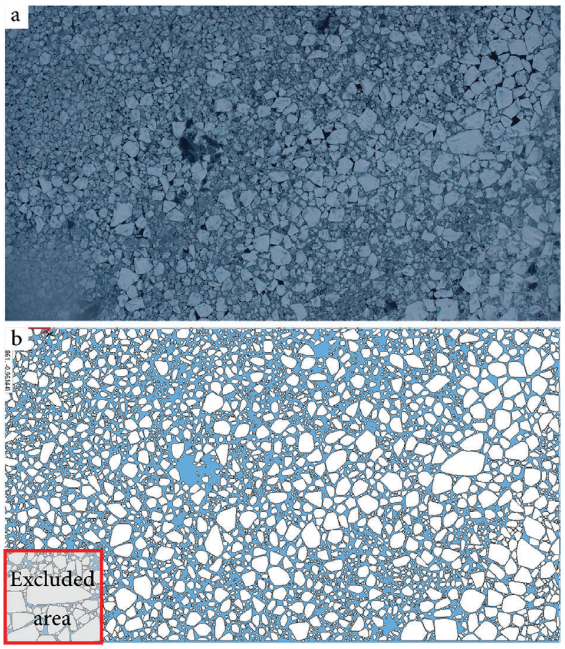

Fig. 8. Digitization of the ice field as observed from a helicopter. Top-view photo (a) and digitized broken ice field (b) (Lubbad et al. [14].

Comparing the digitized broken ice field to the top view photo, we observed that the lower left corner was not digitized correctly. Therefore the digitized floes in this area are not used in the broken ice creation process. The remaining floes are used as the basis for the randomly generated broken ice fields that are used to investigate the floe shape influence. Fig. 9 shows the cumulative floe area distribution of the floes resulting from the digitization of the broken ice field. The inertial properties of the ice floes are determined assuming a constant thickness and ice density, resulting in a COG position in the center of area of a floe (in top view).

Random broken ice fields are produced with the areal coverage as specified in Table 2. The broken ice fields are created by placing the digitized floes randomly inside the simulation domain. Then, the overlaps between floes are resolved, resulting in randomized broken ice fields with the desired areal coverage, having the exact same floe areas and floe area distribution as the digitized broken ice.

For the broken ice fields with shapes other than the natural shapes resulting from image processing, the floe areas from the digitized broken ice fields are used to create floes with the specified shapes, and the floes are placed in the same initial location as their counterparts with the same area. This results in generated broken ice fields with the exact same properties, except for the difference in floe shape. Snapshots of the resulting broken ice fields are shown in Fig. 10.

The simulations are set up such that the simulation duration is not limited by the size of the created broken ice field. The ice field with the specified areal coverage is generated continuously ahead of the structure, and it is always unique. Floes that have passed the structure by 200 m are deleted from the dynamic domain, to increase the efficiency of the simulations. Fig. 11 provides a clarification

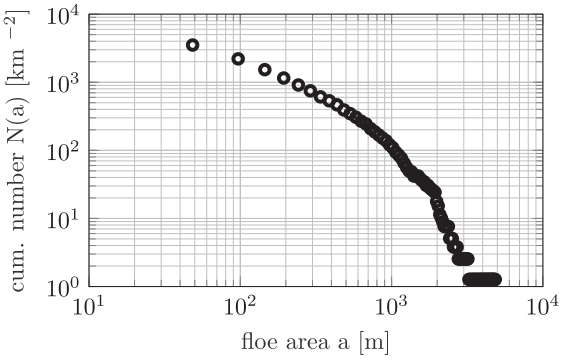

Fig. 9. Floe area distribution.

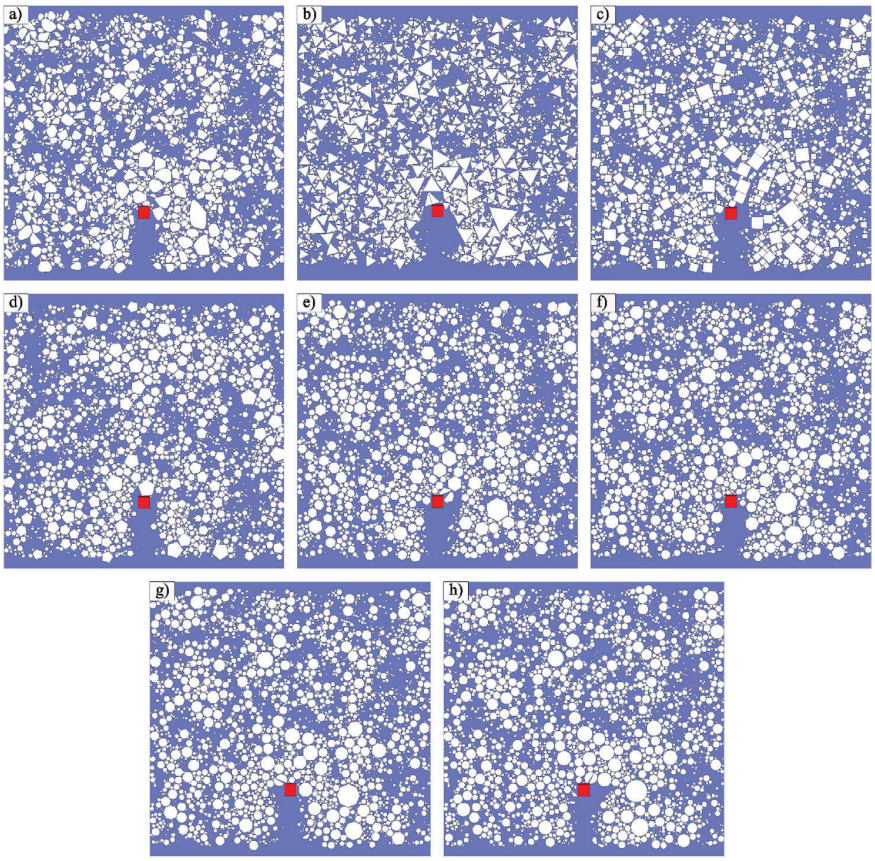

Fig. 10. Generated broken ice fields with different floe shapes, 50% areal coverage. From left to right, top to bottom: 'real' floe shapes (a), 3–8 corner regular shapes (b–g) and circular shapes (h).

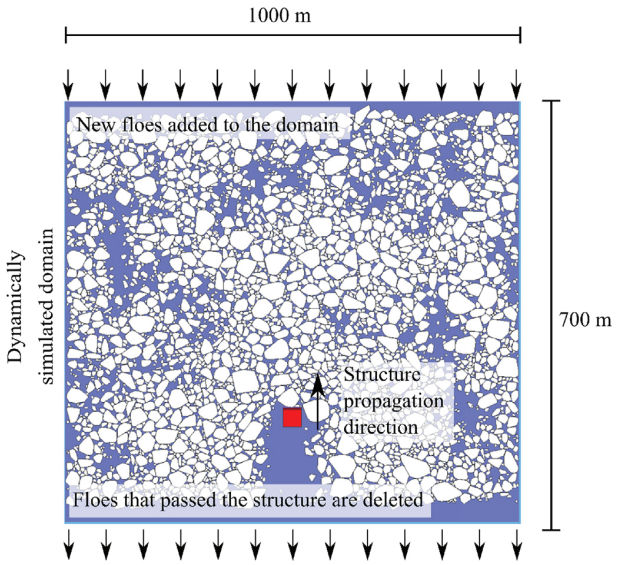

Fig. 11. Clarification of the continuous broken ice field generation process.

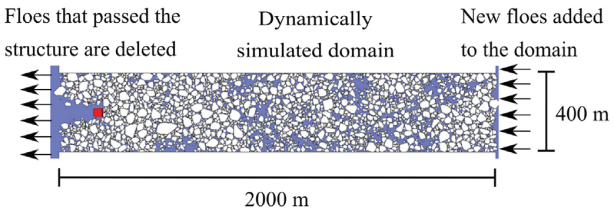

Fig. 12. Dimensions of the simulation domain for the confined cases.

of the floe addition and deletion process.

The ice field generation algorithm generates the ice field in blocks, ensuring for each block that the average areal coverage is equal to the defined areal coverage. The area of the generated blocks is such that the desired areal coverage is reached when placing all digitized floes within the block. Although the specified areal coverage is ensured over each block, subregions of the generated broken ice field may have a higher or lower areal ice coverage than the specified areal coverage, similar to real ice broken ice fields.

The choice of simulation dimensions is closely linked to the confinement conditions we are modelling. The dynamically modelled domain must extend sufficiently far that the contact network extending from the structure does not reach the free boundaries of the modelled domain. Otherwise, the free boundaries will unrealistically influence the simulation results. For the unconfined simulations, we find that a domain of 1000 × 700 m is sufficiently large to ensure that the contact network does not extend to the domain boundaries. In the confined simulations, the confinement wall distance is chosen to match the distance of HSVA ice-tank width. A scaling factor of 40 is applied, leading to a full-scale width of 400 m. The scaling factor is chosen such that the ratio between floe size and tank width is similar to the ratio observed in published ice tank tests (Hoving et al. [2]; Haase et al. [3]. In higher areal coverage fields, the build-up of ice floes in front of the structure in the confined case can be substantial, leading to a required domain length in the surge direction of 2000 m to ensure the structure influence on the broken ice field does not reach the domain boundary. The domain dimensions of the confined domain are shown in Fig. 12. All simulations are performed in full-scale.

3. Results of part 1: the floe shape effect in ice tank tests

As explained in Section 2.2, the results of 100 simulations for each of the simulated floe shapes are compared to the measured data. To further clarify how the P_5, mean and P_{95} values are obtained, the simulated results and the resulting P_5, mean and P_{95} values for the simulations with square floe shapes are shown in Fig. 13.

The aggregated results of the ice-tank test simulations are shown in Figs. 14 and 15. For all tested floe shapes (digitized experimental shapes, triangular, square and circular), the figures show the P_5 and P_{95} lines and the mean value at each time step of the 100 simulations performed. The data show that the digitized experimental floe shapes and the square floe shapes show similar behaviour (note that most of the digitized experimental shapes are rectangular) and that the triangular and circular floe shapes show similar behaviour.

The measured experimental loads mostly fall within the P_5 and P_{95} bounds of the simulations performed with digitized experimental floe shapes and the simulations performed with square floe shapes. The simulations performed with triangular and circular floe shapes have lower mean and P_{95} load values, and the experimental results are higher than the P_{95} load values for a significant

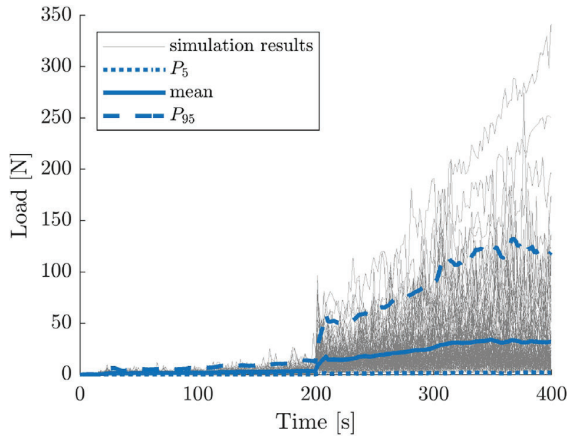

Fig. 13. The 100 simulation results and the resulting P_5, mean and P_{95} values of the simulations performed with square floe shapes. As in the ice tank tests, the structure velocity increases after 200 s, leading to the higher loads in the second part of the simulations.

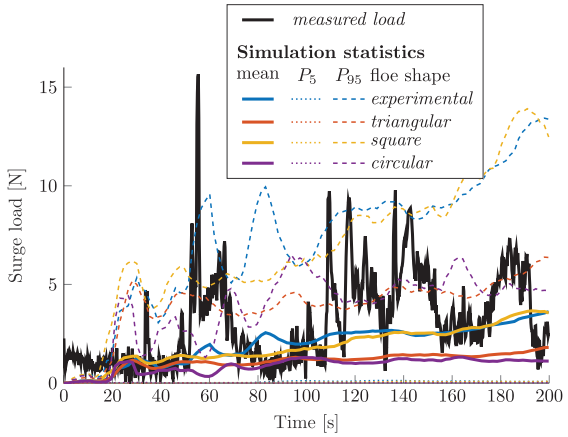

Fig. 14. Statistical properties of the numerical results compared to the loads measured in the ice-tank tests; velocity 0.09 m/s.

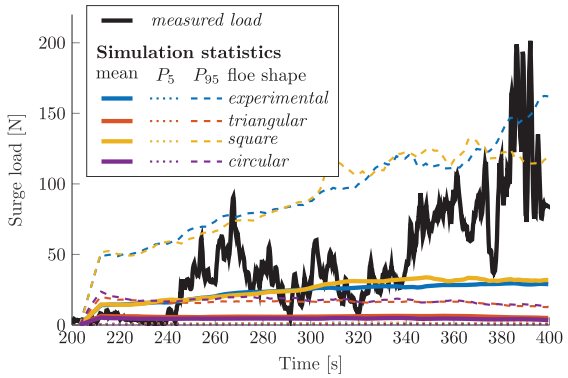

Fig. 15. Statistical properties of the numerical results compared to the loads measured in the ice-tank tests; velocity 0.18 m/s.

portion of the time series. Especially in the segment of the time series where the structure had a velocity of 0.18 m/s, which was the last 200 s of the experiment, the differences between the experimental and square floe shape simulation results and the triangular and circular floe shape simulation results are evident.

4. Results of part 2: the floe shape effect and its correlation with the investigated parameters

The results from the sensitivity study show there is a strong effect of the ice floe shape on the mean and on the standard deviation of the ice load in the surge direction.

The means and standard deviations of the ice loads in the surge direction for the unconfined and confined simulations are illustrated in Figs. 16–19. The coloured bars represent the results of the low friction simulations ($\mu = 0.1$). The square markers represent the results of the high friction simulations ($\mu = 0.5$). For the low-friction simulations, the results for circular and square structures are grouped in the coloured bars, in which the minimum of the bar is the lowest mean load and the maximum of the bar is the highest mean load from both tested structure shapes. In all simulations, the circular structure resulted in loads with a lower mean and standard deviation than the loads from the square structure. The high friction simulations were only performed with the square structure geometry. Note that the y-axes of Figs. 18 and 19 are in log scale. The mean and standard deviation of the 70% areal coverage simulations with triangular and square floes in the confined domain and with a friction coefficient $\mu = 0.5$ are shown in gray, because these simulations did not reach a statistically homogeneous state. Therefore, these values are invalid. The mechanism causing these invalid results is further examined in Section 5.

To further clarify the correlation between the floe shape and the other investigated parameters, the percentage differences of the mean and standard deviation resulting from the simulations with square floe geometries as compared to the mean and standard deviation resulting from the simulations with the real floe geometries are shown in Table 3. The percentage differences are listed separately for the confined and unconfined simulations because the mechanisms responsible for the differences are different for the confined and unconfined simulation cases. The mechanisms are further explained in Section 5.

The data in Figs. 16–19 and Table 3 shows the following:

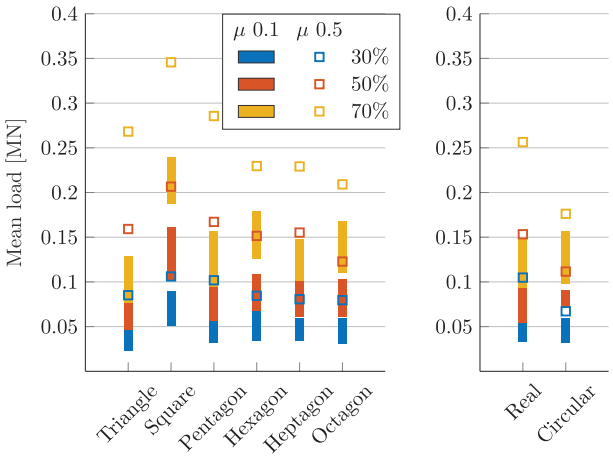

Fig. 16. Mean ice load in the surge direction as a function of floe shape, concentration and friction coefficient, no confinement.

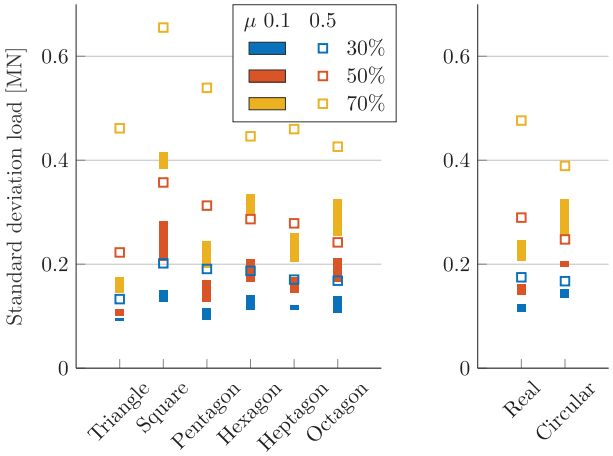

Fig. 17. Standard deviation of the ice load in the surge direction as a function of floe shape, concentration and friction coefficient, no confinement.

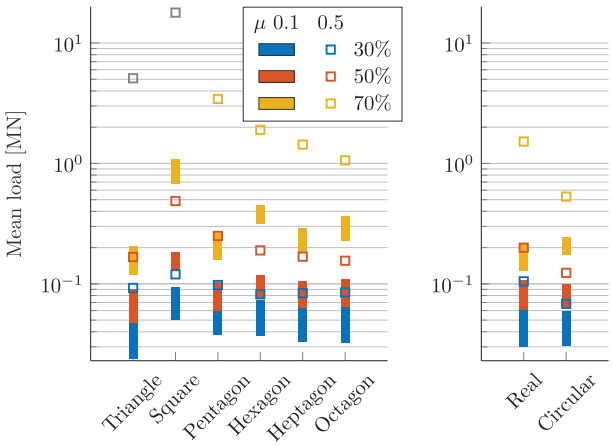

Fig. 18. Mean ice load in the surge direction as a function of floe shape, concentration and friction coefficient, confined domain.

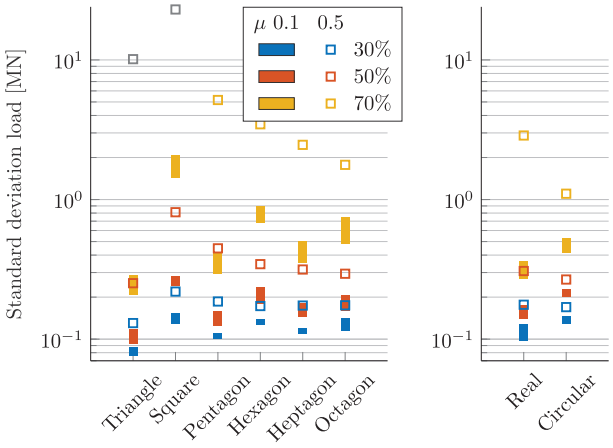

Fig. 19. Standard deviation of the ice load in the surge direction as a function of floe shape, concentration and friction coefficient, confined domain.

Table 3
Percentage difference of square floe results compared to the real floe results for the investigated parameters.

	Mean	Std
Unconfined simulations		
μ 0.1	+66%	+59%
μ 0.5	+28%	+29%
30% coverage	+19%	+18%
50% coverage	+52%	+43%
70% coverage	+55%	+57%
square str.	+38%	+40%
circular str.	+88%	+57%
Confinement effect[a]		
Unconfined	+39%	+33%
Confined	+84%	+79%
Confined simulations [a]		
μ 0.1	+62%	+46%
μ 0.5	+63%	+68%
30% coverage	+22%	+21%
50% coverage	+87%	+79%
70% coverage	+764%	+529%
square str.	+57%	+60%
circular str.	+87%	+45%

[a] Excluding the 70% simulation results, because the confined 70% concentration simulations did not reach a statistically homogeneous state.

- Square ice floes result in ice surge loads with a higher mean and standard deviation.
- Other regular shapes with 'parallel opposite edges', i.e., the hexagonal and octagonal floes, also show a higher mean and standard deviation of the ice load than other floe shapes; however, the effect is not as strong as with square floe shapes.
- The effect of floe shape is strongly related to the confinement conditions. In unconfined simulations, the floe shape effect is weaker than in confined simulations. The higher the ice areal coverage, the stronger the effect of confinement.
- The floe shape effect is stronger for a circular structure geometry than for a square structure geometry.
- The floe 'roundness' appears to play a role in the high-friction simulations, but not in the low-friction simulations.
- Both in the confined and in the unconfined simulation cases, the floe shape effect is stronger for higher ice areal coverage.
- In the unconfined case, the influence of floe shape is inversely related to the friction coefficient. The higher the friction coefficient, the lower the effect of the floe shape.

Parallel opposite edges are defined as edges of the floe that have a parallel edge perpendicularly opposite to the edge across the floe. This is clarified in Fig. 20. Floe roundness is a measure for how closely a body approaches a disk geometry (in 2D). Different definitions are used in the literature to define floe roundness; however, the exact definition is not relevant in this study. Floe roundness is a common way to classify ice floe geometry and is used, for example, by Toyota et al. [24].

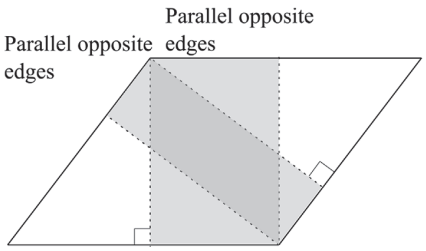

Fig. 20. Parallel opposite edges enable the formation of stable force chains.

5. Discussion

The mechanisms responsible for the floe shape effect as observed in Sections 4 and 3 are discussed in this section. We also elaborate on the limitations of the presented results, and discuss how ice-tank tests with broken ice may be improved.

5.1. Mechanisms responsible for the floe shape effect

The most important phenomenon responsible for the floe shape effect is the greater length and the higher stability of force chains for floes that have parallel opposite edges. In the confined simulations, this phenomenon may lead to bridging of force chains between the structure and the tank walls, exacerbating the floe shape effect. In the high-friction simulations, the results indicate that the floe 'roundness' plays a more important role than in the low friction simulations. In analysing the mechanisms responsible for the floe shape effect, we rely on time-domain visualizations of the numerical simulations performed for the replication of the ice-tank tests and for the sensitivity study. The mechanisms are examined in more detail in the following sections.

Force chain formation. The simulation results show that force chains extending from the structure are longer and more stable when floes have parallel opposite edges. In this paper, force chains are defined as three or more contacting bodies with a maximum body contact force exceeding half the global maximum contact force:

$$\max(\mathbf{f}_{\mathbf{b};t}) \geq 0.5\max(\mathbf{f}_{\mathbf{g};t}) \tag{12}$$

in which $\mathbf{f}_{\mathbf{b};t}$ is a vector of all contact forces for one body at time step t and $\mathbf{f}_{\mathbf{g};t}$ is a vector of all contact forces in the domain at time step t. Note that this definition is different from the definition applied in other literature describing force chains in ice structure interaction. Other literature often applies the definition as given by Paavilainen and Tuhkuri [25]; where force chains are defined based on a load vector that takes both the force magnitude as well as the force direction into account, and requiring that the load vector is higher than the average value of the load vector for an assembly of three or more elements. However, in the simulations performed in this study, most bodies in the domain are free floating and therefore have a contact load vector of 0, resulting in a low mean load vector. This makes the definition by Paavilainen and Tuhkuri [25] less applicable, as it would result in force 'regions' rather than force chains, even though force chains are clearly visible using the definition as described above.

Fig. 21 shows the difference in length and stability of force chains by comparing the maximum body forces from a simulation with real floe geometries to the maximum body forces in a simulation with square floe geometries. In the square floe simulations, the force chains are longer, resulting in a larger region influenced by the moving structure. The ice floes that are pushed ahead of the structure

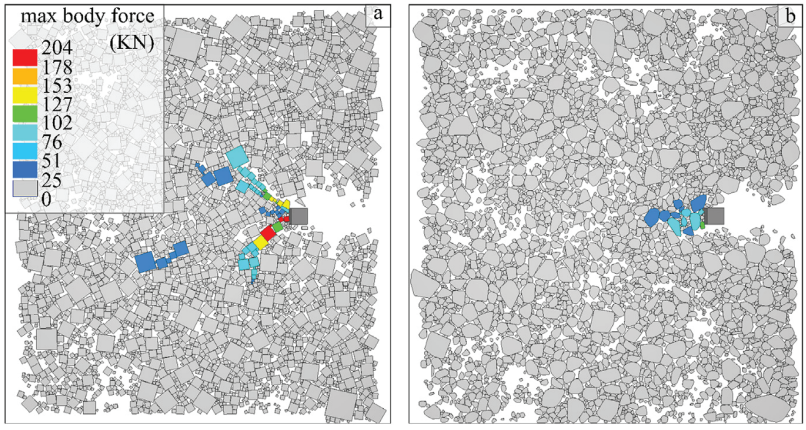

Fig. 21. Difference in force chain formation, square floes (a) and real floes (b).

experience drag forces, which are transferred to the structure through force chains. This transfer leads to a higher average surge load on the structure in the simulation with square floe shapes.

The simulation results show that force chains extending from the structure are longer and more stable when floes have parallel opposite edges. Both the proportion of edges that are parallel and opposite and the length of the parallel opposite edges influence the length and stability of the occurring force chains; in regular shapes with an even number of corners, all edges are parallel and opposite. However, the results show that as the shape approached a circle, the effect of the parallel opposite edges becomes weaker because each edge is shorter. The data in Figs. 16–19 show that the presence of parallel opposite edges leads to a higher mean and a higher standard deviation of the load in both the confined and the unconfined cases, when a friction coefficient $\mu = 0.1$ is used. In the simulations with the friction coefficient $\mu = 0.5$, the effect of parallel opposite edges is only observed in the difference between the triangular and square floe results, but it is no longer present for 5–8 corner regular shapes. This result can be explained by the fact that edges must no longer be exactly parallel for the formation of stable force chains to occur when using a friction coefficient of $\mu = 0.5$. In addition, the data show that the effect of floe roundness starts to play a role in the high-friction coefficient simulations.

To the authors' knowledge, the presence and length of parallel opposite edges is currently not used as a parameter to describe body shapes in discrete element simulations. Rather, authors tend to choose the more general 'roundness' or 'angularity' (similar but opposite to 'roundness') to describe body geometries (e.g., Toyota et al. [24]. However, our results show that a 'roundness' or 'angularity' parameter does not sufficiently describe floe shapes in ice-structure interaction scenarios if the reproduction of ice loads is of interest.

Ice bridging. Both in the confined simulations that were performed for the ice-tank test replication study (part 1) and in the sensitivity study (Part 2), the force chain formation causes bridging between the structure and the tank walls in some of the simulations. When bridging occurs, the effect of the force-chain formation and, by extension, the effect of the floe shape on the ice load, is greatly exacerbated. The bridging is rarely permanent; when ice floes accumulate behind the bridging event, the bridging is usually resolved because of a floe-splitting failure event or instability in a force chain. Instability of force chains was also observed as load limiting mechanism, although in a different setting, by Paavilainen and Tuhkuri [25] and Ranta et al. [26]. An example of how a force chain clears because of splitting failure is provided in Fig. 22.

In Part 1, the ice-tank replication study, typically one of three mechanisms occurs in the simulations with the digitized experimental floes (mostly rectangular) or the square floe shapes; 1) no bridging events, 2) partial bridging events that quickly clear or 3) full bridging. With the digitized experimental floe geometries, no bridging occurs in 79% of the simulations. In 18% of the simulations, partial bridging occurs, and only in 3% of the simulations full bridging occurs. The simulations were identical, apart from the low random initial velocity of the ice floes, as explained in Section 2.2. Fig. 23 illustrates the bridging behaviour of the ice floes. Fig. 24 displays the surge load on the structure for the three different scenarios, comparing them to the measured load. The load-time signal of the partial bridging case most closely resembles the measured load.

In the simulations with triangular and circular floes, bridging does not occur in any of the simulations, and the P_5, mean, and P_{95} lines are lower than the measured load for the majority of the time series.

In the sensitivity study (Part 2), bridging occurs in the 70% areal coverage confined simulations. Usually, the bridging events are unstable; a force chain between the structure and the tank wall is formed and then breaks again a few seconds later. Nevertheless, the formation of these bridging events inhibits the sufficient clearing of ice around the structure, leading to significant accumulation of ice floes in front of the structure. Fig. 25 shows an example of floe bridging and accumulation as it occurs in the sensitivity study.

The bridging and subsequent accumulation of ice greatly exacerbates the effect of the floe shape, leading to mean loads and standard deviations of up to 8 times higher for square floes compared to real floe shapes (shown in gray in Table 3). Often, the accumulation of floes would be so extensive that we consider the simulation results unrealistic. We expect that floe rafting would have occurred if the simulations would have been three dimensional. Thus, the model results for confined simulations with 70% concentration and square floe geometries are considered invalid.

Effect of floe 'roundness'. The data in Figs. 16–19 show that the triangular floe shapes give the lowest mean and standard deviation in all scenarios when using the low friction coefficient $\mu = 0.1$, but result in mean loads as high or higher than the other regular shapes when using a high friction coefficient $\mu = 0.5$, especially in the 70% areal coverage simulations. We attribute this result to the effect of floe 'roundness', which our results indicate starts to play a more important role in the higher friction coefficient simulations.

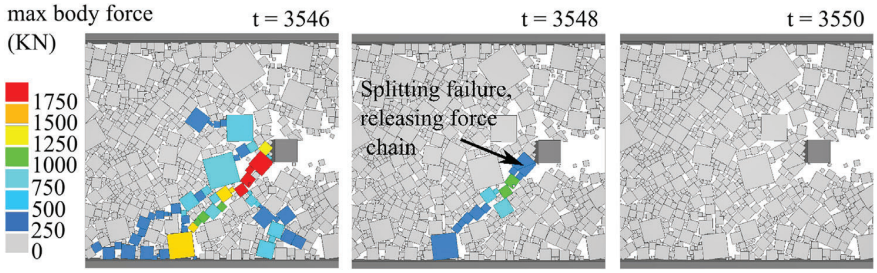

Fig. 22. Example of a force chain that disappears because of splitting failure.

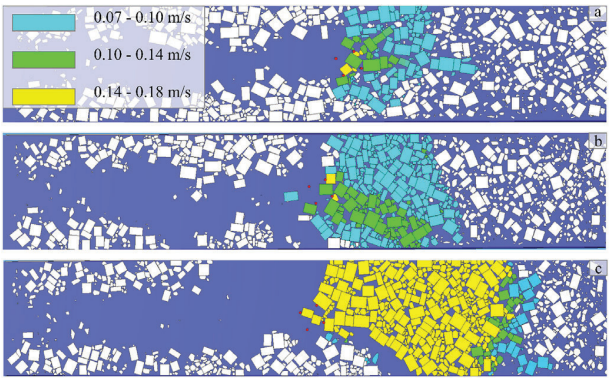

Fig. 23. Mechanisms causing different loading behaviour: no bridging (a), partial bridging (b), and full bridging (c), visualized by floe velocity. Yellow floes move with the same velocity as the structure. (For interpretation of the references to colour in this figure legend, the reader is referred to the Web version of this article.)

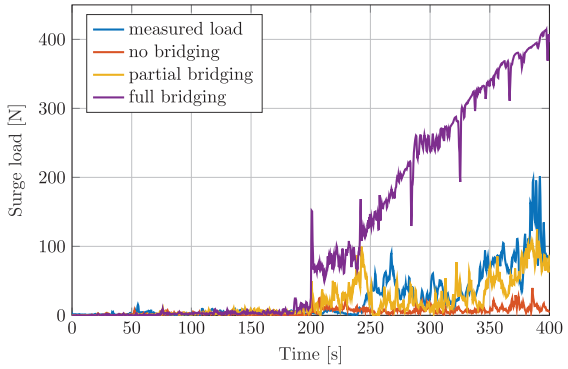

Fig. 24. Loads resulting from the different interaction mechanisms: no bridging, partial bridging and full bridging.

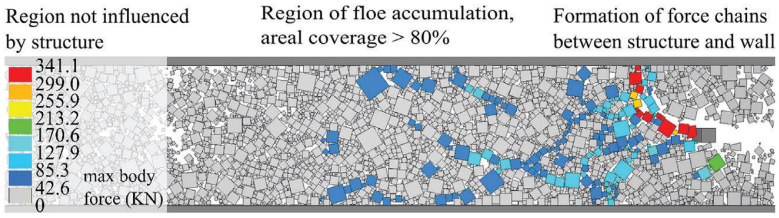

Fig. 25. Bridging of a force chain between the structure and the tank wall, and floe accumulation in front of the structure as a result of multiple bridging events.

5.2. Limitations of the current study

There are several limitations of the performed study, which limit the validity and range of applicability of the results.

Limited parameter combinations tested. Although the correlation of important parameters with the floe shape effect is assessed in the sensitivity study, there nevertheless remain many untested parameter combinations in which the influence of the floe shape effect is unclear. The reasoning behind our parameter choices is explained in Section 2.4. Naturally, the validity of the results is limited to the tested parameter combinations, and the influence of (among other parameters) the interaction velocity, the floe size and size distribution, the structure orientation, rafting and ridging effects and the presence of ice rubble and brash ice remains unstudied. Nevertheless, we consider the tested range of parameters sufficiently broad to conclude that the effect of floe shape is present and relevant in the interaction between broken ice and vertical-sided structures.

Validity of obtained results. Among the results, there are parameter combinations for which the 2D nature of the simulations may have had a significant influence on the results. Three reasons are listed in the following sections:

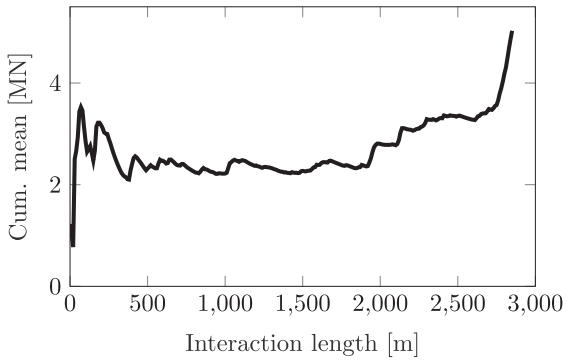

Fig. 26. Cumulative mean, 70% areal ice coverage, confinement, triangular floes and friction coefficient $\mu = 0.5$. Example of simulation in which a statistically homogeneous state is not reached.

- *Parameter combinations for which the mean and standard deviation did not converge.* For two parameter combinations, a statistically homogeneous state was not reached because of excessive build-up of floes in front of the structure. This behaviour occurred in the 70% areal coverage confined simulations with triangular and square floe shapes and a high friction coefficient of $\mu = 0.5$. Figs. 26 and 27 show the cumulative mean and standard deviation for the non-converging simulations with triangular floes. The results for these parameter combinations are considered invalid and are thus shown in gray in Figs. 18 and 19. We expect that floe rafting would have occurred in these simulations if it would have been modelled. The rafting mechanism could reduce the bridging processes that result in the excessive floe build-up.

The above described invalid results do not affect the primary findings as described in Sections 3, 4 and in the current section, i.e., that the effect of floe shape is present and significant for the modelled parameter combinations.

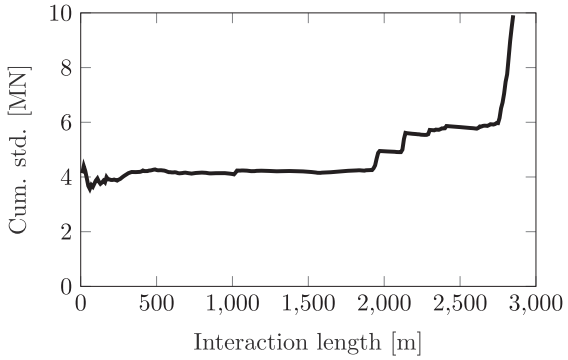

Fig. 27. Cumulative standard deviation, 70% areal ice coverage, confinement, triangular floes and friction coefficient $\mu = 0.5$. Example of simulation in which a statistically homogeneous state is not reached.

- *Simulations in which excessive floe build-up occurs.* For some parameter combinations, the mean and standard deviation did converge to a constant value; however, the floe accumulation and resulting ice load was such that we expect that floe rafting would have occurred if it would have been possible. Simulations in which this occurs include all confined 70% areal coverage high friction ($\mu = 0.5$) simulations, except the one with circular floes, and the confined 70% areal coverage simulations of square floes with the low friction coefficient $\mu = 0.1$. From Part 1, the ice tank test simulations in which full plug formation occurs fall in this category.
- *The effect of floe discretization on the contact force.* In the floe discretization process, the real floe geometries are approximated numerically by a polygon consisting of a limited number of points. Small protrusions as well an any non-verticality of floe edges is filtered out. The resulting numerical approximations of the floes have vertical and planar floe edges. This may lead to contact forces that increase more rapidly in the numerical model than in reality, leading to higher load peaks and a higher standard deviation of the load-time signal.
- *The end-boundary effect in Part 1; the ice tank test simulations.* As explained in Section 2.2, the sloping tank boundary of the HSVA ice tank is not modelled in the numerical representation because of the 2D nature of the simulations. Instead, we extend the ice field with floe ice that has similar properties to the experimental ice field. This difference between the experiments and the simulations has an influence on the numerical simulation results. In the results from the tank experiments, the data show that the ice load increases significantly near the end of the test because of the effect of the sloping boundary. In the numerical simulations this increase in load is not present.

5.3. Recommendations regarding ice tank experiments with broken ice

From the results in the previous sections, we propose that artificial broken ice is created such that the created floe shapes match the floe shapes of the conditions one intends to model. At the same time, we also acknowledge the practical limitations related to the creation of artificial broken ice. It is left to the ice tanks, who are the experts in this field, to properly define real-equivalent broken ice conditions.

One may note that broken ice in real life may also have floe shapes that are close to rectangular or square, and that the use of square or rectangular floes in ice tanks will at least lead to conservative results. However, rather than providing conservative results, ice-tank tests should provide insight into the processes that may occur. As is shown in this paper, these processes can be significantly influenced by the floe shape, especially in combination with confinement effects that may lead to bridging. Bridging can result in the accumulation of ice in front of the structure to such an extent that the ice-tank test no longer represents the scenario for which the test was originally intended. Although the resulting loads may be conservative, they are no longer relevant. Furthermore, the occurrence of ice bridging between the structure and the tank walls, and the floe accumulation that may results, are part of a largely random process. In the numerical reproduction of the ice-tank tests, there is a large difference in ice surge load between runs in which no bridging occurred (79% of the simulations), simulations in which partial bridging occurred (18% of the simulations) and simulations in which full bridging occurred (3% of the simulations). These differences may limit the reproducibility of the ice-tank test results.

6. Conclusion

The numerical experiments show that there is a strong floe shape effect on the mean and standard deviation of the ice load in the surge direction in all tested broken ice conditions. The results from the sensitivity study (Part 2) show that the square floe simulations predict a mean load that is between 19% and 88% higher than the mean load predicted by the real floe shape simulations. The effect of floe shape is correlated to all of the investigated parameters. For instance, a circular structure results in a higher floe shape effect than a square structure, a higher friction coefficient reduces the floe shape effect, the floe shape effect is stronger for higher ice areal coverage and confinement exacerbates the floe shape effect for the tested combinations of floe size, structure size, and confinement conditions. Bridging and floe accumulation are the mechanisms responsible for the correlation between the floe shape effect and confinement. The greater length and stability of force chains is the primary mechanism responsible for the floe shape effect.

The stability and length of force chains is related to the presence and length of parallel opposite edges. The presence and length of parallel opposite edges as a description of floe shape is novel and distinctly different from the often used roundness or (equivalent but opposite) angularity parameter. A quantification of the effect of parallel opposite edges is not provided. The high number of parameters that may influence the floe shape effect and the complexity of the phenomena leading to the shape effect, make such a quantification infeasible. Currently, numerical simulation appears the best tool to assess the influence of floe shape in a particular interaction scenario, possibly in combination with ice-tank tests. The results of this paper lead to two recommendations:

- DEM simulations of broken ice should attempt to approximate the expected real floe shape. If the floe shape is not known, several floe shapes should be modelled to assess the influence of floe shape in the scenario of interest. Approximating the broken ice with square floe shapes will lead to conservative results, but the results may be overly conservative, resulting, in some conditions, in loads that are almost two times greater than if 'real' floe shapes would have been used. Approximating the ice floes with circular floe shapes may lead to an under-prediction of broken ice loads.
- Ice-tank tests of broken-ice-structure interaction should be performed using broken ice with shapes that resemble the floe shapes of the ice condition one intends to model. It is left to the ice tanks to define a realistic 'real-equivalent' floe shape.

Acknowledgements

The authors would like to acknowledge the support of the SAMCoT CRI through the Research Council of Norway and all of the SAMCoT Partners.

References

[1] Comfort G, Singh S, Spencer D. Evaluation of ice model test data for moored structures - PERD/CHC report 26-195 1999. p. 1–77. 1999-04, Technical report.
[2] Hoving JS, Vermeulen R, Mesu AW, Cammaert G. Experiment-based relations between level ice loads and managed ice loads on an arctic jack-up structure. 'Proceedings of the 22nd international conference on port and ocean engineering under arctic conditions', espoo, Finland. 2013.
[3] Haase A, van der Werff S, Jochmann P. DYPIC - dynamic positioning in ice - first phase of model testing. Proceedings of the ASME 2012 31st international conference on ocean. Rio de Janeiro: Offshore and Arctic Engineering; 2012. p. 1–8.
[4] Tuhkuri J, Lensu M. Ice tank tests on rafting of a broken ice field, technical report. Helsinki University of Technology Ship Laboratory - Arctic Offshore Research Centre; 1997.
[5] Hopkins MA, Hibler WD, Flato GM. On the numerical simulation of the sea ice ridging process. J Geophys Res 1991;96(C):4809–20.
[6] Tuhkuri J, Polojärvi A. Effect of particle shape in 2D ridge keel deformation simulations. Proceedings of the 18th international conference on port and ocean engineering under arctic conditions, vol. 2. 2005. p. 939–48.
[7] Konno A, Saitoh O, Watanabe Y. Numerical investigation of effect of channel condition against ship resistance in bras ice channels. 'Proceedings of the 21st international conference on port and ocean engineering under arctic conditions', number 2007, montreal, Canada. 2011.
[8] Rheem CK, Yamaguchi H, Kato H. Distributed mass/discrete floe model for pack ice rheology computation. J Mar Sci Technol 1997;2(2):101–21http://link.springer.com/10.1007/BF02491524.
[9] Yamaguchi H, Rheem CK, Toyada M, Matsuzawa T, Nakayama H, Kato H, Kato K, Adachi M. Influence of floe shape on behaviour of ice floes around a structure.

OMAE - volume IV. Arctic/Polar Technology ASME; 1997. p. 461–8.
[10] Cleary PW, Sawley ML. DEM modelling of industrial granular flows: 3D case studies and the effect of particle shape on hopper discharge. Appl Math Model 2002;26:89–111.
[11] Azéma E, Radjai F, Dubois F. Packings of irregular polyhedral particles: strength, structure, and effects of angularity. Phys Rev E - Stat Nonlinear Soft Matter Phys 2013;87(6):1–14.
[12] Höhner D, Wirtz S, Scherer V. A study on the influence of particle shape and shape approximation on particle mechanics in a rotating drum using the discrete element method. Powder Technol 2014;253:256–65https://doi.org/10.1016/j.powtec.2013.11.023.
[13] ArcISo. arciso.com; 2018.
[14] Lubbad R, Løset S, Lu W, Tsarau A, van den Berg M. An overview of the Oden Arctic Technology Research Cruise 2015 (OATRC2015) and numerical simulations performed with SAMS driven by data collected during the cruise. Cold Reg Sci Technol 2018;156:1–22.
[15] van den Berg M, Lubbad R, Løset S. An implicit time-stepping scheme and an improved contact model for ice-structure interaction simulations. Cold Reg Sci Technol 2018;155:193–213.
[16] Kim E, Gagnon RE. A preliminary analysis of the crushing specific energy of iceberg ice under rapid compressive loading. 'Proceedings of the 23rd IAHR international symposium on ice', ann arbor, Michigan, USA. 2016.
[17] Lu W, Lubbad R, Løset S. In-plane fracture of an ice floe: a theoretical study on the splitting failure mode. Cold Reg Sci Technol 2015;110:77–101.
[18] Tsarau A. Numerical modelling of the hydrodynamic effects of marine operations in broken ice, doctoral thesis. Norwegian University of Science and Technology; 2015.
[19] Parmerter RR. A model of simple rafting in sea ice. J Geophys Res 1975;80(5):1948–52.
[20] Tuhkuri J. Laboratory tests on ridging and rafting of ice sheets. J Geophys Res 2002;107(C9):1–14.
[21] Hopkins M a, Tuhkuri J. Compression of floating ice fields. J Geophys Res 1999;104(C7):15815–25http://doi.wiley.com/10.1029/1999JC900127.
[22] Løset S. Discrete element modelling of a broken ice field - Part I: model development. Cold Reg Sci Technol 1994;22(4):339–47.
[23] Zhang Q, Skjetne R. Image processing for identification of sea-ice floes and the floe size distributions. IEEE Trans Geosci Rem Sens 2015;53(5):2913–24.
[24] Toyota T, Haas C, Tamura T. 'Size distribution and shape properties of relatively small sea-ice floes in the Antarctic marginal ice zone in late winter', *Deep-Sea Research Part II*. Topical Studies in Oceanography 2011;58(9–10):1182–93https://doi.org/10.1016/j.dsr2.2010.10.034.
[25] Paavilainen J, Tuhkuri J. Pressure distributions and force chains during simulated ice rubbling against sloped structures. Cold Reg Sci Technol 2013;85:157–74.
[26] Ranta J, Polojärvi A, Tuhkuri J. Limit mechanisms for ice loads on inclined structures: Buckling. Cold Reg Sci Technol 2018;147:34–44.

Appendix E

The effect of floe shape on the interaction of vertical-sided structures with broken ice

This paper is Published in the Proceedings of the 25th International Conference on Port and Ocean Engineering under Arctic Conditions, 2019, Delft, The Netherlands.

Proceedings of the 25th International Conference on
Port and Ocean Engineering under Arctic Conditions
June 9-13, 2019, Delft, The Netherlands

POAC 2019
DELFT THE NETHERLANDS

The effect of floe shape on the interaction of vertical-sided structures with broken ice

Marnix van den Berg[1], Raed Lubbad[1], Sveinung Løset[1]
[1] SAMCoT, Department of Civil and Environmental Engineering,
NTNU, NO-7491 Trondheim

ABSTRACT

In the interaction of broken ice with vertical-sided structures, the ice floe shape can have a significant influence on the ice loads experienced by the structure. The floe shape is especially important in clearance-dominated interaction regimes. This study investigates the effect of floe shape on the clearance-dominated interactions between a vertical-sided circular structure and an unconfined broken ice field. First, the study shows that the floe shape effect exists. Then, the study focusses on the mechanisms responsible for the floe shape effect by comparing aspects of the interaction mechanism between the broken ice field and the structure. The effect of floe shape on the propagation and dissipation of forces in the broken ice field and the effects on the energy dissipation mechanisms are quantified in order to gain more insight in the processes responsible for the floe shape effect. The results show that both the mean value and the standard deviation of ice loads on a vertical-sided structure are higher in a broken ice field with square floe shapes than in a broken ice field with natural floe shapes. The higher mean load appears to be the result of a larger network of force chains in the broken ice around the structure. The force networks seem to have similar properties otherwise.

KEY WORDS Floe shape effect; Energy balance; Broken ice; Force chains

INTRODUCTION

Loads from broken ice can be the design loads for seasonal operations and structures supported by ice management. Broken ice load estimates are often based on the analysis of full-scale data, model-scale experimental data, and/or results from numerical modelling. Parameters that may influence the loads from broken ice on a structure are the ice material properties, the ice areal coverage, the floe size and size distribution, the ice thickness, the floe shape, the ice drift velocity, wind and current conditions, the presence and quantity of ice rubble or brash ice and the confinement conditions. Because of limited available data, the influence of many of the above mentioned parameters is still unclear.

An understanding of the floe shape effect is important in the design of model-scale ice-tank tests and numerical simulations, which are used in the design phase of structures loaded by broken ice. Currently, ice-tank tests with broken ice are often conducted with square or rectangular ice floes (for instance in Haase et al., (2012) and Hoving et al., (2013)). Numerical modelling results indicate that the loads measured in confined broken ice tests with square or rectangular floes may not be representative for the conditions that the test intends to model

(van den Berg et al., 2019). The effect of floe shape in clearance-dominated ice structure interaction has been studied previously by Rheem et al., (1997) and Yamaguchi et al., (1997). However, the model used by Rheem and Yamaguchi is greatly simplified. For example, no floe rotation is taken into account in their model.

A new and extensive study of the effect of floe shape on the ice load experienced by a vertical-sided structure interacting with broken ice is presented in van den Berg et al. (2019). van den Berg et al. (2019) investigates the effect of floe shape in unconfined conditions and in ice-tank tests, where the broken ice field is confined by the tank walls. The primary finding is that the ice floe shape has a large influence on the mean and standard deviation of the ice load in interaction scenarios dominated by ice accumulation and clearance around the structure. The current study presents an extension to the results presented in van den Berg et al. (2019). The differences in ice-structure interaction mechanisms caused by the floe shape effect are studied in more detail by comparing the contributions of different energy dissipation mechanisms and by studying the force propagation and dissipation within the broken ice field.

Interaction between a vertical-sided circular structure and broken ice with an aerial coverage of 70% is modelled with a two-dimensional (2D) Discrete Element Method (DEM). Random broken ice fields are created using 1) floe shapes digitized from a top-view photo of broken sea ice and 2) square floes with the same floe size distribution as the digitized natural floes. The circular structure is propagated for 10 000 m in the randomly created broken ice fields. The ice load on the structure, force propagation and dissipation within the broken ice, and energy dissipation mechanisms are compared for the natural and square broken ice fields, in order to find the causes of the floe shape effect.

SIMULATION METHOD AND SIMULATED CONDITIONS

We study the effect of floe shape using a 2D non-smooth DEM (NDEM) model. The model is an adapted version of the *Simulator for Arctic Marine Structures* (SAMS). SAMS has been used in earlier studies, which are described in Lubbad, et al., (2018a, 2018b); Tsarau et al., (2018); van den Berg, et al., (2018) and van den Berg et al., (2019). The used model is described in detail in van den Berg et al., (2018). Some additional model capabilities related to the treatment of ice-structure contacts are described in van den Berg et al. (2019). In the model, contact forces are calculated implicitly by solving a mixed linear complementarity problem (MLCP) in each time step. The contact geometry and a constant crushing pressure are used to define the force-penetration behaviour at each contact. The force-penetration behaviour is defined based on an assumption of local ice crushing, leading to plastic contact behaviour. The relationship between force and penetration is used in the MLCP to solve the contact forces occurring between interacting bodies. Apart from the contact compliance resulting from this local crushing assumption, all bodies are considered rigid.

The broken ice conditions used in this study are obtained by digitizing a top view photo of a broken sea ice field. Individual floes are detected and digitized using the method described in Zhang & Skjetne, (2015). The digitized broken ice field is visualized in Figure 1. The digitized ice floes have a floe area ranging from 20 m^2 to 4840 m^2. The floe size distribution is shown in Figure 2. Random broken ice fields are created with the same floe size distribution as the digitized broken ice field. One broken ice field is created using the natural floe shapes of the digitized ice floes, and another broken ice field is created in which all floes have a square shape. In both ice fields, floes with the same area are initiated in the same initial positions. After initiation, the overlaps between the floes are resolved before the dynamic simulation is started. This results in similar floe positions for the ice field with natural floe shapes and the ice field with square floe shapes. Apart from the difference in floe shape and the slightly different floe positions, both ice fields are exactly the same.

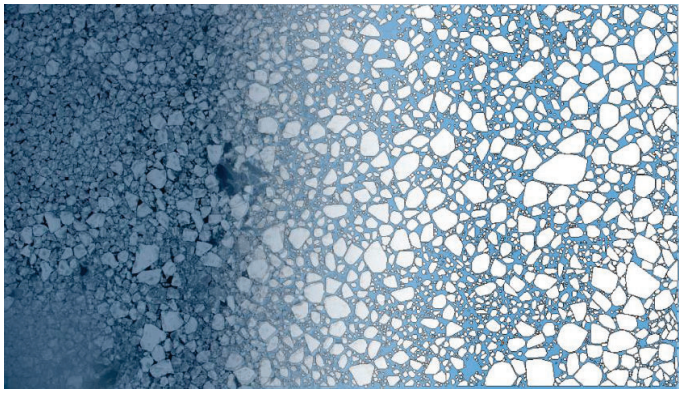

Figure 1. Digitization of a broken ice field from a top view photo. The image merges from photo to digitized ice field from left to right.

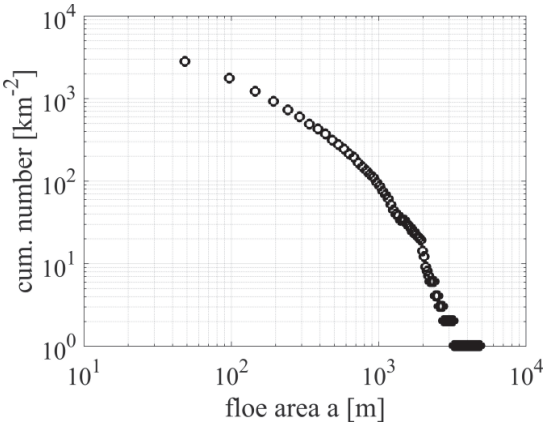

Figure 2. Floe area distribution of the digitized broken ice field.

An interaction length of 10 000 m is simulated for both floe fields. An interaction length of 10 000 m is needed in order to obtain an accurate prediction of the mean load. A domain of 1000 by 900 m around the structure is dynamically simulated. Figure 3 shows the dynamically simulated domain and the structure's position within that domain. The domain size is chosen such that the domain boundaries will not influence the ice load on the structure. The domain is unconfined. Figure 3 also shows the similarity in the floe positions between the broken ice field with natural floe shapes and the broken ice field with square floe shapes. As the structure propagates, floes from the pre-generated floe field that enter the dynamically simulated domain are added. Simultaneously, floes that exit the dynamically simulated domain are removed from the simulation.

Ice splitting failure is implemented following the analytical solutions described by Lu et al., (2015). The contact forces resulting from the DEM simulation are used in each time step to determine if and how an ice floe will split. Because of the 2D nature of the model, ice floe rafting and bending failure is not taken into account. van den Berg et al. (2019) discusses how this simplification may affect the results. Hydrodynamic drag forces resulting from Skin friction and form drag are applied to the ice floes according to their triangulated geometry and the local velocity vector and position of each triangle. The method is described by Tsarau, (2015).

The physical characteristics of the simulated scenarios are given in Table 1. In both scenarios, the structure propagated with a constant velocity in the direction indicated in Figure 3. The structure is fixed in the other degrees of freedom.

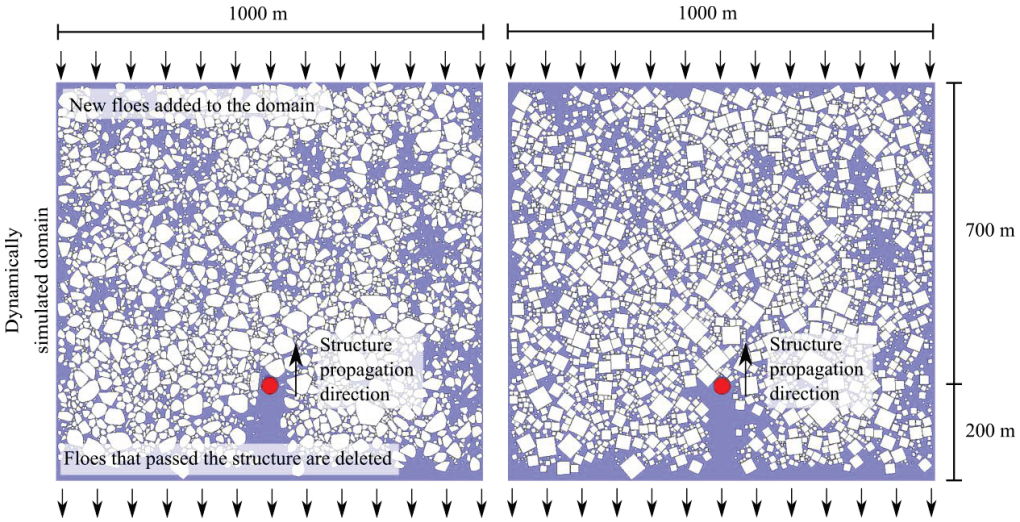

Figure 3. Random broken ice fields created from the digitized broken ice field. Left: natural floe shapes. Right: square floe shapes.

Table 1. Parameters used in the simulations.

Parameter	Value	Parameter	Value
Ice Density	910 kg m^{-3}	Structure diameter	40 m
Ice-ice friction coefficient	0.15	Structure velocity	1.0 m/s
Ice-structure friction coefficient	0.15	Water density	1025 kg m^{-3}
Fracture toughness	150 Pa √m	ice skin friction coefficient	0.005
Crushing pressure	2 MPa	ice form drag coefficient	0.5
Ice thickness	1.0 m	Ice aerial coverage	70 %

RESULTS

We compare the mean value of the ice load, the standard deviation of the ice load, the energy dissipation mechanisms and the size and shape of the force networks within the broken ice in order to identify differences in interaction as a result of the different floe shapes.

Figure 4 shows the mean and the standard deviation of the ice load on the structure (in the direction that is opposite to the structure propagation direction) resulting from the simulations with natural and square floe shapes, respectively. The simulation with natural floe shapes results in a mean ice load of 106 kN and a load standard deviation of 235 kN, while the simulation with square floe shapes results in a mean ice load of 198 kN and a load standard deviation of 398 kN.

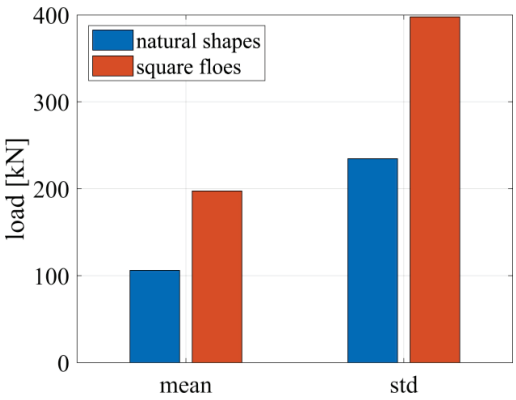

Figure 4. Mean and standard deviation of the ice load on the structure opposite to the structure propagation direction, in the simulation with natural floe shapes and in the simulation with square floe shapes.

We consider the energy balance of the interaction process by comparing the energy input from the structure (ΔE_{str}) and the energy dissipation in the ice field. The latter consists of dissipation in contact normal forces (as a result of local crushing, $\Delta E_{\text{c;n}}$), contact frictional forces ($\Delta E_{\text{c;fr}}$) and hydrodynamic drag (ΔE_{drag}). In addition, there is a small residual energy component resulting from the residual velocity of the ice bodies that are removed from the dynamically simulated domain (E_{res}). In the current implementation of the numerical model, no energy is dissipated in the splitting failure of ice floes. Since the structure is propagated with a constant velocity in both simulations, the energy input from structure propagation is proportional to the mean load from the structure on the ice in the structure propagation direction. Figure 5 shows the energy input and dissipation contributions.

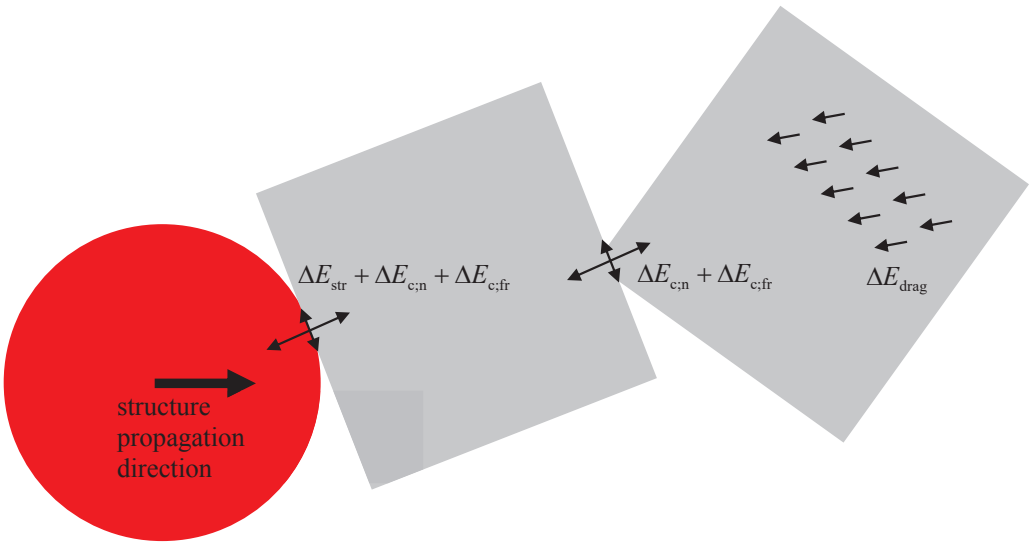

Figure 5. Energy input and dissipation during ice-structure interaction. Energy is introduced in the system by the load component of the ice-structure interaction load in the structure propagation direction. Energy is dissipated in the ice-structure contacts and in ice-ice contacts by contact crushing and friction, and by hydrodynamic drag.

Figure 6 shows the relative contributions of the different energy dissipation mechanisms in the simulation with natural floes and square floes, respectively.

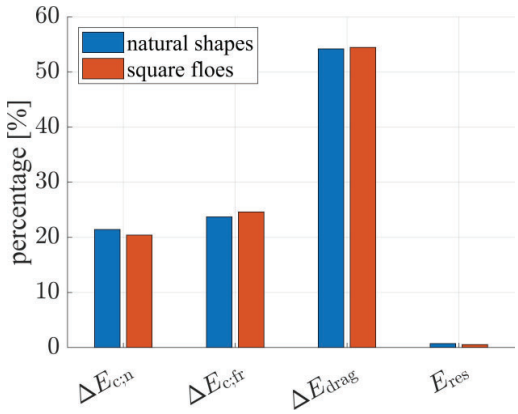

Figure 6. Relative energy dissipation by collisions and drag, natural floe shapes and square floe shapes.

The contributions of the different energy dissipation mechanisms are similar in the natural floe shape simulations and in the square floe shape simulations. In both simulations, 54% of the energy introduced by the moving structure is dissipated by the hydrodynamic drag on the ice floes. The remaining energy is dissipated in the plastic collisions between ice floes and between ice floes and the structure. Frictional contact forces account for a slightly higher proportion of energy dissipation than the normal contact forces. A low proportion of 0.74% (natural) and 0.56% (square) of the introduced energy is removed from the simulation in the form of the residual kinetic energy of bodies that are removed from the simulation domain.

The force propagation and dissipation in the broken ice field is studied both visually and quantitatively. Visual comparison of the simulation results shows that force networks within the broken ice are larger and propagate further from the structure in the simulations with square floes. This results in a higher ice floe area that is accelerated and displaced by the moving structure, leading to a higher ice resistance.

We assign a scalar loading value to each ice floe in order to study the difference in force propagation and dissipation in the broken ice field. The loading value is defined similar to the value used to visualize force chains in Paavilainen & Tuhkuri, (2013), as the maximum eigenvalue of the load tensor $\hat{\alpha}_{ij}$:

$$\hat{\alpha}_{ij} = \sum_{c=1}^{Nc} f_i^c r_j^c \tag{1}$$

in which Nc is the number of contacts of each floe, f_i^c are the contact force vectors, and r_j^c are normalized vectors from the body's centre of gravity to the contact point. Differences in force propagation between the floe fields with natural and square floe shapes are quantified by comparing the mean combined floe area of all floes with a loading value above a range of threshold load values:

$$\bar{A}(F_{thr}) = \frac{\sum_{t=1}^{N_t} A_{\lambda_{max} > F_{thr}}(t)}{N_t} \tag{2}$$

in which $\overline{A}$ is the mean broken ice area with a loading value above threshold load value F_{thr}, N_t is the number of time steps and $A_{\lambda_{\max}>F_{\text{thr}}}(t)$ is the broken ice area with a loading value above load value F_{thr} in each time step.

Figure 7 shows a visual comparison of the force networks occurring in the square floe simulations and the force networks occurring in the real floe simulations. The area of the floes above a load value at a time instance is the summation of the top areas of all coloured floes. A load value of 5 kN is used in the left figures and a load value of 0.25 MN is used in the right figures.

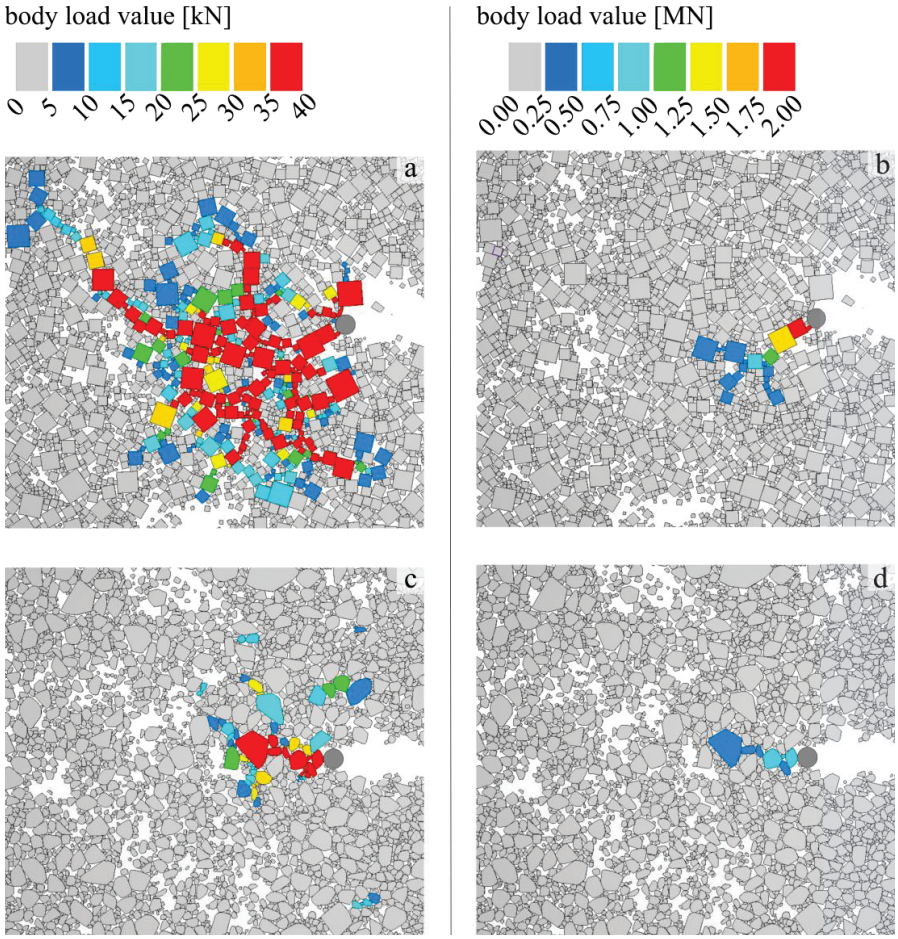

Figure 7. Floes with a load value exceeding a threshold level (coloured floes) for the simulations with square floes (top) and the simulations with natural floe shapes (bottom), and for different threshold levels (left and right).

The resulting load-area curve is shown in Figure 8. Figure 8 shows that the force network is larger in the square floe simulations. Depending on the threshold load level, the mean floe area with a load value higher than the threshold load is 2.15 to 3.13 times higher in the square floe simulations.

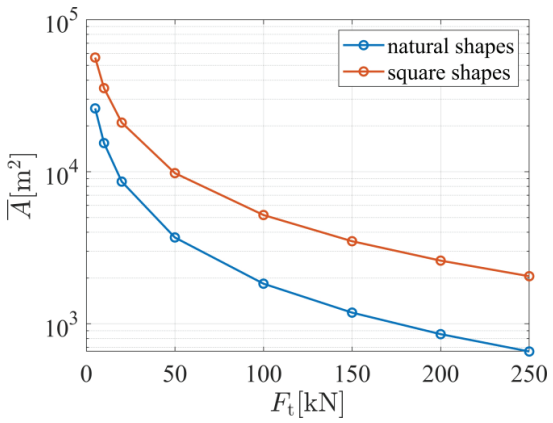

Figure 8. Mean total floe area of the floes exceeding a threshold load level.

DISCUSSION

The mean and standard deviation in the simulation with square floe shapes are almost twice as high as the mean and standard deviation in the simulation with real floe shapes. This difference cannot be explained by comparing the energy dissipation mechanisms. The relative contributions of contact plasticity, friction and drag to the energy dissipation are similar for the simulations with natural and with square floe shapes. Therefore we focus in this section on the force propagation and dissipation behaviour within the broken ice field, in order to clarify the differences between square floe shape and natural floe shape interaction.

In order to gain insight in the differences in force propagation and dissipation, the area-load curved are normalized by scaling the load thresholds with the mean structure load value. The mean area-over-load-threshold as a function of the normalized load thresholds can be described by a power function of the form:

$$\overline{A}(F_{\text{thr}}) = a\left(\frac{F_{\text{thr}}}{\overline{F}_{\text{thr;s}}} + b\right)^{c} + d \tag{3}$$

in which $\overline{F}_{\text{thr;s}}$ is the mean load value of the structure, constants b and c have no units and constants a and d have the unit of m^2. The normalized area-load curves are shown in Figure 9.

The normalized area-load curve of the square floe shape simulation can be scaled to match the area-load curve of the natural floe shape simulation by applying a scaling factor of ~0.7:

$$\overline{A}_{\text{nat}} \approx 0.7\overline{A}_{\text{sq}} \tag{4}$$

The scaled results, as well as a power law fit of the natural and scaled results, are shown in Figure 9. The normalized area-load curve of the natural floe shape simulation and the scaled area-load curve of the square floe simulation can be accurately approximated by the power law function given in Equation (3) with the coefficients $a = 2034$, $b = 0.0127$, $c = -0.891$ and $d = -359.5$. The exact values of coefficient a, b, c and d are not so relevant since they depend on the chosen simulation parameters such as drag and friction coefficients. However, it is an important finding that the normalized area-load curves of both the natural and square floe shape simulations can be approximated with the same power $c = -0.891$. This indicates that the propagation and dissipation processes are similar in the natural and square floe simulations.

The force network in the square floe simulations can be seen as a scaled-up version of the force network in the natural floe simulations.

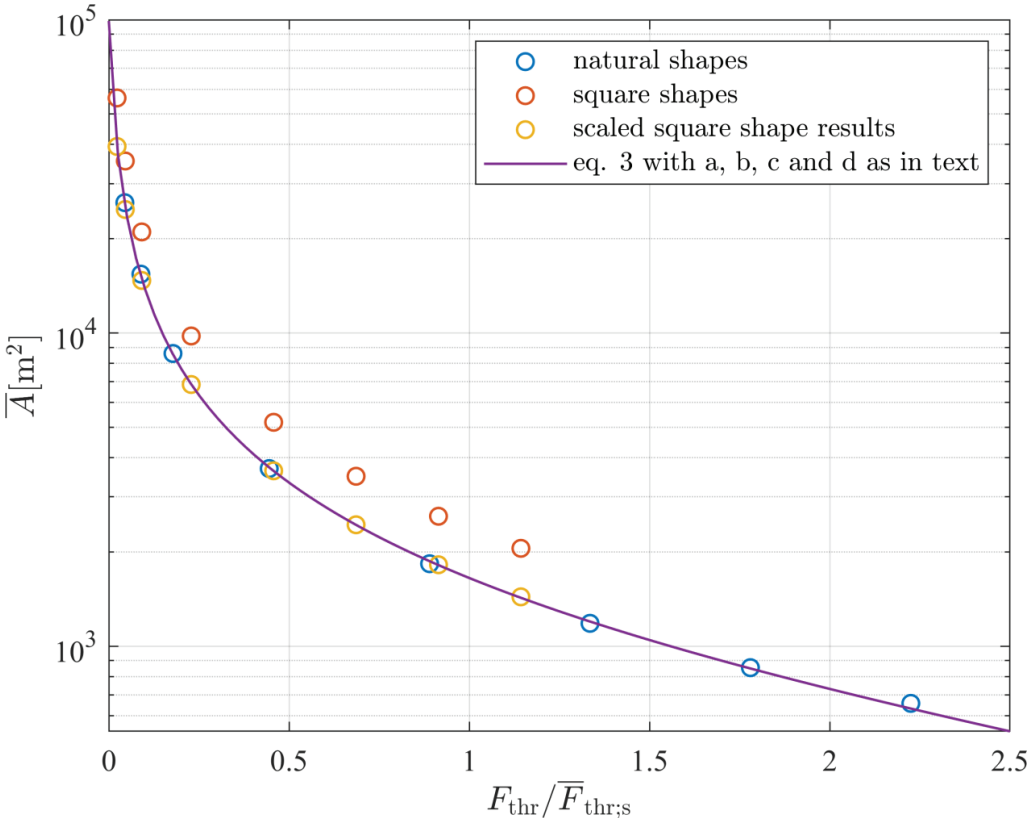

Figure 9. Mean total floe area of the floes exceeding a normalized threshold value, including the scaled square floe results and a power law fit to the natural floe shape and scaled results.

The normalized area-load curve of the natural floe shape simulations can be obtained from the normalized area-load curve of the square floe simulations by applying a scaling factor of ~0.7, while the ratio between the structure load values of the natural and square floe simulations is ~0.51. Based on simple analytical checks considering only hydrodynamic drag forces on the ice floes, we would expect that the normalized area-load curve should scale proportional to the mean structure load values. Clearly, this is not the case.

The reason for the difference between the scaling factor of the area-load curve and the scaling factor of the structure load values is currently unclear. We expect that it is related to the definition of the load value as the maximum eigenvalue of load tensor $\hat{\alpha}_{ij}$. This is supported by the fact that using a different definition of load value leads to a different scaling factor. Using the maximum contact force of each floe in each time step as representative load value leads to a scaling factor of the area-load curve of ~0.8, showing that the scaling factor is dependent on the load value definition. The power c in Equation (3), on the other hand, seems largely independent from the definition of the load value.

Model Limitations

As any numerical model, the model used in this study is a simplification of reality. The simplifications made may influence the modelling results. To investigate the influence of parameter and modelling choices on the simulation results, a sensitivity study was performed by van den Berg et al. (2019). For a further discussion on the influence of modelling and parameter choices on the model results, the reader is referred to this study.

CONCLUSIONS

This study investigates the influence of floe shape on the load experienced by a vertical-sided structure moving through a broken ice field. Numerical simulation results of a simulation with natural ice floe shapes and a simulation with square ice floe shapes are compared. Other than the difference in floe shape, the simulations are identical. The simulation with square floe shapes results in a mean ice load and load standard deviation opposite to the structure propagation direction that is 86% (mean) and 69% (standard deviation) higher than the mean load and standard deviation resulting from the simulation with natural floe shapes.

The energy dissipation mechanisms are similar in the square and natural floe shape simulations. The force networks within the broken ice are larger and propagate further from the structure in the simulations with square floes. This results in a higher ice floe area that is accelerated and displaced by the propagating structure, leading to a higher ice resistance. The force propagation and dissipation behaviour is compared by studying the mean-area-over-load-threshold curves for both simulations. The primary finding is that the normalized area-load curves of the square and natural floe shape simulations can be approximated by a power function with the same power. This indicates that the propagation and dissipation processes are similar in the natural and square floe simulations. The force network in the square floe simulations can be seen as a scaled-up version of the force network in the natural floe simulations.

ACKNOWLEDGEMENTS

The authors would like to acknowledge the support of the SAMCoT CRI through the Research Council of Norway and all of the SAMCoT Partners.

REFERENCES

Haase, A., van der Werff, S., Jochmann, P., 2012. DYPIC - Dynamic Positioning in Ice - First Phase of Model Testing, in: Proceedings of the ASME 2012 31st International Conference on Ocean, Offshore and Arctic Engineering. Rio de Janeiro, pp. 1–8.

Hoving, J.S., Vermeulen, R., Mesu, A.W., Cammaert, G., 2013. Experiment-Based Relations between Level Ice Loads and Managed Ice Loads on an Arctic Jack-Up Structure, in: Proceedings of the 22nd International Conference on Port and Ocean Engineering under Arctic Conditions. Espoo, Finland.

Lu, W., Lubbad, R., Løset, S., 2015. In-plane fracture of an ice floe: A theoretical study on the splitting failure mode. Cold Reg. Sci. Technol. 110, 77–101. doi:http://dx.doi.org/10.1016/j.coldregions.2014.11.007

Lubbad, R., Løset, S., Lu, W., Tsarau, A., van den Berg, M., 2018a. An overview of the Oden Arctic Technology Research Cruise 2015 (OATRC2015) and numerical simulations performed with SAMS driven by data collected during the cruise. Cold Reg. Sci. Technol. 156, 1–22. doi:https://doi.org/10.1016/j.coldregions.2018.04.006

Lubbad, R., Løset, S., Lu, W., Tsarau, A., van den Berg, M., 2018b. Simulator for Arctic Marine Structures (SAMS), in: ASME 2018 37th International Conference on Ocean, Offshore and Arctic Engineering. American Society of Mechanical Engineers, p. V008T07A020-V008T07A020.

Paavilainen, J., Tuhkuri, J., 2013. Pressure distributions and force chains during simulated ice rubbling against sloped structures. Cold Reg. Sci. Technol. 85, 157–174. doi:10.1016/j.coldregions.2012.09.005

Rheem, C.K., Yamaguchi, H., Kato, H., 1997. Distributed mass/discrete floe model for pack ice rheology computation. J. Mar. Sci. Technol. 2, 101–121. doi:10.1007/BF02491524

Tsarau, A., 2015. Numerical Modelling of the Hydrodynamic Effects of Marine Operations in Broken Ice. Norwegian University of Science and Technology.

Tsarau, A., van den Berg, M., Lu, W., Lubbad, R., Løset, S., 2018. Modelling Results With a New Simulator for Arctic Marine Structures-SAMS, in: ASME 2018 37th International Conference on Ocean, Offshore and Arctic Engineering. ASME.

van den Berg, M., Lubbad, R., Løset, S., 2018. An implicit time-stepping scheme and an improved contact model for ice-structure interaction simulations. Cold Reg. Sci. Technol. 155, 193–213. doi:https://doi.org/10.1016/j.coldregions.2018.07.001

van den Berg, M., Lubbad, R., Løset, S., 2019. The effect of ice floe shape on the load experienced by vertical- sided structures interacting with a broken ice field. Mar. Struct. 65, 229–248. doi:10.1016/j.marstruc.2019.01.011

Yamaguchi, H., Rheem, C.K., Toyada, M., Matsuzawa, T., Nakayama, H., Kato, H., Kato, K., Adachi, M., 1997. Influence of Floe Shape on Behaviour of Ice Floes around a Structure, in: OMAE - Volume IV, Arctic/Polar Technology ASME. pp. 461–468.

Zhang, Q., Skjetne, R., 2015. Image processing for identification of sea-ice floes and the floe size distributions. IEEE Trans. Geosci. Remote Sens. 53, 2913–2924. doi:10.1109/TGRS.2014.2366640

Appendix F

Variability in the results of ice-tank tests with broken ice

This paper is submitted to Marine Structures.